BURIAL AND EXHUMATION OF THE TERRA NOVA BAY REGION, TRANSANTARCTIC MOUNTAINS

Jannis Dominik Prenzel

Dissertation zur Erlangung des Doktorgrades der Naturwissenschaften

Fachbereich 5 – Geowissenschaften

Universität Bremen

15.01.2014

Erstgutachter:	PD Dr. Frank Lisker
Zweitgutachter:	Prof. Dr. Wolfgang Bach
Datum des Kolloquiums:	25.04.2014

Name: Jannis Dominik Prenzel Datum: 15.01.2014

Anschrift:
Lunder Straße 11
13189 Berlin
Deutschland

Erklärung

Hiermit versichere ich, dass ich

1. die Arbeit ohne unerlaubte fremde Hilfe angefertigt habe,

2. keine anderen als die von mir angegebenen Quellen und Hilfsmittel benutzt habe und

3. die den benutzten Werken wörtlich oder inhaltlich entnommenen Stellen als solche kenntlich gemacht habe.

Bremen, den 15.01.2014

(Unterschrift)

Acknowledgements

First of all, I thank *Frank Lisker (Universität Bremen)* who initiated this work. Thank you for supervising this thesis, your extensive critical and constructive comments on the manuscripts, and last but not least for all the productive numerous discussions. Many thanks go also to *Cornelia Spiegel (Universität Bremen)* and *Andreas Läufer (Bundesanstalt für Geowissenschaften und Rohstoffe, Hannover)* as co-applicants of the project. Thank you for constructive manuscript reviews and critical discussions. Maria Laura Balestrieri is thanked for providing material and data from Mount Matz and Mount Nansen, and constructive criticism on the manuscripts. I also want to thank Wolfgang Bach for the second opinion of this dissertation. F. Balsamo, G. Di Vincenzo, S. Rocchi, F. Rossetti and F. Storti are acknowledged for constructive comments.

Funding of this work with the DFG research project LI745/12-1 is gratefully acknowledged. I wish to thank the *Bundesanstalt für Geowissenschaften und Rohstoffe* for the invitation to participate in the Antarctic GANOVEX X expedition in 2009/2010. Special thanks go to the crews of *MS Italica* and *Helicopters New Zealand* for logistic support and the members of the *GANOVEX X team* for cooperative fieldwork and stimulating discussions.

The whole *staff of the working group Geodynamics of the Polar Regions (Universität Bremen)* is thanked for help and advice. Special thanks go to *Nina Dörr* for her help during my first year of the work and *Julia Lindow* for proof-reading my manuscripts. *Anke Toltz* and *Carina Werner* are thanked for rock preparation, *Vera Kolb* for IT-support, *Florian Riefstahl* for support with GMT, and *Simon Elfert*, *Gisela Haack*, *Nicole Lucka* and *Wolfgang Reiter* for general help and advice.

Last but not least, I thank my family and all my friends who supported me in any way during my thesis. Special thanks go to my girlfriend *Nadja* for her patience and motivation during my time in Bremen.

Zusammenfassung

Das Transantarktische Gebirge repräsentiert die exponierte Hauptschulter des Westantarktischen Riftsystems, welches sich über ungefähr 3500 km entlang des antarktischen Kontinents erstreckt. Aufgrund des weitgehenden Fehlens mesozoisch – känozoischer Sedimentgesteine, kann die jüngere geologische Geschichte des Gebirges nicht mittels petrologischer oder stratigraphischer Belege rekonstruiert werden. Existierende Rekonstruktionen der Exhumierungsgeschichte beruhen daher vor allem auf thermochronologischen Methoden wie der Apatit-Spaltspuranalyse. Durch die Anwendung qualitativer thermochronologischer Interpretationskonzepte, wie zum Beispiel dem *break in slope*, welcher bei vertikalen Altersprofilen für den Beginn schneller Gesteinsabkühlung steht, wurde die Entstehung des Transantarktischen Gebirges durch Krustenverdickung infolge eines umfangreichen jurassischen Magmatismus und zahlreicher Exhumierungsphasen seit der frühen Kreide erklärt. Dieses Exhumierungsszenario steht jedoch in starkem Widerspruch zu geologischen Beobachtungen, thermischen Indikatoren sowie der Korrelation der Spaltspurdaten und stratigraphischer Informationen. Beobachtungen und Indikatoren implizieren hingegen eine lang anhaltende mesozoische Versenkung der jurassischen Oberfläche, welche vermutlich auf die Existenz eines Sedimentbeckens innerhalb der Rossmeer Region der Antarktis zurückzuführen ist.

Die vorliegende Arbeit konzentriert sich auf die *Terra Nova Bay* Region im Rossmeer Sektor des Transantarktischen Gebirges, in welcher die geologischen Widersprüche zum traditionellen Exhumierungsszenario zuerst erkannt wurden. In dieser Region wird granitisches Grundgebirge kambrisch-ordovizischen Alters von mesozoischen *Beacon Sandsteinen* überlagert, welche ihrerseits von magmatischen Gesteinen des ca. 182 Ma alten *Ferrar Events* durchschlagen und/oder überlagert werden. Für die Überprüfung und Quantifizierung des postulierten Sedimentbeckens wurden Gesteinsproben von vertikalen Profilen in der nördlichen *Terra Nova Bay* Region *(Eisenhower Range, Deep Freeze Range)* mit der Apatit-Spaltspur- und der Apatit (U-Th-Sm)/He-Methode analysiert, und mit Paläotemperaturanalysen an *Beacon Sandsteinen* aus der *Eisenhower Range* und publizierten Spaltspurdaten aus der südlichen *Terra Nova Bay Region* (*Prince Albert Mountains*) erweitert. Unter Berücksichtigung der geologischen und thermischen Rahmenbedingungen wurden mittels thermischer Modellierungen der Spaltspur- und (U-Th-Sm)/He Daten hauptsächlich folgende Themenschwerpunkte bearbeitet: (I) Überprüfung der Gültigkeit qualitativer thermochronologischer Interpretationskonzepte; (II) Quantifizierung der Versenkungs- und Exhumierungsgeschichte der *Terra Nova Bay* Region; (III) Untersuchung der Entwicklungsgeschichte der heutigen regionalen Landschaft, bestehend aus tief eingeschnittenen Hochplateaus in unmittelbarer Nähe zu einer flachen Küstenebene, sowie (IV) die Rekonstruktion der Geometrie, der lateralen Ausdehnung und der lokalen Tiefen des Sedimentbeckens innerhalb der *Terra Nova Bay* Region.

Der thermochronologische Datensatz, bestehend aus 54 analysierten Proben von sieben vertikalen Profilen der *Eisenhower Range* und der *Deep Freeze Range,* zeigt Spaltspuralter zwischen 32±2 Ma und 259±18 Ma sowie (U-Th-Sm)/He-Alter zwischen 28±3 Ma und 274±17 Ma, die mit den Probenhöhen korrelieren (220 – 3120 m). Thermische Modellierungen dieser Daten sowie der publizierten Spaltspurdaten aus den *Prince Albert Mountains* weisen im Anschluss an das *Ferrar*

Event eine lang anhaltende mesozoische Aufheizung der jurassischen Oberfläche von ungefähr 80°C auf und belegen eine schnelle spät-eozäne Abkühlungsphase. Diese Temperaturen stimmen mit post-jurassischen Temperaturen zwischen ~60° und 100°C überein, welche mittels einer Reifegradbestimmung an organischem Material in den *Beacon Sandsteinen* ermittelt wurden. Die Paläotemperaturen der vertikalen Höhenprofile lassen für die gesamte Region auf einen erhöhten jurassischen (~45°C/km) sowie einen moderaten kretazisch-eozänen (~25 – 30°C/km) geothermischen Gradienten schließen. Diese Entwicklung des Wärmeflusses ist auf jurassische Riftprozesse und den *Ferrar* Magmatismus mit anschließender isobarer Abkühlung zurückzuführen.

Der starke Widerspruch der ermittelten thermischen Geschichte zum traditionellen Exhumierungsszenario des Transantarktischen Gebirges zeigt, dass qualitative thermochronologische Interpretationskonzepte wie der *break in slope* weder benutzt werden können, um den Beginn schneller Gesteinsabkühlung zu datieren, noch um thermische Modellierungen zu ersetzen. Modellierungsexperimente demonstrieren den Einfluss verschiedener Faktoren (z.B. die thermische Geschichte vor der schnellen Abkühlung, maximale Paläotemperaturen, Abkühlrate, geothermischer Gradient) auf die Position und das Muster eines *break in slope.* Dies bedeutet, dass die früheren qualitativen thermochronologischen Studien aus dem Transantarktischen Gebirge und ähnliche Studien weltweit durch thermische Modellierungen unter der Berücksichtigung geologischer und thermischer Informationen überprüft werden müssen.

Die mechanische Kompaktion der *Beacon Sandsteine* verweist auf eine höhere Gesteinsüberlagerung, als regional stratigraphisch dokumentiert ist. Die gemeinsame Verwendung der Paläotemperaturen und der geothermischen Gradienten lässt auf eine spät-jurassische bis eozäne Versenkung des Grundgebirges auf eine Tiefe zwischen ~2 km in der nördlichen und ~3.5 km in der südlichen *Terra Nova Bay* Region schließen. Da diese Versenkung vom Jura ins Eozän zunimmt, kann diese nicht allein durch die Überlagerung von *Beacon* und *Ferrar* Gesteinen erklärt werden. Eine notwendige zusätzliche, bis ins Eozän anhaltende, Sedimentablagerung anschließend an das *Ferrer Event*, ist auf die Existenz eines mesozoisch – eozänen Sedimentbeckens in der *Terra Nova Bay* Region zurückzuführen. Berechnungen, basierend auf den Paläotemperaturen, geothermischen Gradienten und Modellen, verweisen auf eine regional einheitliche Sedimentmächtigkeit von ca. 1 km. Die geringere Versenkung der nördlichen *Terra Nova Bay* Region beruht hingegen auf einer regional niedrigeren Mächtigkeit der *Beacon* und *Ferrar* Gesteine von ca. 1 km. Eine mögliche Erklärung dafür wäre die Existenz einer topographischen Mulde innerhalb der heutigen *Prince Albert Mountains* bevor/während des *Ferrar Events*, welche einen Hauptablagerungsraum der Ferrar Gesteine bildete.
Die jurassische Bildung des Beckens wird durch das Einsetzen von Extension innerhalb des Westantarktischen Riftsystems vor ~180 Ma erklärt, während die darauffolgende mesozoisch – eozäne Sedimentakkumulation durch ein stabiles Spannungsfeld und eine langsame E-W Extension während der Öffnung des Ross Meers zu erklären ist. Die schnelle eozäne/oligozäne Exhumierungsphase verweist auf eine vollständige Abtragung der Sedimente sowie die Freilegung der darunterliegenden *Ferrar* Gesteine innerhalb von ~5 myr. Das Einsetzen dieser Beckeninversion ist auf eine Phase erhöhter Extension im Ross Meer durch die

endgültige Trennung der Antarktis von Australien und einer damit verbundenen tektonischen Reorganisation in der Ross Meer Region von kretazisch orthogonalem zu känozoisch schrägem Rifting zurückzuführen. Im überregionalen Maßstab fällt eine, durch die Bildung des Ostantarktischen Eisschildes repräsentierte, klimatische Abkühlung zeitlich mit tektonischen Prozessen, wie der Bildung des Westantarktischen Riftsystems und der Öffnung der Tasmanischen Seepassage zwischen der Antarktis und Australien, zusammen. Regionale Exhumierungsunterschiede seit dem frühen Oligozän lassen auf ein stärkeres glaziales Einschneiden an der Küste schließen. Dies kann durch die Nähe des Westantarktischen Riftsystems sowie einer entsprechenden Hebung der Riftschulter und einem Isostasie-Ausgleich erklärt werden, und impliziert eine rückschreitende Erosion von der Küste entlang der Gletscher ins Landesinnere.

Abstract

The Transantarctic Mountains (TAM) represent the exposed main shoulder of the West Antarctic Rift System that extends along the Antarctic continent over ~3500 km. Since Mesozoic and Cenozoic sedimentary rocks are missing to a large extent, the younger geological history of the TAM cannot be reconstructed by petrological or stratigraphic evidence, and mainly relies on thermochronological record. Based on apatite fission track (AFT) data and qualitative thermochronological interpretation concepts such as the break in slope in vertical age profiles, which works as qualitative marker for the onset of accelerated rock cooling, the origin of the TAM has been related to crustal thickening during extensive Jurassic magmatism followed by numerous exhumation phases since the Early Cretaceous. However, geological evidence together with the correlation of AFT data and stratigraphic information, plus various thermal indicators are in rigorous contrast to the established exhumation scenario, and refer to an alternative, more complex cooling history that involves long-lasting Mesozoic burial related to sediment deposition within an extensive sedimentary basin in the Ross Sea sector of Antarctica.

This thesis focuses on the *Terra Nova Bay* region in the Ross Sea sector of the TAM where conflicts to the traditional exhumation scenario have been recognized firstly. In this region, Cambro-Ordovician granitic basement is covered by Mesozoic *Beacon sandstones* which are overlain or intercalated by rocks of the 182 Ma *Ferrar magmatic suite*. For verification and quantification of the proposed basin scenario, AFT and (U-Th-Sm)/He (AHe) thermochronology was applied on samples from vertical profiles across the basement in the northern *Terra Nova Bay* region (*Eisenhower Range, Deep Freeze Range*) and supplemented by paleotemperature analysis on overlying *Beacon sandstones* from the *Eisenhower Range* and published AFT data of vertical basement profiles from the southern *Terra Nova Bay* region (*Prince Albert Mountains*). Thermal history modeling of the AFT and AHe data incorporating the geological and thermal frame was performed (I) to evaluate the significance of qualitative interpretation concepts of thermochronological data for the reconstruction of thermal histories, and to reconstruct and quantify (II) the burial and exhumation history of the *Terra Nova Bay* region, (III) the development of the present-day landscape consisting of deeply incised high-elevated plateaus in immediate vicinity to a sea-level coastal plain, and (IV) the regional geometry, lateral extension and local depths of the sedimentary basin in the *Terra Nova Bay* region.

The new thermochronological record comprising data of 54 samples of seven vertical profiles from the *Eisenhower Range* and *Deep Freeze Range* yield AFT ages between 32±2 Ma and 259±18 Ma, and AHe ages between 28±3 Ma and 274±17 Ma which closely correlate with samples altitudes (220 – 3120 m). Thermal history modeling of this, and of published AFT data from the *Prince Albert Mountains*, detect long-lasting Mesozoic heating of the regional Jurassic surface to temperatures above ~80°C subsequent to the *Ferrar* magmatism and constrain Late Eocene rapid cooling. These temperatures are in accordance with post-mid Jurassic temperatures of ~60° – 100°C derived by organic maturation data from *Beacon sandstones*. The regression of paleotemperature estimates against sample altitudes refers to a high Jurassic geothermal gradient (~45°C/km) related to rifting processes and *Ferrar*

magmatism and a moderate Cretaceous-Eocene geothermal gradient (~25 – 30°C/km) due to subsequent isobaric cooling.

The strong contrast of the documented thermal history to the traditional exhumation scenario of the TAM shows that qualitative interpretation concepts of thermochronological data such as the *break in slope* neither can be used to directly date onset of rapid rock cooling nor substitute thermal history modeling. It is demonstrated via modeling experiments that position and shape of a *break in slope* results from various factors (e.g. thermal history prior to rapid cooling, maximum paleotemperatures, cooling rate, and geothermal gradient). The weakness of qualitative interpretation concepts for thermal history interpretation implies that earlier studies from the TAM and similar settings elsewhere need to be validated by combining thermal history modeling of thermochronological data and supplementary geological information.

The mechanical compaction of *Beacon sandstones* requires a higher overburden than documented in the regional stratigraphic record. Paleotemperature estimates and geothermal gradients used in tandem refer to substantial Late Jurassic to Eocene burial of the basement between ~2 km in the northern and ~3.5 km in the southern *Terra Nova Bay* region. Since this burial increases from Jurassic to Eocene, it cannot be explained by *Beacon* and *Ferrar* rock overburden only. Additional post-mid Jurassic sediment accumulation persisting until rapid Late Eocene exhumation provides evidence for Mesozoic – Eocene sedimentary basin existence within the *Terra Nova Bay* region. Calculations based on paleotemperatures, geothermal gradients and models infer a quite uniform sediment thickness of ~1 km. Minor burial in the northern *Terra Nova Bay* region refers to a regional ~1 km lower thickness of *Beacon* and *Ferrar* rocks. This is probably attributed to a pre-*Ferrar* position of the *Eisenhower Range* and *Deep Freeze Range* at the margin of a paleodepression within the *Prince Albert Mountains* that hosted the main feeder of *Ferrar magmatism*.

Mid-Jurassic basin formation with subsequent Mesozoic – Eocene sediment accumulation is explained by initiation of extension within the West Antarctic Rift System at ~180 Ma and a continuous stable stress field of low E-W extension during Ross Sea opening until the Late Eocene. Rapid Late Eocene/Early Oligocene exhumation infers complete removal of the sediments and (re-) exposure of underlying *Ferrar* rocks/granitic basement within ~5 myr. This onset of basin inversion is linked to right lateral strike-slip and transtensional faulting attributed to major Eocene tectonic reorganization in the Ross Sea region from Cretaceous orthogonal to Cenozoic oblique rifting related due a phase of increased extension within the Ross Sea due to final Eocene separation of Antarctica from Australia. At supraregional scale, climate change represented by the formation of the East Antarctic continental ice shield overlaps with tectonic processes related to the formation of the West Antarctic Rift System, and the onset of sea floor spreading and opening of the Tasman gateway between Antarctica and Australia. Regional differential exhumation since the Early Oligocene refers to higher incision at the coast compared to the interior. This is related to the vicinity of the West Antarctic Rift System and corresponding necking, rift shoulder uplift and isostatic compensation, and implies backstepping erosion from the coast along the glaciers towards the interior of the *Terra Nova Bay* region.

Contents

1) Introduction

1.1) Setting and preliminary work

The Transantarctic Mountains (TAM) with altitudes of up to ~4500 m cross Antarctica for ~3500 km from the Ross Sea embayment at the Pacific Ocean side to the Weddell Sea embayment at the Atlantic Ocean side dividing the East Antarctic Craton (e.g. Victoria Land, Wilkes Land, and Dronning Maud Land) from the West Antarctic terrane assemblage (e.g. Marie Byrd Land; Fig. 1). Representing the exposed main shoulder of the West Antarctic Rift system, the TAM form the worldwide largest non-compressional mountain belt.

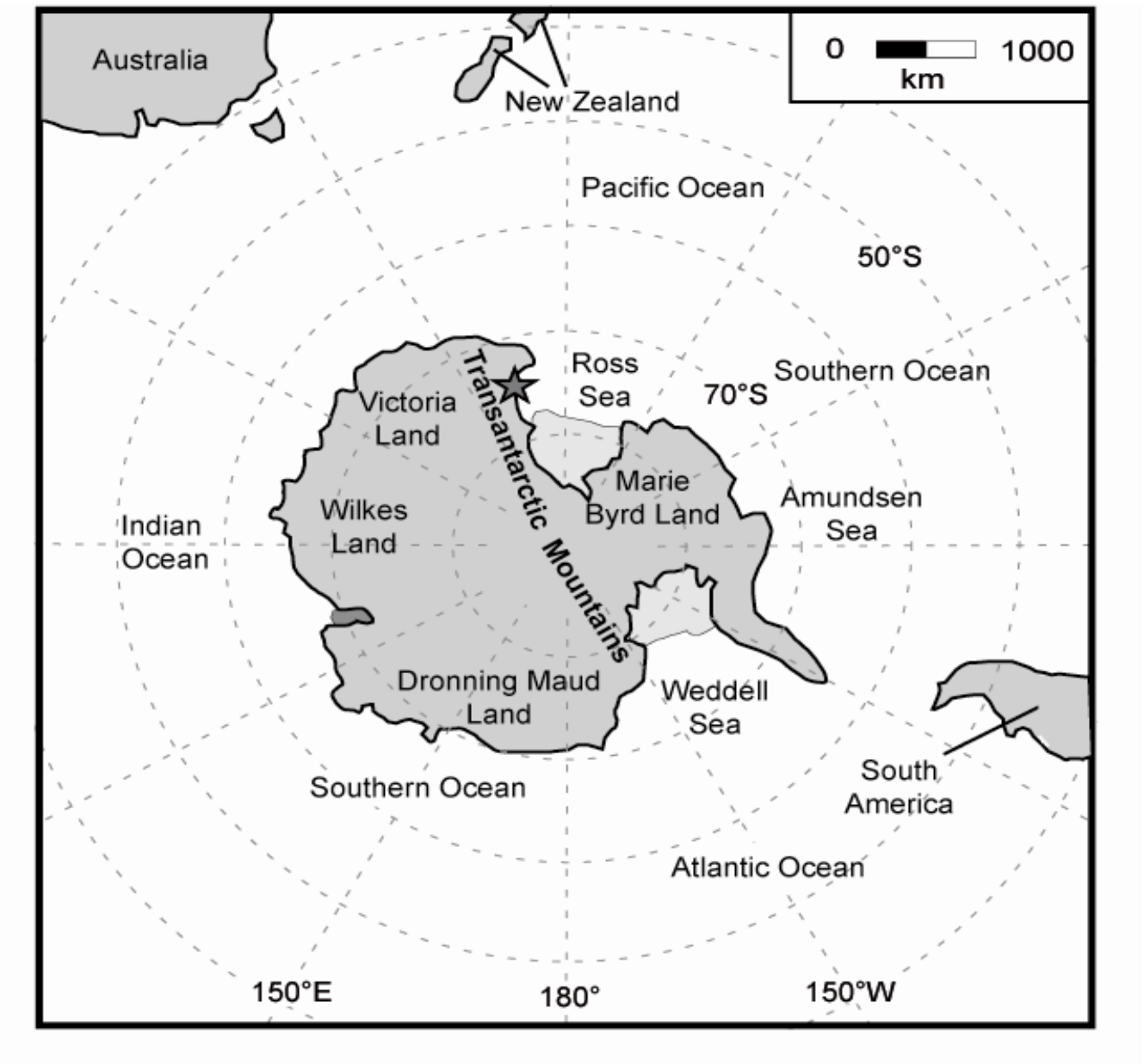

Figure 1: Geographic map of Antarctica and adjoining areas. The Terra Nova Bay region is marked with an asterisk (see Fig. 2).

The geological architecture of the TAM is quite uniform and simple. Basement consists of Proterozoic and Paleozoic magmatic and metamorphic rocks generated or overprinted by the ~490 – 540 Ma Ross Orogeny. Subsequently, the basement was eroded to a low-relief peneplain (Kukri Peneplain) and overlain by Devonian to Early Jurassic alluvial, shallow marine and volcaniclastic sediments. These sedimentary rocks, collectively defined as the Beacon Supergroup, were deposited in the Devonian to Jurassic Transantarctic Basin that occupied large parts of the Ross Sea sector of Antarctica, and locally reach thicknesses of up to a few hundred meters (e.g. Collinson et al., 1994; Elliot, 1992). Basement and Beacon rocks were covered, or intruded in form of dykes, by magmatic rocks during the Ferrar event at 182 Ma (e.g., Heimann et al., 1994: 180±1.8Ma; Encarnación et al., 1996: 183.6±1.8 Ma). The Jurassic Ferrar rocks were identified as a volcanic sequence containing syn-Ferrar pyroclastic and siliciclastic, partially fossil-bearing sedimentary sequences, pillow lavas, and phreatomagmatic structures and diatremes of local hydromagmatic explosive events (Viereck-Götte et al., 2007). Their thickness strongly varies throughout the TAM between a few hundred meters and up to ~1500 m (e.g., Elliot and Fleming, 2008). They form the youngest preserved rocks in most parts of the TAM and basement/Ferrar rocks are only locally overlain by Neogene volcanic rocks or Pliocene sediments and glacial deposits (e.g., GANOVEX Team, 1987).

The TAM have been discovered and investigated as early as in the beginning of the 20th century during the first British Antarctic expeditions (Ferrar, 1907; Priestley and David, 1912). However, since a direct investigation of their post-mid Jurassic geological history is generally handicapped by a large gap in the stratigraphic record between 182 Ma Ferrar magmatism (e.g., Heimann et al., 1994; Encarnación et al., 1996) and 20 Ma Late Cenozoic volcanism (LeMasurier and Thomson, 1990), the exhumation of the TAM is still today one of the most addressed subjects of controversy in Antarctic geology. Due to the missing petrological and stratigraphic evidence, the younger geological history of the TAM predominantly relies on thermochronological, structural and geophysical data, and geomorphological observation. The current thermochronological record consists of more than 500 apatite fission track (AFT) analyses from different segments along the entire mountain chain including horizontal and vertical profiles from northern Victoria Land in the northern Ross Sea region to the Scott Glacier region in the Central TAM (Fig. 3a; summarized by Fitzgerald, 2002, and Lisker, 2002).

AFT thermochronology is based on the temperature-dependent preservation of fission damages/tracks within apatite crystals. The fission track density within apatites provide information about time of rock cooling within/below temperatures of ~60 to 110-125 °C (AFT age) while associated track length shortening depending on the temperature yields additional information about the style of rock cooling (Fission track length distribution; e.g. Wagner et al., 1989; and see 2.2). Early AFT studies on vertical profiles from the TAM documented a transition in the AFT age-elevation regression from a flat gradient of older ages at higher altitudes to a steep gradient of younger ages at lower altitudes (e.g., Fitzgerald and Gleadow, 1988; Balestrieri et al., 1997) that is usually associated with a characteristic fission track length distribution pattern with shortened track lengths related to the flat gradient and longer track lengths associated with the steep gradient (e.g., Fitzgerald and Gleadow, 1988; Fitzgerald et al., 1995). This change of age-elevation regression, referred to as the *break in slope,* was thought to mark the initiation of accelerated rock cooling/exhumation (e.g., Gleadow et al., 1984; Fitzgerald et al., 1986). Correspondingly, the position of a *break in slope* was used to constrain time and amount of rock cooling/exhumation, while rate of rock cooling/exhumation was estimated by the gradient of the steep regression (e.g., Fitzgerald and Gleadow, 1988; Wagner et al., 1989).

Based on the AFT data from the numerous vertical basement profiles along the TAM (Fig. 2a) and the application of qualitative thermochronological interpretation concepts such as the *break in slope* in vertical age profiles, a common cooling scenario has been predicted for the entire mountain chain (e.g., Fitzgerald, 1994, 2002). This scenario presumes monotonous, stepwise cooling without reheating since the Early Cretaceous and that overburden on granitic basement removed until today consists of Beacon and Ferrar rocks (e.g., Fitzgerald, 1994, 2002). Main cooling phases predicted for ~125 Ma, ~95 Ma and ~50 – 45 Ma were converted to exhumation episodes (Fig. 2b) and related to regional rifting events comprising the initial breakup between Australia and Antarctica in the Early Cretaceous, the main extension phase between East and West Antarctica in the Late Cretaceous, and the propagation of seafloor spreading from the Adare Trough into continental crust underlying the Ross Sea in the Eocene (summarized by Fitzgerald, 2002; and Lisker, 2002).

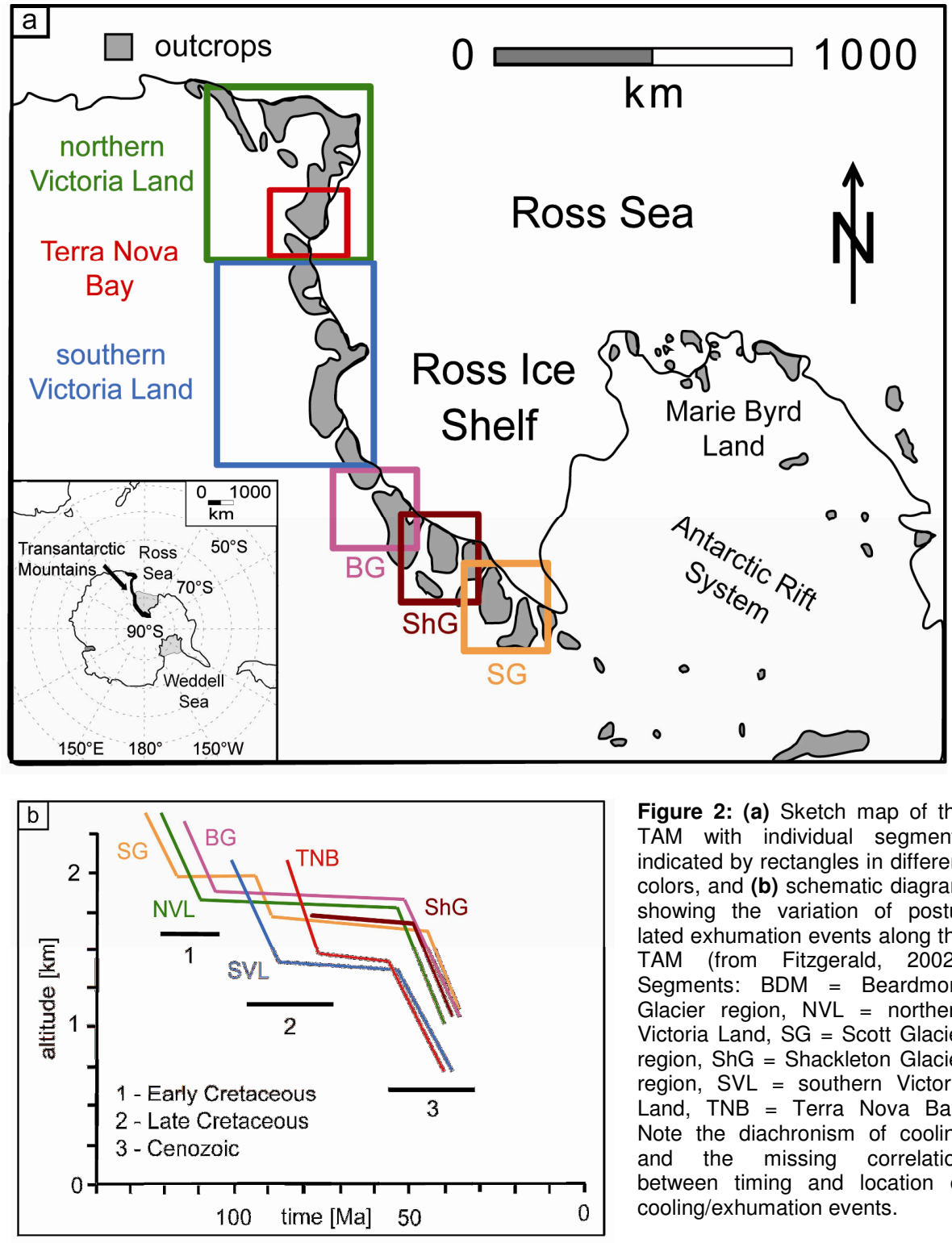

Figure 2: (a) Sketch map of the TAM with individual segments indicated by rectangles in different colors, and **(b)** schematic diagram showing the variation of postulated exhumation events along the TAM (from Fitzgerald, 2002). Segments: BDM = Beardmore Glacier region, NVL = northern Victoria Land, SG = Scott Glacier region, ShG = Shackleton Glacier region, SVL = southern Victoria Land, TNB = Terra Nova Bay. Note the diachronism of cooling and the missing correlation between timing and location of cooling/exhumation events.

This exhumation scenario is in well agreement with structural and geophysical data, and seems to be consistent when considered separately, but significant differential timing and amount of exhumation for the individual TAM segments appear without a systematic spatial pattern (Fig. 2b), and cannot be explained adequately in terms of monotonous, stepwise exhumation since the Early Cretaceous. Only the predicted rapid Eocene exhumation episode is consistent along the entire mountain chain (Fig.

2b). Additionally, the proposed exhumation history is based on a qualitative data interpretation only and could not be verified by thermal history modeling because of too short fission track lengths in most of the samples. Finally, and most importantly, previous studies do not sufficiently incorporate crucial geological information such as the presence and environment of Jurassic Ferrar volcanoclastic rocks (e.g., Viereck-Götte et al., 2007) which cover wide portions of the TAM and imply (near-) surface temperatures of the directly underlying analyzed basement at 182 Ma (Elliot and Fleming, 2008; Lisker and Läufer, 2013).

The contradiction of the stepwise exhumation scenario with the correlation of AFT data and Jurassic surface has been recognized firstly in the Terra Nova Bay region of northern Victoria Land that forms part of the northern TAM segment in the Ross Sea sector of East Antarctica (Figs. 1 and 2). This region comprises from north to south the Deep Freeze Range between Campbell Glacier and Priestley Glacier, the Eisenhower Range between Priestley Glacier and Reeves Glacier, and the northern Prince Albert Mountains between Reeves Glacier and Mawson Glacier (Fig. 3). Its present-day landscape is characterized by high-elevated plateaus and deeply incised, structurally defined glacial troughs. This provides an exceptional good outcrop access with one of the most complete surface exposures of Antarctica, and an exposed relief of up to 3.5 km. In this region, AFT data has been compiled for samples from ~2.5 km high vertical profiles across the granitic basement directly beneath Jurassic Ferrar rocks in the Eisenhower Range at Mount Matz and Mount Nansen (Figs. 3 and 4). AFT ages between ~35 and 200 Ma closely correlate with topographic elevation (Balestrieri et al., 1994). The age-elevation regression shows a pronounced *break in slope* at ~80 Ma, and an age-elevation discontinuity at ~50 Ma, accompanied by a change in the samples' fission track lengths distribution. Based on the *break in slope* and age-elevation discontinuity, the pattern has been interpreted qualitatively in terms of long-lasting tectonic quiescence during which the hanging section of the basement was exposed to temperatures of ~100 °C, followed by monotonous cooling since the Cretaceous with main cooling phases at ~80 and ~50 Ma which were converted into Late Cretaceous and Eocene exhumation (Balestrieri et al., 1994).

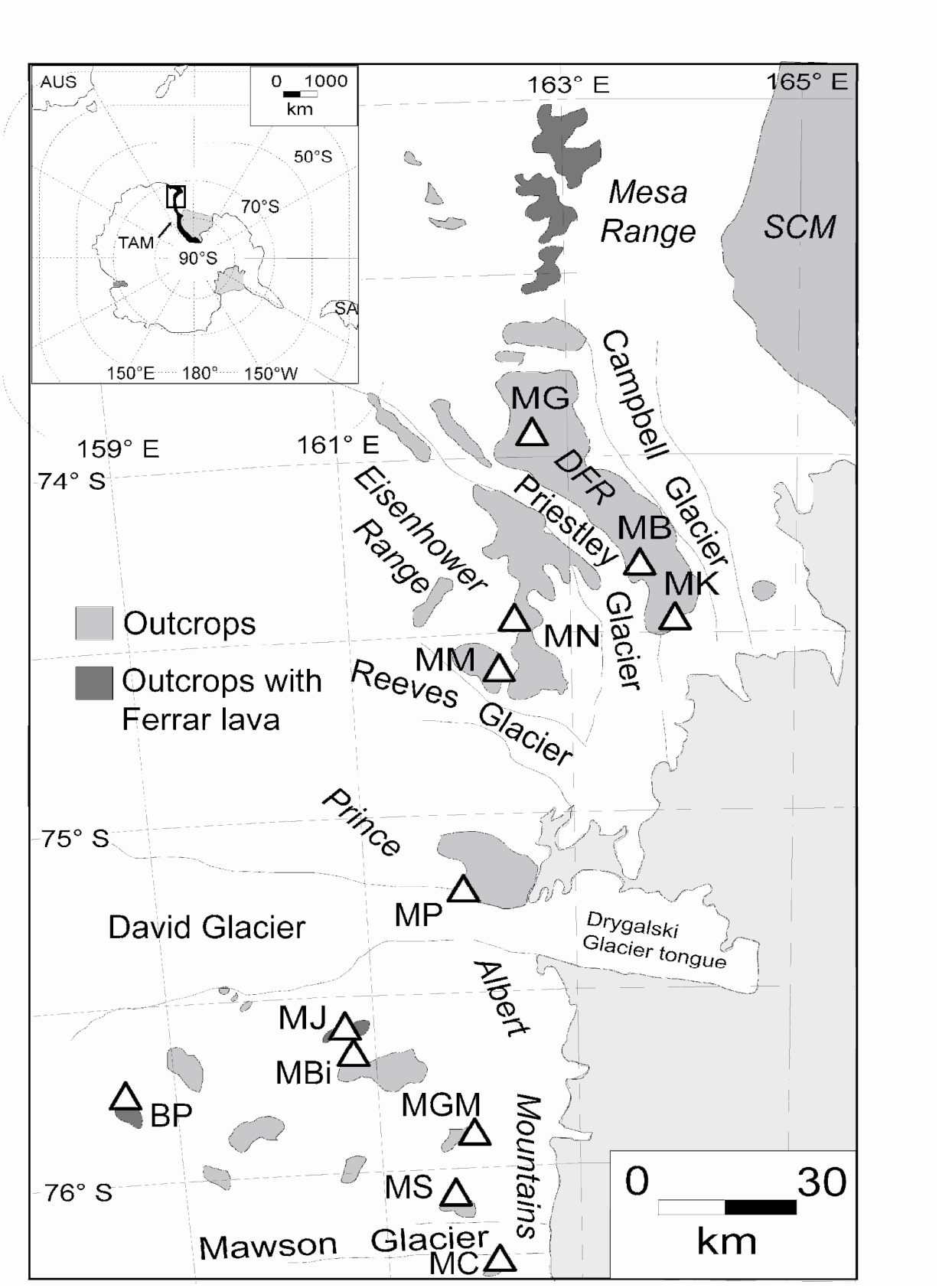

Figure 3: Sketch map of the Terra Nova Bay region comprising from north to south the Deep Freeze Range (DFR), the Eisenhower Range and the northern Prince Albert Mountains. BP: Brimstone Peak; MBi: Mount Billing; MB: Mount Burrows; MC: Mount Chetwynd; MGM: Mount George Murray; MG: Mount Gibbs; MJ: Mount Joyce; MK: Mount Keinath MM: Mount Matz; MN: Mount Nansen; MP: Mount Priestley; MS: Mount Smith; SCM: Southern Cross Mountains.

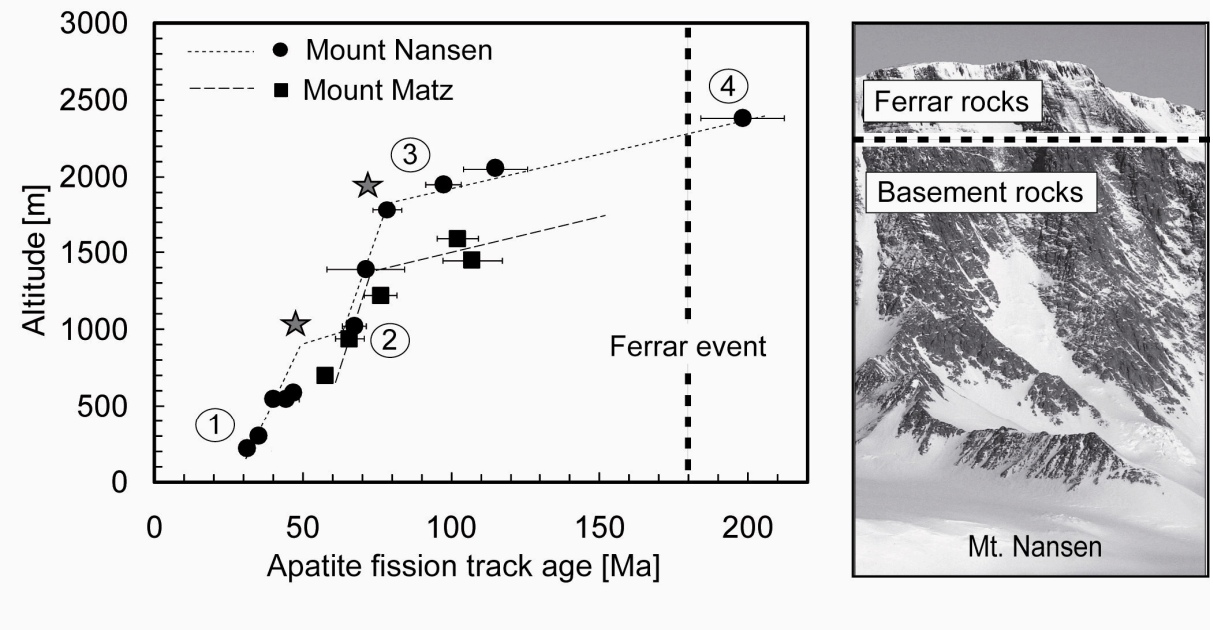

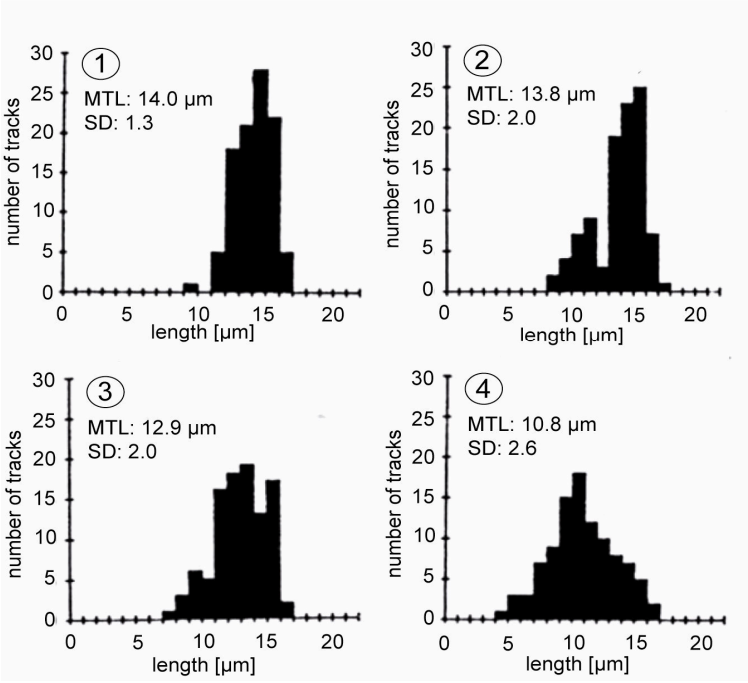

Figure 4: Vertical apatite fission track (AFT) profiles sampled at Mount Nansen and Mount Matz in the Terra Nova Bay region (data from Balestrieri et al., 1994). AFT ages vs. sample altitudes shows a break in slope at ~80 Ma, and an age-elevation discontinuity at ~50 Ma, accompanied by a change in the samples fission track lengths distribution which are marked with asterisks; MTL: Mean track length; SD: standard deviation.

This interpretation is fraught with problems since the presence of Ferrar volcaniclastic rocks places the directly underlying analyzed basement (Fig. 4) at/near surface at 182 Ma. Therefore, the hanging section of the basement must have been reheated to temperatures of ≥100 °C subsequently to the Ferrar event, instead of cooled monotonously since the Cretaceous. Since the AFT ages decrease from basement top towards the lower section of the vertical profiles associated by a coincident increase of fission track lengths annealing (Fig. 4), these temperatures cannot be explained by thermal influence of the Ferrar lava flows. Instead, the AFT pattern from Mount Matz and Mount Nansen requires the emplacement of ~3 – 4 km thick rock

column on basement for any reasonable geothermal gradient. This indicates either a much higher thickness of Ferrar lava flows than preserved or an additional deposition of post-mid Jurassic sediments. The fact that a thickness of Ferrar rocks of up to 4 km would be too resistant against erosion to account for the predicted rapid Eocene exhumation episodes (Fig. 2b), additional post-mid Jurassic sediment accumulation is much more plausible than the emplacement of Ferrar rocks only. Mesozoic burial of the Jurassic surface is supported by a broad range of Late Jurassic and Cretaceous paleotemperatures between ≤60° and ~400 °C for Beacon and Ferrar rocks derived from geochronological, magnetic, mineralogical, and petrographic studies for varies areas throughout the Terra Nova Bay region and the Mesa Range north of it (Fig. 3) which were reached diachronously within horizontal distances of only a few km (e.g. Molzahn et al., 1999; Bernet and Gaupp, 2005). Given that the Jurassic paleosurface at the base of the Ferrar rocks is preserved at similar topographic altitudes over a lateral extension of more than 100 km without major faults and with only very minor vertical displacement, this broad temperature spectrum cannot be explained adequately by tectonic exhumation processes since Cretaceous, and either requires substantial Late Jurassic – Early Cretaceous burial or thermal activity.

Consequently, post-mid Jurassic reheating of the basement attributed to substantial Mesozoic burial due to sediment accumulation refers to a contemporaneous existence of a sedimentary basin within the Terra Nova Bay region (Lisker and Läufer, 2007). Such basin existence is supported by geological indications on the East Antarctic shelf comprising the documentation of (a) Cretaceous and Paleocene terrestrial fossils within Ross Sea deposits (e.g. Villa et al., 2011; Truswell and Drewry, 1984) and (b) terrestrial sediment influx into the Ross Sea by studies of Eocene clay mineral assemblages (Ehrmann, 1998). The extension of the Jurassic paleosurface from northern Victoria Land to the Shackleton Glacier region associated with regional similar AFT patterns (Fig. 3) suggest the existence of a much larger basin in the Ross Sea sector of East Antarctica. In addition, the geological situation of the juxtaposed Australian passive margin that is characterized by the presence of a series of major Mesozoic – Cenozoic rift basins (e.g., Veevers, 2006) suggests the existence of an extensive Mesozoic sedimentary basin between the margins of East Antarctica and SE Australia. This is supported by documented similar AFT patterns in northern Victoria Land and SE Australia (e.g., Moore et al., 1986; Lisker, 2002).

1.2) Scope and aim of the study

The contradiction of the traditional stepwise exhumation scenario with data interpretation and geological observation requires validations of earlier studies from the TAM by combining thermal history modeling of thermochronological data and supplementary geological information, as well as the reconsideration of qualitative thermochronological interpretation concepts such as the *break in slope* in vertical age profiles. The thesis presented here focuses on the post-mid Jurassic geological history of the Terra Nova Bay region (Fig. 3) where conflicts to the traditional exhumation scenario have been recognized firstly (see 1.1), and is divided into three main parts with respective journal articles (see manuscripts I, II, III).

The first manuscript tests the proposed alternative cooling/exhumation scenario that incorporates Mesozoic heating/burial, and evaluates qualitative interpretation concepts of thermochronological data. Therefore, the first paper reverts to the published vertical profiles from Mount Matz and Mount Nansen in the southern Eisenhower Range (Figs. 3 and 4; Balestrieri et al., 1994), as well as provides a new vertical AFT data set from the same region. Since the AFT ages from Mount Matz and Mount Nansen have been determined with the population technique of the AFT method (e.g., Naeser et al., 1989) that neglects important information for thermal history modeling, the samples from these profiles are re-analyzed with the external detector method (e.g. Hurford and Green, 1982, 1983). Thermal history modeling of the AFT data is applied to reconstruct a geological history that is concordant with the geological and thermal frame, i.e. which incorporates mid-Jurassic (near-) surface position and Mesozoic heating/burial of the basement. The significance of qualitative interpretation concepts of thermochronological data and the importance of thermal history modeling for the interpretation of exhumation histories is verified via modeling experiments. This includes the evaluation of the break in slope concept as tool to straightly date cooling events.

The one-dimensional approach of the methodological study only yields local information about the geological history, and can neither resolve the regional burial and exhumation evolution nor the formation of the present-day landscape of the Eisenhower Range that forms a ~70 km long N-S trending escarpment-bound plateau in the Terra Nova Bay region (Fig. 3). Accordingly, based on the results of the pilot study, the second manuscript focuses on a quantitative reconstruction of

timing and amount of burial of the whole Eisenhower Range, and a more detailed investigation of its final exhumation. Therefore, the AFT data set from the southern Eisenhower Range is extended by (a) new AFT analyses on granitic samples from vertical profiles in the northern Eisenhower Range, (b) comprehensive (U-Th-Sm)/He (AHe) analyses on the majority of rock samples analyzed via AFT method, and (c) paleotemperature analyses on Beacon sandstones (vitrinite reflectance, clay mineral analysis, analysis of authigenic phases/mineral reactions, sandstone compaction studies) from various areas throughout the Eisenhower Range.

Maximum paleotemperatures derived by vitrinite reflectance data and authigenic mineralogy are used to estimate the maximal burial of the Eisenhower Range subsequent to the Ferrar event, and are compared with the minimum burial derived by mechanical compaction of Beacon sandstones (e.g. Merino et al., 1997; Ehrenberg, 1989). These approaches provide no indication about the time of maximal burial, and the reconstruction of the burial evolution relies on the application of thermal history modeling of the AFT and AHe data. Paleotemperature estimates derived from the vertical and horizontal sample array of the Eisenhower Range provide the possibility to calculate geothermal gradients for different times and throughout the region. Paleotemperatures in tandem with geothermal gradients are used to quantify the burial evolution, and to differ between Beacon/Ferrar rocks and potential additional post-mid Jurassic sediment deposition. The amount of Jurassic burial reveals the thickness of Beacon and Ferrar rocks, while subsequent burial reflects the thickness of the post-mid Jurassic sediments.

AHe thermochronology provides information about rock cooling below temperatures of ~40° – 80 °C, and crustal depths of ~1.3 – 2.7 km assuming a moderate geothermal gradient of 30 °C/km (Wolf et al., 1998; and see 2.3). This gains a better understanding of the regional geomorphological history including the age of major landscape elements and the magnitude and rate of landscape forming processes. Timing and pattern of exhumation reveals if exhumation occurred rather in response to a single major episode or several discrete stages. Implication on exhumation triggering (tectonic processes vs. climatic influences) together with amount, time and rate of final exhumation supplies detailed information on the formation mechanism of the Eisenhower Range (e.g. downwearing vs. backstepping erosion).

The study along the course of the Eisenhower Range will supply first information about the duration of the sedimentary basin, as well as estimates of the local

sedimentary cover, but does not provide information about the basins geometry, lateral extension or local depths. Accordingly, the third manuscript focuses on the basin evolution within the entire Terra Nova Bay region. Therefore, AFT and AHe analyses are applied on samples from a vertical and horizontal sample set from the Deep Freeze Range in the northern Terra Nova Bay region and supplemented by published AFT data of vertical profiles at the Prince Albert Mountains south of the Eisenhower Range (Fig. 3; Storti et al., 2008). The geological history of the Deep Freeze Range and Prince Albert Mountains derived by thermal history models and correspondent paleotemperatures and geothermal gradients are compared with the burial and exhumation evolution of the Eisenhower Range. In addition, burial of the Jurassic surface derived by AFT and AHe data is correlated with the numerous independent Jurassic – Cretaceous temperature indications that have been derived locally from various areas of the Terra Nova Bay region and the Mesa Range (see section 1.1). Potential regional differences in Beacon and Ferrar rock thickness allow concluding on the paleorelief of the Terra Nova Bay region prior/during the Ferrar event, while thickness estimates of the post-mid Jurassic sedimentary sequence throughout the region gain insights on basin architecture and geometry, as well as local basin depths. Basin reconstruction of the entire Terra Nova Bay region will reveal first important information about regional basin extension, geometry and local depths, and its formation and evolution in the context of geodynamic processes, and serves as case study for further Mesozoic – Eocene basin studies at supraregional scale. Additionally, it may provide details to potential provenances of the Mesozoic sediments and depositional environments subsequent to their removal, and hints on the development of the previous Late Paleozoic and Early Mesozoic Transantarctic Basin (e.g., Collinson et al., 1994).

Summarized, the thesis presented here comprises the evaluation of qualitative interpretation concepts of thermochronological data for the reconstruction of thermal histories, and the investigation of the post-mid Jurassic geological history of the Terra Nova Bay region. This includes the quantification of the regional burial and exhumation evolution and the development of the present-day landscape, as well as the reconstruction of the regional sedimentary basin evolution.

2) Methods

2.1) Field work and sampling

The German Antarctic North Victoria Land expeditions (GANOVEX) IX and X of the "Bundesanstalt für Geowissenschaften und Rohstoffe" (BGR) provided the opportunity for structural and thermochronological research in the Terra Nova Bay region. Field work in this region focussed on mapping and measurement of the brittle kinematic inventory, and sampling of rock specimens from horizontal and vertical basement profiles for AFT and AHe thermochronology, and of specimens from overlying Beacon sandstones for paleotemperature and burial estimations (Fig. 5). This included the observation of morphologically exposed outcrops such as escarpments, glacial valleys and erosion surfaces, and the occurrence of unconformities, sedimentary deposits (Beacon Supergroup), faults, and dykes. Particular interest was directed towards thermal features associated with tectonic structures, such as fault coatings and mineralization (e.g., epidote), secondarily grown minerals (e.g. zeolite), pseudotachylytes, dykes and veins, and aureols.

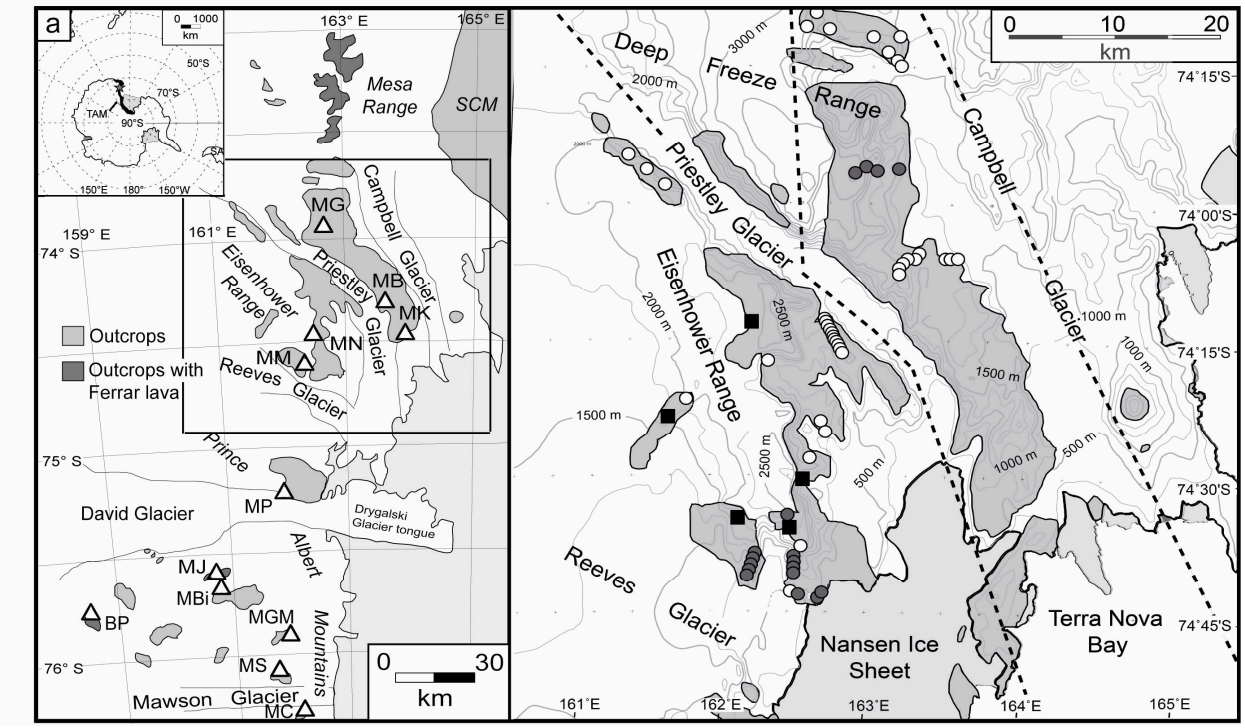

Figure 5: a) Sketch map of the Terra Nova Bay segment of the Transantarctic Mountains (TAM), and (b) simplified map of the Eisenhower Range and Deep Freeze Range. The locations of samples for apatit fission track (AFT) and U-Th-Sm/He (AHe) thermochronology are marked by white circles (GANOVEX expeditions) and grey circles (ItalAntartide expeditions), and the locations of samples for vitrnite reflectance and/or secondary mineral analysis are marked with black squares. The dashed black lines mark main faults contributed to a regionally important Cenozoic right-lateral fault system in northern Victoria Land (e.g., Rossetti et al., 2003; Storti et al., 2007, 2008).

Field work was based on Helicopter operations (*Helicopter New Zealand*) from the German *Gondwana Station* and the research vessel *MS Italica.* Target areas were the Eisenhower Range and Deep Freeze Range south and north of the Priestley Glacier. Sample collection comprises 38 basement samples (Granite Harbour Intrusives) and one sandstone sample (Beacon Supergroup) for AFT and AHe analyses (Fig. 5, white circles), and sandstone samples (Beacon Supergroup) from five locations for vitrinite reflectance and/ or secondary mineral analyses (Fig. 5, triangles). Samples for thermochronological studies were supplemented by 16 granite samples from the Eisenhower Range (Mount Matz, Mount Nansen, Anderson Ridge) and Deep Freeze Range (Mount Gibbs) collected during the ItalAntartide expeditions 1985-93 (Fig. 5, black circles). The 54 samples for AFT and AHe thermochronology together cover an elevation spectrum of ~3 km (220 – 3120 m) extending from the Anderson Ridge at the southern margin of the Eisenhower Range to the Archambault Ridge at the northern end of the Deep Freeze Range.

2.2) Apatite fission track thermochronology

2.2.1) Theoretical background

AFT thermochronology is based on the spontaneous decay of the radioactive isotope ^{238}U. This decay produces lattice defects (fission tracks) within apatite crystals at a constant rate over time. Depending on the apatites chemical composition (Cl-apatites vs. F-apatites), these fission tracks anneal completely due to diffusion at temperatures above 110 – 125 °C (Fig. 6; e.g., Ketcham et al., 1999). At temperatures below this 110 – 125 °C fission tracks remain preserved but still experience partial track annealing (lengths reduction) until temperatures get below ~60 °C (Fig. 6) where track shortening is insignificantly low (e.g., Gleadow and Duddy, 1981). This zone between 125 – 110 °C and ~60 °C is referred to as the Partial Annealing Zone (PAZ) of apatite (Fig. 5; Wagner et al., 1989). The number of preserved tracks per unit volume (fission track density) provides information about the time of rock cooling (AFT age) within/below temperatures of the PAZ, while the fission track lengths distribution of an adequate number of measured tracks supply information about the type/style of rock cooling.

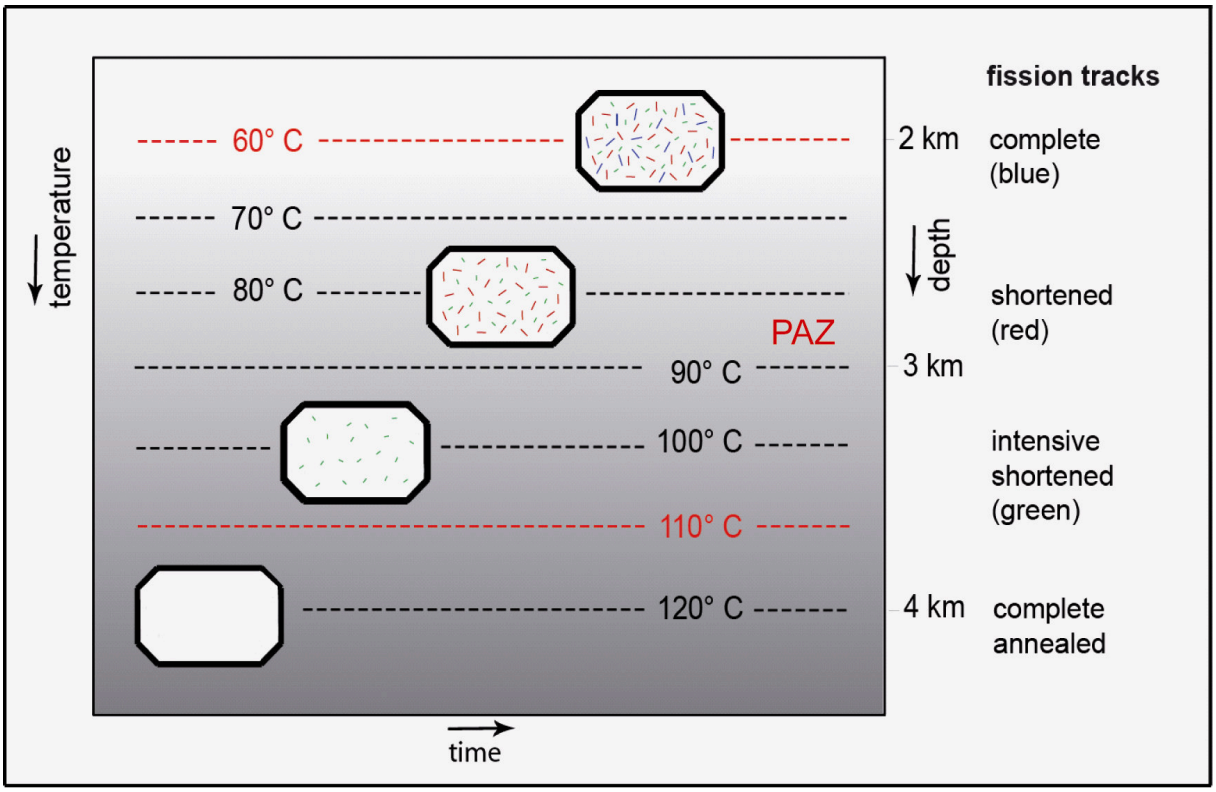

Figure 6: Sketch illustrating (partial) annealing of fission tracks within apatite crystals at different temperatures above and within the Partial Annealing Zone (PAZ). At temperatures ≥110 – 125 °C fission tracks get completely annealed. Within the PAZ (110 – 125 °C to ~60 °C) fission tracks remain preserved but still experience partial track annealing (lengths reduction) depending on the temperature with most intensive track annealing/shortening at the upper temperature boundary of the PAZ. Below temperatures of ~60 °C fission track annealing/shortening gets insignificantly low.

2.2.2) Age calculation

Fission track dating requires the estimation of the relative abundance of ^{238}U atoms (parent product) and the number of spontaneous fission tracks (daughter product) per unit volume. The amount of spontaneous fission tracks is counted on a given surface of an apatite grain after the mineral has been polished and etched under appropriate conditions to reveal spontaneous tracks (see 2.2.5). Thereby, the mean fission track etch pit diameter parallel to the crystallographic c-axis (Dpar) of an analyzed apatite grain serves as an indicator for fission track annealing kinetic properties (e.g. Carlson et al., 1999). For determination of the ^{238}U abundance, the apatite needs to be irradiated with a low-energy thermal neutron flux that induces fission in ^{235}U. Monitoring the thermal neutron flux, the density of induced fission tracks, registered in the apatite or an attached mica detector (see below) reflects the abundance of ^{235}U within this grain. Given that the ratio of ^{235}U and ^{238}U is constant in nature, the abundance of ^{238}U can be estimated from the abundance of ^{235}U.

Since the first application of the AFT method, mainly two different dating techniques are routinely applied to determine AFT ages: the population technique (e.g. Naeser et al., 1989) and the external detector or zeta-calibration technique (e.g. Hurford and Green, 1982, 1983). The population technique relies on the separate measurement of spontaneous and induced fission track densities on two different apatite aliquots of one sample. Due to the fact that the chemical composition of an apatite grain affects its fission track annealing kinetic property (e.g. Green et al., 1986, Barbarand et al., 2003a, b), this technique has the major disadvantage that grains cannot be dated individually and that uniform uranium concentrations, consistent chemical compositions and concordant ages for all single apatites of one sample have to be assumed. For example, this can cause a large spread of single grain ages when applied on sedimentary rocks, which often contain material from different provenances and thus apatites with different chemical compositions (e.g. Green et al., 1986). Contrary, the external detector technique relies on the record of the induced fission track density of a single apatite grain on an attached mica-print (Fig. 7). This allows dating apatite grains individually and avoids the assumption of uniform uranium distribution for apatites of one sample.

The AFT age equation for the external detector technique is:

$$t = \frac{1}{\lambda_d} Ln\left(\lambda_d \frac{\rho_s}{\rho_i} \rho_d \zeta \mathrm{g} + 1\right)$$

t = age
ρs = spontaneous track density
ρi = induced track density
ρd = track density in a dosimeter glass of known uranium concentration which is used to monitor the neutron flux in the reactor
λd = α decay constant of ^{238}U
g = geometry factor
ζ = constant of proportionality made up of the other parameters including the fission decay constant and neutron capture cross section

The ζ calibration factor is determined from a sample of known age and depends on the analyst. The analyst undertakes numerous calibrations for determination of an own ζ value for a given dosimeter to consider the own specific counting habits. An AFT sample age usually consists of individual single grain ages of at least 20 apatite grains, and is commonly reported as mean, pooled or central age. The central age is favored over mean and pooled age since it is most robust to single grain age outliers.

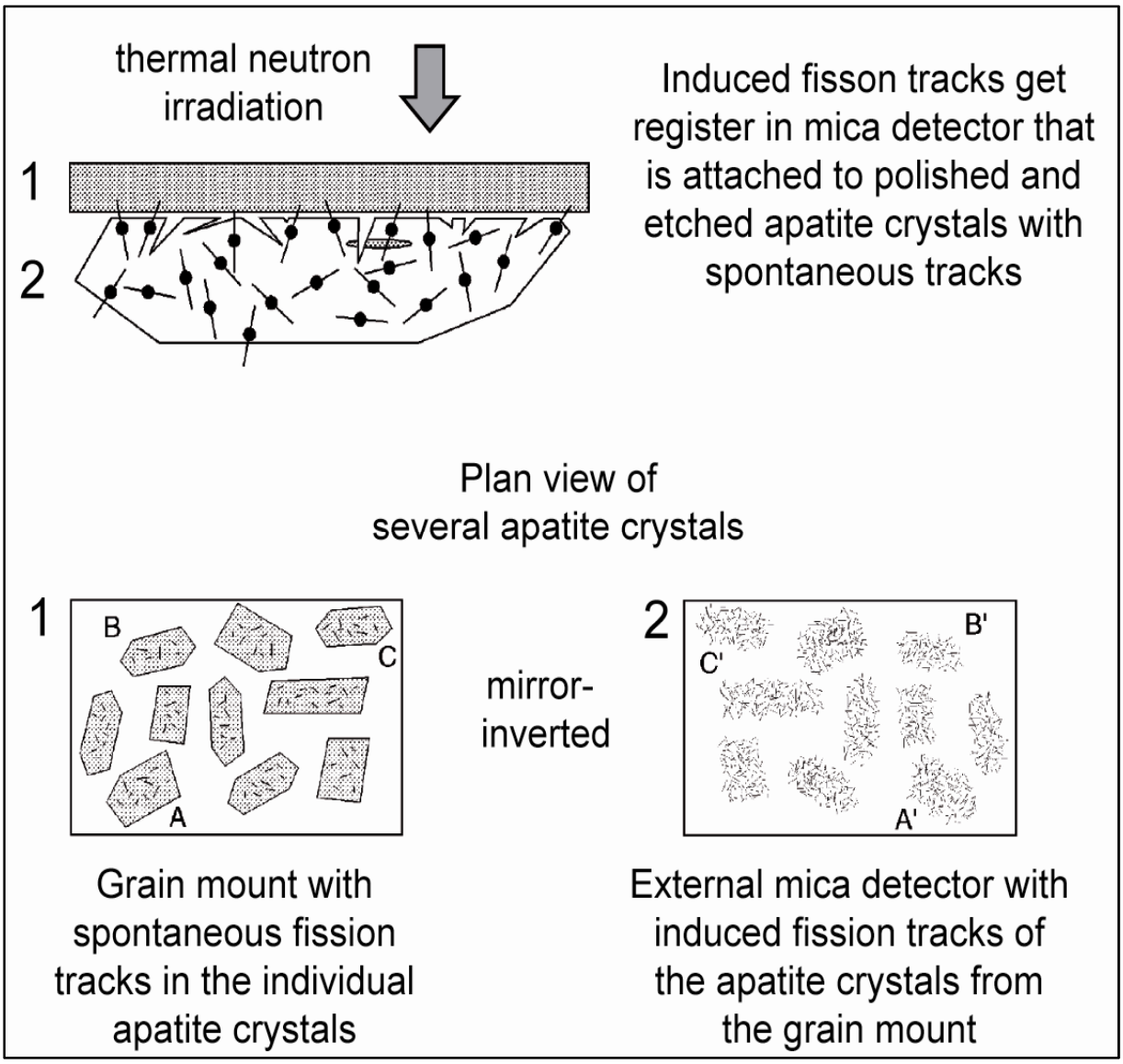

Figure 7: External detector method of apatite fission track (AFT) dating (after Gallagher et al., 1998).

2.2.3) Fission track lengths distribution

The degree of fission track shortening and length distribution within apatites of one sample provide information about the style of rock cooling below 110 – 125 °C. Representative sample length distribution patterns for different cooling scenarios of slow, rapid and complex rock cooling are shown in figure 8. Rapid rock cooling through the PAZ (e.g. undisturbed volcanic rocks; Fig. 8a) produces mainly long tracks with minor standard deviation, while slow rock cooling trough the PAZ (e.g. slow exhumed basement) produces an additional large amount of shortened tracks with a correspondent larger standard deviation (Fig. 8b). Complex thermal histories (e.g. exhumation with temporal burial; thermal reheating) can lead to mixed forms of length distribution patterns (Fig. 8c).

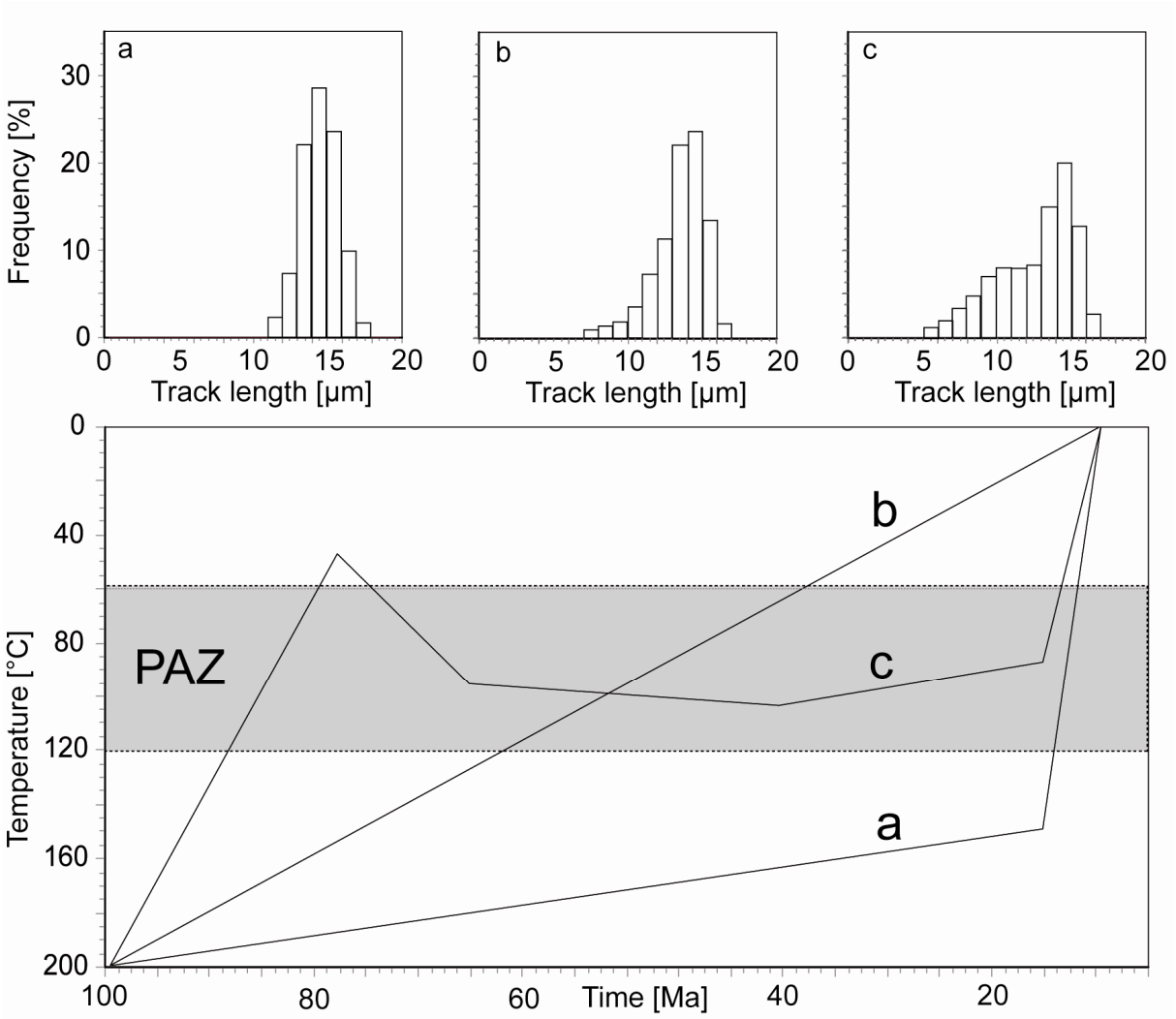

Figure 8: Representative schematic time-temperature paths of (a) rapid, (b) slow and (c) complex cooling with correspondent fission track lengths distribution patterns.

2.2.4) Dpar and lengths measurement

Dpar and fission track lengths measurement is conducted using a digitizing tablet system with a LED cursor that is visible in the microscope via a drawing tube attachment (e.g. Dumitru, 1993). In order to measure track length under the microscope, this tablet needs to be calibrated against a stage micrometer. Tracks which run obliquely or vertically to the surface or intersect the surface do not image their true length under the microscope, and correspondingly cannot be used for thermal history interpretation (e.g., Laslett et al., 1994). Only tracks below the surface and approximately parallel to the polished apatite surface within ~15° of horizontal (referred to as "confined tracks") are usable for lengths measurement. These tracks can be identified by their strong backscattered image under reflected light and their almost simultaneous focus along their total length. If possible, 100 confined fission track lengths are measured for each sample following the recommendations of Laslett et al. (1982). Dpars are measured for each analyzed apatite grain. The precision of Dpar and track length measurement depends on the analyst but the accuracy is usually at ±0.2 µm (Green et al., 1986). Additionally, due to an anisotropy of etching and track annealing processes within apatite with respect to the crystallographic c-axis, the angle between track and c-axis is also measured (e.g. Laslett et al., 1982, Green et al., 1986) and used later in the course of thermal history modeling.

2.2.5) Sample preparation and dating procedure

Rock samples of ~5 – 10 kg were crushed and granulated with screw press and jaw crusher, followed by apatite separation using vibration table, and standard heavy liquid and magnetic techniques. Subsequently, apatite grains were mounted in the epoxide-based mounting medium Petropoxy 154, wet-grinded using sandpaper, polished using aluminum oxide powder and a polishing machine, and etched in 5N HNO_3 at 20 °C and 20 s following the procedures described by Gleadow (1984) and Ketcham et al. (2007) to reveal spontaneous fission tracks. The prepared apatite concentrates were covered with mica plates (Fig. 7) and irradiated at the research reactor facility FRM-II in Garching, Germany. Afterwards, mica plates correspondent to the mounted apatite concentrates were etched with 40% HF at 20 °C for 30 minutes to reveal induced fission tracks. AFT ages were determined by counting

spontaneous and induced fission tracks according to the external detector method (Hurford and Green, 1982, 1983; Green, 1985) for the dosimeter glass CN5, and calculated using the program *Trackkey* (Dunkl, 2002). Several Fish Canyon and Durango standards were analyzed for determining an own Zeta calibration factor (320±10). Counting and measurement procedures were performed manually, using a Zeiss Axioplan microscope at a magnification of x1250 with dry objectives, the FT-Stage program of Dumitru (1993) and a digitizing tablet system.

2.3) Apatite (U-Th-Sm)/He thermochronology

2.3.1) Theoretical background

AHe thermochronology is based on the accumulation and progressive diffusive loss of ^{4}He alpha particles within apatite crystals over time (e.g. Farley, 2002). ^{4}He daughter particles are produced by the decay of ^{238}U, ^{235}U, ^{232}Th and ^{147}Sm parent nuclides, and get totally lost due to diffusion at temperatures >80 °C (Farley, 2002). At temperatures below this ~80 °C, ^{4}He particles remain preserved partially until temperatures get below ~40 °C where they retain almost entirely (Wolf et al., 1998). The zone of partial ^{4}He preservation is referred to as the Partial Retention Zone (PRZ). The ^{4}He retention within apatite crystals provides information about the time of rock cooling within/below the temperatures of the PRZ (Fig. 9), and correspondingly crustal depths of ~1.3 – 2.7 km at a moderate geothermal gradient of 30°C/km.

2.3.2) Age calculation

Since ^{4}He nuclides are produced by the series decay of ^{238}U, ^{235}U, ^{232}Th and ^{147}Sm, AHe dating is based on the ^{4}He intergrowth equation (e.g., described by Farley, 2002) that reads as follows:

$$
\begin{aligned}
{}^{4}\mathrm{He} = {} & 8x^{238}\mathrm{U}(e^{\lambda 238t}-1) \\
& + 7x^{235}\mathrm{U}(e^{\lambda 235t}-1) \\
& + 6x^{232}\mathrm{Th}(e^{\lambda 232t}-1) \\
& + {}^{147}\mathrm{Sm}(e^{\lambda 147t}-1)
\end{aligned}
$$

λ = parental decay constants

t = AHe age

Accordingly, AHe dating requires the measurement of daughter and parent nuclides. This comprises several steps. At first, ^{4}He is extracted by heating of the apatite to temperatures of usually ~500 – 600 °C for ~1 minute using laser radiation (House et al., 2000) followed by ^{4}He purification and mass spectrometer analysis. Subsequently, the apatite grain is dissolved and the parent nuclides get analyzed by an inductively coupled plasma mass spectrometer. This includes an analytical precision usually better than ~1.5 %.

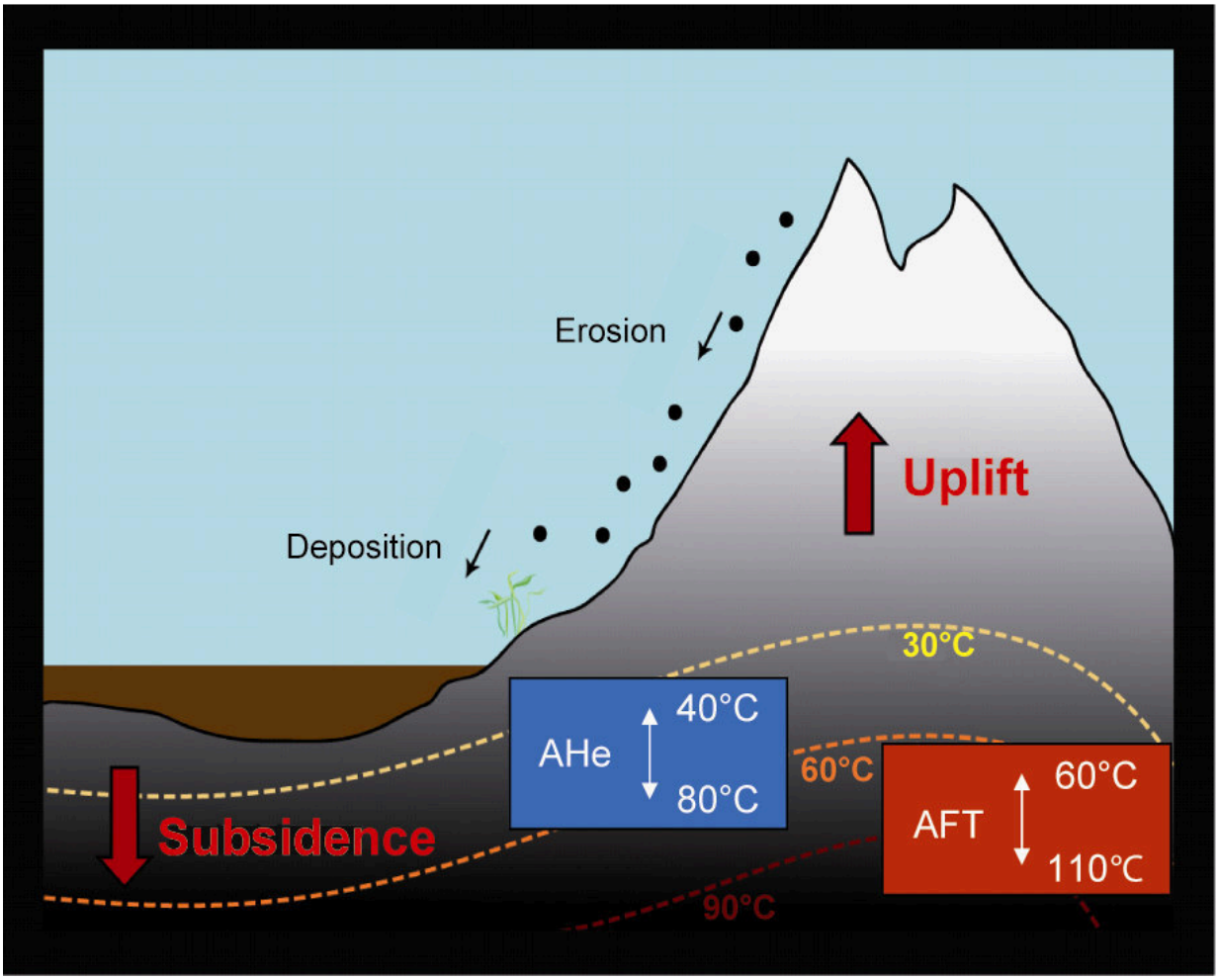

Figure 9: Sketch illustrating the different sensitivity domains for apatite fission track (AFT) and apatite (U-Th-Sm)/He (AHe) thermochronology (for more information see text).

Apatite crystals experience further ^{4}He loss along the crystal rim according to the specific alpha stopping distance of ^{238}U (~19 µm), ^{235}U (~22 µm), ^{232}Th (~22 µm) and ^{147}Sm (~ 6 µm) and the respective position of the parent nuclides within the apatite grain. The effect of alpha ejection results in a loss of ^{4}He particles of more than ~50% for small grains with a radius of ≤30 µm, and still of ~5% for large grains with a radius of ~250 µm (Farley et al., 1996). Hence, AHe ages calculated with the equation

above has to be considered as “raw” ages which need to be corrected for alpha ejection (e.g., Farley et al., 1996). Given that the retention of alpha particles correlates with apatite grain dimension, the alpha ejection correction involves a so-called FT factor that considers the surface to volume ratio of the analyzed apatite crystal and the α-stopping distance of the parent nuclides (Farley et al., 1996). This factor is applied to an idealized apatite grain with homogeneous U, Th and Sm distribution and euhedral shape based on the measured lengths and widths of the analyzed crystal, and weighted to account for the different values of ^{4}He producing isotopes including their different alpha particle stopping distances. Alternatively, the region of an apatite that has experienced ^{4}He loss can be eliminated by abrasion of the outer crystal rim prior to dating (e.g., Spiegel et al., 2009). In this case, the AHe “raw” age represents the “true” age and need no correction. However, according to the alpha stopping distance of ~20 µm for U and Th, removal of the grain rim is only possible for large grains with diameters of at least 100 µm.

2.3.3) Reasons for intra-sample single age dispersion

The most frequent causes for the determination of erroneous grain ages are U-Th-rich mineral or fluid inclusions and cracks. Although every apatite grain is checked by optical grain inspection before analysis, the presence of micro-inclusions holding potential high contents of U and Th are often hard to detect. Besides this, the presence of radiation damages, U-Th-zonation or He-implantation from U-Th-rich host or matrix are possible reasons for the estimation of erroneous AHe ages.

Radiation damages: Radiation damages within apatites are thought to trap ^{4}He atoms. This leads to a decrease of the ^{4}He mobility through the grain interior and consequently to an increase of the ^{4}He retention at a given temperature (Shuster et al., 2006; Flowers, 2009). Thereby, the rate of reduced ^{4}He mobility depends on the amount of accumulated damages to the apatite structure. The temperature threshold for the accumulation of radiation damages is not exactly known but assumed to be not much higher than the upper limit of the PRZ (Shuster et al., 2006). At higher temperatures, radiation damages get completely annealed. Accordingly, the change in ^{4}He retention is especially high when apatite crystals reside for a long time period within temperatures of the PRZ without exceeding this. This accumulates a large amount of radiation damages with a subsequently strong reduced loss of ^{4}He atoms

and may cause AHe ages as old as the corresponding AFT age (Shuster et al., 2006). Besides that, effective ^{4}He diffusion kinetic also depends on the effective U concentration of an apatite crystal. Apatite grains with a higher concentration of effective U are unaffected to a loss of ^{4}He atoms up to higher temperatures than these grains with a lower effective U concentration (e.g. Shuster et al., 2006). Consequently, radiation damages in combination with apatites strongly varying in effective U concentration may result in a large variation of single grain ages in one sample (e.g. Fitzgerald et al., 2006).

U-Th zonation: Non-uniform distributions of the U and Th concentration within apatite grains lead to the determination of an erroneous AHe age when correcting for α-particle loss (e.g. Farley et al., 1996). Depending on the degree and kind of zonation (U-Th-rich vs. U-Th-poor cores), the misinterpretation of retained α-particles may result in ages of up to ~25% younger (U-Th-rich rim; α-ejection under-corrected age) or older (U-Th-rich core, α-ejection over-corrected age) than the "true" age (e.g. Meesters and Dunai, 2002; Farley, 2002). Moreover, apatite grains with different zonings in one sample may lead to considerable single grain age dispersion (e.g. Fitzgerald et al., 2006). Although samples with apatites zoned in U-Th concentration can be identified by the inhomogeneity of fission track distributions within apatites of the corresponding AFT sample, zoned apatite grains are often hard to detect if less fission track densities are present due to a poor concentration of U and Th.

^{4}He implantation from U-Th-rich host or matrix: The implantation of ^{4}He atoms from surrounding U-Th-rich host or matrix may cause an overestimation of AHe single grain ages of up to 50% (Spiegel et al., 2009). An indication therefore is a relationship between single grain ages and effective U concentration opposite to the trend described by Shuster et al. (2006) with lower effective U contents for older grains (Spiegel et al., 2009). Another evidence for ^{4}He implantation is apparent when ages of abraded grains are within these of the uncorrected ages of the non-abraded grains. In this case, the AHe ages of the abraded grains are assumed to show the "real" age due to the mechanical abrasion of the grains rim which holds the "parentless" He implants from the surrounding host.

2.3.4) Grain selection and dating procedure

Apatite grains were handpicked in order to avoid U, Th and Sm-rich mineral inclusions, fluid inclusions and cracks which may produce ^{4}He excess or loss (see 2.3.3). Following the recommendations for an ideal apatite crystal for AHe chronology (euhedral form, grain diameter >60 µm), single grains were selected using optical microscopes at different magnifications and modes of light (reflected, transmitted, polarized). Mechanical abrasion was applied for large apatite crystals with grain diameter >100 µm to avoid potential implantation of ^{4}He particles (see 2.3.3). Selected grains were captured by a microscope camera and measured for the purposes of alpha ejection correction calculation using the imaging program *cell A* for Olympus microscopes. Apatite grains were put into platinum capsules before He, U, Th, and Sm measurement was conducted at the Melbourne University in Australia. AHe ages were calculated based on the ^{4}He intergrowth equation (e.g., described by Farley, 2002) and the first-order Taylor series approximation (Taylor, 1969). Thereby, the age of each apatite grain was determined separately by using the raw data of ^{4}He, ^{238}U, ^{232}Th and ^{147}Sm nuclides and the measured dimensions of the crystal applying the alpha correction for AHe dating (Farley et al., 1996). This calculation incorporates an analytical error of ~5% composed of analytical uncertainties and errors in alpha correction and grain size measurement.

2.4) Paleotemperature analyses and burial estimations

The measurement of vitrinite reflectance (e.g., Sweeny and Burnham, 1990) and the analysis of authigenic phases or mineral reactions (e.g., Bernet and Gaupp, 2005) are widely used tools to assess the maximum paleotemperature experienced by a rock. These temperatures indirectly give indications of maximal rock burial, but in comparison to thermochronological methods do not provide any indication of time. Additionally, constraints of burial can be derived directly by the mechanical compaction of sedimentary rocks (e.g., Merino et al., 1997). Mechanical compaction of sandstones and related reduction of porosity as an important process during sandstone diagenesis serves as an indicator for minimum burial (e.g., Worden and Burley, 2003; Ehrenberg, 1989).

Vitrinite reflectance: Vitrinite is one of the main components of organic material within sedimentary rocks that is formed by thermal alteration processes. Its reflectance increases proportionally with temperature and can be used as indicator for the maturation of organic material (e.g., Burnham and Sweeney, 1989). This allows concluding on the maximal temperature of the analyzed sedimentary rock (e.g. Ritter, 1984), and indirectly constrains maximal rock burial. The reflectance of usually minimum 30 individual vitrinite grains per sample is measured under a microscope, and typically quoted as %Ro. This value represents the measured percentage of reflected light from a sample that is immersed in oil (%Ro = % reflectance in oil), and typically range from 0% Ro to 3% Ro.

Authigenic mineralogy: The occurrence of temperature sensitive phases such as zeolites and clay minerals, or mineral reactions such as detrital feldspar affected by diagenetic albitization, constrains the maximal paleotemperature of a rock. This supplies important information about the diagenetic history of sedimentary rocks and their maximal burial depth (e.g. Merino et al., 1997). Samples detrital and authigenic mineralogy are usually studied petrographically by optical microscopy or get analyzed by X-ray diffraction and electron microprobe.

2.5) Thermal history modeling

Modeling programs visualize and constrain the thermal history of samples based on thermochronological (AFT, AHe) and related data (vitrinite reflectance). The programs consider all given thermochronological parameter (e.g. AFT ages, track lengths, AHe ages), and geological information (e.g. depositional age, present-day temperature), as well as incorporate additional factors such as the varying fission track annealing behaviour depending on the apatites chemical composition or the behaviour of ^{4}He-diffusion depending on the apatites grain-size and parent nuclide concentration. Thermal histories are usually modeled using the HeFTy program by Ketcham (2005) or the QTQt program by Gallagher et al. (2005). HeFTy produces inverse and forward thermal history models for individual samples, while QTQt produces inverse thermal history models for single samples or a set of multiple samples of different heights from boreholes or vertical profiles. Inverse modeling generates a large number of possible t-T paths randomly, and forward modeling allows testing individual t-T paths. The HeFTy program display “goodness of fit”

(GOF) values of fission track ages, track lengths and AHe ages which give an indication about the fit between measured and predicted data. Values close to 1 are the best, values ≥0.5 are considered good, and values between 0.49 and 0.05 are considered acceptable.

Thermal history modeling was conducted via HeFTy and QTQt programs incorporating AFT data (ages, lengths data, Dpar) and AHe ages when available. In both cases, only samples with at least 40 measured confined tracks or the availability of both AFT and AHe ages were modeled. Inverse modeling of the HeFTy program run for all applicable samples individually using the Monte Carlo search method with a minimum of 20,000 random produced cooling paths. Inverse modeling of the QTQt program run for all samples using the transdimensional Markov chain Monte Carlo inversion scheme incorporating a potential varying temperature difference between the individual samples over time (varying geothermal gradient). Both modeling programs allow limiting the time-temperature history in form of manual set constraint boxes (HeFTy) or envelopes (QTQt). These constraints were set considering the given thermochronological data and geological information (see manuscripts for detailed information). In both cases, modeling was compiled using c-axis projected lengths with a lengths reduction in standard of 0.892. Modeling of AFT data were performed applying the annealing model of Ketcham et al. (2007), and modeling of AHe data were performed applying the diffusion model of Flowers et al. (2009). The α-correction and stopping distances were used after Ketcham (2009). The GOF of the AFT length data was determined using the Kuiper's Statistic method.

MANUSCRIPT I

The Eisenhower Range, Transantarctic Mountains: Evaluation of qualitative interpretation concepts of thermochronological data

J. Prenzel, F. Lisker, M.L. Balestrieri, A. Läufer, C. Spiegel

* corresponding author. University of Bremen, PO Box 330440, 28334 Bremen, Germany, Tel.:0049-421-218-65284, Email address: jprenzel@uni-bremen.de

Published at Chemical Geology (2013), 352, 176-187.

Received	24 October 2012	Concept	50%
Received in revised form	3 June 2013	Data collection	80%
Accepted	4 June 2013	Realization	80%
Available online	14 June 2013		

The Eisenhower Range, Transantarctic Mountains: Evaluation of qualitative interpretation concepts of thermochronological data

J. Prenzel[1], F. Lisker[1], M.L. Balestrieri[2], A. Läufer[3], C. Spiegel[1]

[1] University of Bremen, FB5 Geosciences, Klagenfurther Straße, 28359 Bremen, Germany

[2] CNR, Institute of Earth Sciences and Earth Resources, Via La Pira 4, 50121 Florence, Italy

[3] Bundesanstalt für Geowissenschaften und Rohstoffe, Stilleweg 2, 30655 Hannover, Germany

Keywords: Apatite fission track thermochronology**;** Break in slope**;** Population method**;** Transantarctic Mountains**;** Exhumation history**;** Thermal history modeling

Abstract

The Transantarctic Mountains (TAM) were one of the first regions where apatite fission track (AFT) thermochronology was applied routinely to study exhumation processes and long term landscape evolution. Pioneering publications from the region introduced or refined interpretation concepts of thermochronological data such as the break in slope in vertical age profiles as qualitative marker for the onset of accelerated rock cooling.

New AFT data were compiled from vertical profiles in the Eisenhower Range, northern TAM, and compared with published data. Samples originally examined by population technique were re-analysed via the external detector technique. AFT ages increase from 32±2 Ma at an elevation of 220 m to 175±14 Ma at 2380 m. Geological evidence and thermal history modeling of the AFT data require Jurassic to Late Eocene reheating of the samples and an onset of cooling at ~35 – 30 Ma. This requires the deposition of a ~3 to 3.5 km thick sedimentary sequence on the granitic basement subsequent to Jurassic Ferrar magmatism at ~180 Ma. The regression of paleotemperatures against sample altitudes infers a high Jurassic geothermal gradient of ~60°C/km related to rifting processes and Ferrar magmatism, and a moderate Cretaceous/Eocene geothermal gradient of ~30°C/km.

Comparison of ages generated with population and external detector technique shows the importance of determining single-grain ages for each sample, even from granitic rocks of the same intrusion, and thus strongly supports previous cases made for the determination of annealing kinetics and grain-age evaluation. Age comparison additionally illustrates that samples above a break in slope record larger deviations between population and external detector ages than samples below a break in slope.

We demonstrate that position and shape of a break in slope result from various factors, such as the thermal history prior to final cooling, maximum paleo-temperatures, cooling rate, and geothermal gradient. A break in slope does not straightly date the onset of final cooling and cannot substitute thermal history modeling. Therefore, earlier studies from the TAM and similar settings elsewhere need to be validated by combining thermal history modeling of thermochronological data and supplementary geological information.

3.1) Introduction

The Transantarctic Mountains (TAM) cross Antarctica for ~3500 km between the embayments of Ross Sea and Weddell Sea (Fig. M I-1a). The mountain chain forms the main structural and morphological feature of Antarctica and divides the continent into East and West Antarctica. Since upper Mesozoic/Cenozoic sediments are missing to a large extent, the exhumation history cannot be reconstructed on the base of petrological and stratigraphic evidence. In this situation, the TAM became one of the first regions where apatite fission track (AFT) thermochronology was applied routinely to study regional exhumation histories (e.g., Fitzgerald et al., 1986; reviews of Fitzgerald, 2002; Lisker, 2002).

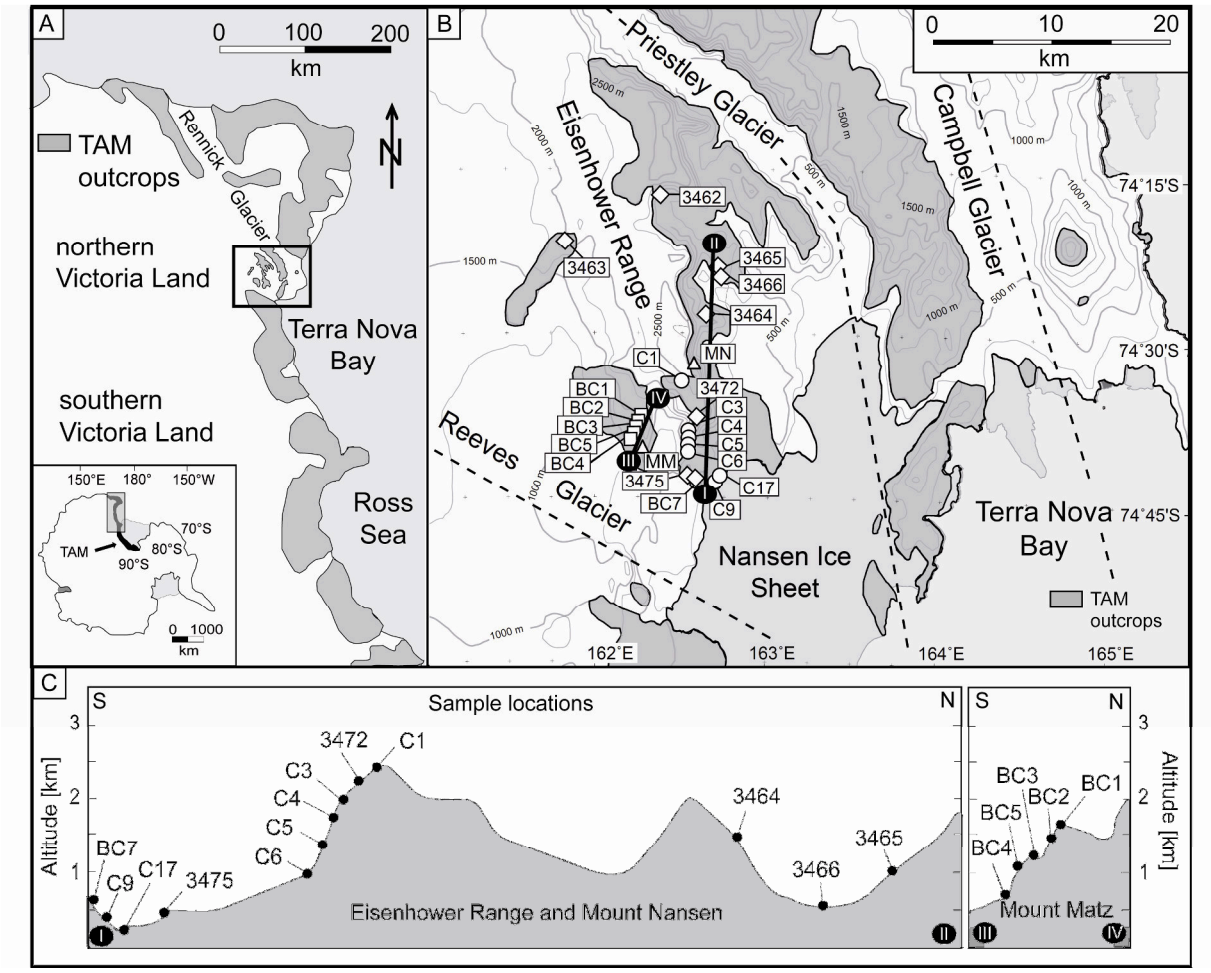

Figure M I-1: (a) Sketch map of the Victoria Land segment of the Transantarctic Mountains, the black box marks the study area of the Eisenhower Range; (b) Simplified map of the Eisenhower Range area. Sample locations are marked by circles (Mount Nansen = MN), squares (Mount Matz = MM) and diamonds (Eisenhower Range). The dashed black lines mark the main faults of the Cenozoic right-lateral fault system in the Eisenhower Range region (e.g., Rossetti et al., 2003; Storti et al., 2007, 2008 and refs. therein); (c) topographic cross-sections along the Eisenhower Range with Mount Nansen (I to II) and Mount Matz (III to IV).

In general, AFT thermochronology is based on the temperature-dependent preservation of fission damages within apatite crystals. This allows to constrain time, amount and rate of rock cooling within/below specific temperature ranges of the upper crust. The fission track density within apatites provides information about time of rock cooling below temperatures of ~125°–110° to ~60°C. This temperature range is referred to as the Partial Annealing Zone (PAZ; e.g., Wagner et al., 1989; originally called partial stability zone; Wagner, 1972). Associated track length shortening within PAZ temperatures yields additional information about the type of rock cooling.

Early AFT studies on vertical profiles from the TAM documented a change in the AFT age-elevation regression from a flat gradient of older ages at higher altitudes to a steep gradient of younger ages at lower altitudes (e.g., Fitzgerald and Gleadow, 1988; Balestrieri et al., 1997). Such a transition is usually associated with a characteristic fission track length distribution pattern with shortened track lengths related to the flat gradient and longer track lengths associated with the steep gradient (e.g., Fitzgerald and Gleadow, 1988; Fitzgerald et al., 1995). The change of age-elevation regression was referred to as the break in slope (e.g., Gleadow et al., 1984; Fitzgerald et al., 1986). It was shown that samples from above the break in slope resided in the PAZ prior to initiation of cooling and hold track components from before and after the change from flat to steep regression while samples from below the break in slope were situated at temperatures higher than those of the PAZ prior to onset of accelerated cooling and only contain tracks accumulated at/ below PAZ temperatures (Gleadow and Fitzgerald, 1987; Fitzgerald and Gleadow, 1988). Samples from above the break in slope show shorter mean track lengths (MTL) with larger standard deviations than samples from below the break in slope. The break in slope was described as the base of an exhumed fossil PAZ and thought to mark the minimum time of cooling to temperatures below ~100° – 60°C, i.e. accelerated rock cooling was supposed to commence prior to the time of the break in slope (Gleadow and Fitzgerald, 1987; Wagner et al., 1989). The concept was used to constrain time and amount of rock cooling/exhumation from the position of the break in slope and the rate of rock cooling/exhumation from the gradient below (e.g., Fitzgerald and Gleadow, 1988; Wagner et al., 1989).

AFT ages and corresponding MTL from numerous vertical profiles along the TAM were interpreted according to the break in slope concept and regional AFT patterns

were explained in terms of monotonous cooling without reheating, involving stages of accelerated exhumation in the Early Cretaceous (~125 Ma), Late Cretaceous (~95 Ma) and Cenozoic (~50-45 Ma; summarized by Fitzgerald, 2002, and Lisker, 2002). However, the proposed cooling history produces severe concerns (Lisker and Läufer, 2013). Firstly, different amounts and times of exhumation have been recorded for different segments of the TAM (Fitzgerald, 2002). The variation appears without a systematic spatial pattern and cannot be explained adequately in terms of monotonous stepwise cooling. Secondly, the proposed cooling histories could not be verified by thermal history modeling of the data due to an incompatibility of fission track lengths data with the proposed cooling histories. Finally and most importantly, the stepwise cooling concept conflicts with geological observations such as the presence of ~180 Ma volcanic rocks throughout the TAM (Lisker and Läufer, 2011). Their superficial emplacement directly above the studied vertical profiles infers a near surface level of the analyzed rocks at this time (Lisker and Läufer, 2013).The contradiction of the proposed stepwise cooling with thermal history modeling and geological observations requires validation of earlier studies from the TAM.

This paper reverts to published sample sets of two sub-vertical profiles from the Eisenhower Range in the TAM of northern Victoria Land (Balestrieri et al., 1994, 1997). AFT ages of granitic basement samples were originally compiled via population technique. However, the population technique has the major disadvantage not to account for uranium concentration and chemical composition of individual apatites within one sample, and not to allow single grain analysis. Accordingly, track annealing kinetic properties and provenances in sedimentary rocks cannot be determined, and thermal histories not modeled (e.g., Green et al., 1986; Barbarand et al., 2003a). O'Sullivan and Parrish (1995) demonstrated that apatite composition may vary considerable even within a plutonic intrusion and that already slightly varying chemical composition of individual apatite grains can result in a significant spread of single grain ages within a sample. Here we present re-analysed AFT data of the samples from the Eisenhower Range originally compiled via population technique applying now the external detector technique (e.g., Gleadow, 1981; Hurford and Green, 1982, 1983) supplemented by new AFT data from the southern part of the range.

Thermal history modeling will show that the traditional monotonous stepwise cooling history proposed for the TAM (Fitzgerald, 2002) is inconsistent with published and new thermochronological data. Resulting thermal history models, paleotemperature estimates and isotherm patterns request an alternative exhumation scenario that is in accordance with independent geological information. Correspondingly, we evaluate the break in slope concept as tool to straightly date cooling events. Paleotemperature models will be used to reconstruct the exhumation history of the Eisenhower Range and to calculate paleogeothermal gradients of the area.

3.2) Geological setting and previous AFT studies

The Eisenhower Range constitutes a ~70 km long and up to 3000 m high escarpment bound plateau along the Priestley Glacier in the Ross sea region of Antarctica (Fig. M I-1). The geological architecture of the region is relatively simple and uniform. Basement units primarily consist of late Proterozoic and Early Paleozoic low- to medium-grade metamorphic rocks and Granite Harbour Intrusives, which are related to the Ross Orogeny along the Palaeo-Pacific active margin of Gondwana (e.g., Borg et al., 1987). Post-Ross orogenic erosion formed a low-relief erosion surface that was overlain by clastic deposits collectively termed Beacon Supergroup (e.g., Barrett, 1991). Triassic to Jurassic Beacon sediments with a thickness varying between ~30 m and ~50 m are preserved in the Eisenhower Range (Casnedi et al., 1994; Schöner et al., 2011). The position of the sub-Beacon erosion surface identifies the Eisenhower Range as a common tectonic block, which is structurally and morphologically separated from the Deep Freeze Range in the northeast by the Cenozoic right-lateral Priestley Fault beneath Priestley Glacier (e.g., Rossetti et al., 2003). Beacon sedimentation was followed by intrusion and extrusion of magmatic rocks in/on basement and sediments during the Ferrar event at ~180 Ma (e.g., Elliot and Fleming, 2008). The subaerial/subaquatic nature of these rocks is recognized by the presence of syn-Ferrar pyroclastic and siliciclastic, partially fossil-bearing sedimentary sequences; pillow lavas; phreatomagmatic structures and diatremes of local hydromagmatic explosive events; vesicles and sediment suspensions in sills; and plastic deformation of Jurassic sediments by Ferrar apophyses (e.g., Elliot, 2000; Schöner et al., 2007; Viereck-Götte et al., 2007; Elliot and Fleming, 2008). West of the study area, basement is locally overlain by Neogene volcanic rocks and/or Pliocene sediments and glacial deposits.

Previous AFT studies in the Eisenhower Range area were carried out at Mount Matz, Mount Nansen and Anderson Ridge (Balestrieri et al., 1994, 1997; Fig. M I-1). AFT data from sub-vertical sample sets have ages between ~31 and 198 Ma that show distinctive correlation with sample elevation (Table I-1; Fig. M I-2a). A break in slope at ~80 Ma and a discontinuity in the age-elevation plot at ~50 Ma (Fig. M I-2a) associated with a characteristic AFT length distribution pattern (Balestrieri et al., 1994) were interpreted to record cooling phases in the Late Cretaceous (~80 Ma) and Early Cenozoic (~50 Ma). These cooling episodes were related to regional exhumation periods associated with the initial break up of Australia and Antarctica and the extension between East and West Antarctica (Balestrieri et. al., 1997).

3.3) Sampling and results

A set of 19 basement samples (Granite Harbour Intrusives) and one sedimentary specimen from the Beacon Supergroup was collected during ItalAntartide expeditions 1985-87 and the German GANOVEX IX field campaign 2005/06. Vertical sample sets from Mount Matz, Mount Nansen and along the southern Eisenhower Range cover altitudes between 220 and 2380 m. The rock column above the highest sample consists of ~200 m granites, ~50 m Beacon sediments and ~100 m Ferrar rocks. The highest sample collected at 2380 m is overlain by a rock column of ~360 m. Twelve out of sixteen samples from Mount Matz, Mount Nansen, and Anderson Ridge originally conducted by Balestrieri et al. (1994, 1997; Fig. M I-2a) via population technique were re-analyzed via external detector technique.

AFT ages of all samples range from 32.0±2.4 to 175.0±14.0 Ma (Fig. M I-3a, Table I-1), and thus considerably postdate the emplacement of the Granite Harbour Intrusive suite (age: ~490-550 Ma; e.g., Goodge, 2007). The corresponding MTL vary between 11.21±0.37 and 14.01±0.13 µm with associated standard deviations of 1.29 – 2.93 µm (Fig. M I-3b, Table I-1). The samples below the break in slope show longer MTL (12.73±0.35 – 14.01±0.13 µm) with smaller standard deviations (1.29 – 2.18 µm) than the samples above the break in slope (11.21±0.37 – 12.26±0.31µm/ 2.02 – 2.93 µm). Moreover, the relation of AFT ages and MTL broadly conforms to a concave “boomerang” pattern that is supported by skewed MTL distributions (cf., Green, 1986; Fig. M I-3c).

Sample	Latitude S Longitude E	Elevation [m]	ξ	ρ_D [10^6cm^{-2}] (N_D)	ρ_S [10^6cm^{-2}] (N_S)	ρ_I [10^6cm^{-2}] (N_I)	P(χ^2) [%]	Dated grains [N]	AFT age [Ma] (predicted age)	MTL [µm] (n)	MTL c-axis [µm] (predicted MTL)	SD [µm]	SD c-axis [µm] (predicted SD)	GOF age/MTL	Dpar mean [µm]	original age [Ma]
Eisenhower Range																
3475	74.71 162.62	430	320 ±10	18.1 (17974)	5.2 (281)	46.5 (2507)	98	22	32.4±2.3 (33.0)	13.79±0.19 (100)	14.54 (14.52)	1.91	1.61 (1.53)	0.79 0.10	2.29	
BC7	74.75 162.63	660	320 ±10	18.1 (17974)	5.6 (251)	46.0 (2057)	100	25	35.3±2.6 (36.3)	13.33±0.23 (70)	14.29 (14.16)	1.95	1.40 (1.72)	0.68 0.50	2.34	*39.9 ± 2.9*
3466	74.44 162.72	780	320 ±10	17.9 (17974)	4.8 (142)	36.9 (1080)	99	20	37.5±3.5 (38.0)	13.45±0.17 (100)	14.31 (14.03)	1.71	1.38 (1.74)	0.90 0.12	2.11	
3465	74.42 162.70	1030	320 ±10	18.0 (17974)	7.9 (367)	58.0 (2697)	100	24	39.1±2.5 (39.8)	13.36±0.20 (100)	14.25 (13.94)	1.99	1.55 (1.80)	0.76 0.61	2.03	
3464	74.47 162.63	1535	320 ±10	18.1 (17974)	5.0 (157)	18.9 (598)	100	25	75.5±7.1 (74.8)	11.58±0.26 (100)	13.08 (13.41)	2.62	1.84 (1.71)	0.92 0.53	1.99	
3462	74.29 162.36	1720	320 ±10	182 (17974)	5.1 (195)	15.9 (606)	99	20	92.9±8.1 (92.6)	11.21±0.37 (43)	12.93 (13.50)	2.45	1.41 (1.60)	0.97 0.53	1.99	
3463	74.36 161.85	2014	320 ±10	18.0 (17974)	10.7 (384)	22.2 (799)	99	23	137.9±9 (135.0)	11.69±0.24 (100)	13.05 (13.47)	2.43	1.85 (1.71)	0.89 0.61	2.34	
3472	74.63 162.58	2180	320 ±10	15.6 (15663)	10.8 (750)	18.4 (1284)	96	25	144.4±7.9 (147.0)	11.22±0.27 (100)	12.88 (13.04)	2.66	1.72 (1.76)	0.74 0.52	2.19	
Mount Matz																
BC4	74.67 162.20	700	320 ±10	23.6 (17974)	3.7 (167)	26.5 (1205)	100	24	52.2±4.6 (50.8)	12.73±0.35 (40)	13.94 (13.73)	2.18	1.49 (1.82)	0.76 0.19	2.14	57.4 ± 4.8
BC5	74.70 162.26	940	320 ±10	23.6 (23364)	5.8 (499)	40 (3426)	100	30	54.8±3.1 (54.8)	13.26±0.22 (80)	14.19 (13.54)	1.97	1.51 (1.93)	0.99 0.05	2.34	65.6 ± 4.9
BC3	74.77 162.37	1220	320 ±10	23.6 (17974)	8.5 (305)	46.4 (1660)	99	20	69.1±4.8 (70.0)	11.60±0.28 (100)	13.22 (13.46)	2.77	1.66 (1.74)	0.84 0.87	2.2	76.1 ± 5.5
BC2	74.92 162.50	1450	320 ±10	23.6 (23364)	7.9 (333)	36.3 (1539)	98	20	81.3±5.5 (80.8)	11.54±0.29 (100)	13.15 (13.38)	2.93	1.77 (1.77)	0.93 0.69	2.36	107 ± 10
BC1	74.77 162.39	1590	320 ±10	23.6 (23364)	8.2 (740)	31.1 (2824)	86	25	98.3±5 (91.0)	11.63±0.27 (84)	13.11 (13.47)	2.68	1.76 (1.60)	0.15 0.74	1.90	102 ± 7
Mount Nansen																
C17	74.72 162.74	220	366 ±12	7.07 (5541)	7.8 (577)	28.04 (2062)	83	20	36.6±2.7 (30.5)	14.01±0.13 (101)	14.76 (14.87)	1.29	1.00 (1.03)	0.01 0.84	1.81	31.1 ± 2.1
C9	74.73 162.69	300	366 ±12	7.07 (5541)	2.3 (281)	9.5 (1133)	70	28	32±2.4 (-)	14.36±0.59 (5)	-	1.31	1.03 (-)	-	1.79	35 ± 2.4
C6	74.78 162.50	1020	366 ±12	7.07 (5541)	4.6 (481)	12.6 (1277)	88	30	48.5±3.1 (-)	13.22±0.55 (18)	-	2.35	-	-	1.57	67.2 ± 4.1
C5	74.68 162.50	1390	366 ±12	7.07 (5541)	4 (113)	6.53 (187)	53	12	77.5±9.8 (-)	-	-	-	-	-	1.61	71 ±13
C4	74.66 162.53	1780	366 ±12	7.07 (5541)	6 (586)	9.1 (903)	7	30	82.1±6.1 (-)	12.85±0.42 (26)	-	2.14	-	-	1.70	78.2 ± 4.9
C3	74.65 162.55	1950	366 ±12	7.07 (5541)	9 (852)	11.4 (1095)	30	30	99.8±6 (102)	12.26±0.31 (43)	13.51 (13.46)	2.02	1.53 (1.56)	0.75 0.65	1.62	97.3 ± 6
C1	74.47 162.62	2380	366 ±12	7.07 (5541)	19.4 (1083)	14.2 (790)	<5	25	175.0±14 (175.0)	11.5±0.26 (101)	12.96 (12.97)	2.63	1.77 (1.55)	0.99 0.70	1.73	198 ± 14

Table M I-1: Apatite fission track (AFT) data of the Eisenhower Range.

AFT ages were determined by counting spontaneous and induced fission tracks according to the Zeta (ζ) calibration method (Hurford and Green, 1982, 1983; Green 1985; ρD, ρS, ρI, Nd, Ns, NI: density and number of counted dosimeter, spontaneous and induced tracks; P(χ2): χ2 probability). Irradiations of AFT mounts were conducted at the thermal facility FRMII (Garching, Germany) using dosimeter glasses CN5 and a neutron flux of 1.0x10^{16} (Mount Nansen), 1.2x10^{16} (Eisenhower Range), and 1.5x10^{16} (Mount Matz) neutrons per cm2. The mounts were etched with 5M HNO_3 at 20°C for 20 seconds and correspondent mica plates were etched with 40% HF at 20°C for 30 minutes. Diameter of etched spontaneous fission tracks (Dpars) we measured for all investigated grains as a proxy of track annealing kinetic properties (e.g. Donelick, 1993; Carlson et al., 1999). AFT ages were calculated using the program Trackkey (Dunkl, 2002). Zeta (ζ) values are 320±10 (Prenzel) and 366±12 (Balestrieri). Errors are quoted as ±1σ (Green, 1981). If possible, 100 fission track lengths for each sample were measured following the recommendations of Laslett et al. (1982). Mean track length (MTL) and standard deviation (SD) is quoted for all samples where fission track lengths were measured. The goodness of fit (GOF) between measured and modeled AFT ages and lengths is quoted for the HeFTy c-axis projected forward models (see also Fig. 4a). AFT ages conducted originally via population method (Balestrieri et al., 1994, 1997) are shown for comparison. For further details cf. appendix.

The older samples show bimodal track length distributions, while the samples below the break in slope display relatively narrow unimodal track length distributions (Fig. M I-3c). Mean Dpar values of the granitic samples vary between 1.57 and 2.34 µm (Table I-1) and thus imply fairly similar fission track annealing kinetic properties. There is no noticeable correlation between single grain ages and Dpars. The majority of re-analysed AFT ages resembles those achieved via population technique within ±1σ. Only two samples from Mount Matz and one sample from Mount Nansen hold significantly younger newly dated ages (Table I-1; Fig. M I-2a; and see below).

Southern Eisenhower Range: AFT data of seven granite samples and one sandstone sample were obtained from the southern Eisenhower Range. AFT ages of samples from altitudes between 430 and 2180 m range between 32.4±2.3 and 144.4±7.9 Ma (Fig. M I-2a) with corresponding MTL and standard deviations of 11.21±0.37 – 13.79±0.19 µm and 1.71 – 2.66 µm, respectively (Table I-1). The AFT ages correlate with sample altitudes with a distinctive break in slope at ~40 Ma and ~1400 m. The re-analysed age from Anderson Ridge (BC7) is within error (±1σ) of the age determined via population technique (Table I-1, Fig. M I-2a).

Mount Matz: A vertical profile of five granite samples between 700 and 1590 m was collected at Mount Matz in the SW Eisenhower Range (Fig. M I-1). AFT ages range between 52.2±4.6 and 98.3±5.0 Ma, and MTL between 11.54±0.29 and 13.26±0.22 µm with associated standard deviations of 1.97 – 2.93 µm. Two samples (BC2, BC5) have significantly younger ages than those dated by population technique (Fig. M I-2a, Table I-1). The new age of sample BC2 defines a new offset in the regression of the age-elevation plot at ~55 Ma and ~1300 m (Fig. M I-2a). This contrasts to the previously postulated break in slope at ~80 Ma (Fig. M I-2a; Balestrieri et al., 1997).

Mount Nansen: Seven granite samples were collected in the southern part of the Eisenhower Range at Mount Nansen from altitudes between 220 and 2380 m (Fig. M I-1). AFT ages of 32.0±2.4 to 175.0±14.0 Ma display a distinctive positive correlation with the altitude, while the MTL cover a wide range between 11.50±0.26 and 14.01±0.13 µm with an inverse correlation with elevation (Table I-1; Fig. M I-2b). The corresponding standard deviations also strongly vary between 1.29 and 2.63 µm. Previous AFT data of this profile comprise broadly similar ages, with the exception of sample C6 which has now a significantly younger age (Table I-1; Fig. M I-2a). Consequently, the original break in slope at ~80 Ma and ~1900 m and the

discontinuity in the age-elevation regression at ~50 Ma and ~800 m (Fig. M I-2a; Balestrieri et al., 1994) are no longer evident. The newly determined break in slope is located at ~45 Ma and ~1500 m (Fig. M I-3a). This approximately agrees with the age but not with the altitude of the previously observed discontinuity in the age-elevation regression.

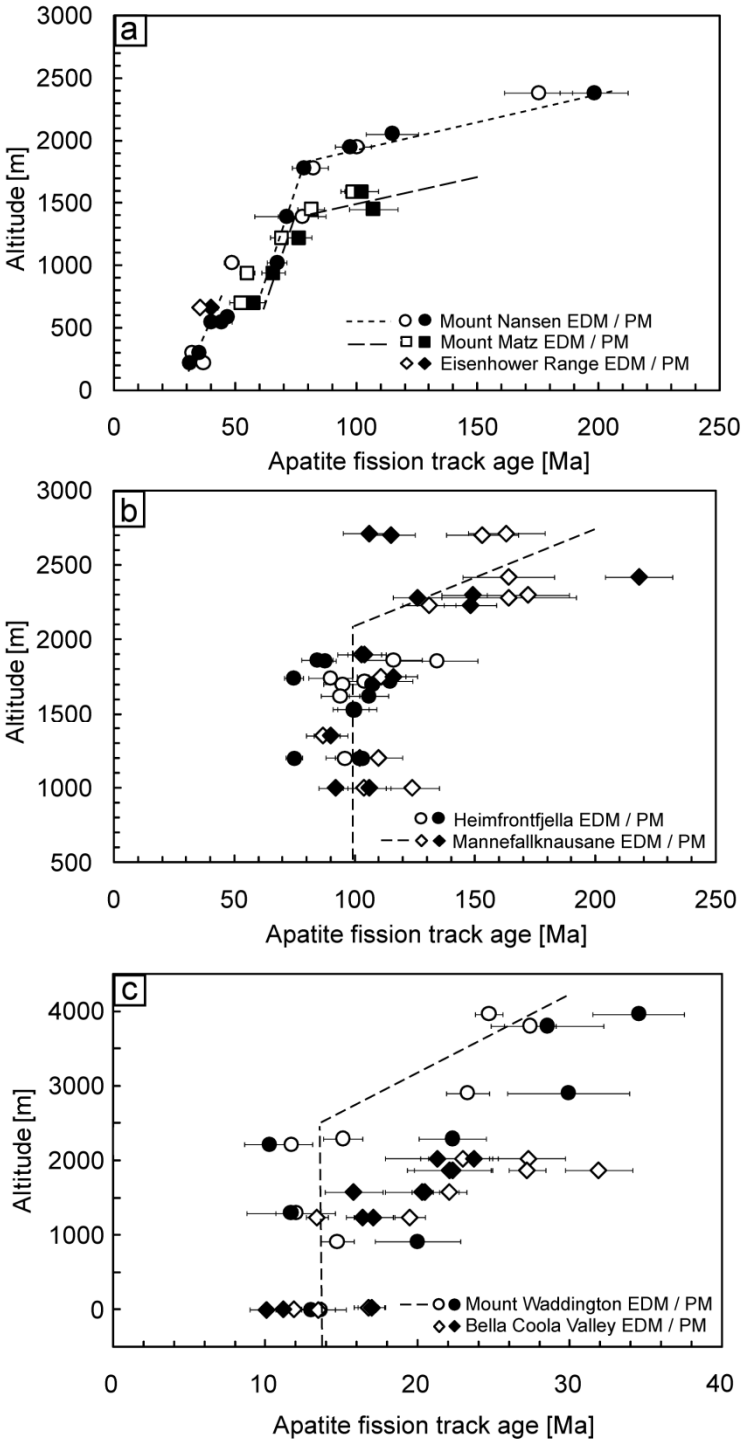

Figure M I-2: Comparison of apatite fission track ages conducted via population (PM) and external detector method (EDM) from (a) the Eisenhower Range area, and from data published by (b) O'Sullivan and Parrish (1995), and (c) Jacobs and Lisker (1999). For more information see text (5.1).

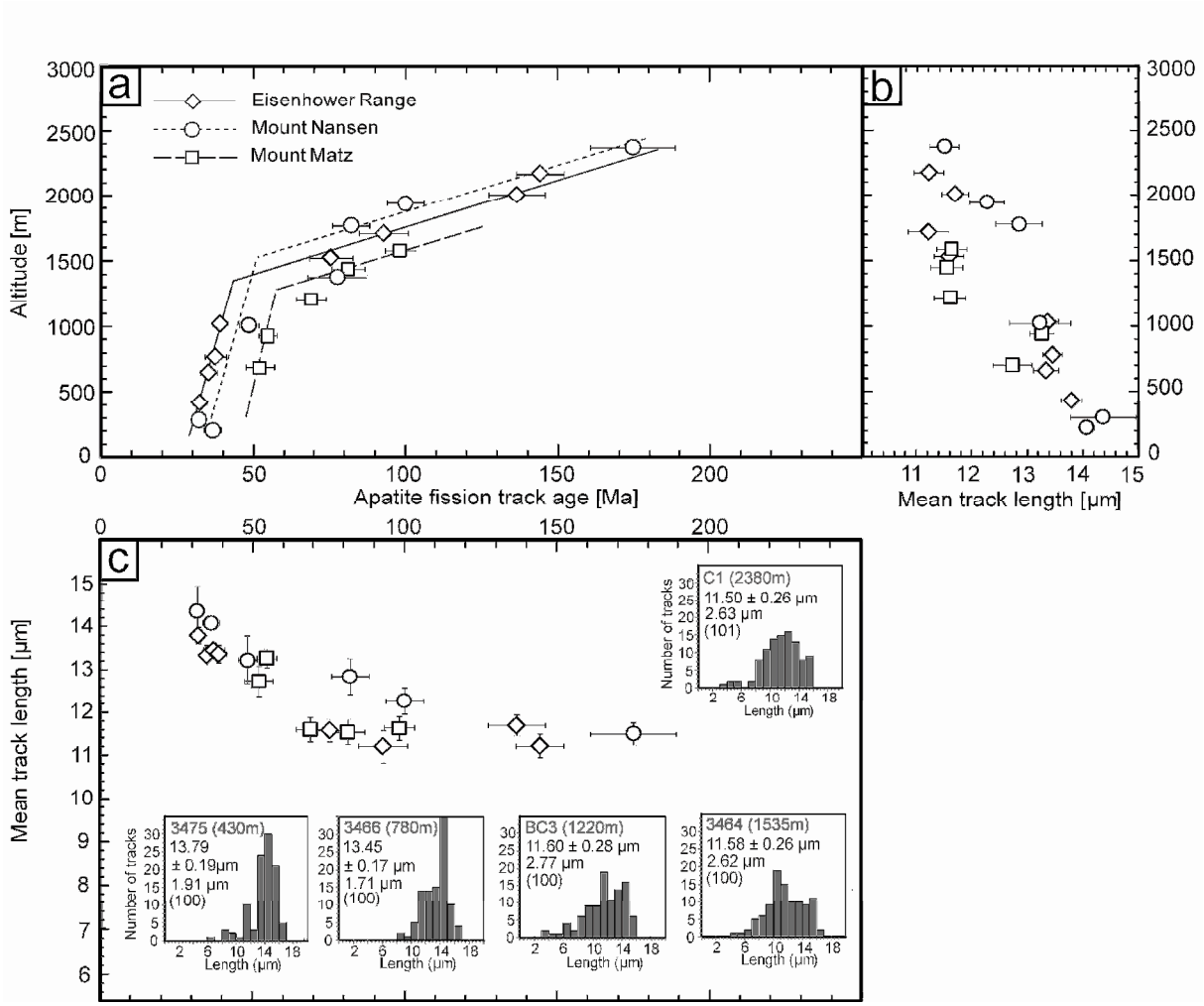

Figure M I-3: Plots showing (a) apatite fission track ages and (b) mean track length vs. sample altitude, and (c) the relation between apatite fission track ages and mean track lengths of three sample profiles from the Eisenhower Range. Mean track length distributions of five representative samples are shown as inset within (c). Errors are quoted as ± 1σ.

3.4) Thermal history modeling

3.4.1) Modeling procedures

Modeling was performed for all samples with at least 40 measured confined track lengths, which accounts for all but four samples (Table I-1). Thermal histories were modeled using HeFTy (Ketcham, 2005) and QTQt (Gallagher et al., 2005; and Gallagher, 2012) programs. Based on AFT age, length and Dpar data, HeFTy generates inverse and forward thermal history models for individual samples, while QTQt is applied to single samples or a set of multiple samples of different heights from boreholes or vertical profiles.

At first, we generated random thermal history paths for all samples individually by inverse HeFTy modeling. Afterwards, the best composite thermal history of individually produced HeFTy forward models served as the base for a common thermal history of all samples. Finally, multiple QTQt modeling validated the common HeFTy thermal history.

3.4.2) Modeling constraints

Initial HeFTy input conditions comprise seven time-temperature constraints (see also Fig. M I-4): (1) initial high temperatures subsequent to the intrusion of the Granite Harbour Intrusives [500 – 450 Ma; 150° – 300°C]; (2) a large temperature range until the emplacement of Ferrar doleritic rocks [500 – 180 Ma; 0° – 300°C]; (3) near surface temperatures concluded from superficially emplaced volcanic rocks of the Ferrar Event at ~180 Ma, depending on individual sample positions in vertical relation to the paleosurface [185 – 175 Ma; 10° – 30°C for the highest sample to 60° – 170°C for the lowermost sample; Jurassic geothermal gradient 15° – 70°C/km]; (4) subsequent maximal paleotemperatures inferred from sample ages <180 Ma [180 – 55 Ma; 40° – 250°C]; (5) decreasing temperatures in Cenozoic times inferred from the boomerang pattern of AFT ages vs. MTL (Fig. M I-2c) and the typical differences between the MTL distributions below and above the break in slope [55 – 25 Ma; 20° – 160°C]; (6) near surface temperatures for the time between break in slope age and present [55 – 0 Ma; -35°– 20°C]; and (7) the present-day mean surface temperature of the Eisenhower Range depending on sample altitude [0 Ma; -35° – 13°C, for a conventional orographic temperature decrease of 1°C per 100 m elevation].

QTQt limits the initial conditions to five time-temperature envelopes. We specified time-temperature constraints for the highest sample analogous to four of those applied for HeFTy inverse modeling (time-temperature constraints: 1-3 and 6), which then automatically were imposed on the other samples. Since QTQt does not allow negative values the present temperature was set to zero.

3.4.3) Thermal histories

HeFTy inverse individual sample modeling produced very similar thermal histories for all samples (Fig. M I-4) with at least 20 good (goodness of fit = GOF >0.5) and 150 acceptable (GOF >0.05) fitting thermal history paths each. Inverse modeling results

generally show low/near surface temperatures at the time of the Ferrar event, subsequent temperature increase during the Jurassic and Cretaceous, and accelerated cooling to surface temperatures commenced between Early Eocene and Oligocene times (Fig. M I-4). Thereby, samples from higher altitudes do not reach temperatures higher than the PAZ (Figs. M I-4a and b) while tracks of samples from the bottom were partially to completely annealed (Figs. M I-4d, e and f). Many samples show a strongly limited Mid-Cretaceous to Eocene/Oligocene temperature range (Figs. M I-4a – d). Rapid cooling of most samples did not commence prior to the Late Eocene (Figs. M I-4b – f). These thermal histories served as the base to detect the best composite thermal history via multiple sample modeling.

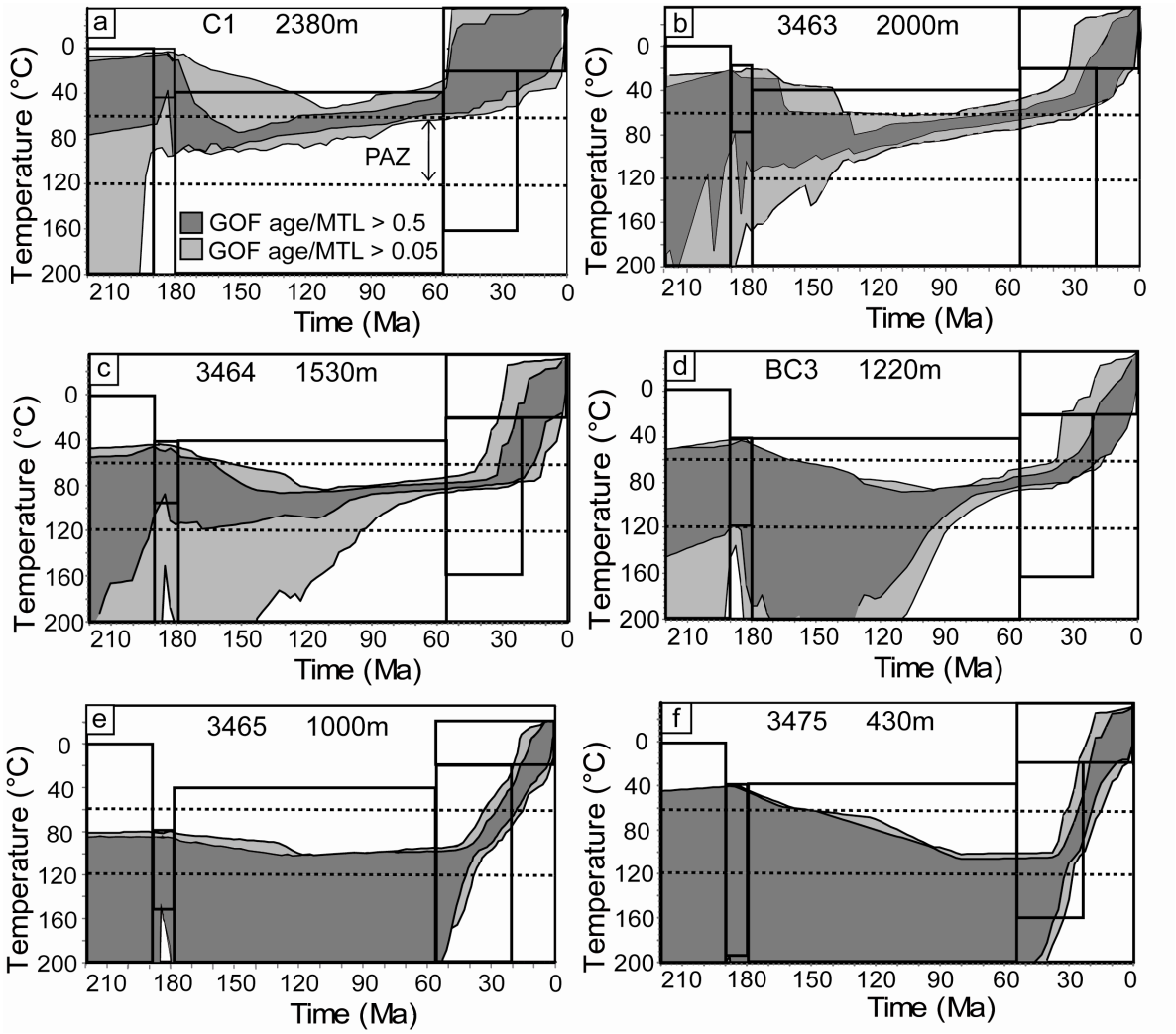

Figure M I-4: Inverse modeling results of six representative samples (a – e) from different altitudes [HeFTy, Ketcham, 2005]; Black boxes mark the time-temperature constraints set for HeFTy modeling (for detailed description see text). The dotted black lines mark the limit of the Partial Annealing Zone (PAZ). HeFTy was performed for all applicable samples using the Monte Carlo search method and a minimum of 100,000 randomly produced t-T-paths. The goodness of fit (GOF) of the apatite fission track (AFT) age data were determined for each sample using the annealing model of Ketcham et al. (2007) and c-axis projection, the GOF of the AFT length data is quoted using the Kuiper's Statistic method. A default initial track length of 15.99 µm and a length reduction of 0.892 µm were measured in Durango standard.

Multiple HeFTy and QTQt modeling of the sample set (Figs. M I-5a and b) detects a common thermal history analogously to HeFTy inverse models. Good fits between measured and modeled data of both approaches indicate a very similar thermal history.

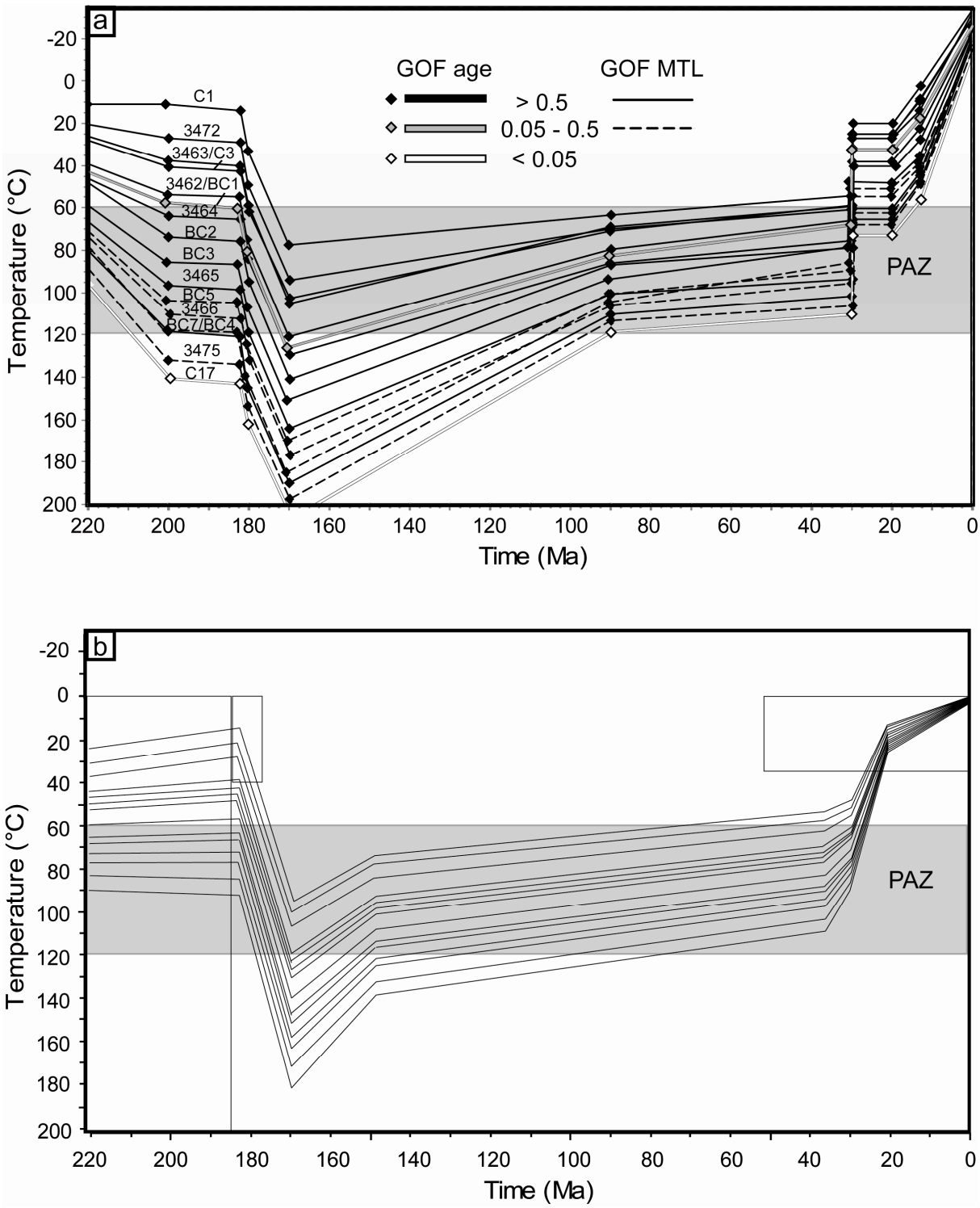

Figure M I-5: Composite models of 16 samples from the Eisenhower Range area produced by (a) c-axis projected HeFTy forward modeling (version 1.6.7) and (b) QTQt (version 3.0). The temperature range of the Partial Annealing Zone (PAZ) is underlain in grey. In (a), the goodness of fit (GOF) of ages and lengths are shown by different contours and shades of grey. In (b), t-T constraints are shown as black boxes. Thermal histories of HeFTy and QTQt were generated allowing a varying temperature difference between the individual samples (varying geothermal gradient) over time.

The best composite thermal history produced by HeFTy includes (I) a period of low/near surface temperatures from the Late Triassic to Early Jurassic; (II) increasing temperatures during the Mid- and Late Jurassic; (III) slightly decreasing temperatures during the Late Jurassic and Early Cretaceous; (IV) almost constant temperatures from the Mid-Cretaceous to Paleocene; (V) considerable decrease to low/near surface temperatures (~15 – 75°C) initiated in the Late Eocene/Early Oligocene (at ~35 – 30 Ma with a better common fit at ~30 Ma); (VI) constant temperatures from Late Eocene to Early Miocene times; and (VII) final decrease to the present-day surface temperature (-35° to -13°C, depending on sample altitude) initiated in the Miocene. HeFTy suggests fast final cooling at ~30 Ma and ~20 Ma intermitted by a period of steady temperatures, while QTQt prefers slightly slower but continuous cooling with a change in cooling rate at ~20 Ma. This difference in the final cooling pattern is probably attributed to the fact that the present-day temperature was set to zero for QTQt modeling (see Fig. M I-5b).

3.5) Evaluation of thermochronological concepts

3.5.1) Dating methods

Ten of thirteen ages of the present study reproduce the ones obtained by population method within error (±1σ), while the ages of two samples from Mount Matz (BC2, BC5) and one sample from Mount Nansen (C6) are two to three times outside of the previous age error (Table I-1; Figs. M I-2a and 3a). The largest age deviations are recorded for samples BC2 and C6, which are ~26 Ma and ~19 Ma younger than the population ages. The new ages of these samples shift the break in slope from ~80 Ma to ~55 Ma at Mount Matz, and from 80 Ma to 45 Ma at Mount Nansen (Table I-1; Figs. M I-2a and 3a).

Previous AFT studies from Bella Coola Valley and Mount Waddington in the Coast Ranges of British Columbia (O'Sullivan and Parrish, 1995) and from Heimefrontfjella and Mannefallknausane in Dronning Maud Land, Antarctica (Jacobs and Lisker, 1999) re-examined samples originally dated via population technique with external detector technique. Comparison of the ages from both techniques shows no common trend for the different sample sets. A general trend of younger re-dated ages is observed for the samples from Mount Matz (Fig. M I-2a) and Mount Waddington (Fig. M I-2b), while a common trend of older re-dated ages is observed for the samples

from Bella Coola Valley (Fig. M I-2b), Heimefrontfjella (Fig. M I-2c), Mannefallknausane (Fig. M I-2c) and Mount Nansen (Fig. M I-2a). All sample sets contain at least one new age that strongly differs from the population technique equivalents (Fig. M I-2). Considerable age deviations are detected for the samples above the break in slope (Fig. M I-2), which are interpreted to have been subjected for longer time periods to elevated paleotemperatures within the PAZ. There, chemical composition of the apatites stronger affects the fission track annealing kinetic properties, and thus may cause a larger spread of single grain ages (O'Sullivan and Parrish, 1995). Accordingly, the new data from Mount Matz, Mount Nansen and Mount Waddington record a modified pattern of AFT ages vs. altitudes and eventually a different thermal history than predicted in earlier studies. The remarkable age differences within the sample sets from British Columbia, Dronning Maud Land and the Eisenhower Range clearly indicate the importance of single grain age analysis even when studying plutonic rocks of the same origin (O'Sullivan and Parrish, 1995).

3.5.2) Break in slope

Early studies in the TAM have described a break in slope in vertical age profiles as the base of a fossil PAZ which is supposed to mark the initiation of accelerated rock cooling due to exhumation (Gleadow and Fitzgerald, 1987; Wagner et al., 1989). A traditional qualitative interpretation of the data from the Eisenhower Range based on this concept infers accelerated sample cooling commencing in the Early/Mid-Eocene (Fig. M I-3a). Instead, thermal history modeling of the AFT data based on independent geological information requires Jurassic to Late Eocene/Early Oligocene reheating of the sample suite and rapid cooling occurring at ~35 – 30 Ma (Figs. M I-4 and 5). Thus, cooling commenced substantially later than anticipated via break in slope (Figs. M I-3, 4 and 5).

The restricted applicability of the break in slope as an immediate time constraint for cooling events can be demonstrated by a HeFTy forward modeling experiment (Fig. M I-6). We modeled thermal history scenarios for a virtual set of six samples vertically aligned between 0 and 1250 m for (1) monotone two-stage cooling with (a) low and (b) high final cooling rate, and (2) complex cooling comprising reheating of the sample set analogously to the thermal history of the Eisenhower Range (Fig. M I-6a).

The monotone cooling models rely on almost constant paleotemperatures within the PAZ until onset of final cooling, while the sample set of the complex thermal history model cooled to near-surface temperatures between 220 and 180 Ma with subsequent reheating to temperatures within the PAZ prior to final cooling. All models cover a time period of 500 Ma, with final cooling to the surface commencing at 60 Ma (Fig. M I-6a). The geothermal gradient is kept constant at 30°C/km for the entire cooling history, and the chemical composition of apatite is set uniform for all samples.

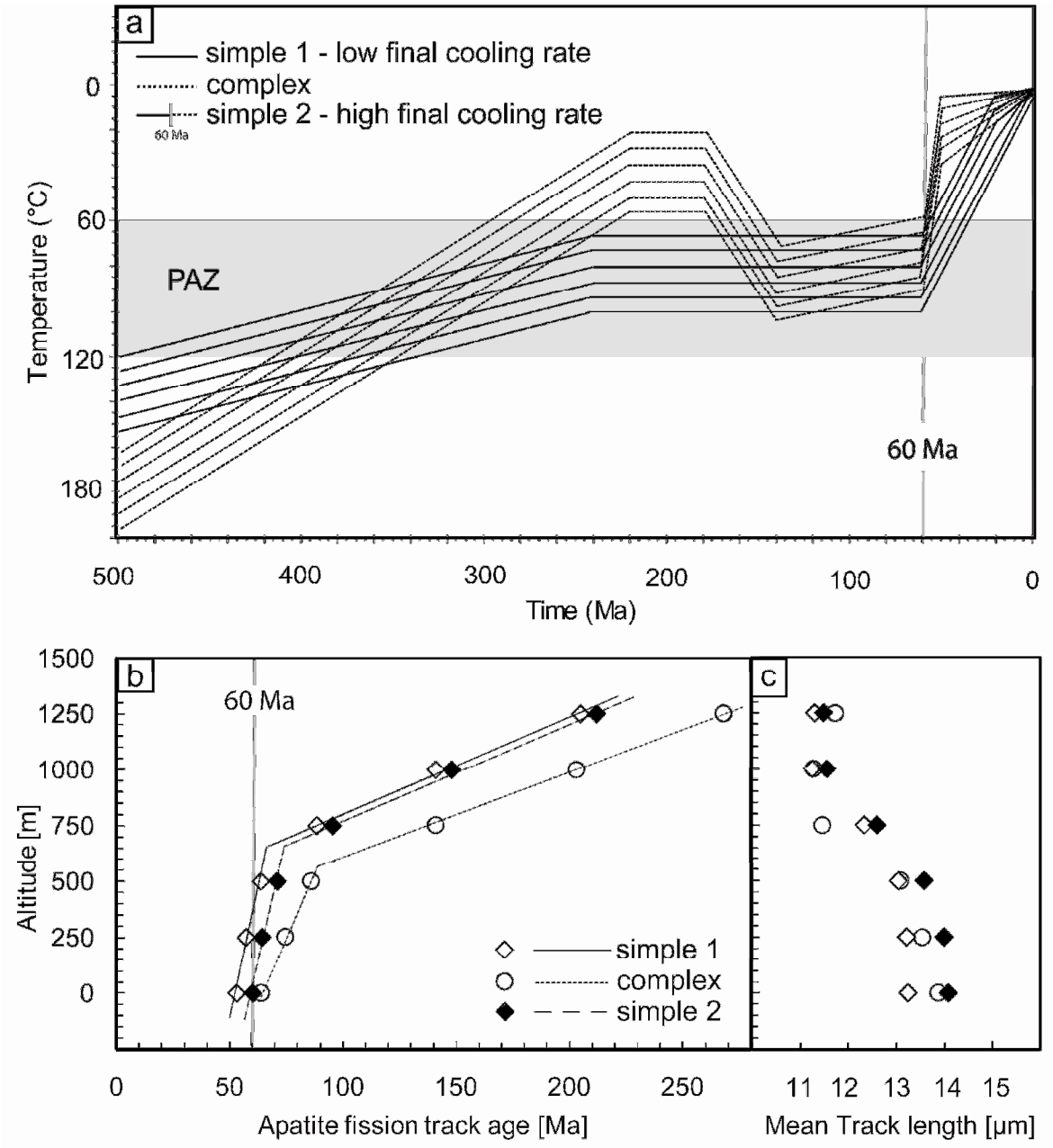

Figure M I-6: (a) Synthetic cooling histories of a vertical sample set produced by HeFTy forward modeling for two monotone two-stage tectonic scenarios with different final cooling rates and a complex thermal history comprising reburial of the sample set; (b) corresponding age-elevation plots; (c) corresponding mean track length-elevation plot. Final rapid cooling starts at 60 Ma for all thermal histories, but the age of the break in slope in the vertical profiles varies between 65 and 90 Ma; Partial Annealing Zone = PAZ. For further details see text (5.2).

Modeled AFT ages of each cooling scenario closely correlate with sample elevation involving a pronounced break in slope (Fig. M I-6b), and associated with substantial MTL reduction in samples above the break in slope (Fig. M I-6c). The break in slope concept should record a change in modeled age-elevation gradient and MTL at ~60 Ma. However, the break in slope of all three scenarios is older than the onset of final cooling (Fig. M I-6). This time-age difference varies, depending on the final cooling rate, between ~5 Ma for monotone cooling with slow final cooling (scenario 1a) and ~10 Ma for monotone cooling with fast final cooling (scenario 1b), to ~30 Ma for the complex thermal history (scenario 2). Thus, a break in slope does not necessarily date cooling. Instead, its position and shape depends on various factors such as (1) rate and amount of final cooling, (2) the thermal history prior to the onset of final cooling, i.e. the time each sample remained within the PAZ, (3) maximum paleotemperatures, and (4) the geothermal gradient. A break in slope only provides a minimum qualitative time constraint for the onset of cooling and cannot substitute thermal history modeling. Different positions of breaks in slopes in adjacent vertical profiles unaffected by tectonic activity do not necessarily mark different cooling times. Therefore, breaks in slopes from different vertical profiles cannot be interpreted collectively and the concept of a composite vertical profile for estimating regional cooling should not be applied. Instead, cooling of a region anticipated via the age of a break in slope needs to be validated by thermal history modeling of each sample. It is also evident that a break in slope cannot resolve complex thermal histories and that a solely qualitative interpretation of an AFT pattern may result in an incorrect record of the thermal history such as shown here for the Eisenhower Range.

3.6) Mesozoic and Cenozoic evolution of the Eisenhower Range

3.6.1) Paleogeothermal gradient

Paleogeothermal gradients can be calculated from the regression of modeled paleotemperatures and sample altitudes. Both HeFTy (Fig. M I-4a) and QTQt (Fig. M I-4b) show consistent t-T-patterns. The correlation of 15 modeled paleotemperatures at ~90 Ma (HeFTy: 64°-114°C; QTQt: 62°-117°C) and sample altitudes of 430 – 2380 m refers to a consistent Cretaceous/Cenozoic geothermal gradient of 26 ± 8°C/km (HeFTy) and 28 ± 9°C/km (QTQt), respectively (Fig. M I-7). This agrees very well with

geothermal gradients of ~25°C/km calculated for the northern TAM and the USARP Mountains by Fitzgerald (1994) and Lisker et al. (2006).

The Jurassic geothermal gradient was estimated from the regression of four modeled maximal paleotemperatures within the PAZ at ~170 Ma (HeFTy: 77-105°C; QTQt: 91-116°C) against sample altitudes between 1950 and 2380m. Both HeFTy and QTQt produce an identical Jurassic geothermal gradient of about 60°C/km (Fig. M I-7).

The high Jurassic geothermal gradient may be attributed to Late Jurassic/ Early Cretaceous rifting processes and associated Ferrar magmatic intrusions and extrusions (e.g., Elliot, 1992) within the extensional setting of the TAM region. Subsequent change to a much lower, moderate Cretaceous to Eocene geothermal gradient is probably related to basal heatflow decline due to isobaric cooling.

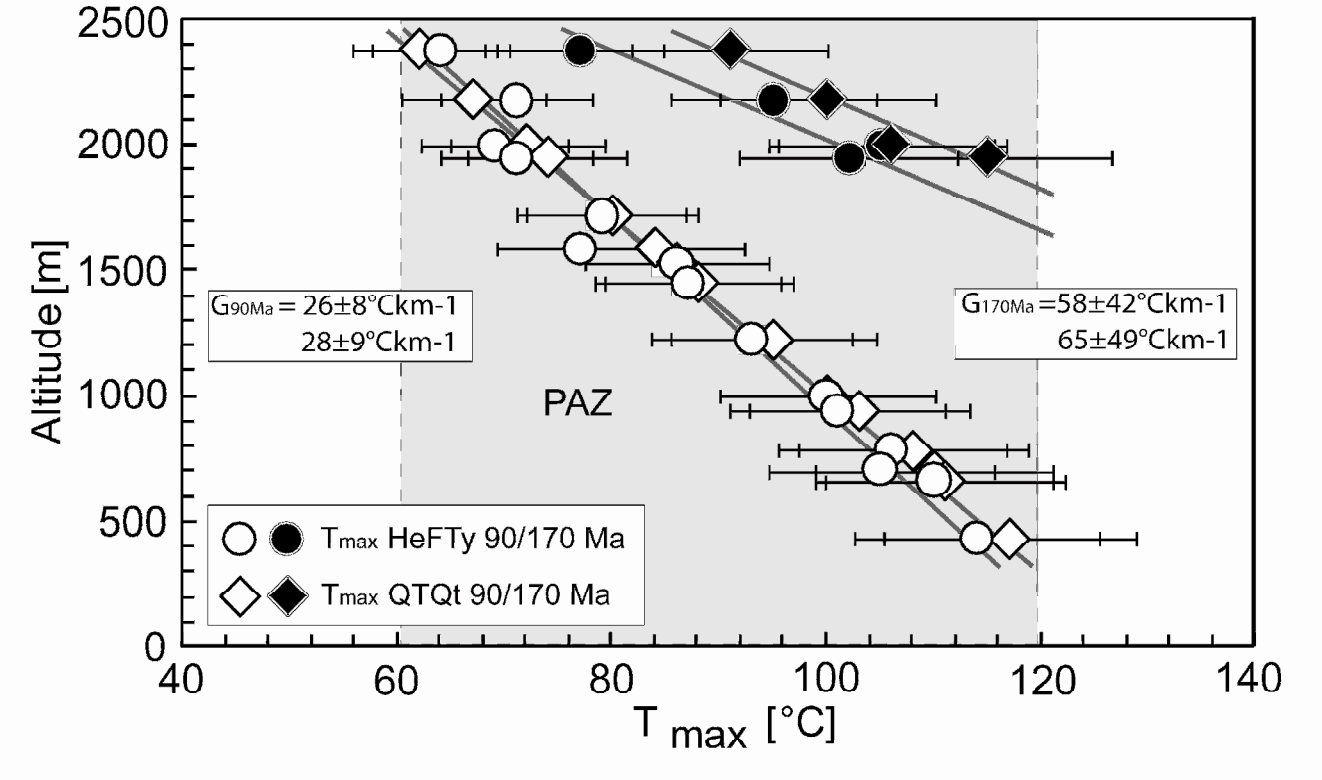

Figure M I-7: Maximal temperature estimates (Tmax) of the Eisenhower Range area modeled with HeFTy (Fig. M I-5a) and QTQt (Fig. M I-5b) at 170 Ma (Middle Jurassic) and 90 Ma (Late Cretaceous). Errors are quoted as ±10%. The temperature range of the Partial Annealing Zone (PAZ) is underlain in grey. The regression of paleotemperature estimates versus sample altitudes refers to a Jurassic geothermal gradient of ~60°C/km and a Cretaceous/Cenozoic geothermal gradient of ~27°C/km.

3.6.2) Burial and exhumation of the Eisenhower Range

The emplacement of subaerial Ferrar rocks on granitic basement places the sampled granitic rocks close to the surface at ~180 Ma (Figs. M I-4, 5 and 8). Thermal history models require long-lasting reheating of the Eisenhower Range subsequent to the Ferrar event until onset of accelerated cooling at the Late Eocene/Early Oligocene (Figs. M I-4 and 5). This can be explained solely by deposition of sedimentary rocks on basement and Ferrar rocks between Jurassic and Eocene times (cf., Lisker and Läufer; 2013; Fig. M I-8). A Cretaceous to Cenozoic sedimentary cover of up to ~3.5 km (Fig. M I-8) can be inferred from the Cretaceous-Cenozoic geothermal gradient of ~27°C/km, and temperature estimate (~65°C) and position of the highest sample (~360 m below Ferrar surface) at this time.

The burial and exhumation history of the Eisenhower Range outlined here is in rigorous contrast to the traditional exhumation concept of the TAM assuming monotonous stepwise cooling without reburial (e.g., Fitzgerald, 2002). Instead, geological observation and AFT data require the existence of a Late Jurassic to Eocene sedimentary basin on both basement and Beacon/Ferrar rocks in the Eisenhower Range area as recognized by Lisker and Läufer (2013). The authors suggest the existence of an extensive sedimentary “Mesozoic Victoria Basin” between Australia and Antarctica. Based on qualitative interpretation of AFT and thermal data they predicted maximum basin depths of ~2.5 – 5 km for northern Victoria Land. This agrees well with the sedimentary overburden of ~3.5 km in the Eisenhower Range. Rapid cooling of the Eisenhower Range commenced at ~35 – 30 Ma and thus substantially later than proposed in previous studies (e.g., Balestrieri et al., 1994, 1997). The basin hence prevailed until the onset of fast erosion of the sedimentary sequence and the (re-) exposure of the underlying Ferrar rocks in the Late Eocene/Early Oligocene. Enhanced exhumation at the Eocene/Oligocene transition may be triggered by tectonic processes, climatic change or a combination of both, such as (I) rifting of the West Antarctic Rift System, (II) onset of sea floor spreading and opening of the Tasman gateway between Antarctica and Australia at ~34 Ma (e.g., Stickley et al., 2004), and (III) the incipient formation of the East Antarctic continental ice shield at ~33 Ma (e.g., Ehrmann and Mackensen, 1992). Tectonic activity during the Late Eocene in northern Victoria Land is evident by ~34 Ma old pseudotachylytes from the Priestley Fault (Di Vincenzo et al., 2004; Rossetti

et al., 2006) and indirectly by AFT data from the Rennick Glacier area (Rossetti et al., 2003). Continental ice shield formation is documented by clay mineral assemblages from drill cores off the Victoria Land in the western shelf of McMurdo Sound (Ehrmann, 1998). Oligocene drill core sediments record numerous ice shield advances and retreats with ice movement predominantly from the west. Furthermore, the drill core sediments contain high illite concentrations indicative for sedimentary terrestrial source rocks. Hence, a glacial removal of the "Mesozoic Victoria Basin" deposits due to ice flow from the west with subsequent discharge into the Ross Sea may explain the fast uncovering of the Ferrar rocks over less than 1 my.

Fast basin inversion and erosion placed the samples at/near surface (~15°C – 75°C) at ~35 – 30 Ma while exhumation stagnated from the Early Miocene onwards (Fig. M I-5). Cooling to the present-day surface temperature (-35°) is very likely confined to differential lateral and vertical exhumation of the granitic basement due to Miocene inception of the main ice sheet (Kerr and Huybrechts, 1999) and glacial incision along tectonic structures such as the Priestley Fault/Glacier (Fig. M I-8).

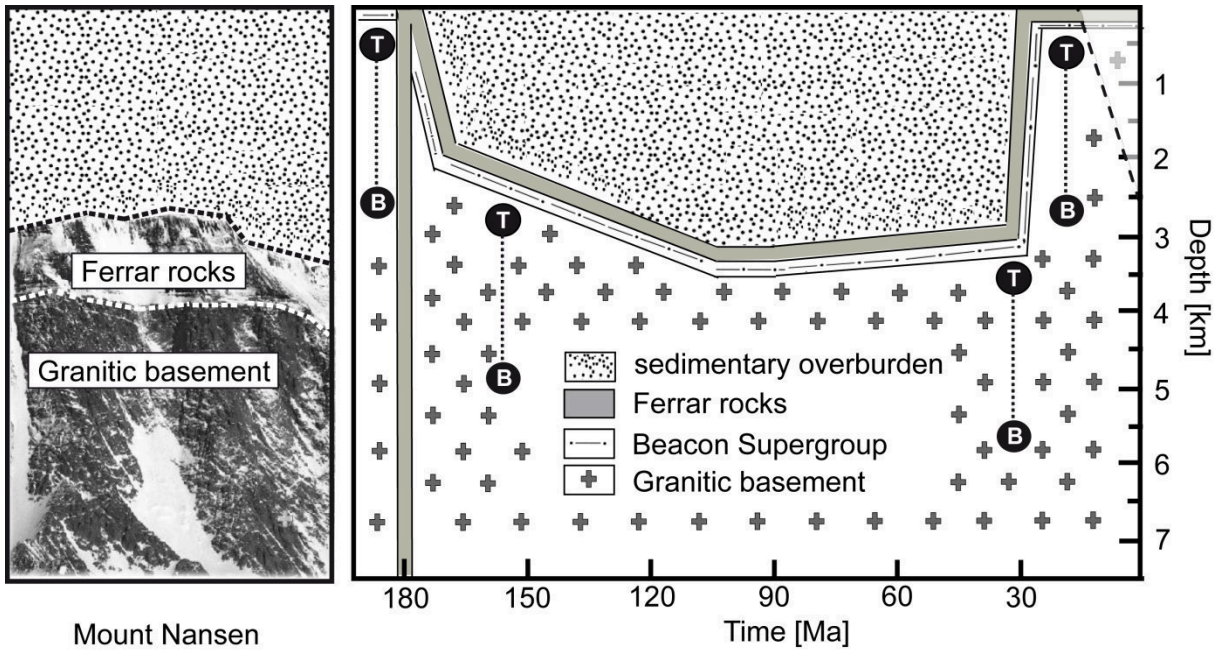

Figure M I-8: Simplified sketch of the burial and exhumation history of the Eisenhower Range and the evolution of the sedimentary basin above Ferrar rocks and granitic basement. Top (T) and bottom (B) of the analysed section are given as reference points for different times. The dashed black line marks the progress of lateral exhumation starting at ~20 Ma.

3.7) Conclusions

The comparison of AFT data produced with population and external detector technique strongly supports previous cases made for integration of kinetic parameters and individual grain-age evaluation, even from granitic rocks of the same intrusion (O'Sullivan and Parish, 1995). Age comparison additionally illustrates that samples above a break in slope usually record larger deviations between population and external detector ages than samples below a break in slope. This is attributed to varying residence times of apatites with different chemical composition and track annealing kinetic properties within the PAZ.

Thermal history models of AFT data from the Eisenhower Range area record a complex history of Mesozoic burial and exhumation since Late Eocene/Early Oligocene. This contrasts with the traditional qualitative interpretation of thermochronological data based on a break in slope concept which infers a monotonous episodic cooling scenario with substantially earlier onset of rapid cooling since the Paleocene. We demonstrated that a break in slope does not necessarily date cooling events and that its position and shape are the result of various factors, such as the thermal history prior to the onset of final cooling, maximum paleotemperatures, cooling rate, and geothermal gradient. A break in slope only provides minimum time constraints for the onset of cooling, and cannot resolve complex thermal histories or substitute thermal history modeling. The same caution generally applies to steep age gradients with altitude. Earlier thermochronological studies of vertical profiles from the TAM and elsewhere need to be validated by thermal history modeling. Particular attention should be paid to composite vertical profiles.

Instead of the traditional stepwise exhumation concept of the TAM, geological observation and AFT data require burial of the basement between Jurassic and Late Eocene/Early Oligocene times and infer the existence of a sedimentary basin, which is thought to form a part of the superordinated "Mesozoic Victoria Basin" between Australia and Antarctica. The modeled Cretaceous/Cenozoic geothermal gradient of ~27°C/km is consistent with published geothermal gradients of adjacent areas, and combined with the sample paleotemperatures, constrains the thickness of the Cretaceous to Cenozoic sedimentary cover to ~3.5 km. Rapid Late Eocene/Early Oligocene cooling infers fast erosion of these sediments and the exposure of

underlying Ferrar and basement rocks at ~30 – 35 Ma. Therefore, rapid exhumation commenced substantially later than predicted in previous studies. The Late Eocene/Early Oligocene exhumation phase can be linked with tectonic processes, such as rifting of the West Antarctic Rift System and the opening of the Tasman Gateway, and/or climatic changes as the onset of the East Antarctic continental ice shield formation. Final, differential cooling from ~20 Ma onwards is attributed to lateral and vertical exhumation of the granitic basement probably triggered by glacial incision along structures.

Acknowledgments

This study was funded by DFG grant LI745/12-1. Frank Lisker and Jannis Prenzel thank the Bundesanstalt für Geowissenschaften und Rohstoffe, Hannover, for the invitation to participate in the Antarctic GANOVEX X expedition. We wish to thank the crews of MS Italica and Helicopters New Zealand for logistic support and the members of the GANOVEX team for cooperative fieldwork and stimulating discussions. F. Balsamo, G. Di Vincenzo, N. Dörr, J. Lindow, S. Rocchi, F. Rossetti and F. Storti are acknowledged for helpful comments. P. O'Sullivan and an anonymous reviewer are thanked for constructive reviews that substantially improved the paper. At last, U. Brand is thanked for his editorial handling of the paper.

Appendix

Sampling and preparation procedure: Sample altitudes were measured barometrically with altimeter and GPS and calibrated against 1:250,000 topographic maps (U.S. Department of the Interior, 1968a-d). Apatites of rock samples of ~5-10 kg in weight were crushed and separated using standard heavy liquid and magnetic techniques, mounted in Petropoxy 154, and etched in 5N HNO3 at 20°C and 20 s following the procedures described by Gleadow (1984) and Ketcham et al. (2007). Subsequently, the mounted apatite concentrates were irradiated at the research reactor facility FRM-II in Garching, Germany. Apatite fission track (AFT) ages were measured by the external detector method following the methods described by Hurford and Green (1982). Fish Canyon and Durango standards were used for Zeta calibration. Counting and measurement procedures were performed manually, using a Zeiss Axioplan microscope at a magnification of x1250 under dry objectives and the AFT-Stage program of Dumitru (1993).

Supplementary data M I-1

	AFT age [Ma]			*MTL [µm]*		
sample	measured	HeFTy (predicted)	QTQt (predicted)	measured	HeFTy (predicted)	QTQt (predicted)
3475	32.4±2.3	33.0	36.6	14.54	14.52	14.45
BC7	35.3±2.6	36.3	37.0	14.29	14.16	14.36
3466	37.5±3.5	38.0	39.5	14.31	14.03	14.22
3465	39.1±2.5	39.8	40.0	14.25	13.94	14.15
3464	75.5±7.1	74.8	73.8	13.08	13.41	13.33
3462	92.9±8.1	92.6	87.3	12.93	13.50	13.23
3463	137.9±9	135.0	134.9	13.05	13.47	13.11
3472	144.4±7.9	147.0	150.7	12.88	13.04	12.87
BC4	52.2±4.6	50.8	48.9	13.94	13.73	13.92
BC5	54.8±3.1	54.8	52.4	14.19	13.54	13.76
BC3	69.1±4.8	70.0	69.8	13.22	13.46	13.43
BC2	81.3±5.5	80.8	88.2	13.15	13.38	13.28
BC1	98.3±5	91.0	91.6	13.11	13.47	13.25
C17	36.6±2.7	30.5	32.4	14.76	14.87	14.58
C3	99.8±6	102	98.7	13.51	13.46	13.08
C1	175.0±14	175.0	172.6	12.96	12.97	12.69

Supplementary data M I-1: Measured apatite fission track (AFT) ages and mean track length (MTL), and AFT ages and MTL predicted by HeFTy and QTQt modeling (Fig. M I-5).

Supplementary data M I-2

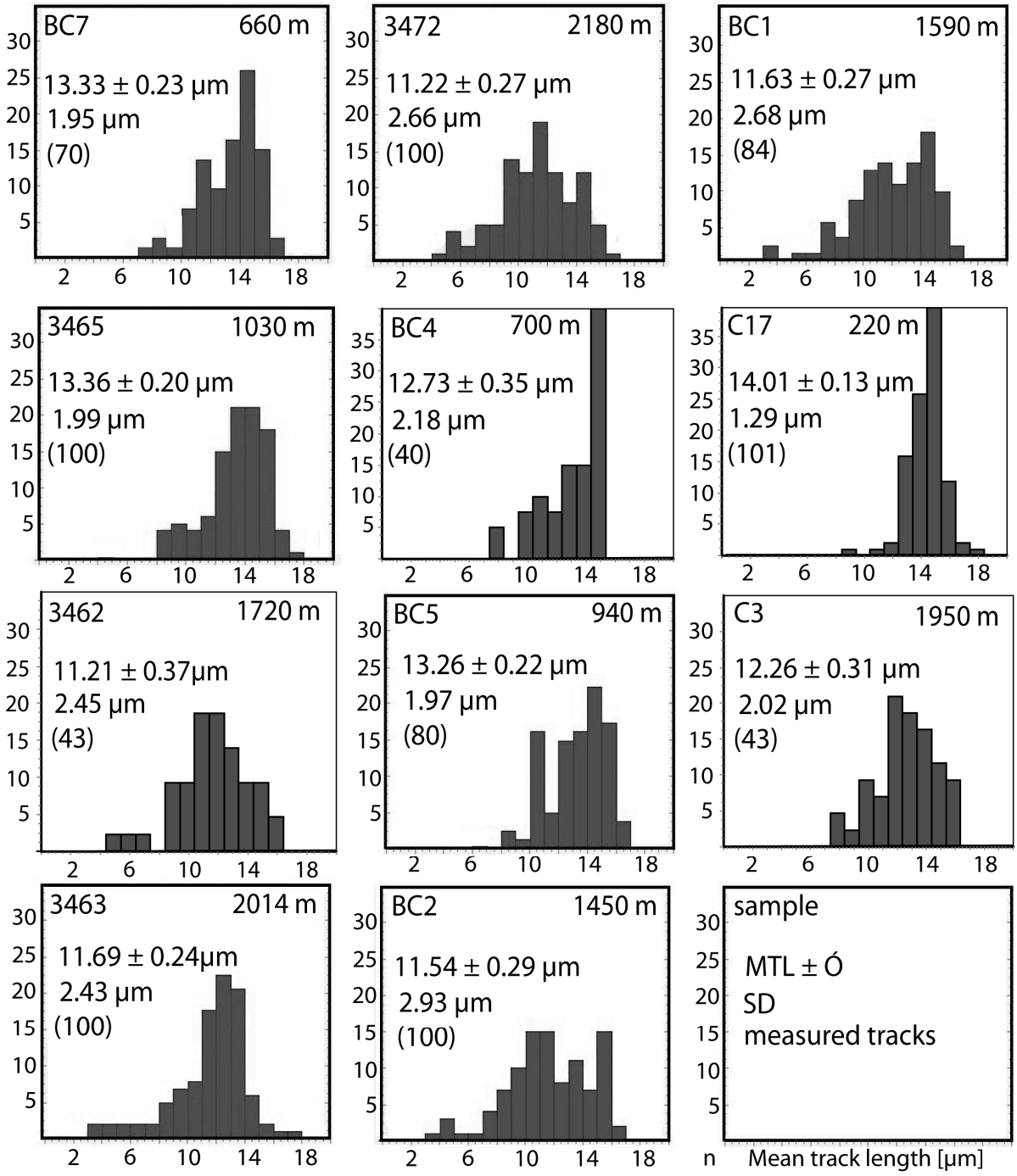

Supplementary data M I-2: Fission track length distributions of the samples with more than 40 confined tracks which are not shown in figure M I-3c.

Supplementary data M I-3

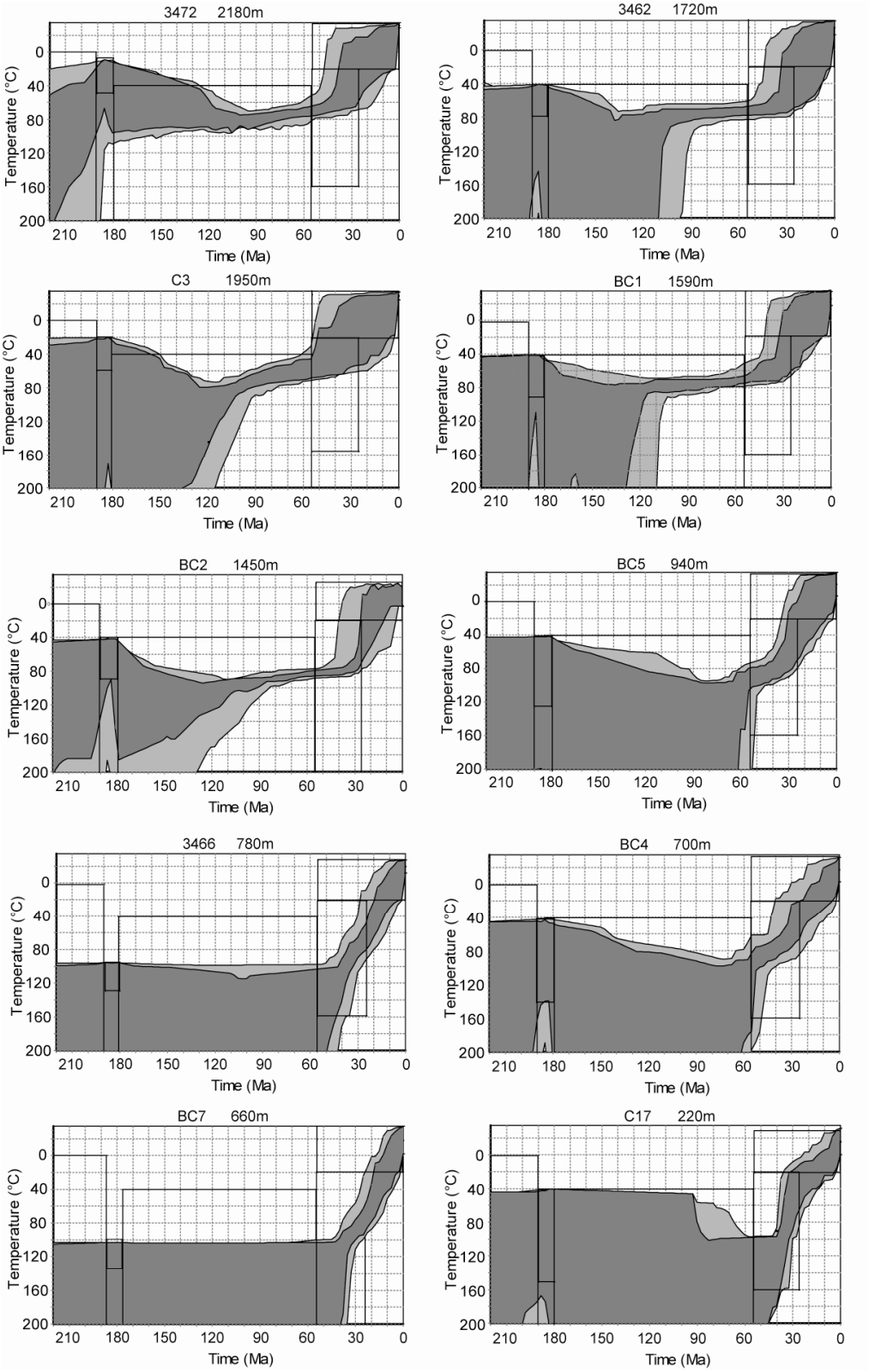

Supplementary data M I-3: Inverse modeling results of the samples which are not shown in figure M I-4 [HeFTy, Ketcham 2005]; HeFTy run for all applicable samples using the Monte Carlo search method and a minimum of 100,000 random produced cooling paths. The goodness of fit (GOF) of the apatite fission track (AFT) age data were determined for each sample using annealing model and c-axis projection of Ketcham et al. (2007). GOF of the fission track length data is quoted using the Kuiper's Statistic method. Black boxes mark the time-temperature constraints.

Supplementary data M I-4

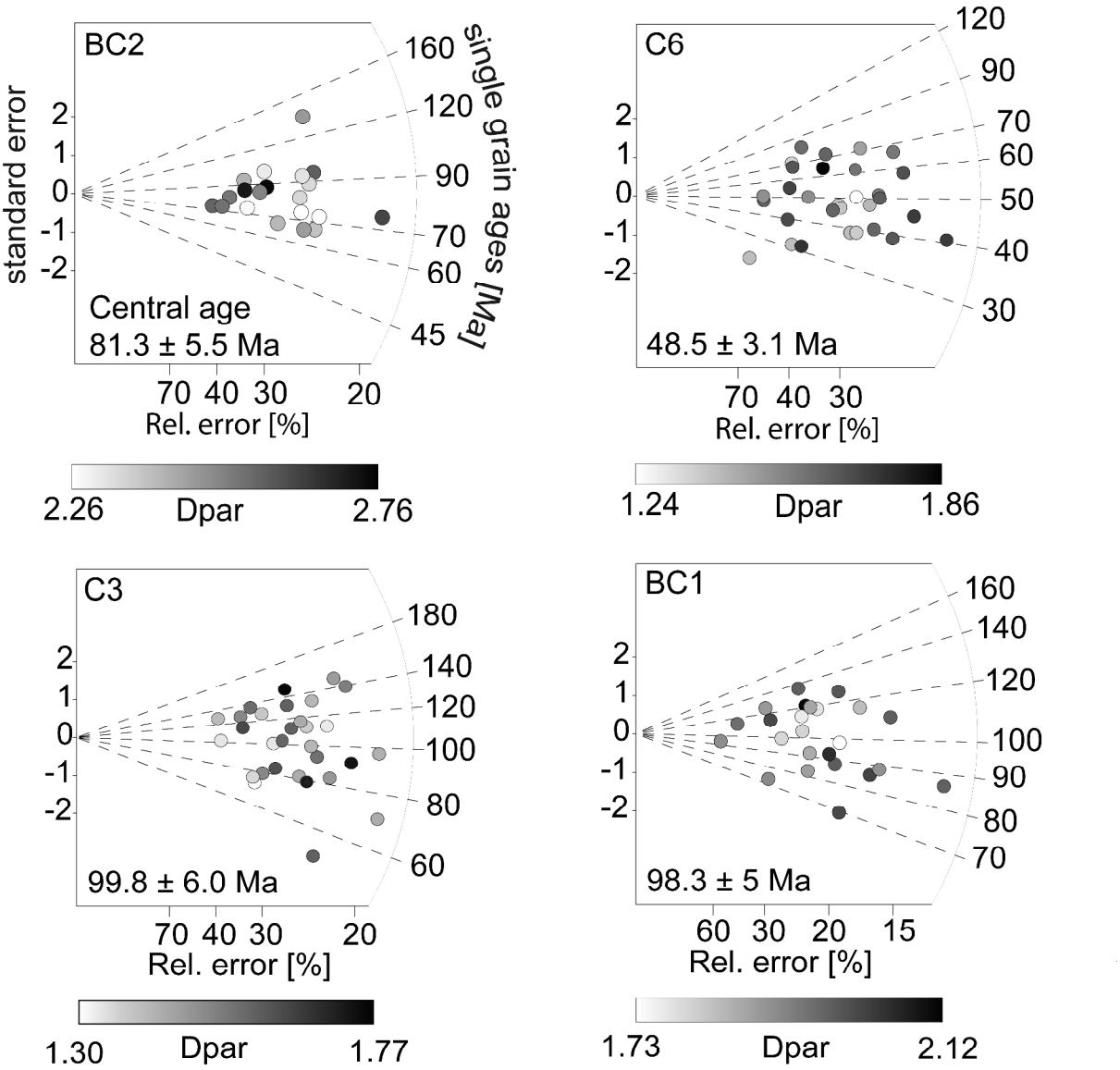

Supplementary data M I-4: Radial plots show single grain ages and Dpar values of four representative samples from Mount Matz and Mount Nansen [Radialplotter, Vermeesch, 2009].

Supplementary data M I-5

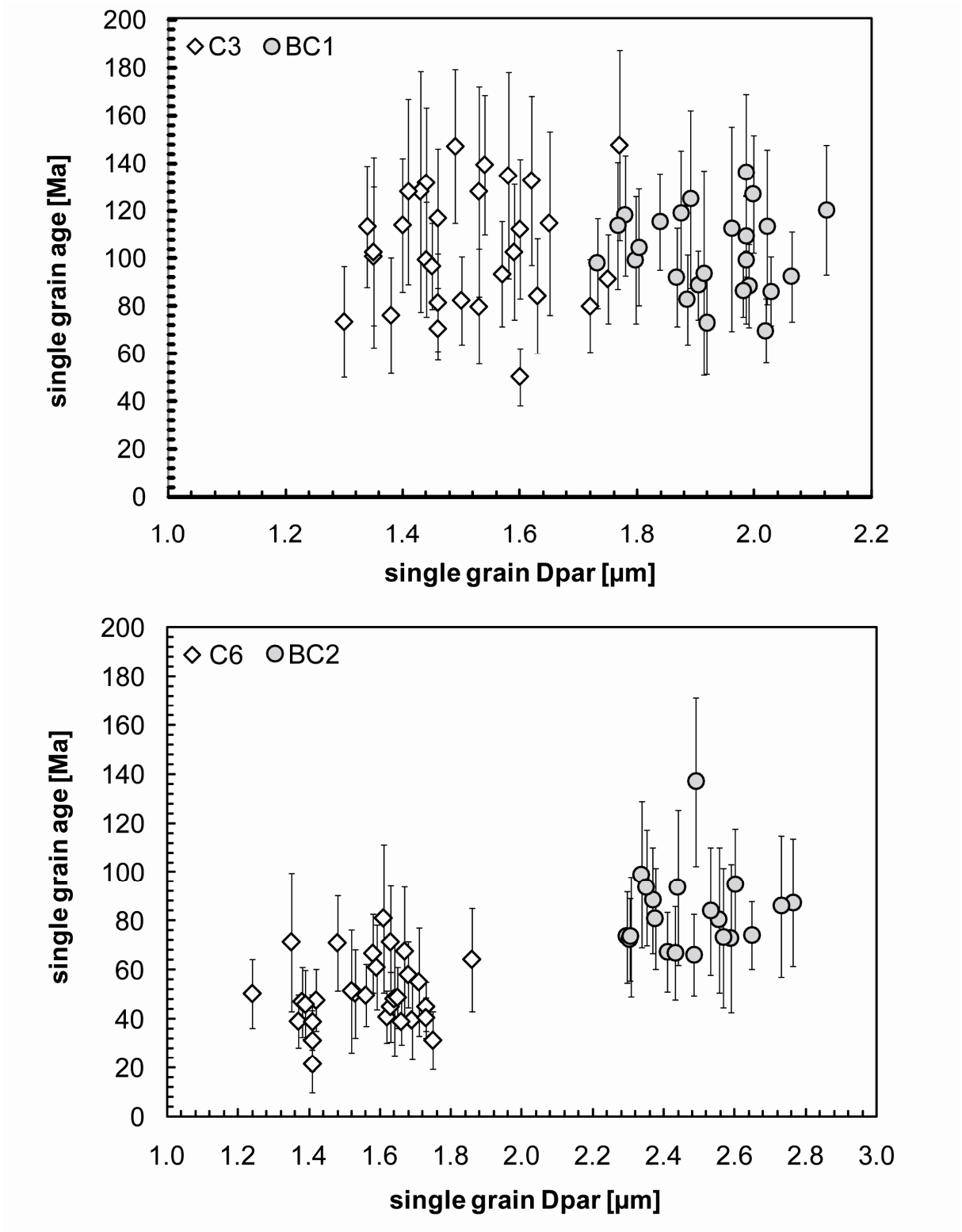

Supplementary data M I-5: Single grain ages vs. Dpar values of four representative samples from Mount Matz and Mount Nansen.

MANUSCRIPT II

Burial and exhumation of the Eisenhower Range, Transantarctic Mountains, based on thermochronological, maturity and sediment petrographic constraints

J. Prenzel, F. Lisker, M. Elsner, R.Schöner, M.L. Balestrieri, A.L. Läufer, U. Berner, C. Spiegel

* corresponding author. University of Bremen, PO Box 330440, 28334 Bremen, Germany, Tel.:0049-421-218-65284, Email address: jprenzel@uni-bremen.de

Published at Tectonophysics (2014), DOI information: 10.1016/j.tecto.2014.05.020

Received	30 December 2013	Concept	50%
Received in revised form	07 May 2014	Data collection	90%
Accepted	13 May 2014	Realization	80%
Available online	21 May 2014		

Burial and exhumation of the Eisenhower Range, Transantarctic Mountains, based on thermochronological, maturity and sediment petrographic constraints

J. Prenzel[1], F. Lisker[1], M. Elsner[2], R.Schöner[3], M.L. Balestrieri[4], A.L. Läufer[5], U. Berner[6], C. Spiegel[1]

[1] University of Bremen, FB5 Geosciences, Klagenfurter Straße, 28359 Bremen, Germany

[2] Schöneckstraße 9, 86163 Augsburg, Germany

[3] Landesamt für Bergbau, Energie und Geologie, Stilleweg 2, 30655 Hannover, Germany

[4]CNR, Institute of Earth Sciences and Earth Resources, Via La Pira 4, 50121 Florence, Italy

[5] Bundesanstalt für Geowissenschaften und Rohstoffe (BGR), Stilleweg 2, 30655 Hannover, Germany

[6] EXP BPSA PSA, Statoil ASA, Sandsliveien 90, Sandsli, Norway

Keywords: Apatite fission track thermochronology; backstepping erosion; basin inversion; burial; exhumation; thermal history modeling; Transantarctic Mountains; U-Th-Sm/He thermochronology

Abstract

The Eisenhower Range is a N-S trending mountain range in the Transantarctic Mountains (TAM) adjacent to the NW Ross Sea Embayment. There, Precambrian granitic basement is covered by a sequence of Mesozoic Beacon sandstones and magmatic rocks of the 182 Ma Ferrar suite. New apatite fission track (AFT) and apatite (U-Th-Sm)/He (AHe) data from vertical basement profiles of the Eisenhower Range supplemented by paleotemperature and pressure estimates derived from Beacon sandstones constrain the regional burial and exhumation history. AFT ages between 32±2 and 259±18 Ma and AHe ages of 37±3 – 173±16 Ma correlate positively with sample elevations. Thermal history modeling of these data and complementary thermal indications detect heating of the paleosurface on the Eisenhower Range to temperatures above 80°C subsequent to Ferrar magmatism, and constrain Late Eocene rapid cooling. A locally confined mid-Cretaceous heat pulse of ~100°C is recognized, too. Regression of modeled paleotemperatures against sample elevations refers to a high Jurassic (~45°C/km) and a moderate Cretaceous – Eocene (28±8°C/km) geothermal gradient. The texture of Beacon sandstones supports strong mechanical compaction that requires a higher

overburden than preserved in the stratigraphic record. Modeled paleotemperatures and pressures suggest basement burial that increases from Late Jurassic (~0.7 – 1.1 km) to Eocene (~1.8 – 2.1 km). The overburden comprises maximum ~1.1 km of cumulative Beacon and Ferrar rocks and up to 1.4 km of Jurassic – Eocene sediments. Rapid cooling between ~35 and 30 Ma implies rapid erosion of the post-Ferrar sedimentary sequence and (re-) exposure of underlying magmatic rocks. Subsequent differential sample cooling to present-day surface temperature infers ongoing exhumation by glacial incision enhanced by isostatic response to basin inversion. Decreasing exhumation from the coast (~3.3 km) towards the interior (~1.8 km) represents backstepping erosion along the Priestley Glacier. Acceleration of cooling in the northern Eisenhower Range at ~15 Ma is in accordance with the development of a persistent ice sheet on East Antarctica and the preservation of the frozen landscape of the TAM.

4.1) Introduction

The Transantarctic Mountains (TAM) represent the exposed main shoulder of the West Antarctic Rift System that bounds the Ross Sea embayment and divides the continent into the East Antarctic Craton and the West Antarctic terrane assemblage. The Eisenhower Range forms a ~70 km long N-S trending escarpment-bound plateau in northern Victoria Land with one of the most complete surface exposures of Antarctica (Fig. M II-1). The exposed rock column consists of up to ~2500 m basement rocks, mainly Cambro-Ordovician Granite Harbour Intrusives, and up to ~500 m Triassic to Jurassic sandstones of the Beacon Supergroup with intercalated ~182 Ma Ferrar dolerite sills (e.g., Heimann et al., 1994: 180±1.8 Ma; Encarnación et al., 1996: 183.6±1.8 Ma). No post-Ferrar sedimentary strata are preserved in the Eisenhower Range that would allow any direct reconstruction of the geological and exhumation history during most of Mesozoic and Cenozoic times. Therefore, exhumation studies based on thermochronological data have been conducted in the Eisenhower Range since more than twenty years. Apatite fission track (AFT) ages between ~31 and 198 Ma from vertical profiles in basement rocks were interpreted qualitatively in terms of monotonous cooling and stepwise exhumation since the Early Cretaceous (Balestrieri et al., 1994, 1997). Exhumation of the Eisenhower Range in two episodes at 80 – 60 Ma and at ~40 Ma is in accordance with earlier studies from different segments of the TAM (e.g., Fitzgerald, 2002; Lisker, 2002).

Though, previous studies did not sufficiently pay attention to geomorphological and geological features such as the relevance of paleosurfaces and the ~182 Ma Ferrar volcaniclastic rocks that cover wide portions of northern Victoria Land. Such indicators of exposition imply Jurassic (near-) surface temperatures of the directly underlying basement. Lisker and Läufer (2013) recognized that crossover age relationships between these reference horizons and AFT data confute the hypothesis of monotonous, stepwise exhumation of the TAM since the Cretaceous, and instead require long-lasting burial within a *Mesozoic Victoria Basin*. A recent methodological AFT study of Prenzel et al. (2013) evaluated qualitative interpretation concepts of thermochronological data by thermal history modeling of vertical sample arrays and revealed that exhumation of the southern Eisenhower Range did not commence prior to Early Oligocene. However, the one-dimensional approach of the pilot study gained little insight in regional basin evolution and did not resolve the origin of the

Eisenhower Range, escarpment formation, and development of its high-elevated, low-relief plateaus in immediate vicinity to a sea-level coastal plain. Answering these questions requires quantitative reconstruction of timing and amounts of burial and exhumation of the whole range including a more detailed investigation of final exhumation. Particular attention also deserves composition and thickness of the vanished rock column. Up to ~1850 m Beacon and Ferrar rocks are cumulatively preserved in northern Victoria Land, with maximum ~600 m Beacon strata (Permian to Early Jurassic) and ~500 m Ferrar sills and volcaniclastica (e.g., Elliot and Foland, 1986). Further ~750 m Ferrar lava flows are documented in the Mesa Range ~50 km north of the Eisenhower Range (e.g., Elliot, 1992; Elliot and Fleming, 2008). Therefore, a restoration of overburden has to consider both, variations within the Beacon and Ferrar package of the Eisenhower Range and post-Ferrar sediments.

Our approach to reconstructing burial and exhumation history and long-term landscape evolution of the Eisenhower Range relies on the combined application of thermochronological, maturity and sedimentary petrographic methods. Maximum paleotemperatures will be derived from AFT and AHe thermochronology, vitrinite reflectance data and authigenic phases, and estimates of minimum burial obtained from mechanical compaction of Beacon sandstones (Elsner, 2010). The research particularly depends on thermal history modeling of AFT and AHe data from basement samples collected across and along the Eisenhower Range. AFT and AHe thermochronology used in tandem records time of rock cooling below temperatures of ~125° – 110° to ~40°C (e.g., Wagner et al., 1989; Wolf et al., 1998) or depths of ~1 to 5 km, respectively, and in combination with temperatures derived by sensitive minerals/reactions and organic maturation data provide substantial information about the thermal state of the upper crust. In addition, geothermal gradients at different times will be calculated from the regression of paleotemperature estimates from vertical sample arrays. Paleotemperatures and geothermal gradients then provide the key to reconstructing burial since the Ferrar event and differentiating composition and thickness of overburden. Timing and pattern of exhumation further help to constraining the age of major landscape elements as well as magnitude and rate of landscape forming processes. They elucidate whether final exhumation occurred in response to a single major event or several discrete stages, and whether exhumation was rather triggered by tectonic processes, climatic influences, or a combination of

both. Finally, amount, rate and pattern of final exhumation will supply details on course and formation mechanism of the range, as for example the influence of backstepping incision along predetermined structures.

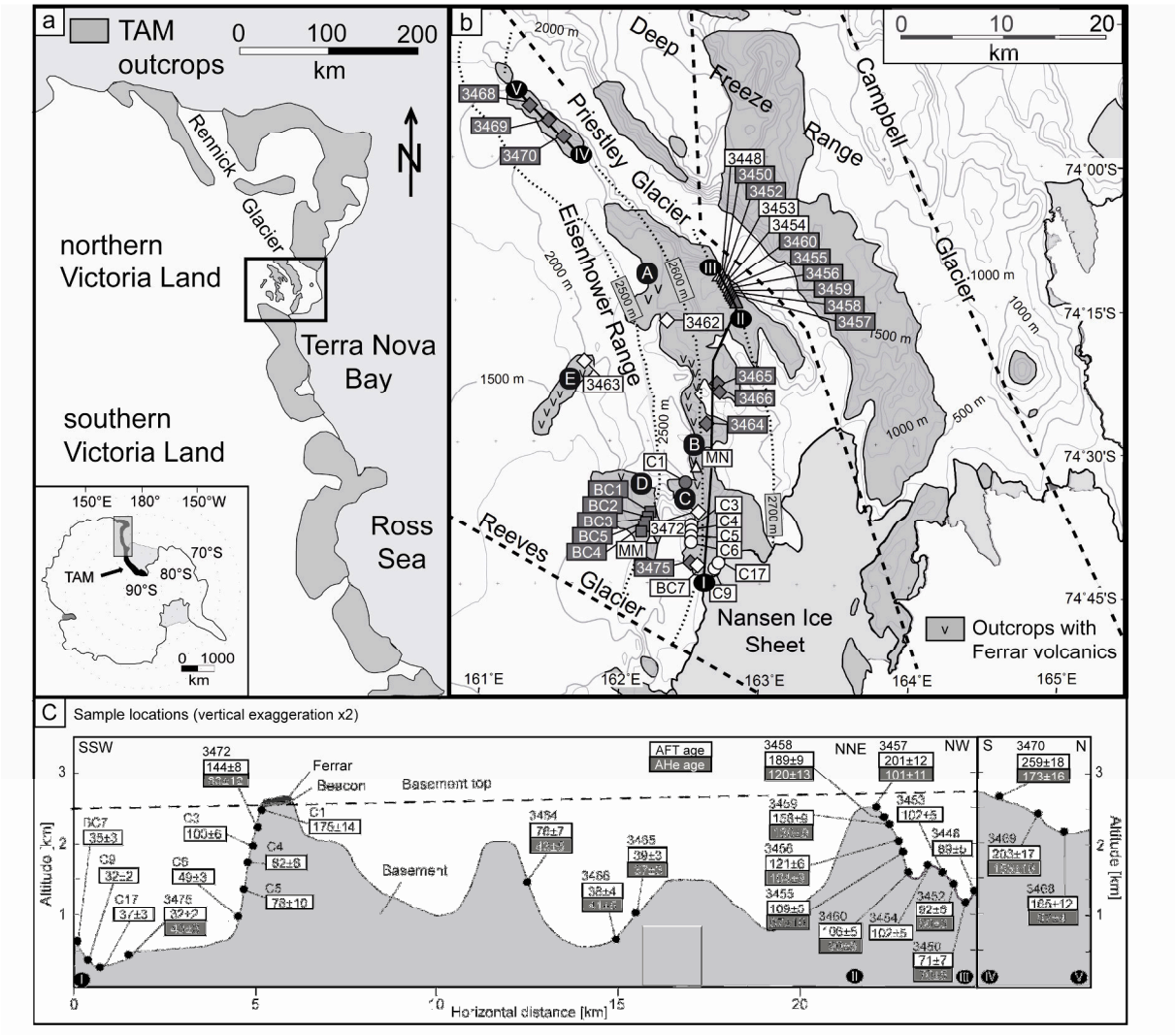

Figure M II-1: (a) Simplified map of the Ross Sea sector. The dashed black box marks the study area. (b) Simplified map of Eisenhower and Deep Freeze Ranges. The location of rock samples are marked by small circles (Mount Nansen = MN), squares (Mount Matz = MM), diamonds (Eisenhower Range) and triangles (Priestley Glacier). Samples which comprise apatite fission track (AFT) and (U-Th-Sm)/He (AHe) data are shown with grey symbols, and those comprising only AFT data are shown with white symbols. Circles mark the new sample set of this study (northern Eisenhower Range, Priestley Glacier) whereas rectangles refer to samples dated by Prenzel et al. (2013; AFT data from Mount Matz, Mount Nansen and the southern Eisenhower Range). Black circles labelled with the capitals A – E indicate localities, where thermal indications could be inferred from Beacon sedimentary rocks. Dashed black lines mark the Reeves, Priestley and Campbell Faults which constitute main structures of the Cenozoic right-lateral fault system in northern Victoria Land (e.g., Rossetti et al., 2003; Storti et al., 2007, 2008 and refs. therein). Dotted black lines mark different elevation contours of basement top/pre-Beacon erosion surface (2500 m, 2600 m, and 2700 m). (c) Topographic cross-sections with sample locations and AFT and AHe ages along the Eisenhower Range from the coast to the margin of the Priestley Glacier (I to III), and along the northern tip of the northern Eisenhower Range parallel to the Priestley Glacier (IV to V).

4.2) Geological setting

The Eisenhower Range is located between the Priestley Glacier in the north and east, the Nansen Ice Sheet and the Reeves Glacier in the south, and the Polar Plateau in the west (Fig. M II-1). It is characterized by a simple geological architecture and a uniform geomorphological pattern. The basement consists of Ross-orogenic Late Proterozoic to Early Paleozoic metamorphic rocks, and plutonic rocks of the Cambro-Ordovician Granite Harbour Igneous complex (e.g., Borg et al., 1987). It was eroded to a peneplain subsequent to the Ross Orogeny and then overlain by clastic deposits collectively termed as Beacon Supergroup. These sedimentary rocks were deposited in the Transantarctic Basin that occupied large parts of the Ross Sea sector of Antarctica from the Devonian to the Jurassic (Collinson et al., 1994). The position of the pre-Beacon erosion surface identifies the Eisenhower Range as a common tectonic block separated from the Deep Freeze Range in the northeast by the Priestley Glacier (Fig. M II-1). Priestley and Reeves Glaciers follow major faults of a regionally important Cenozoic right-lateral fault system in northern Victoria Land (e.g., Rossetti et al., 2003; Storti et al., 2008 and refs. therein). The pre-Beacon erosion surface slightly dips (~3°) towards the west under the Polar Plateau, and the elevation of the basement top correspondingly varies between ~2700 m at the margin of the Priestley Glacier and ~2000 m in the west towards the Polar Plateau (Fig. M II-1). Beacon deposits were then intruded and/or overlain by magmatic rocks (dolerites, volcanoclastica, lava flows) during the Ferrar event at ~182 Ma. Volcaniclastic deposits, partially interbedded with fossil-bearing sedimentary units and pillow lavas indicate the earliest eruptive events of the Ferrar Group in northern Victoria Land (e.g., Viereck-Götte et al., 2007; Bomfleur et al., 2011). They imply a superficial emplacement of the Jurassic Ferrar rocks and attest that the directly underlying Beacon and basement rocks were at/near the surface at ~182 Ma. In the Eisenhower Range, preserved rocks above the basement consist of an up to ~500 m thick sequence of Beacon rocks and Ferrar sills. Lava flows of the Ferrar group are not exposed in the Eisenhower Range, but they reach a thickness of up to more than ~750 m further north in the Mesa Range (e.g., Elliot, 1992; Elliot and Fleming, 2008). Late Mesozoic to Paleogene rock units are generally missing along the entire TAM, but the basement or Beacon/Ferrar rocks are locally overlain by Neogene volcanics (e.g., GANOVEX Team, 1987).

4.3) Paleotemperature and burial estimations for the Beacon Supergroup

4.3.1) Vitrinite reflectance

Vitrinite reflectance data were measured at one locality in the northern part of the Eisenhower Range (Fig. M II-1, A), where about 80 m of Beacon deposits are exposed between two Ferrar Dolerite sills (Schöner et al., 2011). Ten samples were taken from an approximately 4 m thick succession of carbonaceous mudstones and coal in a distance of about 15 m from the lower sill during the German GANOVEX IX field campaign of *Bundesanstalt für Geowissenschaften und* Rohstoffe (BGR) in 2005/06. This sedimentary succession contains a well-preserved *Dicroidium*-flora (Triassic) in cuticular preservation (e.g., Bomfleur et al., 2011).
Samples have been investigated by standard organic petrographic methods (e.g., Berner et al, 2009). Measured vitrinite reflectance values increase from 0.4 %-Rr to 0.9 %-Rr towards the sedimentary rock/dolerite contact. This increase in vitrinite reflectance within a few meters is probably related to the thermal influence induced by the sill intrusion. The lowest values of 0.4 – 0.6 %-Rr can be regarded as maximum background maturity caused by burial of the Beacon. Burial related thermal maturities may hence have reached the (lower) oil window in the northern part of the Eisenhower Range. Organic maturation is strongly dependent on the time-temperature history of the basin (e.g., Tissot and Welte, 1984). Assuming moderate and constant heating rates, the corresponding temperature window may be in the range of 60° – 100°C (Sweeny and Burnham, 1990; Barker and Pawlewicz, 1994).

4.3.2) Authigenic mineralogy

Samples from Beacon sedimentary rocks were collected from four sections in the Eisenhower Range (Fig. M II-1; B – E) during GANOVEX IX. Outcrops B, C, and D (Fig. M II-1) refer to the localities Eisenhower Range (east cliff), Anderton Glacier, and Thern Promontory described by Schöner et al. (2011). The analyzed successions include conglomerates, sandstones and siltstones of the Beacon Supergroup directly overlying the basement. Outcrop E is located at Skinner Ridge (Schöner et al., 2011). Here, conglomerates are absent, and top and base of the outcrop are formed by doleritic (Ferrar) sills. The samples were taken in a distance of more than 10 m to the closest sedimentary rock/sill contact. In total, 14 thin sections

from these four outcrops were investigated petrographically by optical microscopy, and analyzed by X-ray diffraction (XRD) and electron beam microprobe (EMP) to study their detrital and authigenic mineralogy (Elsner, 2010). Paleotemperature estimation includes a variety of temperature sensitive phases and mineral reactions, such as zeolites, clay minerals and detrital feldspar affected by diagenetic albitization.

Partial albitization of plagioclase observed in a sample from the westernmost section (Fig. M II-1, E) refers to dissolution-precipitation processes commonly observed at temperatures between ~75° and 100°C (Morad et al., 1990). Authigenic laumontite in the same sample is likely to be related to the albitization process, thus inferring maximum temperatures above ~90°C (Noh and Boles, 1993). However, neither an earlier formation of laumontite at lower temperatures nor maximal burial temperatures of more than 100°C can be excluded. In sandstone samples from the three southernmost sections (Fig. M II-1; B, C, D), authigenic kaolinite minerals are abundant, which are likely to have formed at low temperatures. As a distinction between kaolinite and dickite was inconclusive, no maximum burial temperature can be deduced. Therefore, a maximum paleotemperature of the Beacon sandstones in the Eisenhower Range below 100°C seems to be likely, but higher temperatures cannot be ruled out.

4.3.3) Sandstone compaction

The generally moderate to poor sorting of the Beacon sandstones from the Eisenhower Range implies an initial porosity of ~30 to 35 % (Beard and Weyl, 1973). The studied sandstones are lithic subarkoses/arkoses, litharenites and feldspathic litharenites (Elsner, 2010). Evidence for strong mechanical compaction comes from low intergranular volumes (i.e. intergranular porosities plus intergranular cements) of less than 10 %, which is only possible by ductile deformation of altered, mechanically instable grains and mica. Altered volcanic and low-grade metamorphic lithoclasts or kaolinized feldspar are abundant in most sandstone samples from the Eisenhower Range to afford this process. Porosity-depth relationships of common sandstones rich in ductile grains infer sedimentary burial of at least 2.5 km to explain the observed intergranular volumes (Worden and Burley, 2003). This depth is equivalent to a lithostatic pressure of 50 MPa for a sedimentary overburden with densities

between 1.8 g/cm³ at the surface and 2.4 g/cm³ at depth. However, overburden might have been less thick when constituted partially or completely by volcanic rocks. For a density of ~3.0 g/cm³ as typical for the dolerite sills, a pressure of 50 MPa can be generated already by a rock column of merely 1.7 km. On the other hand, overburden might have even exceeded a thickness of 2.5 km, because any further increase in pressure would have a minor effect on mechanical compaction of the sandstones with less than 10 % intergranular volumes.

4.4) Thermochronological studies

4.4.1) Sampling

Thirty-three samples from Granite Harbour Intrusives and one specimen from the overlying Beacon Supergroup were collected during the ItaliAntartide expeditions 1985 – 93 and GANOVEX IX (Fig. M II-1; Table M II-1). The samples cover the entire length of the Eisenhower Range and include vertical profiles at Mount Matz, Mount Nansen, the southern Eisenhower Range and the southern margin of the Priestley Glacier with an elevation range of 2400 m. Due to the dip of the pre-Beacon erosion surface, the elevation of basement top in the sampling area varies slightly between ~2700 m at the margin of the Priestley Glacier and ~2500 m in the south-western Eisenhower Range. An exception constitutes one sample (3463) at the western end of the Eisenhower Range with the basement top at ~2000 m.

4.4.2) Apatite fission track data

Fourteen new AFT ages from northern Eisenhower Range and Priestley Glacier and 20 published AFT ages from southern Eisenhower Range are in a range between 32.0±2.4 and 259.0±18.0 Ma (Table M II-1; Figs. M II-1, 2, Appendix M II-1; cf. Prenzel et al., 2013). Sample ages considerably postdate the emplacement of the Granite Harbour Intrusive suite (~550 – 490 Ma; e.g., Goodge et al., 2012) and are mostly younger than the ~182 Ma Ferrar event. Samples from the same level below basement top show consistent ages (±1σ) near the Ross Sea coast (distance <15 km) and slightly higher ages further inland towards the margin of the Priestley Glacier and at the northern tip of the range. Only sample 3463, collected at the western end of the range, yields a considerably younger age than sample equivalents at equal position below basement top.

Sample	Lat. S Long.E	Elevation [m]	ξ	ρ_D [10^6cm^{-2}] (N_D)	ρ_S [10^6cm^{-2}] (N_S)	ρ_I [10^6cm^{-2}] (N_I)	P(χ^2) [%]	Dated grains [N]	AFT age [Ma] (predicted age)	MTL [µm] (n)	MTL c-axis [µm] (predicted MTL)	SD [µm]	SD c-axis [µm] (predicted SD)	Dpar mean [µm]	AHe central age [Ma]	unc. AHe single age [Ma] (predicted age)	GOF AFT age/MTL AHe age
Northern Eisenhower Range																	
3468	73.909 161.457	2132	320 ±10	17.9 (17974)	9.2 (389)	15.7 (666)	99	25	165.0±12.0 (158.0)	11.00±0.24 (106)	12.67 (12.77)	2.46	1.51 (1.55)	1.89	86.55±4.24	91.3±9.0/81.3±8.0 (93.8./82.8)	0.53/0.52 0.79/0.85
3469	73.931 161.569	2401	320 ±10	17.9 (17974)	12.7 (289)	17.7 (401)	100	20	203.0±17.0 (205.0)	11.15±0.22 (104)	12.86 (12.85)	2.27	1.34 (1.43)	1.91	152.9±17.94	94.8±5.3 (92.7)	0.92/0.28 0.70
3470	73.978 161.692	2620	320 ±10	18.0 (922)	12.9 (470)	14.1 (513)	93	20	259.0±18.0 (268.0)	11.22±0.23 (104)	12.75 (13.27)	2.39	1.48 (1.31)	1.92	172.98±16.28	109.2±6.8 (106.1)	0.64/0.52 0.65
Priestley Glacier																	
3450	74.198 162.749	1150	320 ±10	15.8 (15653)	8.1 (157)	28.5 (555)	99	20	71.0±6.8 (84.5)	12.20±0.31 (57)	13.53 (13.45)	2.36	1.64 (1.63)	2.15	70.45±5.19	72.0±5.0 (61.5)	0.05/0.12 0.08
3448	74.185 162.717	1300	320 ±10	23.4 (17974)	19.8 (547)	83.2 (2292)	95	24	88.6±5.0 (87.5)	12.29±0.20 (100)	13.51 (13.44)	2.04	1.46 (1.56)	2.04	-	-	0.83/0.51 -
3452	74.205 162.748	1430	320 ±10	15.7 (15653)	26.3 (358)	71.3 (970)	100	30	92.4±6.4 (93.8)	12.49±0.24 (70)	13.64 (13.60)	2.02	1.48 (1.57)	2.15	50.32±3.39	36.4±2.3 (36.0)	0.82/0.50 0.91
3453	74.21 162.748	1625	320 ±10	15.7 (15653)	28.7 (991)	70.4 (2429)	99	20	102.0±5.0 (104.0)	12.46±0.21 (100)	13.64 (13.66)	2.05	1.50 (1.53)	2.12	-	-	0.68/0.59 -
3460	74.217 162.533	1675	320 ±10	15.7 (15653)	23.1 (1004)	54.4 (2362)	59	20	106.0±5.0 (104.0)	12.13±0.22 (103)	13.37 (13.57)	2.2	1.61 (1.57)	1.96	90.03±8.40	56.1±3.5 (42.3)	0.74/0.96 0.07
3454	74.216 162.758	1780	320 ±10	15.7 (15653)	18.7 (901)	45.7 (2200)	74	20	102.3±5.0 (104.0)	12.35±0.22 (107)	13.71 (13.58)	2.3	1.61 (1.60)	1.99	-	-	0.70/0.62 -
3455	74.218 162.757	1900	320 ±10	15.7 (15653)	16.3 (1443)	37.1 (3291)	85	30	109.3±5.0 (112.0)	11.72±0.22 (111)	13.25 (13.61)	2.36	1.40 (1.50)	1.99	66.82±9.84	43.2±2.7 (38.8)	0.54/0.27 0.11
3456	74.224 162.76	2070	320 ±10	15.7 (15653)	21.2 (902)	43.4 (1848)	77	20	121.0±6.0 (124.0)	11.43±0.24 (100)	13.00 (13.50)	2.38	1.54 (1.53)	2.03	104±9.36	73.5±4.6 (56.3)	0.71/0.62 0.06
3459	74.231 162.768	2280	320 ±10	15.6 (15653)	29.8 (605)	46.8 (950)	100	20	157.6±9.0 (163.0)	11.14±0.24 (101)	12.74 (12.98)	2.41	1.54 (1.72)	1.96	130.09±8.82	134.7±8.3 (135.1)	0.58/0.65 0.97
3458	74.235 162.773	2400	320 ±10	15.6 (15653)	42.5 (1561)	55.6 (2042)	100	20	188.6±9.0 (189.0)	11.19±0.23 (100)	12.80 (13.15)	2.30	1.44 (1.55)	2.07	120.22±12.76	75.2±4.7 (76.8)	0.92/0.51 0.72
3457	74.241 162.784	2530	320 ±10	15.6 (15653)	24.6 (680)	30.2 (833)	100	20	201.0±12.0 (206.0)	11.20±0.24 (110)	12.86 (13.27)	2.52	1.61 (1.51)	2.02	100.51±11.14	69.9±4.3/72.8±4.5 (68.3/62.5)	0.68/0.50 0.71/0.09

Table M II-1: Apatite fission track (AFT) and (U-Th-Sm)/He (AHe) data of the Eisenhower Range. AFT ages were determined by counting spontaneous and induced fission tracks according to the Zeta (ζ) calibration method (Hurford and Green, 1982, 1983; ρD, ρS, ρI, Nd, Ns, Ni: density and number of counted dosimeter, spontaneous and induced tracks; P(χ_2): χ_2 probability) for dosimeter glass CN5, and calculated using Trackkey program of Dunkl (2006). Errors are quoted as ±1σ (Green, 1981). If possible, 100 track lengths for each sample were measured following the recommendations of Laslett et al. (1982). Dpar was measured as indicator for track annealing kinetic properties (e.g., Donelick, 1993; Carlson et al., 1999). Corresponding AHe central ages are shown if available. The goodness of fit (GOF) between measured and predicted AFT ages, track lengths, and AHe single grain ages is quoted for HeFTy c-axis projected forward models using the radiation damage model of Flowers et al. (2009; see also Table M II-2 and Fig. M II-4).

AFT ages closely correlate with sample elevation (Fig. M II-2) with a change in age-elevation regression (break in slope) at ~40 – 60 Ma. The samples above the break in slope yield shorter mean track lengths (MTL; 11.21±0.37 – 12.26±0.31µm) with larger standard deviations (2.02 – 2.93 µm) than samples below the break in slope (MTL: 12.73±0.35 – 14.01±0.13 µm/standard deviations: 1.29 – 2.18 µm). An inverse correlation between sample elevation and MTL is discernable. Moreover, AFT ages and MTL correlate in a concave "boomerang" pattern as described by Green (1986; Fig. M II-2) with longest MTL for the youngest samples, shortest MTL for samples with intermediate ages, and intermediate MTL for the oldest samples. Mean Dpar values are in a range between 1.57 and 2.34 µm (Table M II-1).

Southern Eisenhower Range: AFT ages of previously analyzed samples from profiles at Mount Matz, Mount Nansen and along the southern Eisenhower Range vary between 32.4±2.3 and 175.0±14.0 Ma (Fig. M II-2; for detailed information cf. Prenzel et al., 2013). They correlate with sample elevation (430 – 2320 m) and corresponding MTL/standard deviations of 11.21±0.37 – 14.01±0.13 µm/1.29 – 2.93 µm. The age-elevation regressions show breaks in slope at slightly different times at ~55 Ma (Mount Matz), ~45 Ma (Mount Nansen) and ~40 Ma (southern Eisenhower Range).

Northern Eisenhower Range: Three AFT ages from the northern tip of the range (Fig. M II-1; elevations 2130 – 2620 m) vary between 165.0±12.0 and 259.0±18.0 Ma, and show no age signature of the Ferrar event. Corresponding MTLs of 11.00±0.24 – 11.22±0.23 µm are associated with standard deviations of 2.27 – 2.46 µm (Table M II-1). AFT ages and MTL are generally in agreement with the data from the southern Eisenhower Range and the Priestley Glacier (Fig. M II-2).

Priestley Glacier: An elevation profile of eleven granitic samples between 1150 and 2530 m at the southern margin of the Priestley Glacier (Fig. M II-1) yields AFT ages between 71.0±6.8 and 201.0±12.0 Ma and MTL of 11.14±0.24 to 12.49±0.24 (standard deviations 2.02 – 2.52 µm; Table M II-1). The oldest sample pre-dates the Ferrar event, while the youngest sample is still older than the break in slope observed at ~40 to 55 Ma for the other profiles (Fig. M II-2). A distinctive break in slope is not evident in the age-elevation regression of the Priestley Glacier, but a discontinuity in the relation of AFT ages and MTL appears at ~105 – 90 Ma (Fig. M II-2).

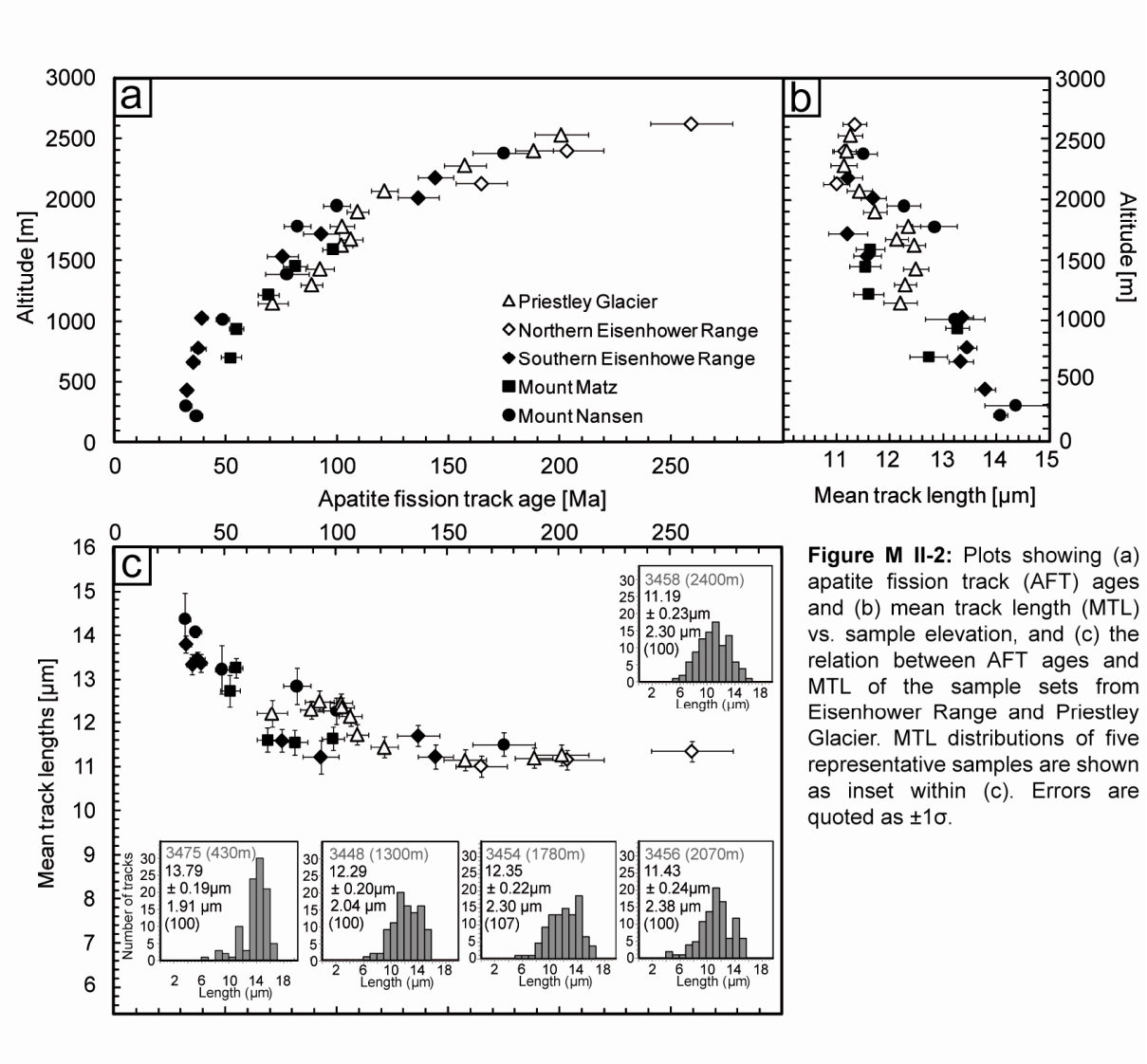

Figure M II-2: Plots showing (a) apatite fission track (AFT) ages and (b) mean track length (MTL) vs. sample elevation, and (c) the relation between AFT ages and MTL of the sample sets from Eisenhower Range and Priestley Glacier. MTL distributions of five representative samples are shown as inset within (c). Errors are quoted as ±1σ.

4.4.3) Apatite (U-Th-Sm)/He data

AHe data were obtained from 21 samples from the Priestley Glacier (eight), Mount Matz (five), and along the Eisenhower Range (eight; Fig. M II-1; Table M II-1). Sample ages were compiled from two to seven single grain ages per sample (Table M II-2).

AHe single grain ages spread considerably between 35.3±4.2 and 238.5±28.1 Ma, with substantial dispersion within most samples (Table M II-2; Fig. M II-3). Ages of grains from samples above a break in slope in the corresponding AFT age-elevation plot generally show a larger spread than those from samples below. Mean, weighted mean and central age of each sample were calculated without age outliers (Table M II-2), and are consistent for all samples.

Sample	Elevation [m]	Length [µm]	Width [µm]	Sp.radius [µm]	shape	Mass [µg]	4He [ncc]	eU [ppm]	Total Sm [ppm]	Total Th [ppm]	Total U [ppm]	Uncor. age [Ma]	FT corr.	Cor. age [Ma]	2σ error [Ma[	AFT age [Ma]
Eisenhower Range																
3475-a	430	143	62	36	2	1.38	0.08	20.27	17.30	15.37	16.54	22.12	0.63	35.26	4.15	32.4±2.3
3475-b	430	150	81	45	2	2.46	0.18	22.65	18.56	10.19	20.11	26.57	0.70	37.82	4.45	32.4±2.3
3475-c	430	185	98	61	2	4.46	0.40	22.90	20.76	15.73	19.05	32.64	0.76	43.21	5.08	32.4±2.3
3475-d	430	124	86	51	2	1.46	0.17	35.47	25.66	15.25	31.67	27.71	0.70	39.86	4.69	32.4±2.3
3475-e (A)	430	79	65	41	3	0.97	0.11	17.59	19.93	38.75	8.40	51.26		51.26	3.18	32.4±2.3
3475-f (A) #	430	92	83	49	3	1.66	0.15	19.54	13.56	25.86	13.41	38.07		38.07	2.36	32.4±2.3
Mean														40.91	4.15	
Wt mean														41.06	3.49	
Central														42.98	3.30	
3466-a	780	108	70	42	2	1.31	0.13	30.83	62.45	37.00	21.62	26.99	0.64	42.39	4.99	37.5±3.5
3466-b	780	131	92	55	2	1.77	0.22	35.97	68.64	31.67	27.94	28.03	0.71	39.35	4.63	37.5±3.5
Mean														40.87	4.81	
Wt mean														40.76	4.80	
Central																
3465-a	1030	159	80	45	2	2.58	0.28	35.12	57.08	34.91	26.45	25.35	0.70	36.07	4.24	39.1±2.5
3465-b #	1030	159	98	60	2	2.50	0.46	53.79	93.46	68.86	36.88	28.28	0.73	38.54	4.53	39.1±2.5
3465-c #	1030	126	79	47	2	1.29	0.27	70.41	102.37	78.61	51.15	24.50	0.67	36.50	4.30	39.1±2.5
Mean														37.04	4.36	
Wt mean														36.98	4.35	
Central														37.48	3.32	
3464-a #	1530	137	64	37	1	1.10	0.08	24.15	94.06	21.72	18.17	25.08	0.58	42.94	5.05	75.5±7.1
3464-b *	1530	88	65	35	2	0.58	0.16	19.70	122.76	19.46	13.95	112.52	0.59	191.83	22.57	75.5±7.1
3468-a x	2130	145	84	50	2	1.71	0.32	17.89	86.79	22.45	11.81	85.79	0.69	124.22	14.62	164.9±11.6
3468-b x	2130	93	66	39	2	1.03	0.24	23.83	63.92	26.54	17.03	80.81	0.61	132.60	15.60	164.9±11.6
3468-c x	2130	172	79	45	1	2.24	0.42	19.96	73.76	15.36	15.65	77.50	0.67	115.95	13.64	164.9±11.6
3468-d (A) #	2130	78	65	41	3	0.63	0.06	9.15	51.70	14.54	5.26	81.25		81.25	5.04	164.9±11.6
3468-e (A) #	2130	75	64	40	3	0.57	0.13	21.20	65.89	26.19	14.46	91.34		91.34	5.66	164.9±11.6
Mean														83.34	5.17	
Wt mean														84.95	5.27	
Central														86.55	4.24	
3472-a #	2180	196	103	66	2	3.58	0.75	28.90	26.70	25.41	22.73	59.60	0.76	78.94	9.29	144.4±7.9
3472-b	2180	137	76	46	2	1.36	0.54	48.03	30.56	71.69	31.09	67.31	0.66	101.27	11.92	144.4±7.9
3472-c	2180	113	95	55	2	1.53	0.27	25.38	22.03	21.68	20.13	56.19	0.71	78.72	9.26	144.4±7.9
3472-d	2180	110	70	38	2	1.11	0.17	23.50	17.21	24.04	17.75	52.15	0.60	87.18	10.26	144.4±7.9
Mean														81.61	10.18	
Wt mean														81.25	9.98	
Central														82.48	12.32	
3469-a	2400	149	71	43	2	1.31	0.49	28.24	65.00	40.43	18.21	108.27	0.65	167.85	19.75	203.5±16.5
3469-b #	2400	120	82	48	2	1.28	0.57	38.45	79.16	57.27	24.38	94.80	0.68	140.39	16.52	203.5±16.5
3469-c	2400	262	109	71	2	7.76	1.09	11.04	34.36	17.55	6.63	103.99	0.79	132.12	15.55	203.5±16.5
3469-d	2400	172	119	73	2	3.93	1.03	19.36	54.48	30.24	11.80	107.81	0.78	138.97	16.35	203.5±16.5
3469-e	2400	124	60	39	2	0.78	0.30	28.97	65.89	55.72	15.38	108.87	0.58	188.99	22.24	203.5±16.5
Mean														153.66	17.04	
Wt mean														148.40	16.78	
Central														152.90	17.94	
3470-a *	2620	164	74	48	1	1.80	0.15	14.05	46.80	23.13	8.22	47.59	0.64	74.50	8.77	259.5±18.4
3470-b #	2620	140	64	43	2	1.43	0.39	20.19	63.83	42.01	9.80	109.18	0.63	174.29	20.51	259.5±18.4
3470-c	2620	169	82	53	2	2.83	1.00	20.95	57.94	33.99	12.48	137.27	0.71	193.71	22.79	259.5±18.4
3470-d	2620	174	79	52	2	1.93	0.27	12.26	57.58	27.18	5.38	94.86	0.68	140.09	16.48	259.5±18.4
Mean														169.36	19.93	
Wt mean														163.21	19.20	
Central														172.98	16.28	
Mount Matz																
BC4-a	700	170	93	60	2	3.70	0.42	14.98	25.30	24.26	9.10	62.59	0.74	84.93	9.99	52.2±4.6
BC4-b *	700	136	101	61	2	2.20	0.58	21.30	56.11	23.39	15.31	101.73	0.73	138.45	16.29	52.2±4.6
BC4-c	700	209	78	52	2	2.29	0.55	35.34	38.13	64.01	20.10	55.44	0.68	81.15	9.55	52.2±4.6
BC4-d	700	119	110	63	2	2.05	0.15	12.87	20.01	18.71	8.33	47.31	0.74	63.58	7.48	52.2±4.6
BC4-g (A)	700	81	80	45	3	0.85	0.10	19.22	35.00	27.91	12.39	49.82		49.82	3.09	52.2±4.6
BC4-e (A)	700	95	93	52	3	1.33	0.38	31.91	45.08	56.11	18.45	73.01		73.01	4.53	52.2±4.6
BC4-f (A)	700	84	82	47	3	1.00	0.36	33.57	46.62	63.57	18.36	88.41		88.41	5.48	52.2±4.6
Mean														73.48	10.29	
Wt mean														64.69	3.73	
Central														69.59	7.11	

Table continued

Sample	Elevation [m]	Length [µm]	Width [µm]	Sp.radius [µm]	shape	Mass [µg]	4He [ncc]	eU [ppm]	Total Sm [ppm]	Total Th [ppm]	Total U [ppm]	Uncor. age [Ma]	FT corr.	Cor. age [Ma]	2σ error [Ma[	AFT age [Ma]
BC5-a	940	139	103	62	2	2.30	0.45	43.96	36.10	57.20	30.33	36.50	0.74	49.32	5.80	54.1±3.8
BC5-b	940	147	95	58	2	2.16	0.36	41.25	43.83	53.66	28.36	33.66	0.72	46.51	5.70	54.1±3.8
BC5-c	940	150	113	61	1	3.96	0.51	31.22	29.55	42.36	21.10	33.73	0.74	45.52	5.36	54.1±3.8
Mean														47.12	5.62	
Wt mean														47.03	5.61	
Central														47.37	3.44	
BC3-a	1220	141	94	58	2	3.11	0.46	21.82	6.03	23.71	16.26	56.05	0.73	76.96	9.06	69.1±4.8
BC3-b	1220	115	80	49	2	1.83	0.38	27.44	7.06	38.05	18.54	61.05	0.68	90.12	10.60	69.1±4.8
BC3-c	1220	124	95	57	2	1.72	0.13	11.20	36.89	18.00	6.65	54.98	0.72	76.86	9.04	69.1±4.8
BC3-d	1220	158	119	71	2	5.59	0.87	21.63	7.50	21.61	16.54	59.39	0.78	76.17	8.96	69.1±4.8
BC3-e (A)	1220	65	64	36	3	0.44	0.13	30.60	11.35	59.95	16.58	79.67		79.67	4.94	69.1±4.8
Mean														79.96	8.52	
Wt mean														79.46	7.25	
Central														81.56	4.98	
BC2-a	1450	217	70	47	2	2.69	0.40	23.76	15.89	23.24	18.21	51.57	0.69	75.23	8.85	81.3±5.5
BC2-b	1450	136	77	49	2	1.37	0.15	25.01	41.13	37.35	15.94	35.91	0.67	53.86	6.34	81.3±5.5
BC2-c *	1450	122	76	47	2	1.20	0.30	19.15	43.27	31.78	11.35	110.81	0.63	169.03	19.89	81.3±5.5
BC2-d	1450	137	68	44	2	1.10	0.21	33.46	20.01	30.20	26.25	46.37	0.63	73.30	8.62	81.3±5.5
Mean														67.46	7.94	
Wt mean														62.32	7.57	
Central														67.80	5.36	
BC1-a	1590	145	101	63	2	3.74	0.43	13.41	12.58	17.17	9.30	70.36	0.75	94.35	11.10	98.3±5.0
BC1-b	1590	121	87	48	1	1.91	0.16	19.85	18.21	25.71	13.70	34.73	0.67	51.98	6.12	98.3±5.0
BC1-c	1590	129	87	54	2	2.48	0.20	12.19	14.44	18.55	7.75	55.05	0.71	77.83	9.16	98.3±5.0
BC1-d	1590	159	80	46	1	2.14	0.26	20.52	20.70	26.17	14.24	49.30	0.67	74.02	8.71	98.3±5.0
BC1-e	1590	146	98	61	2	2.95	1.00	35.68	33.94	49.63	23.83	77.93	0.73	106.39	12.52	98.3±5.0
Mean														80.91	9.52	
Wt mean														71.42	8.40	
Central														79.59	10.16	
Priestley Glacier																
3450-a	1150	167	129	77	2	7.00	0.48	11.58	1.20	3.51	10.75	48.91	0.80	61.35	7.22	71.0±6.8
3450-b	1150	143	112	67	2	4.49	0.35	10.53	2.16	2.75	9.87	56.63	0.77	74.03	8.71	71.0±6.8
3450-c (A) #	1150	80	77	44	3	0.77	0.35	50.87	6.32	21.96	45.71	72.16		72.16	4.47	71.0±6.8
3450-d*	1150	117	89	53	3	1.20	0.17	46.34	3.95	8.91	44.23	26.23	0.69	38.28	4.50	71.0±6.8
Mean														69.18	6.80	
Wt mean														69.94	5.79	
Central														70.45	5.19	
3452-a *	1430	112	62	39	2	1.10	0.42	28.21	13.55	32.44	20.55	112.27	0.61	184.40	21.70	92.4±6.4
3452-b #	1430	169	114	70	2	3.56	0.84	53.55	14.56	10.91	50.87	36.35	0.77	47.08	5.54	92.4±6.4
3452-c	1430	211	86	57	2	3.96	0.70	36.86	10.45	31.55	29.44	39.53	0.74	53.74	6.32	92.4±6.4
Mean														50.41	5.93	
Wt mean														49.97	5.88	
Central														50.32	3.39	
3460-a #	1675	99	83	51	2	1.01	0.41	59.85	32.59	38.26	50.65	56.10	0.67	83.47	9.82	106.2±5.2
3460-b *	1675	157	78	50	2	2.40	0.54	12.61	4.71	6.58	11.03	145.26	0.70	207.96	24.47	106.2±5.2
3460-c	1675	154	128	75	2	6.33	2.73	39.33	23.68	22.45	33.88	83.51	0.79	105.67	12.43	106.2±5.2
Mean														94.57	11.13	
Wt mean														92.00	10.82	
Central														90.03	8.40	
3455-a	1900	182	99	62	1	3.67	0.89	50.81	51.86	36.41	41.84	39.37	0.73	54.28	6.39	109.3±4.8
3455-b*	1900	162	77	87	2	2.70	1.20	35.19	25.09	25.15	29.10	117.03	0.72	168.76	19.86	109.3±4.8
3455-c	1900	191	108	68	2	5.61	0.79	19.35	21.72	18.04	14.95	61.42	0.77	80.40	9.46	109.3±4.8
3455-d #	1900	119	88	56	1	2.68	0.32	32.06	29.78	23.06	26.41	43.15	0.67	64.24	7.56	109.3±4.8
Mean														66.31	7.80	
Wt mean														67.86	7.98	
Central														66.82	9.84	
3456-a	2070	153	84	50	1	2.28	0.89	49.13	28.47	22.35	43.66	65.68	0.68	96.59	11.37	121.4±6.2
3456-b *	2070	248	92	61	2	5.27	0.92	54.34	30.15	22.29	48.86	26.38	0.76	34.89	4.11	121.4±6.2
3456-c #	2070	203	81	59	2	3.34	1.66	55.53	26.08	15.30	51.72	73.53	0.72	102.06	12.01	121.4±6.2
3456-d	2070	166	114	70	2	5.40	1.77	31.32	30.69	21.17	26.10	85.94	0.78	110.74	13.03	121.4±6.2
Mean														103.13	12.14	
Wt mean														102.49	12.06	
Central														104.00	9.36	
3459-a	2280	150	66	41	1	1.34	1.94	156.98	48.54	78.73	138.23	75.91	0.60	125.74	14.79	157.6±9.5
3459-b	2280	126	92	56	1	1.38	0.97	39.36	19.00	24.50	33.48	145.68	0.61	238.54	28.07	157.6±9.5
3459-c	2280	147	67	42	2	1.67	0.67	63.04	31.39	33.56	54.94	52.54	0.71	73.74	8.68	157.6±9.5
3459-d (A)	2280	62	59	30	3	0.34	0.14	26.68	25.51	30.26	19.40	125.68		125.68	7.79	157.6±9.5
3459-e (A) #	2280	63	59	30	3	0.34	0.27	49.28	31.60	37.20	40.34	134.72		134.72	8.35	157.6±9.5
Mean														139.68	10.31	
Wt mean														133.13	8.92	
Central														131.38	11.07	

Table continued

Sample	Elevation [m]	Length [µm]	Width [µm]	Sp.radius [µm]	shape	Mass [µg]	4He [ncc]	eU [ppm]	Total Sm [ppm]	Total Th [ppm]	Total U [ppm]	Uncor. age [Ma]	FT corr.	Cor. age [Ma]	2σ error [Ma[	AFT age [Ma]
3458-a	2400	142	131	76	3	3.77	2.64	67.60	18.89	15.80	63.75	85.11	0.79	108.36	12.75	188.6±8.5
3458-b #	2400	136	80	41	1	1.79	1.36	82.93	22.62	22.78	77.42	75.19	0.69	114.54	13.48	188.6±8.5
3458-c	2400	136	76	48	2	1.94	1.62	75.50	17.61	17.22	71.33	90.92	0.61	133.64	15.72	188.6±8.5
Mean														118.85	13.98	
Wt mean														117.04	13.77	
Central														120.22	12.76	
3457-a #	2530	153	68	44	2	1.25	0.35	33.11	25.13	28.08	26.34	69.86	0.64	109.96	12.94	201.1±12.0
3457-b	2530	141	76	48	2	2.07	0.22	18.10	16.19	18.98	13.53	49.13	0.68	71.88	8.46	201.1±12.0
3457-c	2530	115	104	60	2	1.78	0.88	46.18	28.20	42.04	36.14	87.31	0.73	119.12	14.02	201.1±12.0
3457-d #	2530	135	76	48	2	1.98	0.43	24.22	17.55	21.29	19.11	72.79	0.68	106.88	12.58	201.1±12.0
Mean														101.96	13.18	
Wt mean														93.85	13.12	
Central														100.51	11.14	

Table M II-2: (U-Th-Sm)/He (AHe) single grain data. Grains were selected to obtain ideal apatite crystals (euhedral form, no inclusions, grain diameter >60 µm). Mechanical abrasion was applied to large apatite crystals with diameter >100 µm. ^{4}He intergrowth equation (e.g., described by Farley, 2002) was applied to determine the AHe age of each apatite grain based on raw data of ^{4}He, ^{238}U, ^{232}Th and ^{147}Sm isotopes, and the measured dimensions of the crystal for the alpha correction (Farley et al., 1996). The table shows dimension, shape (1 = complete; 1.5 = one termination missing; 2 = both terminations missing; 3 = rounded), mass, raw data (^{4}He, effective U, ^{238}U, ^{232}Th, ^{147}Sm), FT correction factor, uncorrected and FT-corrected age of each analyzed apatite single grain. Single grains with "A" in brackets of the grain label mark mechanical abraded grains. The error of each single grain is quoted as 2σ. Mean, weighted mean (Wt) and central age of each sample were calculated after single grain outliers (*) have been excluded. Central ages were calculated with the HelioPlot program of Vermeesch (2010). Single grain age outliers were identified via the statistical criterion of Chauvenet (Long and Rippeteau, 1974). Grains of sample 3468 marked with "x" were supposedly affected by ^{4}He implantation, and hence the uncorrected ages were used for age calculation (see also appendix M II-2). Single grain ages marked with "#" were used for HeFTy modeling. The corresponding apatite fission track age of each sample is shown for comparison.

Central ages between 37.5±3.3 and 173.0±16.3 Ma closely correlate with sample elevation. Central ages of samples from above the break in slope are usually younger than the corresponding AFT age, while the samples from below the break in slope generally coincide with the corresponding AFT age (Fig. M II-3). Exceptions constitute the samples from Mount Matz (see below and appendix M II-2). Analogously to the AFT data, samples from same level below basement top show consistent central ages (±1σ) near the Ross Sea coast (distance <15 km) and slightly higher ages further inland at the margin of the Priestley Glacier and the northern tip of the range. The effective U concentration of the majority of samples varies between 12 and 60 ppm (Table M II-2) with no common relationship to single grain ages or radius (supplementary material M II-1). An explanation of intra-sample AHe single grain age dispersion is provided in appendix M II-2.

Southern and northern Eisenhower Range: Single grain ages range from 35.3±4.2 to 193.7±22.8 Ma and produce central ages between 37.5±3.3 and 173.0±16.3 Ma (Table M II-2). The age-elevation regression runs parallel to that of the AFT ages

(Fig. M II-3) with a break in slope of similar age (~40 Ma). Two samples from above the break in slope (3470, 3472) have older single grain ages probably due to higher effective U concentrations (supplementary material M II-1).

Mount Matz: The AHe single grain ages of the Mount Matz samples spread considerably between 45.5±5.4 and 169.9±19.9 Ma (Table M II-2, Fig. M II-3). Central ages (47.4±3.4 – 81.6±5.0 Ma) are partially older than the corresponding AFT ages and show no recognizable relationship with elevation. Only sample BC5 comprises single grain ages that replicate and are younger than the corresponding AFT age.

Priestley Glacier: The majority of single grain ages between 38.3±4.5 and 238.5±28.1 Ma are within the error of the sample central age (50.3±3.4 and 131.4±11.1 Ma; Table M II-2, Fig. M II-3). Rejected age outliers are usually significantly older than the corresponding AFT age. The age-elevation regression generally resembles that of the AFT data but does not display the discontinuity at ~105 – 90 Ma. Two samples show a correlation between U concentration and single grain ages. Ages of sample 3457 increase with effective U concentration, while sample 3460 shows a reverse trend (supplementary material M II-1).

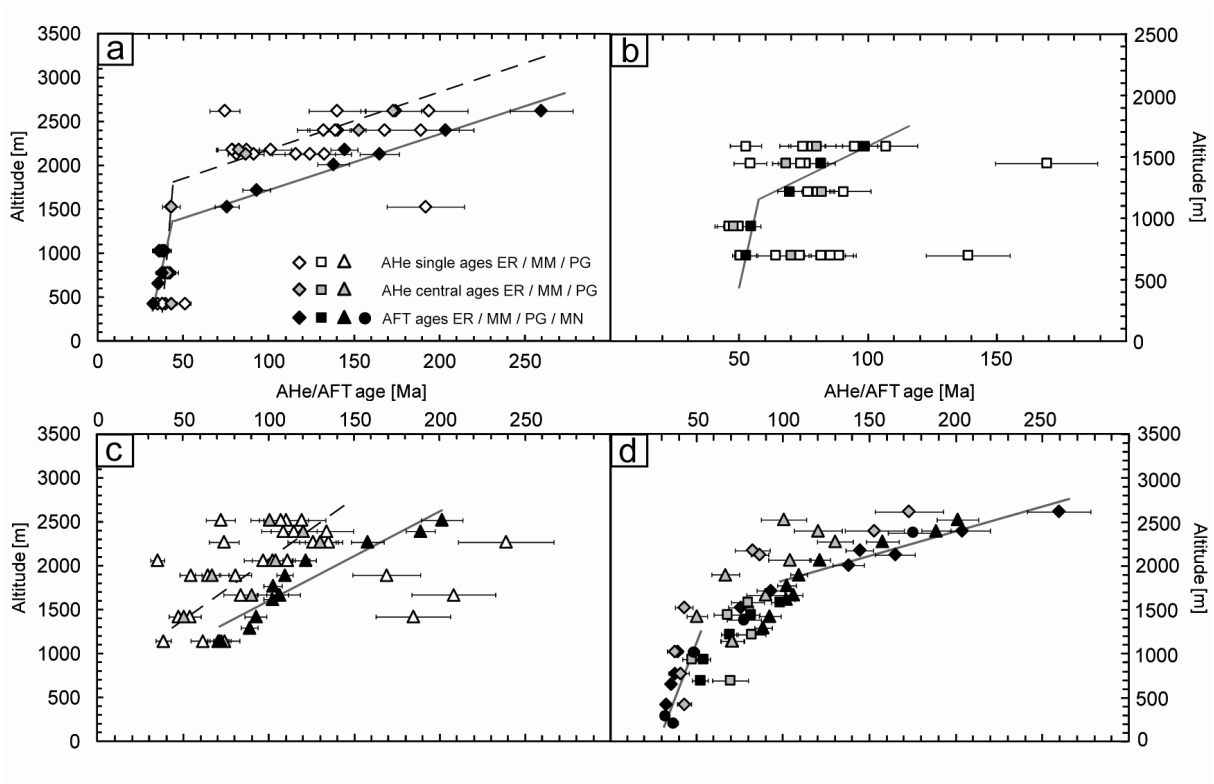

Figure M II-3: Plots showing (U-Th-Sm)/He (AHe) single grain ages, AHe central ages and apatite fission track (AFT) ages of a) the Eisenhower Range, b) Mount Matz, c) the Priestley Glacier, and d) the whole Eisenhower Range area vs. elevation.

4.5) Thermal history modeling

Thermal histories were modeled by using HeFTy and QTQt programs (Ketcham, 2005; Gallagher et al., 2005 and Gallagher, 2012) based on AFT data (age, lengths, Dpar; Table M II-1) and AHe data (Table M II-2). HeFTy produces inverse and forward thermal history models for each sample individually while QTQt generates inverse models either of individual samples or of a set of multiple samples from different heights. Inverse modeling generates a large number of possible t-T paths randomly, and forward modeling allows testing individual t-T paths. Modeling constraints are explained in appendix M II-3.

Intra-sample variation of AHe single grain ages (Fig. M II-3) did not allow common modeling of all dated grains. Modeling results with best fits between measured and predicted data were produced by using the single grain age(s) next to the sample´s central age (Table M II-2). HeFTy inverse modeling of the individual samples are quite similar to each other, and generally reproduced thermal histories derived from AFT data of the southern Eisenhower Range (Prenzel et al., 2013; and see supplementary material M II-2). Only the Mount Matz profile comprises results that are not compatible to collective modeling of the thermochronological data. Nevertheless, inverse modeling of only the AFT data from Mount Matz produces thermal histories consistent with those from the other profiles (Table M II-1; Prenzel et al., 2013).

Multiple HeFTy forward modeling generally produced a common thermal history for all samples with acceptable to good fits between measured and predicted data (Table M II-1; Fig. M II-4). This thermal history implies (I) low/near surface temperatures during the Late Triassic and Early Jurassic; (II) increasing temperatures immediately subsequent to the Ferrar event; (III) decreasing temperatures from mid-Jurassic to Early Cretaceous times; (IV) subsequent constant to slightly decreasing temperatures until the Eocene; and (V) fast final cooling to surface temperatures since Late Eocene (~35 Ma) with decelerated cooling rate since the Early Oligocene (~30 Ma).

Thermal histories show minor regional differences (Fig. M II-4). The implementation of a reheating pulse (~100°C) at ~90 Ma in the Priestley Glacier profile optimises the fit between measured and predicted data, and may explain discontinuities in the plots of AFT ages against elevation and MTL at ~105 – 90 Ma (Figs. M II-2, 3).

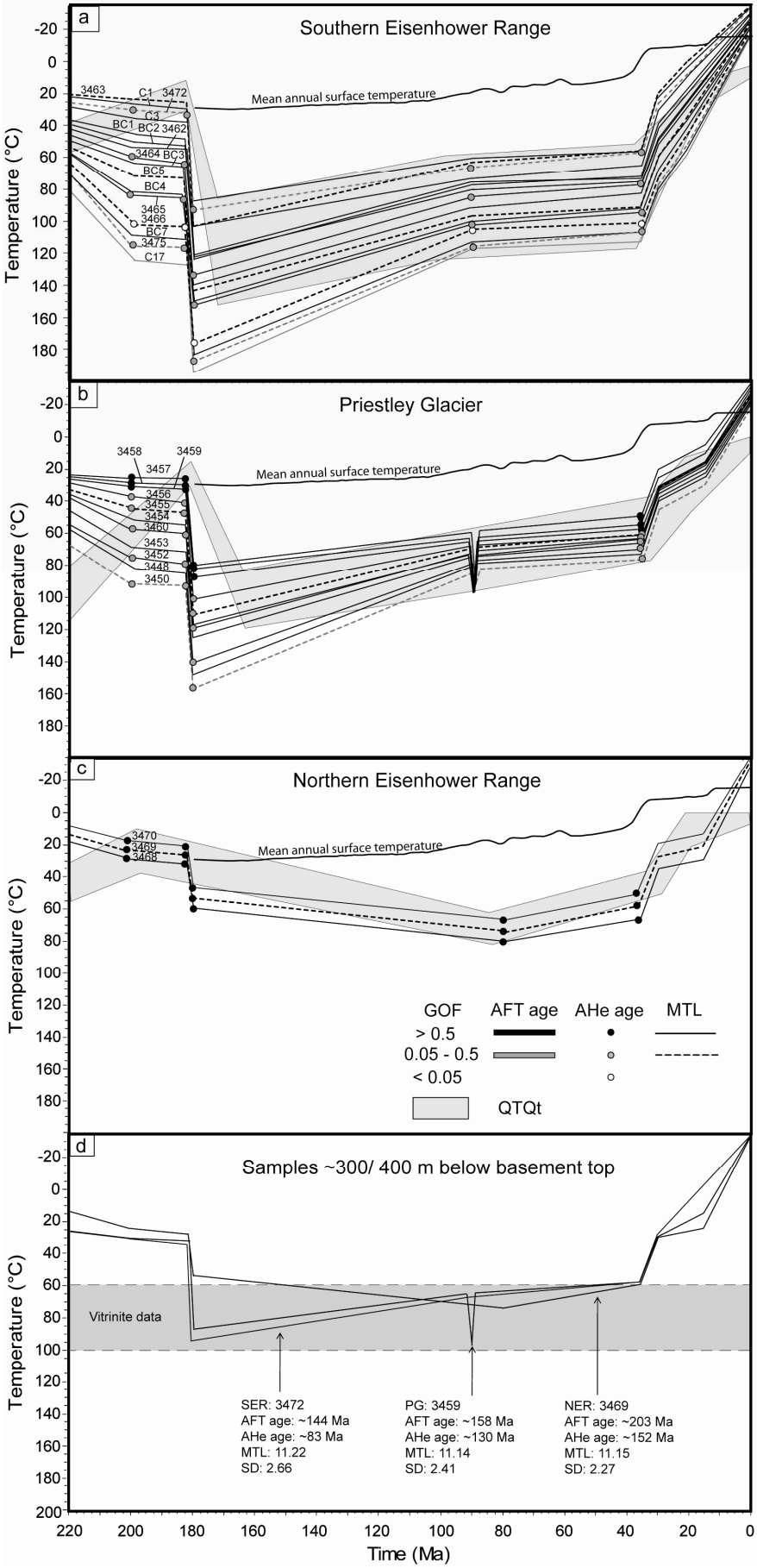

Figure M II-4: Thermal history models from (a) southern Eisenhower Range (including Mount Matz and Mount Nansen), (b) Priestley Glacier, and (c) northern Eisenhower Range produced by c-axis projected HeFTy forward modeling (version 1.7.5) and QTQt (version 3.0) using the annealing model of Ketcham et al. (2007). Goodness of fit (GOF) of fission track (AFT) ages, track lengths and U-Th-Sm/He (AHe) ages are illustrated by different shades of grey, contours and symbols (for GOF values see also table 1). The GOF value gives an indication about the fit between measured and predicted data. Values close to 1 are the best, values ≥0.5 are considered good, and values between 0.49 and 0.05 are considered acceptable. The GOF of the AFT length data is quoted using the Kuiper's Statistic method. Corresponding QTQt models of each area are underlain in grey. For reasons of clarity and comprehensibility only the cooling pattern between highest and lowest sample is shown (for more information see text). Mean annual surface temperature since the Late Jurassic, adapted from Jenkyns et al. (2012), Thorn and DeConto (2006), Poole et al. (2005), and Barrett (1999), is shown as black line. In (d) cooling of samples from different areas but same reference level near basement top are shown for comparison.

Samples from northern Eisenhower Range experienced Early Jurassic – Early Cretaceous temperatures than equally high samples from the southern Eisenhower Range and Priestley Glacier whereas mid-Cretaceous – Eocene temperatures were slightly higher in the north. Moreover, post-Ferrar heating was less intense in the Priestley Glacier profile than in the southern Eisenhower Range. The thermal history of the sandstone sample 3463 from the western end of the range (Fig. M II-1) generally conforms to the one of the southern Eisenhower Range, but requires ~20°C higher Late-Jurassic/Early Cretaceous temperatures than the other samples from this area. Its maximum Late Jurassic temperature (~105°C) agrees well with the maximum post-mid-Jurassic temperature of maximum ~100° – 125°C derived by minerals/reactions and vitrinite reflectance data for the Beacon sandstone. Varying the cooling patterns of the three areas since ~30 Ma optimises the fit with measured data. Rapid, continuous sample cooling of the southern Eisenhower Range contrasts with two-stage cooling of Priestley Glacier and northern Eisenhower Range, with slow cooling between ~30 and 15 Ma and subsequent acceleration of cooling.

Thermal histories modeled with QTQt resemble the HeFTy models (Fig. M II-4) with minor variation in the Late Jurassic temperature offset of the individual samples and in the Late Eocene cooling pattern. Subtle differences of this kind may be attributed to the excluded Sm component of the apatites and the disregarded negative present-day temperature for QTQt modeling (Appendix 3). Accordingly, the HeFTy model is used for further discussion.

4.6) Burial and exhumation of the Eisenhower Range

4.6.1) Paleogeothermal gradient

Paleogeothermal gradients can be calculated from the regression of paleo-temperatures against sample elevations (e.g., Bray et al., 1992; Prenzel et al., 2013). The variation of modeled post-mid Jurassic temperatures from the same reference level along the range require an individual consideration of the sample sets from southern Eisenhower Range, Priestley Glacier and northern Eisenhower Range (Fig. M II-4). Geothermal gradients were calculated at the time of maximum paleo-temperatures at 180 Ma (southern Eisenhower Range, Priestley Glacier) and at 80 Ma (northern Eisenhower Range) as well as at the time before onset of accelerated cooling at 35 Ma (Figs. M II-4, 5).

Almost identical Eocene geothermal gradients of 30±6°C/km (southern Eisenhower Range), 29±25°C/km (northern Eisenhower Range), and 24±7°C/km (Priestley Glacier; Fig. M II-5) rely on the regression of paleotemperatures between 57°C and 113°C against sample elevations at 35 Ma. A weighted mean of 28±8°C/km is in tight accordance with a coeval geothermal gradient of ~25°C/km calculated for the northern TAM and the USARP Mountains (Fitzgerald, 1994; Lisker et al., 2006). The regression of the three maximum paleotemperatures of the northern Eisenhower Range at 80 Ma against sample elevations (67° – 80°C/2130 – 2620 m) suggest a Cretaceous geothermal gradient in the order of ~30°C/km. This gradient based on only three data appears of poor statistic significance but is supported by a coeval gradient of ~27°C/km from southern Eisenhower Range and Priestley Glacier (Prenzel et al., 2013) and the regionally stable Eocene gradient in the order of ~30°C/km (Figs. M II-4, 5).

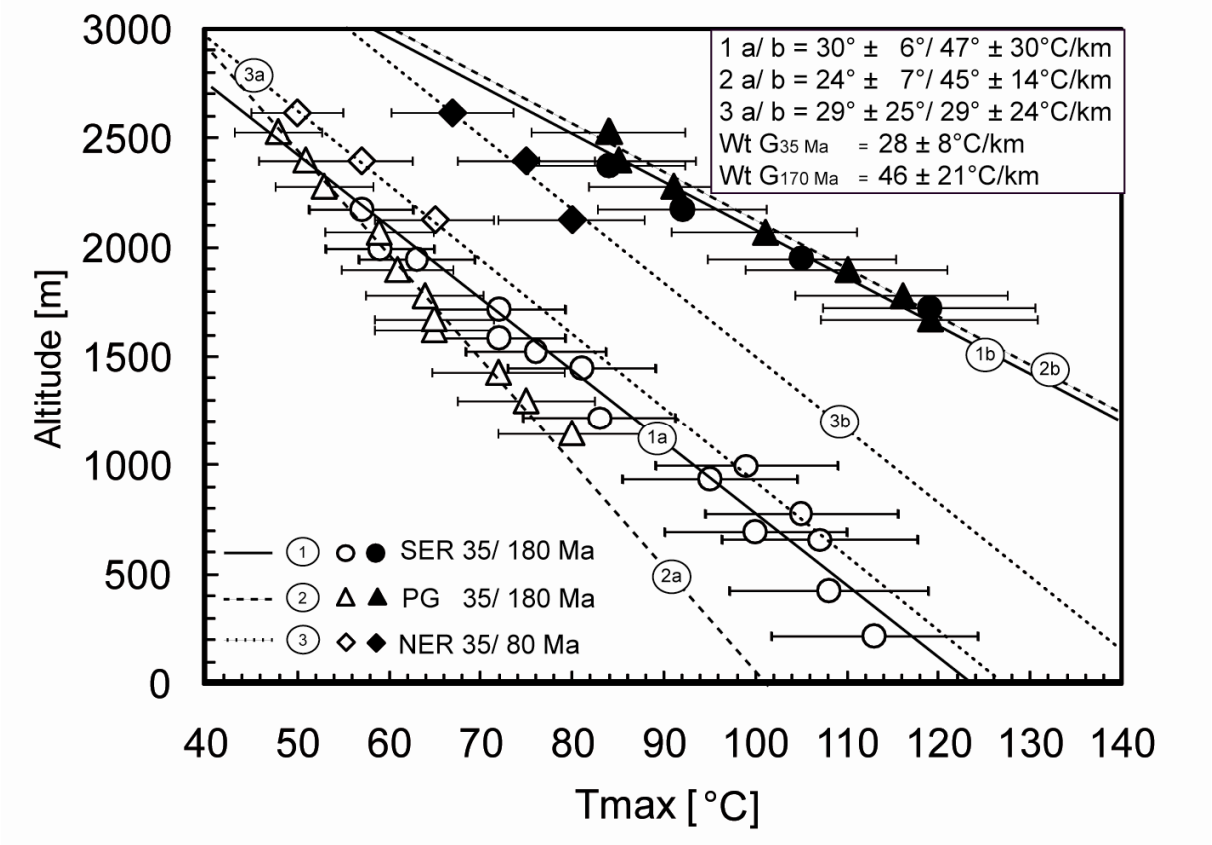

Figure M II-5: Maximum paleotemperatures (T_{max}) of southern and northern Eisenhower Range and Priestley Glacier at different times (180, 80, and 35 Ma) modeled with HeFTy (Fig. M II-4) plotted against sample elevations. Temperature regressions refer to a high Jurassic (~45°C/km) and moderate Cretaceous/Eocene (~30°C/km) geothermal gradient. Errors are quoted as ±10%.

In contrast to the Cretaceous/Eocene, maximum temperatures at 180 Ma against elevations from southern Eisenhower Range (65° – 119°C) and Priestley Glacier (85° – 119°C) suggest a considerable higher Jurassic geothermal gradient of ~45°C/km (Fig. M II-5). The conformity of calculated gradients for the Jurassic, and the Cretaceous – Eocene, respectively, suggests a similar development from a high Jurassic (~45°C/km) to a moderate Cretaceous – Eocene geothermal gradient (~30°C/km) for the entire range.

4.6.2) Basin evolution

Subaerial emplacement of Ferrar volcaniclastic rocks places the subjacent granitic basement rocks at near-surface position at ~182 Ma. Thermal history modeling infers reheating of the Eisenhower Range subsequent to the Ferrar event until onset of rapid cooling at the Late Eocene (Figs. M II-4, 5). Maximum post-Ferrar temperatures of ~65° – 85°C modeled from thermochronological data of samples near the basement top agree well with temperatures of ~60° – 100°C derived from organic maturation data of overlying Beacon sandstones. Long-term Late Jurassic to Eocene heating associated with decreasing geothermal gradients can only be explained by burial due to Ferrar load and post-Ferrar sediment accumulation persisting until ~35 Ma (Figs. M II-4, 6).

Basement burial was calculated for the time slices of 180, 80 and 35 Ma (Table M II-3; Figs. M II-4, 5). Positions and maximum paleotemperatures of the highest samples from southern Eisenhower Range (~85°C) and Priestley Glacier (~80°C) at ~180 Ma, a Late Jurassic geothermal gradient of ~45°C/km, and a surface temperature of ~25° – 30°C (e.g., Jenkyns et al., 2012) refer to an initial burial depth of ~0.9 – 1.1 km inferring a rather uniform load of Ferrar rocks and/or sediments above basement (Table M II-3; cf. section 4.1). This reconstruction exceeds the maximum Jurassic Beacon and Ferrar thickness of ~500 m observed in the Eisenhower Range but is lower than a cumulation of individual Beacon sequences and Ferrar sills and flows in northern Victoria Land that pile up to a hypothetic stack of up to ~2 km (e.g., Elliot and Foland, 1986). Such differences of overburden within a lateral distance of ~50 km may point to an external position of the Eisenhower Range with respect to the central locus of Ferrar rock extrusion beneath the Mesa Range, in a belt parallel and inboard to the Gondwana plate margin, or result from considerable paleorelief (e.g.,

Elliot, 1992). The high Jurassic geothermal gradient reflects increased heatflow associated with Ferrar magmatic activity and extension and rift-related crustal thinning across the TAM.

The distinctive change of the paleotemperature pattern of the Eisenhower Range profile between 180 and 80 Ma can be explained only by combined effects of both heat flow and burial. Basal heat flow decline due to isobaric cooling subsequent to the Ferrar event reduced the geothermal gradient from ~45°C/km (~180 Ma) to 28±8°C (~80 Ma). Application of this gradient to maximum temperatures then infers Cretaceous burial of the Eisenhower Range to depths of ~1.3 – 1.8 km (Table M II-3; Figs. M II-4 and 5). This thickness includes ~0.7 – 1.1 km of Beacon/Ferrar rocks and up to 1.1 km of Jurassic – Cretaceous sediments.

Thermal history modeling tentatively suggests an additional, locally confined mid-Cretaceous heat pulse to temperatures in the order of ~100°C in the Priestley Glacier area. Post-Ferrar temperatures of such magnitude are supported by minerals/reactions within Beacon sandstones throughout the Eisenhower Range. They may be attributed to circulation of hydrothermal fluids along faults during late Mesozoic – Cenozoic rifting (Fig. M II-6; e.g., Fleming et al., 1993).

Time [Ma]	region (sample)	gradient [°C/km]	surface T [°C]	sample T [°C]	T - difference [°C]	position b.t. [km]	burial of b.t. [km]	Beacon/Ferrar rocks [km]	Mesozoic/Eocene sediments [km]
180	SER (C1)	45	25 – 30	85	55 – 59	0.2	1.0 – 1.1	0.7 – 1.1	0 - 0.4
	PG (3457)	45	25 – 30	80	50 – 54	0.2	0.9 – 1	0.7 – 1	0 - 0.3
80	NER (3470)	30	10 – 15	65	50 – 55	x	1.6 – 1.8	0.7 – 1.1	0.5 – 1.1
	SER (C1)	30	10 – 15	65	50 – 55	0.2	1.4 – 1.6	0.7 – 1.1	0.3 – 0.9
	PG (3457)	30	10 – 15	60	45 – 50	0.1	1.3 – 1.5	0.7 – 1	0.3 – 0.8
35	NER (3470)	30	-5 – -10	50	55 – 60	x	1.8 – 2	0.7 – 1.1	0.7 – 1.3
	SER (3472)	30	-5 – -10	60	65 – 70	0.3	1.9 – 2.1	0.7 – 1.1	0.8 – 1.2
	PG (3457)	30	-5 – -10	55	60 – 65	0.2	1.8 – 2	0.7 – 1	0.8 – 1.3

Table M II-3: Sample details and thermal history constraints: position and maximum temperature of samples at/near basement top from southern Eisenhower Range (SER), northern Eisenhower Range (NER), and Priestley Glacier (PG) at 180, 80 and 35 Ma, coeval geothermal gradients and mean annual surface temperature areas, temperature difference between sample and surface, and calculated coeval burial of basement top and correspondent cover estimates of Beacon/Ferrar rocks and Mesozoic/Eocene sediments on basement (for more information see text).

Late Eocene basement burial of ~1.8 to 2.1 km as calculated on the basis of thermal history models, the geothermal gradient at ~35 Ma, and climatically induced Paleogene surface cooling of ~30°C (Table M II-3; Fig. M II-4; e.g., Poole et al., 2005; Thorn and DeConto, 2006) infer a thickness of ~0.7 to 1.4 km sediments prior to onset of rapid cooling. Persistent Mesozoic – Eocene sedimentation within the Eisenhower Range is consistent with geological indications from the region, such as Cretaceous and Paleocene terrestrial palymorphs within the Ross Sea (Truswell and Drewry, 1984: Villa et al., 2011), and Eocene terrestrial sediment influx into the Ross Sea (Ehrmann, 1998) which both may represent discharges from the sedimentary overburden (Lisker and Läufer, 2013).

4.6.3) Basement exhumation

Thermal history modeling identifies a Late Eocene – Oligocene cooling episode for the entire Eisenhower Range (Figs. M II-4, 7). Samples close to basement top cooled from ~55° – 60°C at 35 Ma to temperatures of ~25° – 30°C at 30 Ma. This temperature decrease superimposed by climatic cooling of ~5°C refers to rapid erosion of the complete ~0.7 – 1.4 km thick post-Ferrar sedimentary sequence with an average rate of ~140 – 280 m/Ma, and to (re-) exposure of the underlying Ferrar rocks within ~5 myr (Table M II-3; Fig. M II-6). Rapid exhumation at ~35 Ma coincides with Late Eocene surface cooling evident by the ~34 Ma shift from fluvial to glacial erosion in northern Victoria Land (e.g., Strand et al., 2003; Baroni et al., 2005), and with tectonic activity apparent from ~34 Ma old pseudotachylites along the Priestley Glacier (Di Vincenzo et al., 2004; Rossetti et al., 2006). Eocene exhumation of similar magnitude has been recorded via AFT data from the Rennick Glacier area north of the Eisenhower Range (Rosetti et al., 2003). Glacial erosion initiated due to formation of the East Antarctic continental ice sheet is more or less coeval with rifting of the West Antarctic Rift System and the opening of the Tasman gateway between Antarctica and Australia (e.g., Ehrmann and Mackensen, 1992; Stickley et al., 2004; Pfuhl and McCave, 2005). Consequently, a combination of climate and tectonic processes may have triggered sediment removal and basement exposition at the Late Eocene.

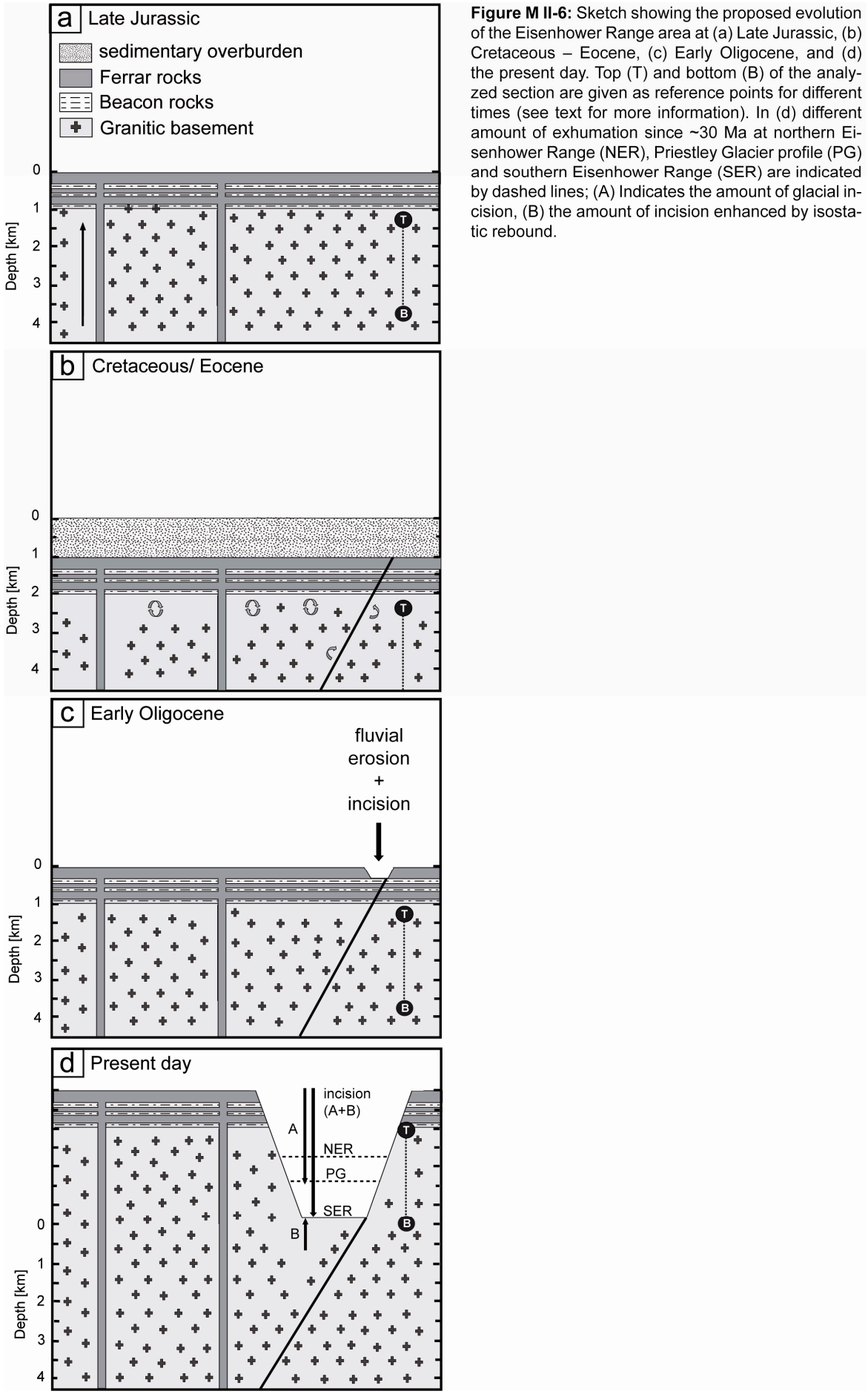

Figure M II-6: Sketch showing the proposed evolution of the Eisenhower Range area at (a) Late Jurassic, (b) Cretaceous – Eocene, (c) Early Oligocene, and (d) the present day. Top (T) and bottom (B) of the analyzed section are given as reference points for different times (see text for more information). In (d) different amount of exhumation since ~30 Ma at northern Eisenhower Range (NER), Priestley Glacier profile (PG) and southern Eisenhower Range (SER) are indicated by dashed lines; (A) Indicates the amount of glacial incision, (B) the amount of incision enhanced by isostatic rebound.

Exhumation stagnated at ~30 Ma (Fig. M II-7) probably due to exposure of Ferrar rocks which are much more resistant to erosion than a poorly consolidated sedimentary sequence. High weathering resistance of paleosurfaces is witnessed by extremely old exposure ages >10 Ma from summit plateaus in northern Victoria Land (e.g., Van der Wateren et al., 1999). The difference between the paleotemperatures of samples (~25° – 30°C near basement top) and surface (~-5° to -10°C; Thorn and DeConto, 2006) places the basement top to depths of ~0.7 – 1.1 km which coincides with the calculated thickness of Beacon and Ferrar rocks.

The Neogene thermal history of the Eisenhower Range is characterized by a more differentiated paleotemperature pattern and deviating cooling rates of the sampled profiles. A difference between apparently continuous cooling at the south and two-stage cooling at the northern part of the range (Figs. M II-4, 7) appears to be related to a fundamental change of exhumation style from downwearing to basement incision. Baroni et al. (2005) recognized by means of quantitative geomorphic analysis that the valley network of northern Victoria Land initiated as a regional fluvial drainage system along main structures of the Cenozoic fault system since the early Eocene (e.g., Priestley and Reeves Glaciers/Faults; Figs. M II-1, 6). Rock cooling since ~30 Ma (Figs. M II-4, 7) may then be related to exhumation by glacial incision of these predestined structures subsequent to the shift from fluvial to glacial conditions during the Early Oligocene (e.g., Strand et al., 2003). Enhanced by isostatic rebound due to sediment removal at ~30 Ma, this provides an adequate explanation for basin inversion and formation of the present-day landscape at the Eisenhower Range with high-elevated plateaus that preserve Ferrar or basement rocks at the top, and deeply incised troughs within the basement (Fig. M II-6). Minor cooling of ~5°C in the northern Eisenhower Range between ~30 and 15 Ma refers to incision of ~0.2 km within the first 15 m.y. after basement exposition (~10 m/Ma), while coeval cooling of ~20°C at the Priestley Glacier and of ~50°C at southern Eisenhower Range suggest considerably deeper incision of ~0.7 km (~50 m/Ma) and 1.6 km (~110 m/Ma), respectively (Fig. M II-7). The incision decrease of ~1 – 1.5 km over a length of ~25 – 40 km from the coast towards inland (Fig. M II-1) infers backstepping erosion with ~40 m less of incision per 1 km distance to coast. Higher amounts and rates of incision at the coast may result from rift shoulder uplift of the West Antarctic Rift System, an effect that fades towards the interior.

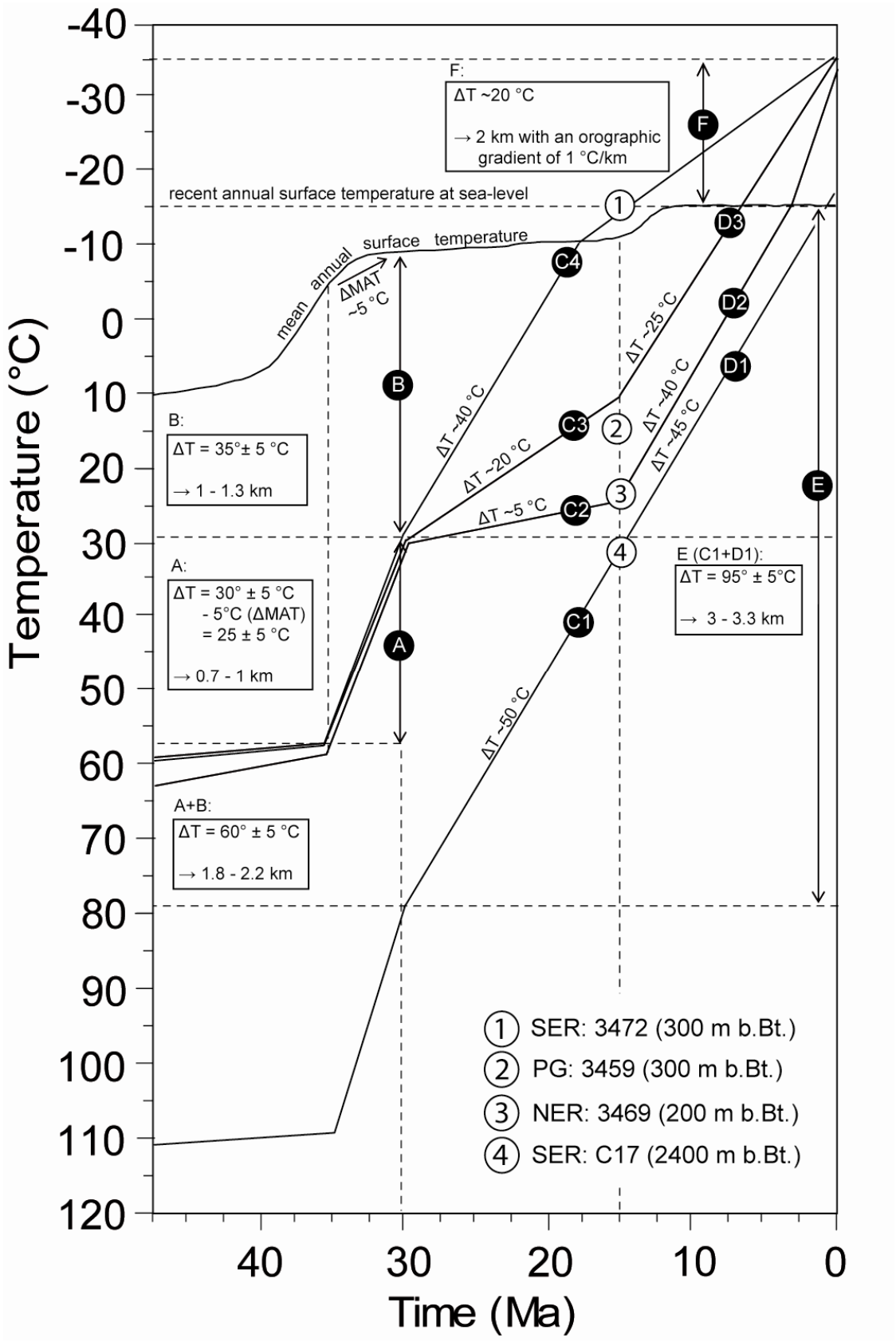

Figure M II-7: Exhumation of samples at/near basement top (1-3) from southern Eisenhower Range (SER), northern Eisenhower Range (NER), and Priestley Glacier (PG), and of the lowermost sample (4) since ~50 Ma. Capitals mark different stages of sample cooling to the recent annual surface temperature (for more information see text). The mean annual surface temperature (MAT) adapted from Thorn and DeConto (2006) and Barrett (1999) is shown as black line.

Enhanced incision at northern Eisenhower Range and Priestley Glacier commencing at ~15 Ma coincides with the development of a persistent ice sheet in East Antarctica and landscape freezing along the TAM (e.g., Flower and Kennett, 1994; Sudgen and Denton, 2004). Glacial incision intensified since ~15 Ma due to the concurrence of freezing erosive-protecting conditions at higher elevations and wet-based erosive-strengthening conditions at low elevation glaciers (e.g., Stern et al., 2005). Cooling pattern and recent exposure of the lowermost sample infer ongoing incision with ~110 m/Ma until today to depths of ~1.7 km during the last ~15 Ma., and total incision depths of ~1.9 km in the northern Eisenhower Range, ~2.4 km in the Priestley Glacier, and ~3.3 km in the southern Eisenhower Range (Figs. M II-6, 7). This regional differentiation produced varying times for the exposure of the basement top at southern Eisenhower Range (~18 Ma), Priestley Glacier (~8 Ma), and northern Eisenhower Range (~3 Ma). Additional minor surface cooling may be explained by the development of an orographic gradient due to ongoing basement incision and uplift.

We explain net incision of the Eisenhower Range as resulting from the interference of glacial erosion and isostatic surface rebound in response to the sediment removal between ~35 and 30 Ma. If the Eisenhower Range was at isostatic equilibrium at ~35 Ma when loaded with a ~1 km thick sedimentary cover (Table M II-3) with an assumed density of ~1.7 – 2.5 g/cm^3, complete erosion of this sequence at ~30 Ma triggers subsequent isostatic surface rebound of ~0.5 to 0.8 km (e.g., Middleton and Willcock, 1994). Assuming regional present-day isostatic equilibrium, an average uniform rate of isostatic rebound of ~20 – 30 m/Ma for the entire Eisenhower Range suggests a counteracting incision rate of the glaciers of ~80 – 90 m/Ma for the southern Eisenhower Range, and correspondingly lower rates for Priestley Glacier area (~50 – 60 m/Ma) and northern Eisenhower Range (~30 – 40 m/Ma) to attain total vertical incision varying from approximately 3.3 km in the south to 1.8 km in the north (Fig. M II-6).

4.7) Conclusions

This study presents for the first time in the Transantarctic Mountains a combined data set of independent and complementary thermochronological, maturity and sediment petrographic data to reconstruct regional burial, exhumation and long-term landscape

evolution in a resolution that is not matched by any case study in Antarctica. Combined research of sensitive minerals/reactions and organic maturation data within Beacon sandstones, and thermal history modeling of AFT and AHe data infers burial of the Eisenhower Range within a sedimentary basin subsequent to Early Jurassic Ferrar magmatism (~182 Ma) and constrains Late Eocene basin inversion. It also suggests a locally confined mid-Cretaceous short-term heat pulse of ~100°C adjacent to the Priestley Fault. The regression of paleotemperatures against sample elevations refers to a high Jurassic (~45°C/km) and a moderate Cretaceous – Eocene geothermal gradient (28±8°C/km). Thermal history models and thermal indications account for a rather uniform overburden on basement consisting of ~0.7 – 1.1 km Beacon and Ferrar rocks, and ~0.7 – 1.4 km of Mesozoic – Eocene sediments. The reconstructed thickness of Beacon and Ferrar rocks resembles the maximum thickness of these rocks preserved in the Eisenhower Range but is lower than observed in the Mesa Range. Varying thickness of Ferrar rocks across northern Victoria Land is probably related to an external position of the Eisenhower Range with respect to the central locus of Ferrar rock extrusion probably beneath the Mesa Range, in a belt parallel and inboard to the Gondwana plate margin.

Late Eocene/Early Oligocene basin inversion coincides with the shift from fluvial to glacial erosion in northern Victoria Land and an episode of faulting along the Priestley Fault. At supraregional scale, climate change represented by the formation of the East Antarctic continental ice sheet overlaps with tectonic processes related to the formation of the West Antarctic Rift System, and the onset of sea floor spreading and opening of the Tasman gateway between Antarctica and Australia.

Rapid exhumation stagnated at ~30 Ma with the exposure of Ferrar/ basement rocks. Regional differential sample cooling to the present-day surface temperature documents basement incision along main tectonic structures due to glacial erosion and isostatic rebound. Total incision within the Eisenhower Range since ~30 Ma declines from the south (~3.3 km) along the length of the Priestley Glacier (~2.3 km) to the northern tip of the escarpment (~1.8 km) suggesting backstepping erosion from the coast northwards with incision depth decreasing for ~40 m per 1 km distance to coast. Differential incision is presumably related to the vicinity of the West Antarctic Rift System and corresponding necking, rift shoulder uplift and isostatic compensation. Increased incision since ~15 Ma in the northern Eisenhower Range is

in accordance with the date suggested for the development of a persistent ice sheet in East Antarctica and the protection of the frozen landscape along the TAM.

Acknowledgements

This work was supported by grants LI745/12-1 (F.L.), LA1080/7-1 (A.L.) and GA 457/11+13 (R.S.; M.E.) of the Deutsche Forschungsgemeinschaft (DFG) within priority program SPP 1158 “Antarctic Research with comparative investigations in Arctic ice areas”. F.L., J.P., and R.S. are grateful to the BGR for the invitation to participate in the GANOVEX IX and X campaigns 2005/06 and 2009/10. We especially thank the personnel of Mario Zucchelli Station, the crews of MS *Italica* and *Helicopters New Zealand* for logistic support, and the members of the GANOVEX teams for cooperative fieldwork and stimulating discussions. Sincere thanks go also to our field guides Maurice Conway, Brian Staite and Mike Aitkinson. J. Lindow and B. Ventura are acknowledged for constructive comments.

Appendix

(M II-1) Sampling and processing procedure: The elevation of each sample was measured barometrically with altimeter and GPS and subsequently calibrated against a 1:250,000 topographic map (U.S. Department of the Interior, 1968a-d). Apatites of rock samples between ~5-10 kg in weight were crushed and separated using standard heavy liquid and magnetic techniques, mounted in the epoxide-based mounting medium Petropoxy 154, and etched in 5N HNO3 at 20°C and 20 s following the procedures described by Gleadow (1984) and Ketcham et al. (2007). Subsequently, the mounted apatite concentrates were irradiated at the research reactor facility FRM-II in Garching, Germany. FT ages were measured by the external detector method following the method described by Hurford and Green (1982). Fish Canyon and Durango standards were used for Zeta calibration. Counting and measurement procedures were performed manually, using a Zeiss Axioplan microscope at a magnification of x1250 under dry objectives and the FT-Stage program of Dumitru (1993).

Apatite single grains for (U-Th-Sm)/He analysis were selected using an Olympus SZ61 microscope at a magnification of x45 under reflected light and an Olympus SZX16 microscope at a magnification of x10 to x140 under transmitted and polarized light, following the recommendations for an ideal apatite crystal for (U-Th-Sm)/He chronology (euhedral form, no inclusions, grain diameter >60 µm). He degassing and ICP-MS measurement were performed at the University of Melbourne.

(M II-2) Explanation of intra-sample AHe single grain age dispersion: Most frequent causes for deviating grain ages (U-Th-rich mineral/fluid inclusions; cracks) have been excluded by optical grain inspection prior to analysis. Instead, intra-sample single grain age dispersion may be explained by radiation damage, U-Th-zoning and He-implantation.

Radiation damages: Radiation damages within apatite crystals trap 4He atoms that may cause AHe ages as old as AFT ages (e.g., Shuster et al., 2006; Flowers, 2009). The rate of radiation damage accumulation is especially high when apatites reside within the temperature sensitive range of the AHe system. Accordingly, post-Jurassic reheating of the Eisenhower Range entailing long-lasting (~100 m.yr.), low temperatures (~50° – 80°C) for the samples above the break in slope (Fig. M II-4) provides appropriate conditions for the accumulation of radiation damages within the

apatites of these samples (Wolf et al., 1998; Shuster et al., 2006). In contrast, samples below the break in slope were heated to higher temperatures where radiation damages get completely annealed. Consequently, a large variation of the single grain ages in samples above the break in slope (Fig. M II-3a) may be explained by radiation damages. This assumption is supported by the relationship between effective U concentration and single grain ages of three older samples (Table M II-2; Fig. M II-A1).

U-Th grain zonation: The AFT samples from Mount Matz contain several apatite grains with inhomogeneous track distributions. These apatites are patchy or concentrically zoned with cores richer and rims poorer in U and Th (Appendix: Fig. M II-A3). Such U-Th distribution may lead to a misinterpretation of the retained α-particles and thus to the calculation of a wrong, α-ejection-overcorrected age which is older than the "true age" (e.g., Farley et al., 1996). This effect is intensified here by the long sample residence within temperatures of the AHe system (Fig. M II-4; e.g., Fitzgerald et al., 2006). Moreover, most apatites from Mount Matz are broken (Table M II-2), and it cannot be specified with confidence which part of an apatite, potentially inhomogeneous in U-Th, was measured.

^{4}He implantation: Sample 3460 reveals a correlation of effective U concentration and single grain ages with lower effective U contents for older grains. This is opposite to the trend described by Shuster et al. (2006) and indicates ^{4}He implantation from a surrounding U-Th-rich host or matrix (Spiegel et al., 2009). Implantation of ^{4}He atoms is also evident for sample 3468 where single grain ages of mechanical abraded grains replicate the uncorrected age of non-abraded grains (Table M II-2).

(M II-3) Thermal history modeling constraints: HeFTy inverse modeling was performed for all samples with a minimum number of 40 measured confined tracks, which accounts for 29 samples (Table M II-1). Previously modeled data (Prenzel et al., 2013) were re-modeled if additional AHe data were available (Table M II-1). Inverse models then serve as basis to detect the best composite thermal history by HeFTy forward modeling. Since the ages of samples from the same level below basement top slightly vary along the length of the Eisenhower Range (Fig. M II-1c), we modeled the sample sets from northern Eisenhower Range, Priestley Glacier, and southern Eisenhower Range (including Mount Matz and Mount Nansen) independently from each other.

Time-temperature constraints for HeFTy were set for each sample set analogously to the ones of Prenzel et al. (2013) for the southern Eisenhower Range. They comprise (1) initial high temperatures after intrusion of the Granite Harbour Intrusives [500 – 450 Ma; 150° – 300°C]; (2) a long time period allowing a generous temperature range until the Ferrar event [500 – 180 Ma; 0° – 300°C]; (3) near surface temperatures at the time of Ferrar emplacement [185 – 175 Ma; 10° – 30°C for the highest sample to 60° – 170°C for the lowermost sample; Jurassic geothermal gradient 15° – 70°C/km]; (4) subsequent temperature increase inferred from sample ages younger than the genetic Ferrar rock age [180 – 55 Ma; 40° – 250°C]; (5) decreasing Cenozoic temperatures inferred from the age-elevation and age-MTL pattern of the AFT data [Fig. M II-2a; 55 – 25 Ma; 20° – 160°C]; (6) near surface temperatures after the break in slope [55 – 0 Ma; -35° – 20°C]; and (7) the present-day mean surface temperature depending on the sample elevation [0 Ma; -35° to 15°C]. For detailed description check Prenzel et al. (2013).

Subsequently, QTQt modeling was applied to validate the HeFTy forward models. The program only implements U and Th components of non-abraded grains. Initial conditions for QTQt were specified analogously to time-temperature constraints 1 – 3 and 5 – 6 of HeFTy. These constraints were set for the highest sample and imposed automatically on the other samples. Since QTQt does not consider negative values the present temperature was set to zero instead of the real present-day negative mean surface temperature, and an orographic gradient (~1°C/100 m) was neglected.

Supplementary data M II-1

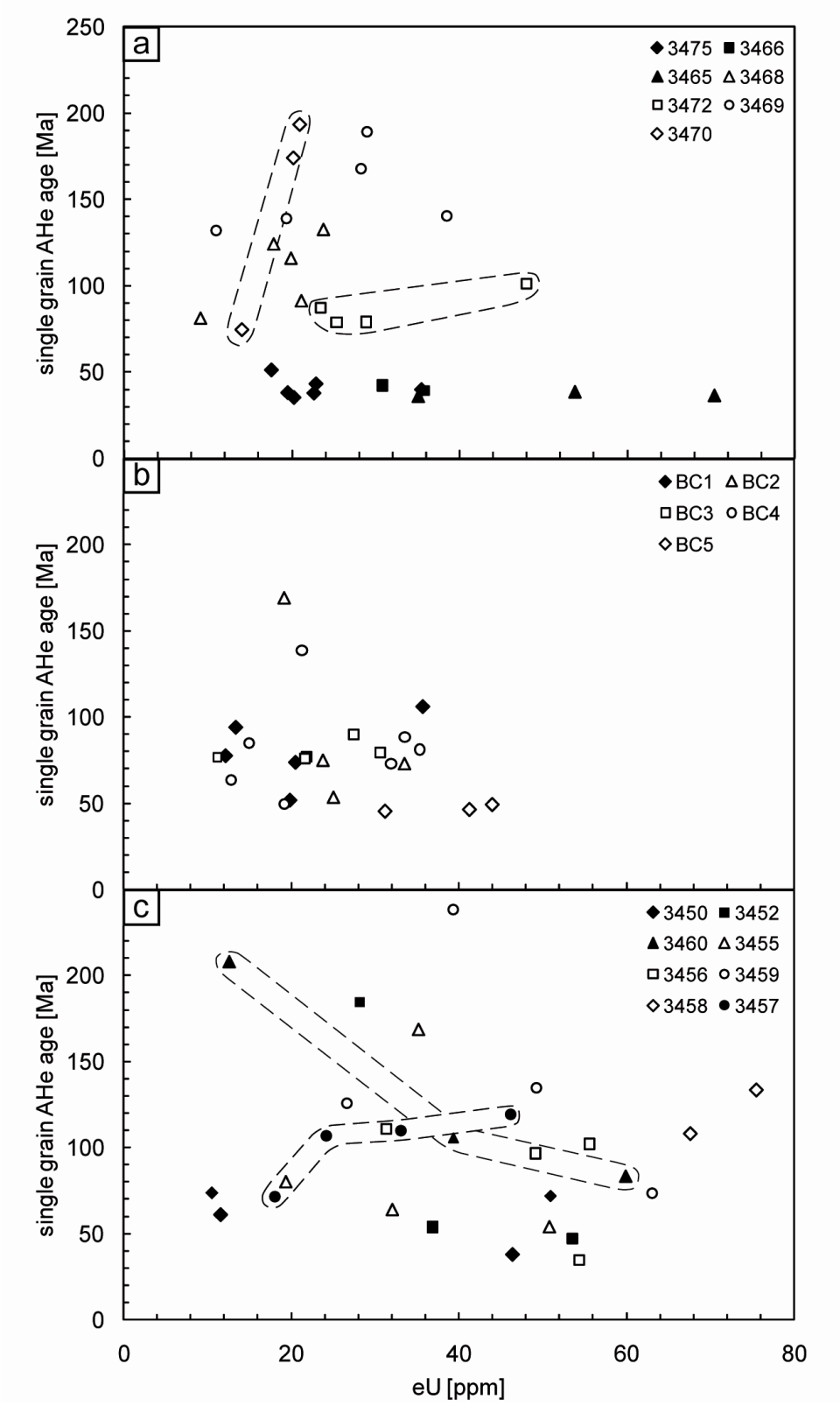

Supplementary data M II-1: (U-Th-Sm)/He (AHe) single grain ages vs. effective U concentration (eU) for the samples from (a) the southern and northern Eisenhower Range, (b) Mount Matz and (c) the profile at the southern margin of the Priestley Glacier. Single grains encircled by dashed white lines demonstrate a distinctive pattern between ages and eU concentration.

Supplementary data M II-2

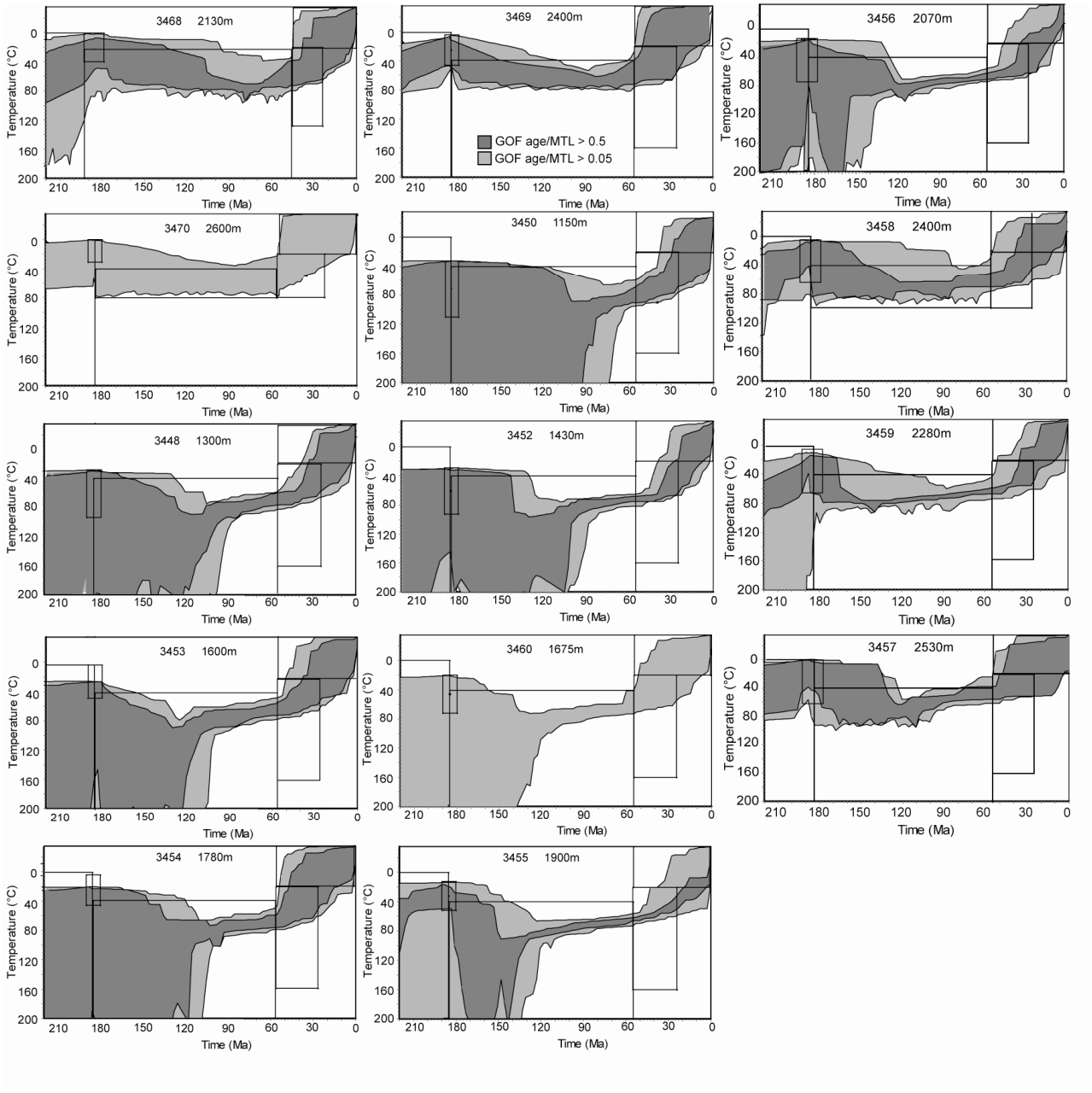

Supplementary data M II-2: Inverse modeling results of representative samples from (a) southern Eisenhower Range, (b) Priestley Glacier, and (c) northern Eisenhower Range (HeFTy, Ketcham 2005); Black boxes mark the time-temperature constraints set for HeFTy modeling (for detailed description see text). The dotted black lines mark the limits of the temperature sensitive range of the apatite fission track (AFT) and U-Th-Sm/He (AHe) system. HeFTy was performed using the Monte Carlo search method with a minimum of 100,000 randomly produced t-T-paths, the annealing model of Ketcham et al. (2007) and c-axis projection. The goodness of fit (GOF) gives an indication about the fit between observed and predicted AFT age and length data. Values close to 1 are the best, values ≥0.5 are considered good, and values between 0.49 and 0.05 are considered acceptable. The GOF of the AFT length data is quoted using the Kuiper's Statistic method. A default initial track length of 15.99 µm and a length reduction of 0.892 µm were measured in Durango standard.

Supplementary data M II-3

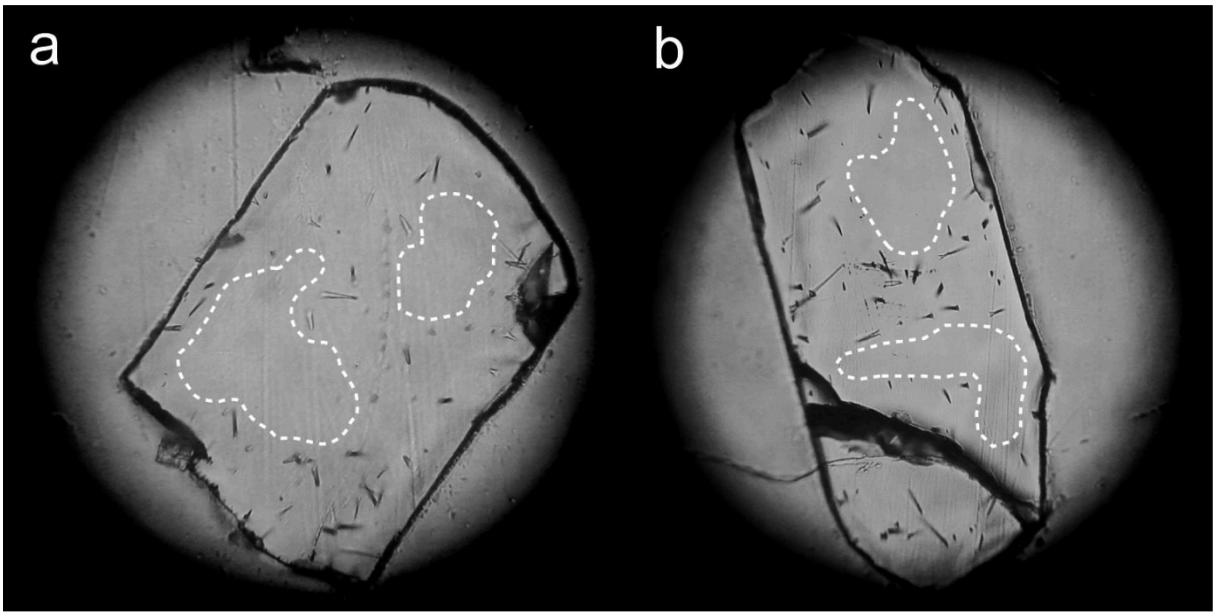

Supplementary data M II-3: Representative apatite grains from Mount Matz after etching. Distribution of spontaneous fission tracks indicates uranium zoning patterns with (a) patchy and (b) concentrically zoned distributions. Track-free sectors are encircled by dashed white lines.

MANUSCRIPT III

Mesozoic basin evolution of the Terra Nova Bay region, Transantarctic Mountains – Insights from thermochronological studies between Deep Freeze Range and Prince Albert Mountains

J. Prenzel, F. Lisker, M.L. Balestrieri, A.L. Läufer, C. Spiegel

* corresponding author. University of Bremen, PO Box 330440, 28334 Bremen, Germany, Tel.:0049-421-218-65284, Email address: jprenzel@uni-bremen.de

Concept	50%
Data collection	95%
Realization	70%

Mesozoic basin evolution of the Terra Nova Bay, Transantarctic Mountains – Insights from thermochronological studies between Deep Freeze Range and Prince Albert Mountains

J. Prenzel[1], F. Lisker[1], M.L. Balestrieri[2], A. Läufer[3], C. Spiegel[1]

[1] University of Bremen, FB5 Geosciences, Klagenfurther Straße, 28359 Bremen, Germany

[2] CNR, Institute of Earth Sciences and Earth Resources, Via La Pira 4, 50121 Florence, Italy

[3] Bundesanstalt für Geowissenschaften und Rohstoffe, Stilleweg 2, 30655 Hannover, Germany

Keywords: Apatite fission track and apatite U-Th-Sm/He thermochronology; burial and exhumation history, sedimentary basin evolution

Abstract

The Terra Nova Bay region in the Ross Sea sector of the Transantarctic Mountains comprises three N-S extending mountain ranges, the Deep Freeze Range, Eisenhower Range and northern Prince Albert Mountains. Recent thermo-chronological studies in the Eisenhower Range evidenced the existence of a Mesozoic basin of at least local scale. For reconstructing basin architecture, extension and geometry, and to gain first important information about the basins evolution in the context of supraregional geodynamic processes, we here present a regional comprehensive apatite fission track (AFT) and apatite U-Th-Sm/He (AHe) data set for the entire Terra Nova Bay providing new data and thermal history models of vertical sample profiles from the Deep Freeze Range, and new thermal history models of published data from the northern Prince Albert Mountains.

New thermochronological ages (28±3 – 274±17 Ma) from Deep Freeze Range positively correlate with elevations (1060 – 3120 m) with AHe ages which are usually 10 – 20 Ma younger than corresponding AFT ages. Thermal history modeling detects for the entire Terra Nova Bay region common Mesozoic – Eocene heating/burial of the Jurassic surface and constrains rapid Late Eocene cooling/exhumation. Sample paleotemperatures versus sample elevations indicate an increased Jurassic (44±15°C/km) and a moderate Cretaceous – Eocene (24±7°C/km) geothermal gradient. Paleotemperatures and gradients used in tandem infer basement burial of ~2 km for Deep Freeze and Eisenhower Ranges and higher burial of ~3.4 km for

Prince Albert Mountains. This is attributed to a higher thickness of Beacon and Ferrar rocks in the southern Terra Nova Bay region probably related to regional differences in the (pre-) Ferrar topography. Similar post-Ferrar sediment thickness in the order of 1 km for the entire region indicates a regional continuous, uniform Mesozoic – Eocene sedimentary basin. Mid-Jurassic basin formation and subsequent sediment accumulation until the Late Eocene is explained by initiation of extension within the West Antarctic Rift System at ~180 Ma with a continuous stable stress field of low E-W extension during Ross Sea opening until ~35 Ma. Late Eocene/Early Oligocene basin inversion is linked with right lateral strike-slip and transtensional faulting attributed to major Eocene tectonic reorganization in the Ross Sea region from Cretaceous orthogonal to Cenozoic oblique rifting. Subsequent final exhumation with deepest incision at the coast is obviously related to a change of exhumation style from downwearing to backstepping incision from the coast towards the interior by a combination of glacial incision, climate cooling, and isostatic surface rebound in response to sediment removal at ~30 Ma.

5.1) Introduction

The Terra Nova Bay region of northern Victoria Land forms part of the Transantarctic Mountains in the Ross Sea sector of East Antarctica (Fig. M III-1). It is characterized by deeply glacial incised high-elevated inland plateaus in immediate vicinity to a sea-level coastal plain. Several large glaciers divide the regional mountain ranges of Deep Freeze Range, Eisenhower Range and northern Prince Albert Mountains, and border the region to the Mesa Range in the north, and to southern Victoria Land in the south, respectively. The Deep Freeze and Eisenhower Ranges, and the Mesa Range north of them, reach mountains elevations up to ~3000 m, while the Prince Albert Mountain show considerable lower elevations between ~1300 m at the coast, and up to ~2400 m inland. The extensive glacial network provides an exceptional good outcrop access with a relief of up to 3.5 km exposing Proterozoic – Paleozoic crystalline basement that is unconformably overlain by Permian to Early Jurassic sediments and covered/intruded by magmatic rocks of the 182 Ma Ferrar event (e.g., Elliott, 1992). Present-day exposure of the Ferrar magmatic suite or older rocks forming the top of the high-elevated plateaus over wide portions of northern Victoria Land reflects either non-deposition or complete erosion of mid-Jurassic to Neogene strata.

Since the Ferrar magmatic rocks have been identified as a predominantly volcanic sequence containing syn-Ferrar pyroclastic and siliciclastic, partially fossil-bearing sedimentary sequences, pillow lavas, and phreatomagmatic structures and diatremes (e.g., Viereck-Götte et al., 2007; Bomfleur et al., 2011), the Jurassic paleosurface is of crucial significance for the reconstruction of the subsequent Mesozoic and Cenozoic evolution. The subaerial nature of the Ferrar rocks indicates Jurassic near surface position of the directly underlying Beacon and basement rocks, while apatite fission track (AFT) data from vertical basement profiles refer to subsequent substantial Mesozoic burial (e.g., Lisker and Läufer, 2013). Such burial can be only explained by a much higher thickness of Ferrar rocks than documented in the regional stratigraphic record (Elliott and Fleming, 2008), or by a now vanished post-mid Jurassic rock cover. The relevance of the Jurassic paleosurface has been recognized only recently (Lisker and Läufer, 2013; Prenzel et al., 2013).

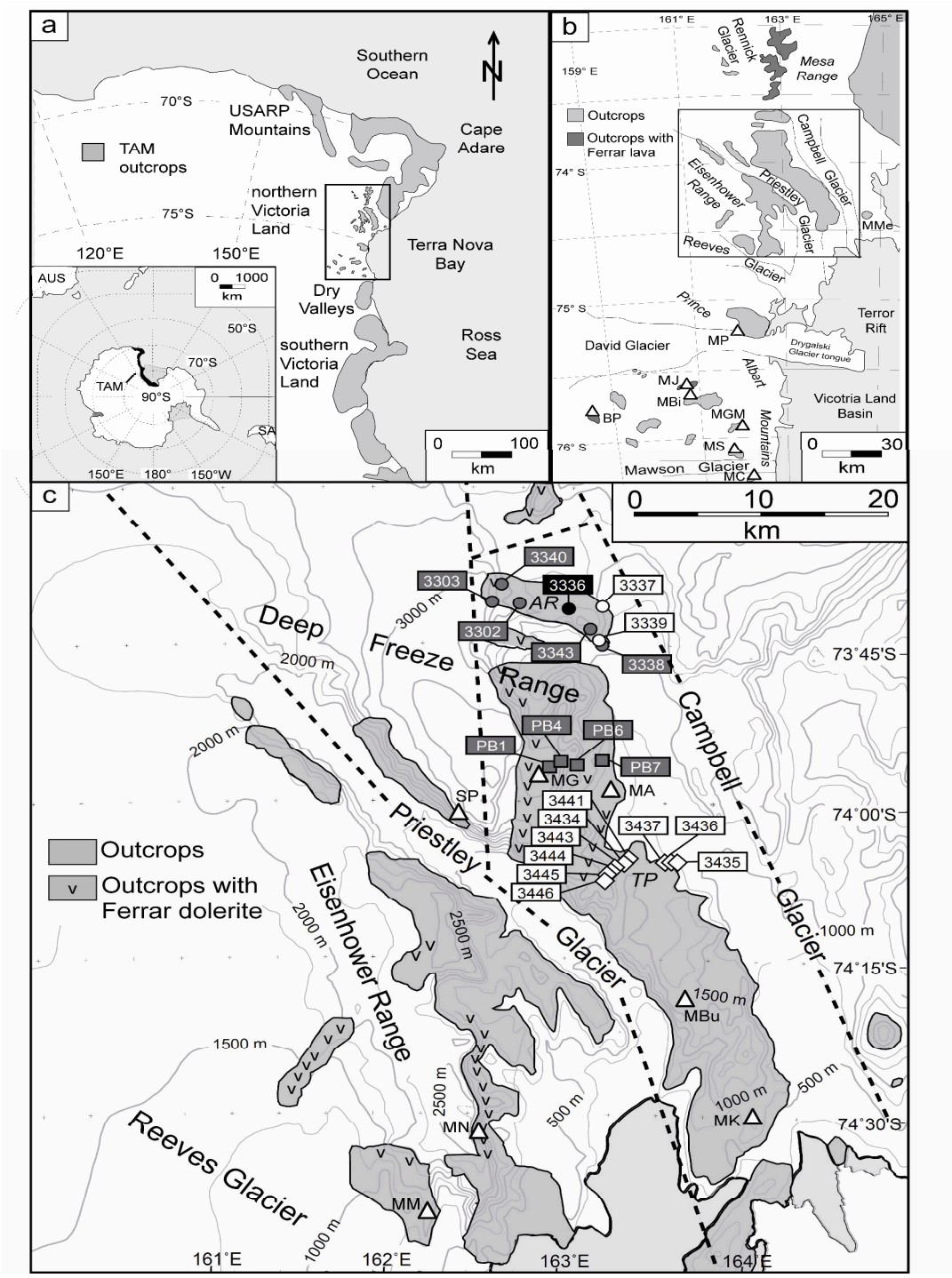

Figure M III-1: (a) Simplified map of the Ross Sea sector of the Transantarctic Mountains (TAM). The black box marks the Terra Nova Bay region. (b) Sketch map of the Terra Nova Bay region; BP: Brimstone Peak MBi: Mount Billing; MC: Mount Chetwynd; MGM: Mount George Murray; MJ: Mount Joyce; MMe: Mount Melbourne; MP: Mount Priestley; MS: Mount Smith. (c) Simplified map of Deep Freeze Range and Eisenhower Range; AR: Archambault Ridge; MA: Mount Adamson; MBu: Mount Burrows; MG: Mount Gibbs; MK: Mount Keinath; MM: Mount Matz; MN: Mount Nansen; SP: Shafer Peak; TP: Tourmaline Plateau. Locations of analyzed rocks are marked by circles (Archambault Ridge), squares (Mount Gibbs) and diamonds (Tourmaline Plateau). Grey symbol fillings: samples with apatite fission track and (U-Th-Sm)/He (AHe) data, empty symbols: fission track data only, black filling: only AHe data. Dashed black lines mark faults of Cenozoic right-lateral fault system (e.g., Rossetti et al., 2003; Storti et al., 2006, 2008).

First quantitative thermochronological studies of vertical basement profiles in the Eisenhower Range considering (near-) surface position of the basement during the Ferrar event indicated regional Mesozoic – Eocene burial related to sediment accumulation within a sedimentary basin (Prenzel et al., in review, 2013) that probably occupied large parts of the Ross Sea region (Lisker and Läufer, 2013). However, these studies evidenced basin existence on a very local scale and gain no insights on regional basin extension and geometry. Besides thermochronological investigations on a regional larger scale, reconstruction of basin architecture, formation and duration has to consider the regional geomorphological, structural and tectonic pattern. For example, the sedimentary basin has to be integrated in the geodynamic situation of the Ross Sea region comprising Mesozoic – Cenozoic rifting and crustal thinning in the West Antarctic Rift system, and Cenozoic right lateral strike-slip motion together with regional crustal extension in the western Ross Sea region (Salvini et al., 1997). Moreover, basin inversion needs to be considered in context with the origin, development and timing of the extensive glacial network shaping the present-day landscape (Baroni et al., 2005; Prenzel et al., in review). Consequently, burial reconstruction of the entire Terra Nova Bay region will reveal first important information about regional basin extension, geometry and local depths, and its formation and evolution in the context of geodynamic processes, and serves as case study for further Mesozoic – Eocene basin studies at supraregional scale.

For reconstructing the post-mid Jurassic geological evolution of the entire Terra Nova Bay region, we provide new AFT and AHe data from three vertical basement profiles along a horizontal transect in the Deep Freeze Range, and revert to published AFT data from vertical profiles in the southern Deep Freeze Range (Mount Burrows, Balestrieri et al., 1997) and in the Prince Albert Mountains (Mount Priestley, Mount George Murray; Storti et al., 2008) as well as the AFT and AHe data from the Eisenhower Range (Fig. M III-1; Prenzel et al., in review). The reconstruction of the burial and exhumation history relies on the application of thermal history modeling of the thermochronological data set. Paleotemperatures of the vertical sample arrays derived from the thermal history models allow to calculate geothermal gradients for Deep Freeze Range and Prince Albert Mountains. Subsequently, gradients in tandem with paleotemperatures allow elucidating regional burial evolution. Thereby, Mesozoic – Eocene burial reconstruction of the granitic basement has to consider the Ferrar rock emplacement, and a thickness of these rocks potentially much higher

than preserved (Prenzel et al., in review). The amount of burial derived for the Jurassic reveal the thickness of Ferrar rocks, while subsequent burial provides information about the amount of additional post-mid Jurassic sedimentary overburden. Collectively with the burial of the adjacent Eisenhower Range, this provides new insights on the basin architecture within the entire Terra Nova Bay region including potential regional differences of the basin depth. In addition, burial can be correlated with numerous independent Jurassic/Cretaceous temperature indications documented locally for various areas of the Terra Nova Bay region, and the Mesa Range north of it (Fig. M III-1; e.g., Molzahn et al., 1999). The quantification of Ferrar rock and post-mid Jurassic sediment thicknesses throughout the region allow concluding on the Jurassic paleorelief in the Terra Nova Bay region. Reconstruction of basin duration and extension linked with the regional geomorphological and structural pattern may provide conclusions on potential provenances of the sediments and their depositional environment, and probably details to the development of the previous *Transantarctic Basin* that occupied large parts of East Antarctica during Late Paleozoic and Early Mesozoic time (e.g., Collinson et al., 1994).

5.2) Geological setting

The onshore geology of the Terra Nova Bay region and the adjacent Mesa Range is relatively simple and uniform (Fig. M III-1). Basement consists of Late Proterozoic to Early Paleozoic metamorphic and magmatic rocks of the Granite Harbour Igneous complex emplaced or overprinted during the ~550 – 490 Ma Ross Orogeny (e.g., Goodge 2007; Goodge et al. 2012). Subsequently, the basement was eroded to a flat Peneplain (Kukri Peneplain) and occupied by a sedimentary foreland (sub-) basin that formed part of the large Devonian to Jurassic sedimentary Transantarctic Basin along the Palaeo-Pacific margin of Gondwana (e.g. Collinson et al., 1994). The Kukri Peneplain can be traced throughout large parts of the region. In the northern Terra Nova Bay region, the Kukri Peneplain gently dips between 3° and 5° from NE to SW with a corresponding elevation decline from Deep Freeze Range (2700 – 3100 m) to Eisenhower Range (2000 – 2700 m; e.g., Elsner, 2010). Both, dip and elevation of the Kukri Peneplain are lower in the Prince Albert Mountains (~1°, ~1250 m; e.g., Skinner and Ricker, 1968; Wörner, 1990) and the Mesa Range (~0° – 2°, 1000 – 1600 m; e.g., Elsner, 2010). The clastic infill of the Transantarctic Basin, collectively

defined as the Beacon Supergroup, was intruded or overlain by Ferrar magmatic rocks and sills emplaced at 182 Ma (e.g. Elliot and Fleming, 2008) which represent a predominantly volcanic sequence (e.g., Viereck-Götte et al., 2007; see section 1).
The thickness of Beacon and Ferrar rocks above basement varies throughout the region. In the Eisenhower Range, siliciclastic-volcaniclastic rocks with intercalated Ferrar sills are up to 500 m thick, while Ferrar lavas are entirely missing (e.g., Prenzel et al., in review). Similarly thick Beacon rocks and Ferrar sills which are partially overlain by a few to several ten meters thick Ferrar lava sequence, e.g. in the region at and south of Mount Adamson (Fig. M III-1), is documented for the Deep Freeze Range (Elliot and Fleming, 2008; Schöner et al., 2011). In the northern Prince Albert Mountains, Beacon rocks are almost absent and only preserved as rafts within Ferrar dolerites at/near the coast, or in form of few ten to hundred meters thick sequences of Late Triassic to Early Jurassic Beacon sandstones at the internal nunataks (e.g., Wörner, 1990; Bernet and Gaupp, 2005). The Ferrar dolerites form sills with a cumulative thickness of usually not more than 20 – 50 m near the coast such as present at the summit of Mount Smith in form of a dolerite capping (Fig. M III-1b; Skinner and Ricker, 1968) but reach a considerable higher cumulative thickness up to 800 – 1000 m in the internal western Prince Albert Mountains (Wörner et a., 1990). This region additionally preserves Ferrar lava flows with a thickness between a few meters at Mount Joyce and up to 700 m at Brimstone Peak (Fig. M III-1; Skinner and Ricker, 1968; Wörner, 1990). An equally high cumulative thickness of Beacon and Ferrar sills of up to 1000 m and Ferrar lava flows up to 750 m occurs in the Mesa Range (Fig. M III-1; e.g., Elliot and Fleming, 2008; Elliot, 1992).
Except for a roughly N-S elongated occurrence of Cenozoic magmatic rocks along the coast (e.g., LeMasurier and Thomson, 1990; Tonarini et al., 1997) and some local Pliocene sediments and glacial deposits (GANOVEX Team, 1987), the Jurassic Ferrar magmatic suite forms the regional youngest preserved unit. In spite of this large stratigraphic gap, independent thermal indications derived from Beacon sandstones and Ferrar flood basalts in several locations of Terra Nova Bay region and Mesa Range suggest Jurassic/Cretaceous temperatures of locally up to ~400°C (e.g., Molzahn et al., 1999; Ballance and Watters, 2002).

Offshore, the Terra Nova Bay region is characterized by the N-S elongated Victoria Land Basin that developed during Mesozoic opening of the Ross Sea, and the Terror Rift that originated within this basin as a result of Cenozoic right-lateral transtensional

tectonics (Fig. M III-1; e.g., Salvini et al., 1997; Storti et al., 2001). Victoria Land Basin and Terror Rift both roughly extend parallel to the coastal region of the Prince Albert Mountains from the area south of Priestley/Campbell Glacier to the Ross Ice Shelf. Seismic-reflection data across the Victoria Land Basin record sediment infillings of up to 12 km consisting presumably of Cretaceous – Neogene rift deposits with an Eocene – Oligocene seismic unconformity in the sedimentary rocks (Cooper et al., 1987; Brancolini et al., 1995) that is thought to separate Mesozoic from Cenozoic strata (Salvini et al., 1997).

The regional structural pattern is dominated by a NW-SE and N-S trending fault system that has been (i) originated during the Ross Orogeny due to collision of separate terranes along a convergent plate boundary (e.g., Stump, 1995), (ii) reactivated during Mesozoic deformation due to rifting between East and West Antarctica (e.g., Salvini and Storti, 1999), and (iii) overprinted by right-lateral strike slip motion and transtension during the Cenozoic (Salvini et al., 1997). Today, the Campbell, Priestley, Reeves and David Faults underlying same-named glaciers (Fig. M III-1) constitute a key feature of the regionally important Cenozoic right-lateral fault system (e.g., Rossetti et al., 2003; Storti et al., 2008 and refs. therein). These NW-SE striking faults are delimited to the N-S striking basin boundary fault system of the Victoria Land Basin and the central Ross Sea (Salvini et al., 1997). Structural investigations in the southern Terra Nova Bay region comprising two major N-S striking slip faults immediately south of the NW-SE striking fault system at the tip region of the Reeves Glacier point to transfer of the dextral shear from the NW-SE right-lateral striking slip fault system in northern Victoria Land into N-S ones along the western shoulder of the Ross Sea (cf. Storti et al., 2008).

Based on quantitative geomorphic parameters and morphometric analysis, Baroni et al. (2005) ascribed the glacial valley network in northern Victoria Land to fluvial origin that adapted to the N-S to NW-SE structures of the major regional fault system. The date of fluvial initiation and of first glacier development is considerably uncertain, but considering the main exhumation phase of the TAM at ~55 – 50 Ma (summarized by Fitzgerald, 2002) and the much-cited date of ~34 Ma for the change from fluvial to glacial erosion in Antarctica (e.g., Strand et al., 2003; Sudgen and Denton, 2004), fluvial erosion was supposed to have occurred from at least Early Eocene to Early Oligocene (Baroni et al., 2005). Minimum age for the initiation of a drainage system in the Terra Nova Bay region is given by the dissection of Cenozoic magmatic rocks

along regional glaciers (Baroni et al., 2005). The ages of these rocks range between 48 Ma and Quaternary in the coastal region at and north of Mount Melbourne and in the western Ross Sea, and between 38 and 29 Ma along the Priestley Fault (Fig. M III-1; Tonarini et al., 1997; Armienti and Baroni, 1999).

5.3) Thermochronological data

5.3.1) Apatite fission track data

AFT ages of twenty samples from Archambault Ridge, Mount Gibbs and Tourmaline Plateau range between 50.4±5.9 and 251.6±11.4 Ma (Table M III-1, Fig. M III-2), and thus considerably postdate the genetic age of the Granite Harbour Intrusives. Most ages predate the 182 Ma Ferrar Event. The AFT ages of all three profiles correlate with sample elevations between 1060 and 3120 m and show a similar change of the regression gradient at 75 – 85 Ma and ~2000 m. Mean track lengths (MTL) and associated standard deviations are 11.04±0.22 – 12.81±0.33 µm and 1.91 – 3.36 µm, respectively. Samples above the change of the regression gradient hold shorter MTL with longer standard deviations (11.04±0.22 – 11.83±0.55 µm/1.91 – 3.36 µm) than samples below (12.0±0.70 – 12.81±0.33 µm/1.78 – 2.69 µm).

The relation of AFT ages and MTL is characterized by a distinctive concave “boomerang” pattern as described by Green (1986) with shortest MTL for samples with intermediate ages, longer MTL for older samples and longest MTL for the youngest samples. This pattern is supported by skewed MTL distributions with bimodal track length distributions for the older samples and more narrow track length distribution for the younger samples (Fig. M III-2c). The samples mean fission track etch pit diameter parallel to the crystallographic c-axis (Dpar) used as indicator for fission track annealing kinetic properties (e.g., Donelick, 1993; Carlson et al., 1999) vary between 1.81 and 2.05 µm.

Sample	Lat. S Long.E	Elevation [m]	ξ	ρ_D [10^6cm^{-2}] (N_D)	ρ_S [10^6cm^{-2}] (N_S)	ρ_I [10^6cm^{-2}] (N_I)	P(χ^2) [%]	Dated grains [N]	AFT age [Ma] (predicted age)	MTL [µm] (n)	MTL c-axis [µm] (predicted MTL)	SD [µm]	SD c-axis [µm] (predicted SD)	Dpar mean [µm]	Wt mean age [Ma]	unc. AHe single age [Ma] (predicted age)	GOF AFT age/MTL AHe age	original age [Ma]
Archambault Ridge																		
3338	73.75 163.15	1590	320 ±10	14.5 (7360)	13.4 (168)	51.7 (652)	100	20	59.6±5.5 (63.2)	12.38±0.21 (100)	13.63 (13.52)	2.06	1.50 (1.72)	1.83	58.2±6.9	39.3±4.0 (21.8)	0.54/0.10 0.00	
3339	73.75 163.15	1740	320 ±10	14.5 (7360)	15.1 (160	54.7 (580)	100	20	63.7±6.0	12.43±0.51 (16)		2.04		1.84				
3337	73.69 163.16	2000	320 ±10	14.5 (7360)	31.6 (530)	96.1 (1615)	97	20	75.8±4.5 (76.7)	11.76±0.23 (105)	13.25 (13.49)	2.3	1.50 (1.64)	1.91			0..67/0.10	
3343	73.73 163.1	2310	320 ±10	14.5 (7360)	42.0 (866)	86.4 (1712)	93	20	112.7±5.9 (115)	11.3±0.24 (100)	12.96 (13.31)	2.36	1.50 (1.53)	1.92	104.7±12.3	63.4±5.0 (60.9)	0.68/0.861 0.63/0.05	
3302	73.69 162.74	2560	320 ±10	14.5 (7360)	38.3 (368)	54.9 (527)	98	20	160±12.0 (165)	11.04±0.22 (100)	12.71 (13.15)	2.17	1.40 (1.51)	1.89	133.4±15.9	134.8±10.0 (128.5)	0.52/0.72 0.56	
3336	73.69 162.99	2600	320 ±10												137.1±16.1			
3340	73.65 162.65	2690	320 ±10	14.5 (7360)	15.7 (190	21.7 (262)	100	20	166.7±16.7 (169)	11.05±0.87 (15)	13.04 (12.37)	3.36	21.0 (1.67)	1.92	30.0±3.4	18.8±2.0 (18.7)	0.59/0.74 0.58	
3303	73.68 162.6	2790	320 ±10	14.5 (7360)	16.9 (216)	19.9 (313)	100	20	194.4±17.3 (223)	11.35±0.88 (15)	12.84 (13.62)	2.19	1.66 (1.23)	1.91	112.8±13.5	82.7±5.2 (80.0)	0.96/0.94 0.00	
Mount Gibbs																		
PB7		1800	320 ±10	17.1 (8556)	30.1 (472)	101.2 (1589)	64	20	80.8±5.0 (89.4)	12.03±0.18 (100)	13.38 (13.40)	1.78	1.32 (1.60)	1.95	66.2±7.8	38.9±2.4 (32.6)	0.05/0.10 0.32	87±7
PB6		2470	320 ±10	20.8 (10402)	31.5 (865)	77.5 (2131)	17	20	134.3±7.0 (137)	11.35±0.22 (120)	12.75 (12.96)	2.46	1.74 (1.83)	2.05	110.1±14.0	110.1±6.8 (106.6)	0.55/0.63 0.80	111±10
PB4		3000	320 ±10	20.8 (10402)	43.2 (1454)	69.7 (2348)	42	20	205.2±9.9 (205)	11.26±0.22 (120)	12.76 (13.11)	2.43	1.54 (1.58)	2.01	130.9±16.5	99.5±6.2/97.1±6.0 (102.6/87.0)	0.99/0.87 0.64/0.05	208±19
PB1		3120	320 ±10	20.8 (10402)	42.4 (1565)	55.1 (2032)	57	20	251.6±11.4 (246)	11.5±0.23 (116)	12.92 (12.92)	2.45	1.60 (1.50)	2.05	181.8±21.8	121.8±7.5/134.5±8.3 (115.9/137.9)	0.69/0.82 0.88/0.34	270±24
Tourmaline Plateau																		
3435	74.09 163.57	1060	320 ±10	13.5 (13562)	6.1 (98)	25.9 (420)	100	20	50.4±5.9 (46.5)	12.53±0.38 (42)	13.75 (13.68)	2.47	1.67 (1.83)	1.87			0.75/0.99	
3436	74.09 163.57	1200	320 ±10	13.5 (13562)	9.1 (152)	38.2 (642)	100	20	51.1±4.9 (48.0)	12.81±0.33 (101)	14.11 (13.70)	2.21	1.46 (1.73)	1.93			0.88/0.94	
3437	74.09 163.56	1380	320 ±10	13.6 (13562)	4.9 (148)	17.6 (531)	100	20	60.2±5.9 (57.2)	12.29±0.26 (104)	13.83 (13.72)	2.61	1.53 (1.74)	1.88			0.95/0.65	
3434	74.1 163.33	1570	320 ±10	13.6 (13562)	4.5 (107)	14.5 (342)	100	20	67.6±7.8 (67.0)	12.03±0.24 (97)	13.45 (13.60)	2.38	1.55 (1.68)	1.92			0.50/0.08	
3441	74.1 163.32	1640	320 ±10	13.6 (13562)	8.6 (193)	27.7 (620)	95	20	67.6±5.8	12.0±0.7 (12)		2.41		1.85				
3443	74.11 163.28	1830	320 ±10	13.6 (13562)	9.7 (149)	27.5 (424)	100	20	76±7.6 (80.2)	12.12±0.25 (99)	13.60 (13.47)	2.51	1.52 (1.64)	1.91			0.52/0.52	
3444	74.11 163.27	1950	320 ±10	13.6 (13562)	6.8 (106)	18.8 (291)	100	20	78.8±9.3 (84.6)	12.01±0.21 (101)	13.44 (13.64)	2.14	1.46 (1.60)	1.89			0.87/0.51	
3445	74.12 163.23	2040	320 ±10	13.7 (13562)	17.7 (256)	44.8 (650)	100	20	85.6±6.8	11.83±0.55 (12)		1.91		1.89				
3446	74.12 163.22	2215	320 ±10	13.7 (13562)	11.8 (99)	25.4 (213)	100	15	101.2±12.7	(3)				1.81				
Mount Burrows																		
PB-10	74.3 163.65	900								14.15± (117)	14.75±0.13 (1: 14.39) (2: 14.95)	1.46	1.05 (1: 1.82) (2: 1.14)	1.84			2: 0.53/0.77 1: 0.50/0.50	45.1±4.2 (1: 41.8) (2: 41.3)
PB8	74.3 163.65	1350								14.21±0. (50)	14.86±0.24 (1: 14.23) (2: 15.07)	1.68	1.25 (1: 2.12) (2 :0.98)	1.93			2: 0.86/0.50 1: 0.73/0.58	45.2±3.4 (1: 44.5) (2: 43.5)
PB-1b	74.3 163.65	2250								14.32± (42)	14.77±0.02 (1: 14.19) (2: 15.11)	1.03	0.91 (1: 2.16) (2: 0.86)	1.44			2: 0.75/0.52 1: 0.57/0.52	47.9±3.5 (1: 46.0) (2: 44.8)

Table M III-1: Apatite fission track (AFT) and (U-Th-Sm)/He data (AHe). Twenty-four basement samples from the Granite Harbour Igneous complex covering elevations between 900 m and 3120 m were collected in the Deep Freeze Range area at Archambault Ridge, Mount Burrows, Mount Gibbs and the Tourmaline Plateau during the ItalAntartide expeditions 1985 – 93 and GANOVEX IX (Fig. M III-1). The samples from Mount Burrows and Mount Gibbs have been already dated earlier by Balestrieri et al. (1997) via population method (PM). For the purpose of thermal history modeling, we here provide samples re-analyzed with the external detector method (EDM) for Mount Gibbs, and lengths and Dpar measurements for Mount Burrows (see Balestrieri et al. [1997] for detailed sample information). AFT ages were determined by counting spontaneous and induced fission tracks according to the Zeta calibration method (Hurford and Green, 1982, 1983; Green 1985) for the dosimeter glass CN5, and calculated using the Trackkey program (Dunkl, 2006). The Zeta value is quoted as ±1σ (Green, 1981). If possible, 100 fission track lengths for each sample were measured following the recommendations of Laslett et al. (1982). We measured the fission track etch pit diameter parallel to the crystallographic c-axis (Dpar) for all investigated grains to include an indicator for fission track annealing kinetic properties (e.g. Donelick, 1993; Carlson et al., 1999), quoting here the mean Dpar of each sample. Corresponding AHe central ages are shown if existent. The goodness of fit (GOF) between measured and predicted apatite fission track ages, fission track lengths, and (U-Th-Sm)/He single grain is quoted for the HeFTy c-axis projected forward models (see also Table M III-2 and Fig. M III-5). The GOF of the AFT age data were determined for each sample using the annealing model of Ketcham et al. (2007) and the GOF of the AFT length data is quoted using the Kuiper's Statistic method. A default initial track length of 15.99 µm and a length reduction of 0.892 µm were measured in Durango standard. AHe single grain ages are quoted using the radiation damage model of Flowers et al. (2009).

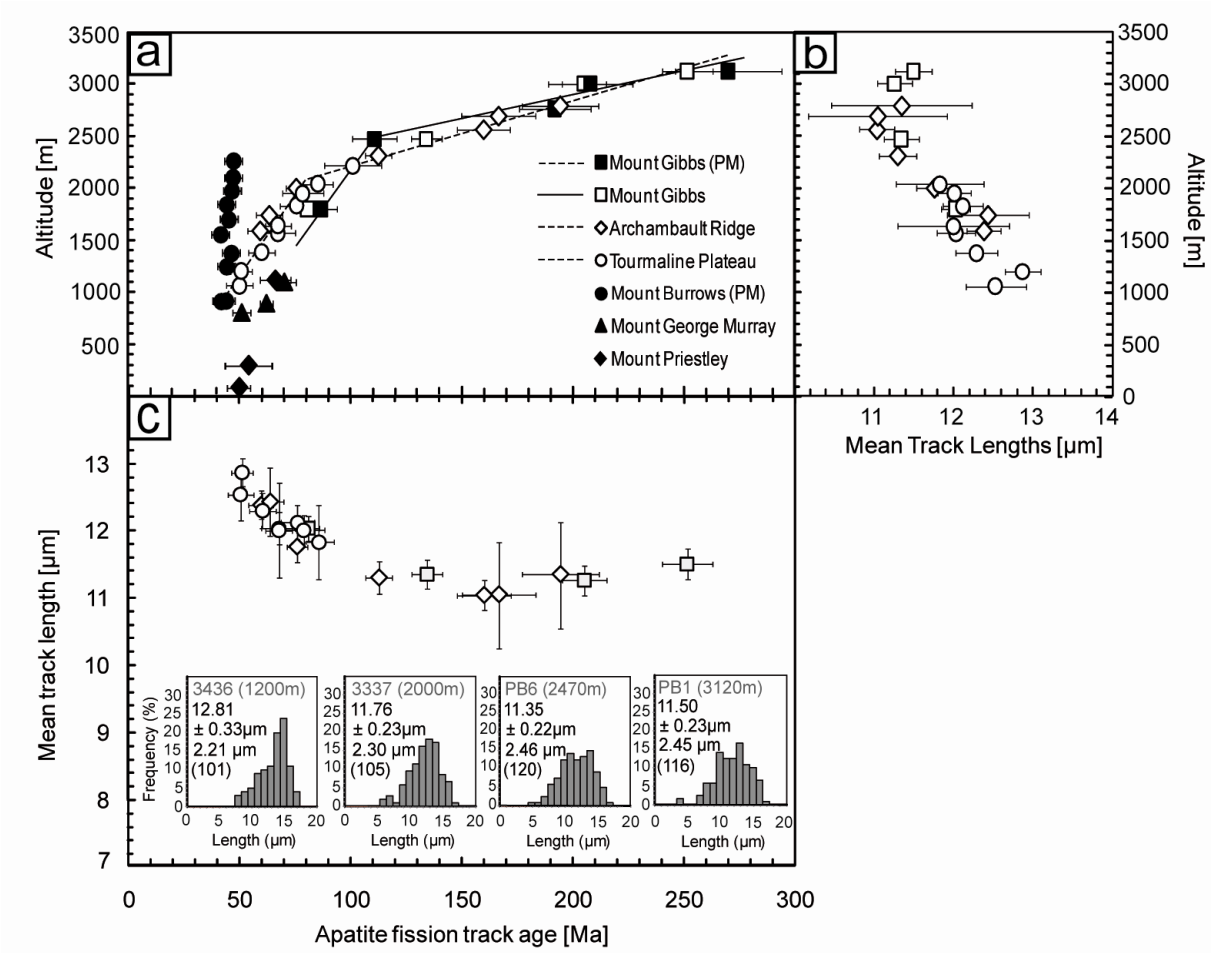

Figure M III-2: Apatite fission track (AFT) ages vs. sample elevation of new (white symbols) and published (black symbols) samples from the Terra Nova Bay region (a), mean track length (MTL) vs. sample elevation (b), and MTL vs. AFT age of the new sample sets (c). Track lengths distributions of four representative samples are shown as inset within (c). Errors are quoted as ±1σ. The ages of three re-dated samples from Mount Gibbs reproduce (within ±1σ) the ages previously dated via population method (PM), while the new age of sample PB6 from 2470 m relocates the offset in the regression from ~100 Ma (Balestrieri et al., 1994) to ~80 Ma (see also table M III-1).

5.3.2) Apatite (U-Th-Sm)/He data

Thirty-six AHe single grain analyses were conducted on four samples from Mount Gibbs and six samples from Archambault Ridge (Table M III-2, Figs. M III-1, 3). Depending on apatite yield and quality, two to seven apatite grains have been analyzed per sample. Single grain ages range between 27.7±3.3 and 273.5±17.0 Ma, and are usually younger than the corresponding AFT age (Fig. M III-3). Samples from Mount Gibbs generally show stronger intra-sample age dispersion than samples from Archambault Ridge. Excluding single grain age outlier, we calculated mean, weighted mean and central ages of the samples (Table M III-2). These average ages are quite consistent for the individual samples and we use samples weighted mean ages in the following.

Sample	Elev. [m]	Length [µm]	Width [µm]	Sp.radius [µm]	Mass [µg]	4He [ncc]	eU [ppm]	Total Sm [ppm]	Total Th [ppm]	Total U [ppm]	Uncorr. age [Ma]	FT corr.	Corr. age [Ma]	2σ error [Ma]	AFT age [Ma]
Mount Gibbs															
PB7-a #	1800	115	64	41	0.80	0.37	96.72	118.43	91.09	74.40	38.88	0.60	64.51	7.59	77.1±4.7
PB7-b	1800	120	64	41	1.25	0.40	61.98	62.08	14.90	57.91	42.71	0.63	67.99	8.00	77.1±4.7
Mean													66.25	7.80	77.1±4.7
Wt mean													66.16	7.78	77.1±4.7
PB6-a	2470	182	89	58	2.52	1.56	64.65	96.61	41.96	53.95	78.68	0.72	109.28	12.86	134.3±7.0
PB6-b	2470	182	67	81	5.10	6.41	87.99	140.02	48.57	75.32	117.02	0.80	146.09	17.19	134.3±7.0
PB6-c	2470	160	85	55	2.90	1.33	44.40	57.31	16.19	40.07	84.85	0.72	118.04	13.89	134.3±7.0
PB6-d	2470	151	81	55	1.94	0.57	38.14	71.76	17.36	33.39	62.85	0.71	88.74	10.44	134.3±7.0
PB6-e	2470	189	91	60	2.74	1.62	56.65	91.76	20.45	50.99	85.59	0.73	117.73	13.85	134.3±7.0
PB6-f(A)#	2470	71	66	38	0.48	0.37	58.37	69.92	23.98	52.11	110.08		110.08	6.83	134.3±7.0
Mean													114.99	12.51	
Wt mean													110.13	13.98	
Central													115.40	14.04	
PB4-a	3000	91	77	45	0.80	0.10	19.33	97.67	22.31	13.18	54.24	0.64	84.69	9.97	205.2±9.9
PB4-b #	3000	167	82	53	1.97	1.36	56.95	129.84	31.76	48.29	99.53	0.70	143.01	16.83	205.2±9.9
PB4-c	3000	150	65	43	1.14	0.40	28.92	57.98	23.83	22.81	99.85	0.62	160.38	18.87	205.2±9.9
PB4-d #	3000	228	103	63	4.97	2.03	34.64	69.38	28.37	27.36	97.09	0.74	130.58	15.36	205.2±9.9
PB4-e (A)	3000	80	75	42	0.69	0.971	68.27	125.38	42.76	57.09	167.75		167.75	10.40	205.2±9.9
Mean													137.28	15.37	
Wt mean													130.89	16.51	
Central													136.93	14.26	
PB1-a #	3120	214	96	63	4.97	3.47	42.52	70.42	12.04	39.02	134.50	0.76	177.24	20.85	251.6±11.4
PB1-b	3120	154	121	64	4.65	1.29	21.38	51.33	7.16	19.20	107.03	0.76	141.46	16.64	251.6±11.4
PB1-c	3120	200	86	53	3.07	4.62	72.29	77.04	14.42	68.17	170.01	0.70	243.18	28.61	251.6±11.4
PB1-d #	3120	176	70	46	1.56	1.10	47.57	70.58	16.20	43.10	121.83	0.65	186.72	21.97	251.6±11.4
PB1-e (A)	3120	79	75	43	0.71	1.18	95.22	99.97	80.54	75.54	142.54		142.54	8.84	251.6±11.4
PB1-f (A)	3120	88	86	49	1.06	2.22	61.69	80.38	12.20	58.06	273.49		273.48	16.96	251.6±11.4
PB1-g (A)	3120	71	65	38	0.47	1.18	54.04	62.70	19.54	48.88	236.47		236.47	14.66	251.6±11.4
Mean													200.16	18.36	
Wt mean													181.79	21.75	
Central													211.46	26.89	
Archambault Ridge															
3338-a #	1590	152	109	66	4.51	0.72	30.68	65.67	22.42	24.83	42.85	0.76	56.23	6.62	59.6±5.5
3338-b #	1590	91	77	45	1.35	0.31	48.70	26.92	8.77	46.39	39.29	0.65	60.42	7.11	59.6±5.5
Mean													58.32	6.86	
Wt mean													58.17	6.88	
3343-a #	2300	91	67	40	0.63	0.64	99.25	44.85	11.05	96.23	63.36	0.60	104.78	12.33	112.7±5.9
3343-b #	2300	119	83	50	1.31	0.82	72.09	44.80	8.26	69.73	71.67	0.68	104.69	12.32	112.7±5.9
3343-c*	2300	249	77	49	3.08	4.41	115.0	44.38	11.40	111.90	102.24	0.68	150.37	17.69	112.7±5.9
Mean													104.73	12.32	
Wt mean													104.73	12.32	
3302-a X	2560	109	73	41	1.21	0.70	37.59	38.72	5.70	35.88	126.57	0.62	205.79	24.21	160.0±12.0
3302-b X	2560	89	66	36	0.80	0.59	48.18	38.59	13.35	44.69	125.33	0.56	223.18	26.26	160.0±12.0
3302-c X	2560	99	76	41	1.17	0.61	31.53	33.67	9.53	28.98	135.33	0.62	219.91	25.87	160.0±12.0
3302-d (A)*	2560	50	47	31	0.18	0.07	56.75	49.80	140.54	23.65	53.31		53.31	3.31	160.0±12.0
3302-e (A) #	2560	72	65	38	0.46	0.14	18.57	31.90	11.40	15.61	134.77		134.77	8.36	160.0±12.0
Mean											130.50	15.8			
Wt mean											133.35	15.9			
3336-a	2600	108	75	45	0.97	0.54	50.30	44.90	11.21	47.25	90.17	0.65	138.58	16.31	
3336-b	2600	120	70	41	1.22	0.49	39.66	39.43	12.18	36.44	82.63	0.61	135.56	15.95	
Mean													137.07	16.13	
Wt mean													137.04	16.13	
3340-a #	2690	120	72	42	1.31	0.08	25.76	42.49	30.71	18.21	18.80	0.62	30.51	3.59	166.7±16.7
3340-b #	2690	95	70	42	0.73	0.07	45.08	44.08	45.68	34.04	17.15	0.62	27.71	3.26	166.7±16.7
Mean													29.11	3.43	
Wt mean													28.98	3.44	

Table continued

Sample	Elev. [m]	Length [µm]	Width [µm]	Sp.radius [µm]	Mass [µg]	4He [ncc]	eU [ppm]	Total Sm [ppm]	Total Th [ppm]	Total U [ppm]	Uncorr. age [Ma]	FT corr.	Corr. age [Ma]	2σ error [Ma]	AFT age [Ma]
3303-a	2800	112	80	44	1.47	0.11	8.67	29.53	17.85	4.24	67.43	0.63	106.76	12.56	194.4±17.3
3303-b #	2800	120	87	53	1.42	0.21	14.78	34.46	33.90	6.57	82.73	0.69	120.48	14.18	194.4±17.3
Mean													113.62	13.37	
Wt mean													112.79	13.47	

Table M III-2: (U-Th-Sm)/He (AHe) single grain data. For apatite selection we followed the recommendations for an ideal apatite crystal (euhedral form, no inclusions, grain diameter > 60 µm), and applied mechanical abrasion for apatites with grain diameter >100 µm. Due to a sparse amount of adequate apatite crystals, we only analyzed two grains for most of the samples. Applying the ^{4}He intergrowth equation (e.g. described in Farley, 2002), the AHe age of each apatite grain was determined separately by using the raw data of ^{4}He, ^{238}U, ^{232}Th and ^{147}Sm nuclides and the measured dimensions of the crystal considering the alpha correction for AHe dating (Farley et al., 1996). The table shows dimension, mass, raw data (^{4}He, effective U, ^{238}U, ^{232}Th, ^{147}Sm), FT correction factor, uncorrected and FT-corrected age of each analyzed apatite single grain. Single grains with "A" in brackets of the grain label mark mechanical abraded grains. The error of each single grain is quoted as 2σ. The mean, weighted mean (Wt) and central age of each sample were calculated after single grain outlier marked with "*" have been excluded. To identify single grain age outlier from the observed data, we used the statistical criterion of Chauvenet (Long and Rippeteau, 1974). Single grain ages with "#" have been used for HeFTy modeling. The corresponding apatite fission track age of each sample is shown for comparison. Note that sample 3336 and 3302 were collected at similar elevations. Given that the corrected single grain ages of sample 3336 are consistent with the uncorrected and abraded single grain ages of sample 3302 (Table M III-2), implantation of ^{4}He atoms from a surrounding U-Th-rich host or matrix (Spiegel et al., 2009) can be inferred for sample 3302. In the case of sample 3302, grains marked with "x" are assumed to have been affected by ^{4}He implantation, and we thus used the uncorrected ages of these grains for the calculation of the average ages.

Archambault Ridge: Six out of nine samples from the Archambault Ridge produced single grain AHe ages between 27.7±3.4 and 138.6±16.3 Ma (Table M III-2; Fig. M III-3). The single grain ages of each sample replicate within error (±1σ) and result in weighted mean ages between 29.0±3.4 and 137.0±16.1 Ma. These are all younger than the corresponding AFT age and correlate with elevation. The single effective U concentration of the grains varies between 9 and 115 ppm. Correlation between effective U concentration and single grain ages is problematic due to the small number of analyzed grains per sample (see supplementary material M III-1).

Mount Gibbs: Single grain ages of the four samples from Mount Gibbs range between 64.5±7.6 and 273.5±16.7 Ma and, with exception of sample PB7, show considerable dispersion (Table M III-2, Fig. M III-3). Weighted mean ages between 66.2±7.8 and 181.8±21.8 Ma are all younger than the corresponding AFT ages and correlate with elevation. The single grains effective U concentration varies between 19 and 97 ppm and correlate with grain ages (Table M III-2, supplementary material M III-1; cf. Shuster et al., 2006).

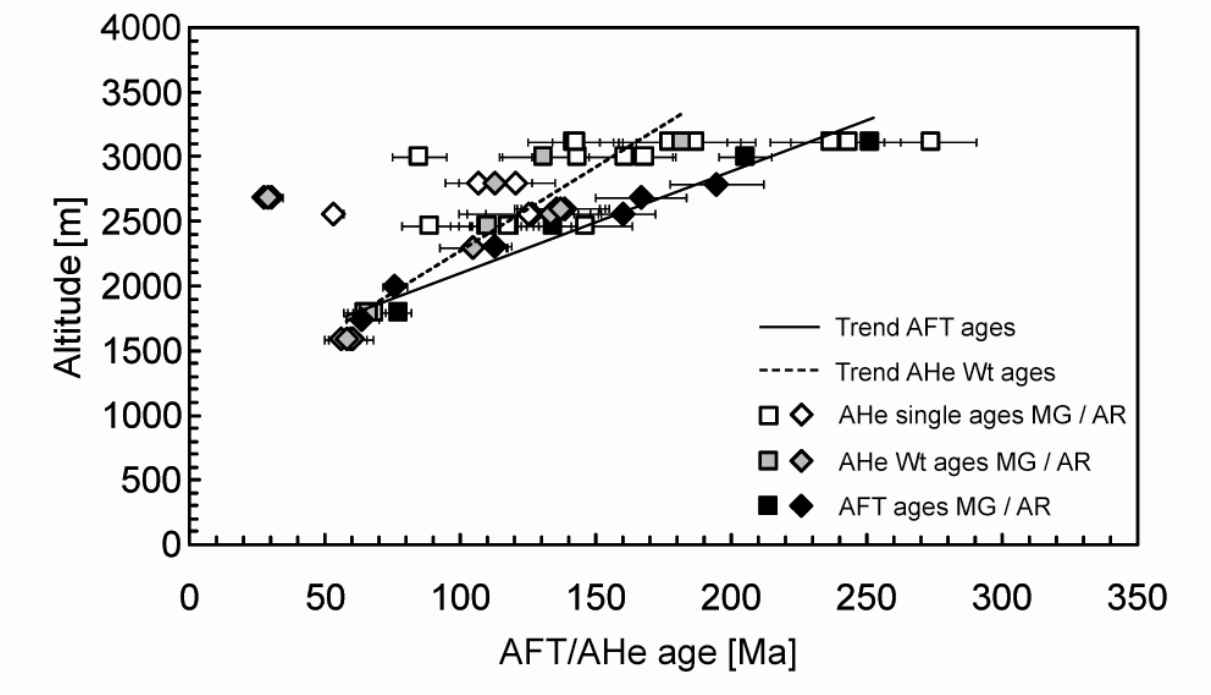

Figure M III-3: Plots of (U-Th-Sm)/He (AHe) single grain ages, AHe weighted (Wt) ages and apatite fission track (AFT) ages from Archambault Ridge (AR) and Mount Gibbs (MG) vs. elevation. Black lines mark the trend of AFT (consistent line) and AHe Wt ages (dotted line).

5.4) Thermal history modeling

Thermal history modeling of the AFT data (age, lengths, Dpar) and AHe data (Tables M III-1, 2) was performed with HeFTy and QTQt programs (Ketcham, 2005; Gallagher et al., 2005; Gallagher, 2012). HeFTy generates inverse and forward thermal history models for each sample individually while QTQt is used to model the thermal history of sample sets from vertical profiles. We modeled all samples with at least 40 measured confined tracks or the availability of both AFT and AHe ages, which accounts for 16 samples (see appendix for modeling procedure and constraints).

The uniform age-elevation pattern of all three vertical profiles from the *Deep Freeze Range* allows to model one common thermal history for the whole range. HeFTy inverse modeling produces very similar time – temperature paths for all samples comprising long-lasting Mesozoic heating subsequent to the Ferrar event, and Paleogene cooling (Fig. M III-4). An exception constitutes sample 3340 from the Archambault Ridge that additionally requires short Eocene/Oligocene heating in the order of 100°C to account for both AFT and AHe data.

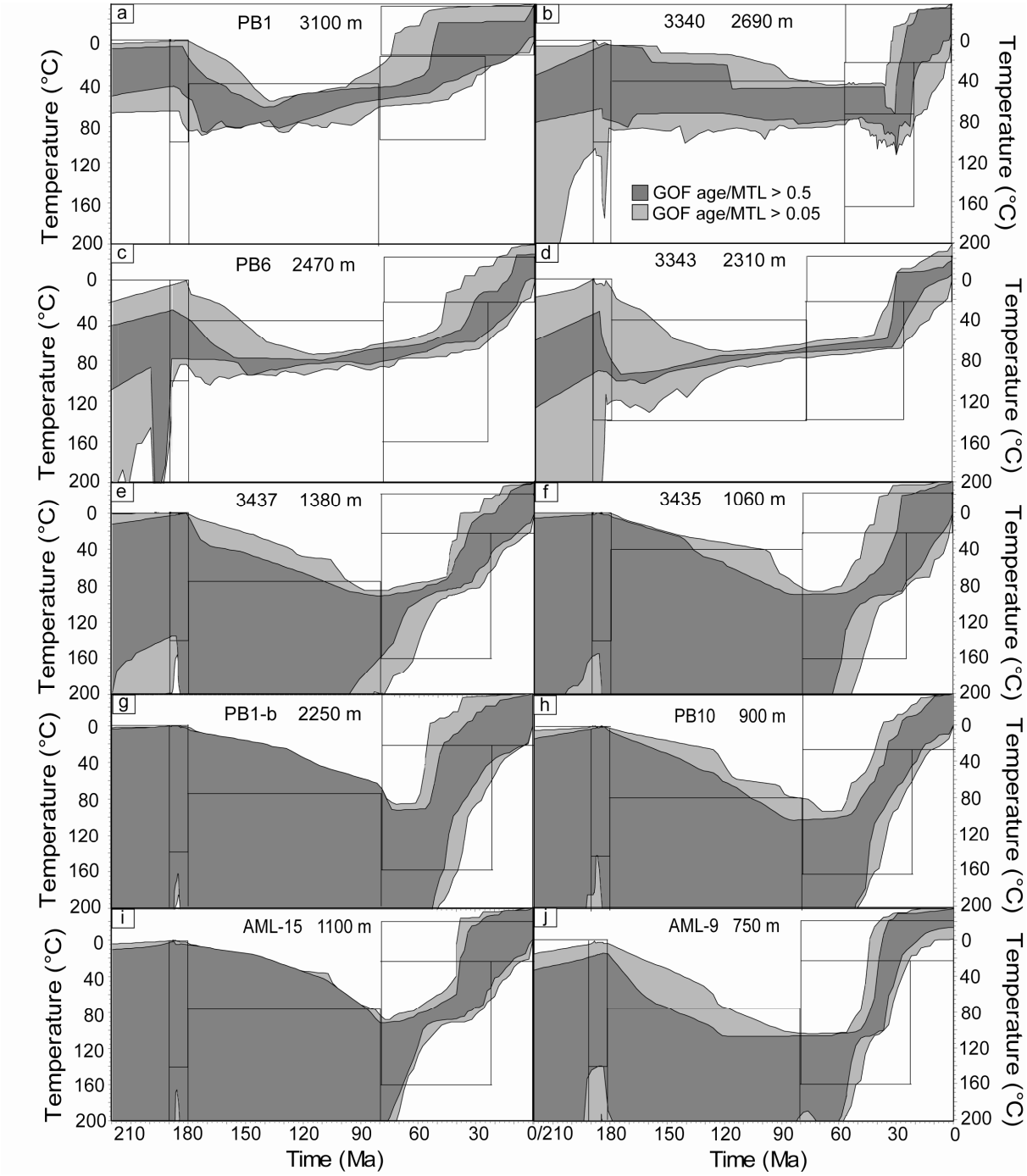

Figure M III-4: Inverse modeling results of representative samples from Deep Freeze Range (a-f), Mount Burrows (g,h), and Prince Albert Mountains (i,j; HeFTy, Ketcham, 2005). Black boxes mark the time-temperature constraints of HeFTy modeling (see appendix for detailed description). HeFTy was performed for all applicable samples using the Monte Carlo search method and a minimum of 100,000 randomly produced t-T-paths. The goodness of fit (GOF) of the AFT age data were determined for each sample using the annealing model of Ketcham et al. (2007) and c-axis projection; the GOF of the AFT length data is quoted using the Kuiper's Statistic method. A default initial track length of 15.99 µm and a length reduction of 0.892 µm were measured in Durango standard.

The common thermal history forward model for the complete sample set comprises (I) near surface temperatures during Late Triassic and Early Jurassic, (II) temperature increase of up to ~80°C for basement top during the mid- and Late Jurassic followed by (III) a temperature decrease until (IV) rapid Late Eocene/Early Oligocene cooling; and (V) minor temperature decrease since Late Eocene until (VI) rapid cooling to the present-day mean surface temperature since the Miocene (Fig. M III-5). Stagnating cooling between Early Oligocene and Early Miocene optimizes the fit between measured and predicted data especially of the samples from lower basement sections.

The QTQt thermal history model generally resembles the HeFTy one, with some minor variation (Fig. M III-5). HeFTy predicts fast cooling intermitted by a period of slow cooling in Oligocene times, while the QTQt model prefers slower but consistent sample cooling. The QTQt model additionally suggests a short period of reheating of ~100°C at ~85 Ma. The differences between HeFTy and QTQt models can be related to the missing Sm component of the apatites and the non-negative present-day temperature set for QTQt modeling. Thus, the thermal history of the HeFTy approach appears more solid and is used for further discussion.

Potential analogous Mesozoic – Eocene heating of the Jurassic surface of the more southern *Deep Freeze Range* can be examined by thermal history modeling of published AFT data from *Mount Burrows* in the southern part of the range (Fig. M III-1; Balestrieri et al., 1997). Correspondent ages of ten samples between 42.3±3.0 and 47.9±3.5 Ma that define a steep slope with elevations of 900 – 2260 m (Fig. M III-2) have been determined with the AFT population method which ignores potential single grain age variation within one sample (e.g. Naeser et al., 1989). However, expecting only minor single grain age deviation for magmatic samples with such steep age-elevation regression (e.g., O'Sullivan and Parish, 1995; Prenzel et al., 2013), samples central ages can be used for thermal history modeling. Since the published fission track length data contain numerous TINCLEs (track-in-cleavage) which are considered to be longer as the true length (Barbarand et al., 2003a), we performed new lengths measurements of an adequate number of TINTs (track-in-track). New samples' MTL and standard deviations of three representative samples from different elevations marginally vary between 14.15±0.23 and 14.32±0.23 µm, and 1.03 and 1.68 µm, respectively (Table M III-1).

HeFTy inverse modeling of these three samples resemble the thermal histories of the main *Deep Freeze Range* but show more intensive heating prior to onset of rapid Paleogene cooling (Fig. M III-4). The highest sample from *Mount Burrows* requires heating of at least 30°C higher than approximately equal high samples from the Archambault Ridge and the Tourmaline Plateau. In comparison to main *Deep Freeze Range*, common thermal history forward model for *Mount Burrows* needs either considerable higher Mesozoic heating and earlier onset of rapid cooling at ~45 Ma (model 1), or equal high Mesozoic – Eocene heating that includes a Late Eocene short-term heat pulse of ~110°C before onset of rapid cooling at ~35 Ma (model 2; Fig. M III-5). Thermal history model 2 is favoured because of its conformity to the Jurassic to mid-Eocene thermal history and Late Eocene cooling of main *Deep Freeze Range*. This is supported by the documented Late Eocene heat pulse of the one sample from the Archambault Ridge (Fig. M III-4b).

The thermal history reconstruction of the *Prince Albert Mountains* relies on AFT data of six samples from profiles at Mount Priestley and Mount George Murray published by Storti et al. (2008). Corresponding sample ages between 50±5 and 71±5 Ma correlate with sample elevations of 100 – 1100 m (Fig. M III-2) and MTL/standard deviations of 12.16±0.33 – 14.25±0.23 µm/3.30 – 1.95 µm (see supplementary material M III-2). The highest sample from Mount Priestley and all three samples from Mount George Murray contain sufficient fission track lengths for thermal history modeling. For these samples, we additionally measured Dpars which vary between 2.0 and 2.5 µm (see supplementary material M III-2).

HeFTy inverse modeling of all four samples resembles the thermal histories of the *Deep Freeze Range* while the common thermal history forward model shows minor differences for the final cooling stage(s) (Figs. M III-4, 5). These consist of insignificantly earlier onset of Late Eocene/Early Oligocene cooling and subsequent faster ongoing Oligocene – Miocene sample cooling. The best-fit common forward model favors rapid cooling between 38 Ma and 33 Ma with subsequent ongoing cooling until sample surface exposure at ~18 Ma. QTQt modeling reproduces the HeFTy thermal history within given temperature resolution.

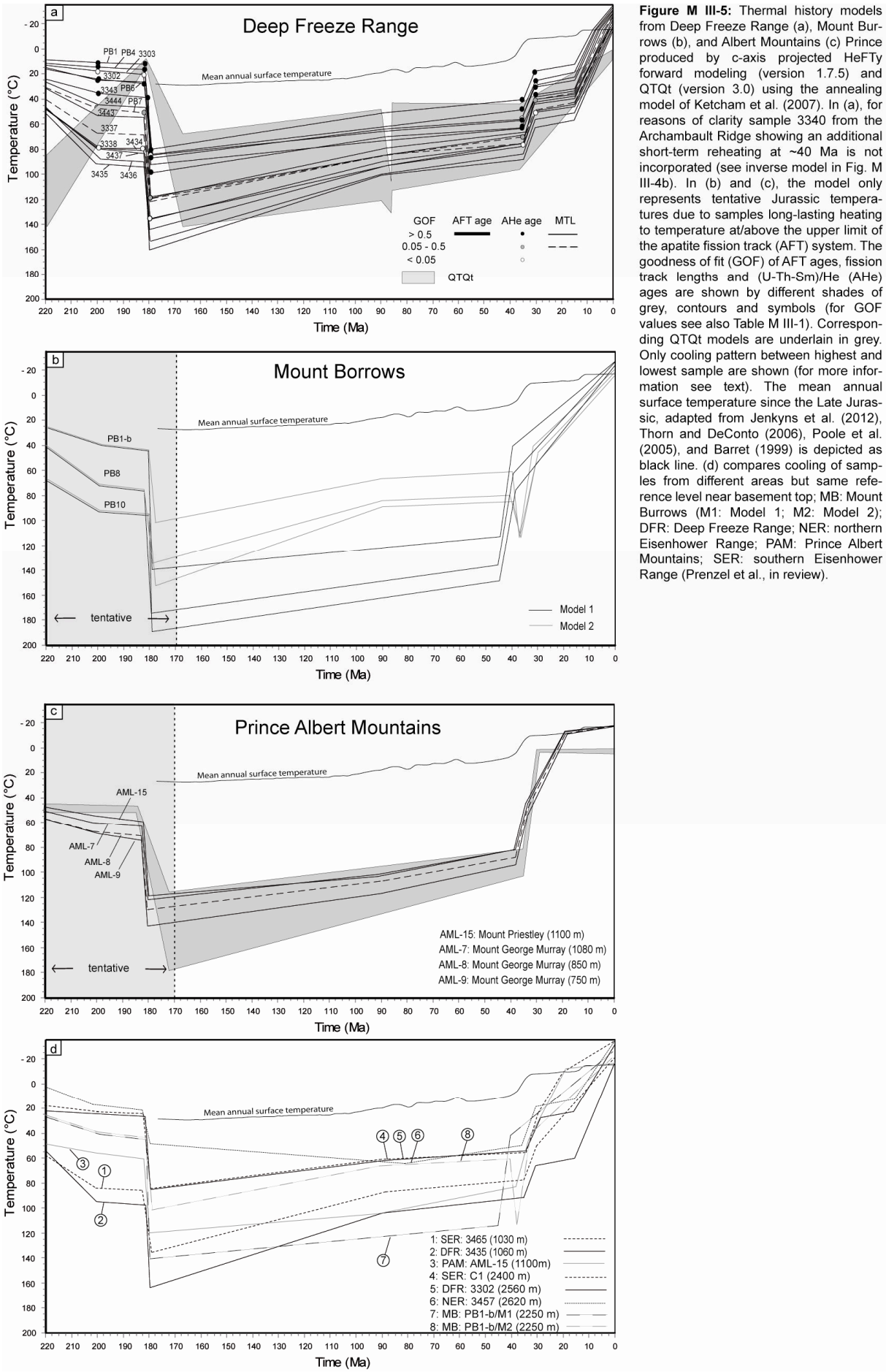

Figure M III-5: Thermal history models from Deep Freeze Range (a), Mount Burrows (b), and Albert Mountains (c) Prince produced by c-axis projected HeFTy forward modeling (version 1.7.5) and QTQt (version 3.0) using the annealing model of Ketcham et al. (2007). In (a), for reasons of clarity sample 3340 from the Archambault Ridge showing an additional short-term reheating at ~40 Ma is not incorporated (see inverse model in Fig. M III-4b). In (b) and (c), the model only represents tentative Jurassic temperatures due to samples long-lasting heating to temperature at/above the upper limit of the apatite fission track (AFT) system. The goodness of fit (GOF) of AFT ages, fission track lengths and (U-Th-Sm)/He (AHe) ages are shown by different shades of grey, contours and symbols (for GOF values see also Table M III-1). Corresponding QTQt models are underlain in grey. Only cooling pattern between highest and lowest sample are shown (for more information see text). The mean annual surface temperature since the Late Jurassic, adapted from Jenkyns et al. (2012), Thorn and DeConto (2006), Poole et al. (2005), and Barret (1999) is depicted as black line. (d) compares cooling of samples from different areas but same reference level near basement top; MB: Mount Burrows (M1: Model 1; M2: Model 2); DFR: Deep Freeze Range; NER: northern Eisenhower Range; PAM: Prince Albert Mountains; SER: southern Eisenhower Range (Prenzel et al., in review).

The thermal history patterns of *Deep Freeze Range* and *Prince Albert Mountains* and of the adjacent *Eisenhower Range* (Prenzel et al., in review) commonly comprise Jurassic to Eocene (re-) heating to maximal temperatures at ~180 Ma and accelerated cooling commencing at Late Eocene. Final cooling of the *Deep Freeze Range* including Oligocene stagnation and rapid Miocene cooling coincides with that of the northern *Eisenhower Range*, while the final cooling pattern of *Prince Albert Mountains* agrees with that of southern *Eisenhower Range* with basement tops cooling to surface temperatures at Early Miocene.

5.5) Geological evolution of Deep Freeze Range and Prince Albert Mountains

5.5.1) Paleogeothermal gradient

Paleogeothermal gradients can be calculated from modeled paleotemperature estimates versus sample elevations (Table M III-1; Figs. M III-5, 6; e.g., Bray et al., 1992; Prenzel et al., 2013).

A Jurassic geothermal gradient of 46±15°C/km of the Deep Freeze Range relies on the regression of ten maximal paleotemperatures between 75° and 119°C at 180 Ma from sample elevations of 1800 – 3120 m. This gradient is identical with the coeval gradient of ~45°C/km from the Eisenhower Range (Prenzel et al., in review). Systematic decline of the temperature difference of the individual samples between 180 and 80 Ma reduces the geothermal gradient that then remains stable until at least Late Eocene when samples cool below ~40°C. A Cretaceous – Eocene geothermal gradient of 24±7°C/km for the Deep Freeze Range relies on 15 paleotemperatures of 41° – 90°C at 35 Ma against sample elevations between 1060 and 3120 m. A coeval gradient in the order of ~26°C/km was calculated analogously for the Prince Albert Mountains (82° – 91°C/750 – 1060 m).

Both Cretaceous – Eocene gradients agree with Cretaceous geothermal gradients of 25° – 30°C/km from the Eisenhower Range (Prenzel et al., in review) and ~25°C/km from northern TAM and USARP Mountains (Fitzgerald, 1994; Lisker et al., 2006). The high Jurassic geothermal gradient probably reflects heatflow increase induced by Ferrar magmatism.

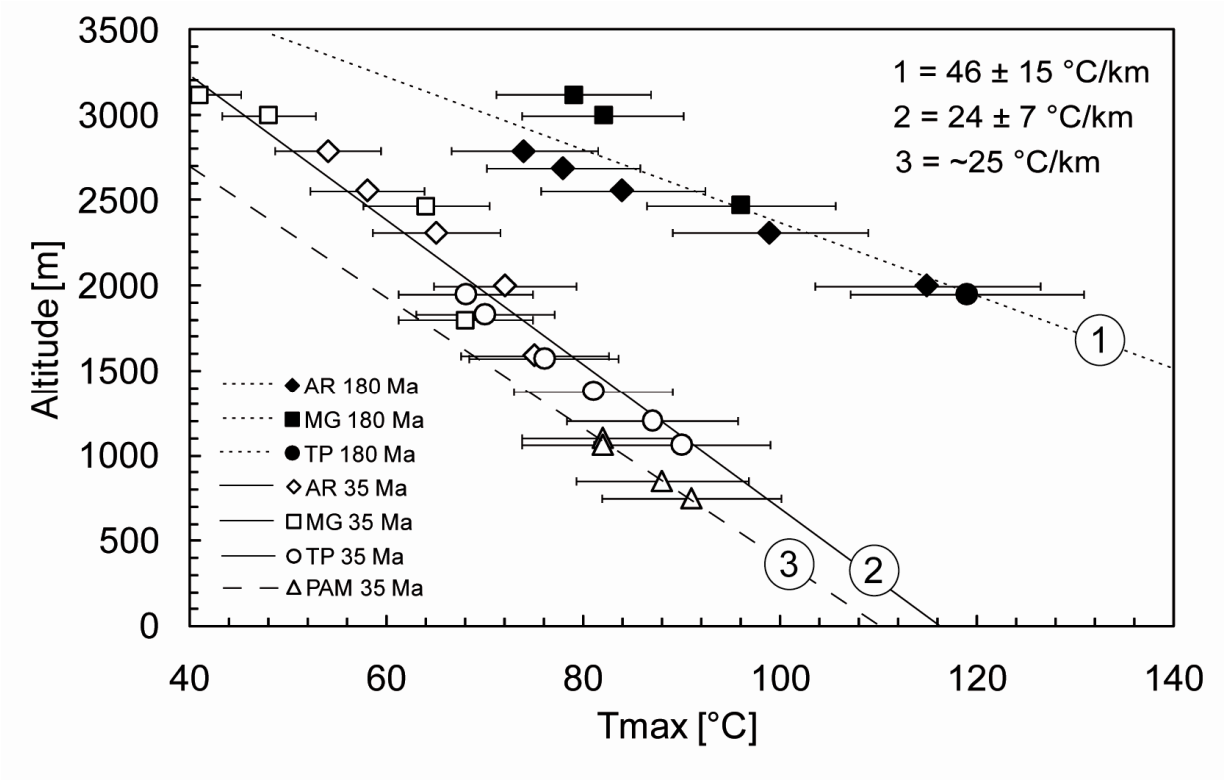

Figure M III-6: Maximal temperature estimates (T_{max}) of samples from Archambault Ridge (AR), Mount Gibbs (MG), Prince Albert Mountains (PAM) and Tourmaline Plateau (TP) estimated for the HeFTy model (Fig. M III-5) for the time of maximal temperatures at 180 Ma and the time before onset of final cooling at 35 Ma. Errors are quoted as ±10%. Geothermal gradients in the order of 45°C/km for the Jurassic, and of 25°C/km for the Cretaceous/Eocene are calculated from the regression of paleotemperature estimates and sample elevations.

5.5.2) Basement burial

The presence of subaerial Ferrar rocks, and syn-Ferrar pyroclastic and siliciclastic, partially fossil-bearing sequences of the youngest Beacon sandstones, place directly underlying basement rocks at/near the surface before/at 182 Ma (cf. section 1). In the Deep Freeze Range, such evidence of mid-Jurassic (near-) surface position of basement is given in the region at and south of Mount Adamson (Fig. M III-1) where basement top at ~2700 m is covered by a ~600 m succession of Beacon and Ferrar rocks containing siliclastic and volcaniclastic deposits and sills overlain by Ferrar lava flows that partially show pillow textures (Schöner et al., 2011). Regional (near-) surface position of the basement is supported by fossil-bearing Late Triassic to mid-Jurassic sedimentary Beacon sequences covering basement top between 2800 and 3000 m at Archambault Ridge and Shafer Peak (Fig. M III-1; Bomfleur et al., 2011). Besides abundant fossil wood and compressions of horsetails and ferns within the sedimentary sequences at both locations (Bomfleur et al., 2011), intercalated black

shale at the Shafer Peak contains microflora of Early Jurassic age (Musumeci et al., 2006). Similar fossil-bearing sequences within youngest Beacon sequences overlying basement top are documented for several regions in the Eisenhower Range and Mesa Range (e.g., Bomfleur et al., 2011). In the Prince Albert Mountains, nunataks most distal from the coast (e.g. Brimstone Peak, Mount Billing; Fig. M III-1) consist almost entirely of subaerial Ferrar lava flows and sills. Exceptions constitute locally exposed Late Triassic – Early Jurassic Beacon sequences at the base of the lava flows at ~1500 m which partially consist of volcaniclastic breccias and tuffites (Wörner, 1990; Bernet and Gaupp, 2005). Basement rocks are not exposed in the internal area, but basement top exposed at ~1250 m at Mount Chetwynd near the coast (Fig. M III-1; Wörner, 1990) together with regional low basement declination of ~1° implies regional quite similar basement top elevation, and correspondingly mid-Jurassic (near-) surface position of the basement within the entire northern Prince Albert Mountains.

Thermal history models require reheating of the basement subsequent to the Ferrar event until onset of rapid cooling at the Late Eocene (Fig. M III-5). Maximal post-Ferrar temperatures of 75° – 80°C modeled for the basement top of the Deep Freeze Range agree well with independent paleotemperature indications of 50° – 125°C derived from authigenic mineral paragenesis (e.g. Clinoptilolite, kaolinite, smectite) and incompletely albitizised feldspar within Beacon sandstones overlying basement in different areas of the Deep Freeze Range (Archambault Ridge, Shafer Peak, Mount Adamson) and Mesa Range (Figs. M III-1 and 7 – 2-I; Elsner, 2010). The thermal history models of the Prince Albert Mountains show higher Jurassic temperatures beyond the upper limit of the AFT system (Fig. M III-5) which are supported by temperatures of 200 – 300°C derived by secondary mineral phases within Beacon sandstones from the regional internal nunataks (Ballance and Watters, 2002; Bernet and Gaupp, 2005). In both regions, modeled Late Mesozoic – Eocene temperatures systemically increase from basement top to bottom. Thus, post-mid Jurassic reheating can be not explained by thermal influence of overlying Ferrar lava flows. Instead, long-lasting Late Jurassic to Late Eocene heating indicates basement burial due to Beacon and Ferrar rock overburden and/or Mesozoic – Eocene sediment deposition with persistence of this overburden until ~35 Ma.

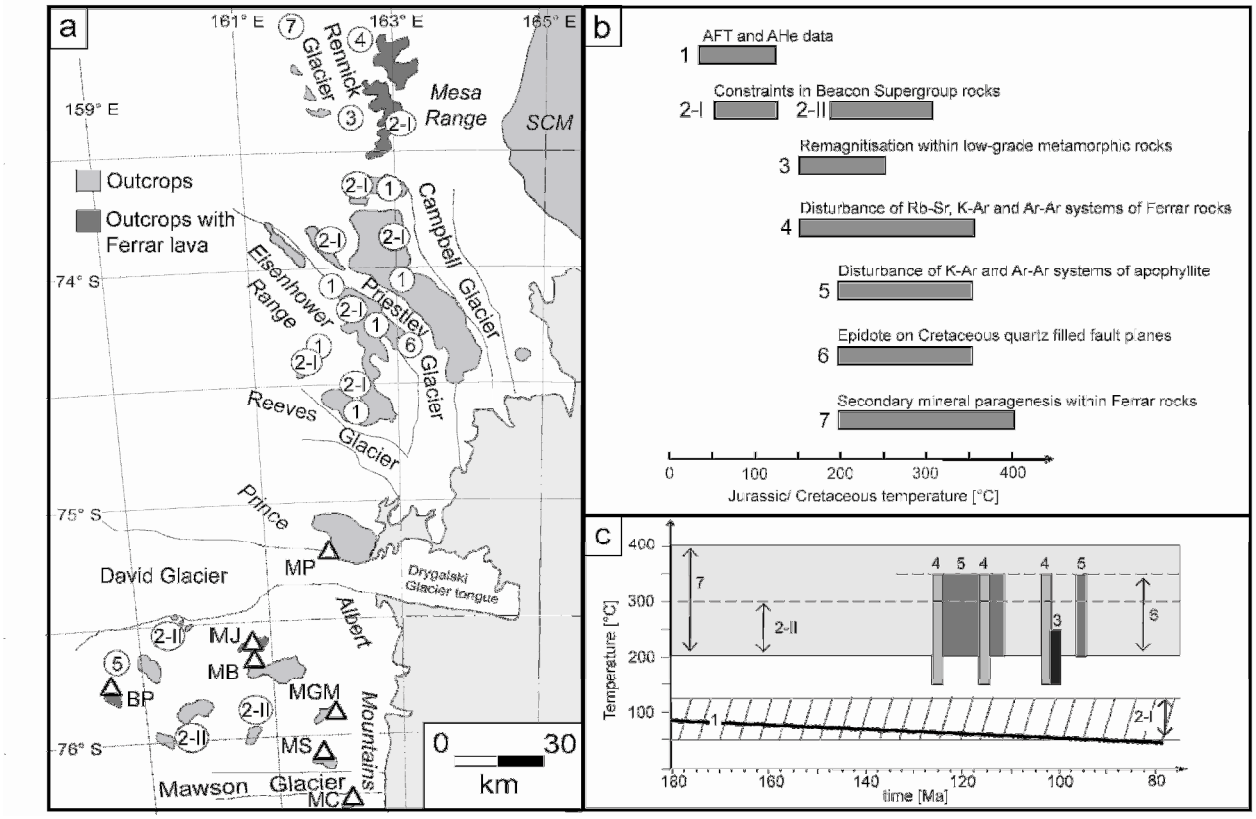

Figure M III-7: Locations (a) and temperature estimates (b) of independent Jurassic/Cretaceous temperature indications from Terra Nova Bay region and Mesa Range. (c) temperature estimates in relation to their potential age: (1) AFT data (summarized by Lisker, 2002); (2) Diagenetic constraints in Beacon Supergroup rocks of (I) northern Terra Nova Bay region and Mesa Range (Elsner, 2010; Prenzel et al., in review), and (II) southern Terra Nova Bay region (Ballance and Watters, 2002; Bernet and Gaupp, 2005); (3) Remagnitisation within low-grade metamorphic rocks (Delisle and Fromm, 1984, 1989); (4) Disturbance of Rb-Sr, K-Ar and Ar-Ar systems of Ferrar rocks (Fleming et al., 1996; Faure and Mensing 1993); (5) Disturbance of K-Ar and Ar-Ar systems of apophyllite (Molzahn et al., 1999); (6) Epidote on Cretaceous quartz filled fault planes (observed by authors; Bird and Spieler, 2004); (7) Secondary mineral paragenesis within Ferrar rocks (Hornig, 1993). BP: Brimstone Peak MB: Mount Billing; MC: Mount Chetwynd; MGM: Mount George Murray; MG: Mount Gibbs; MJ: Mount Joyce; MM: Mount Matz; MP: Mount Priestley; MS: Mount Smith; SCM: Southern Cross Mountains.

The overburden on basement can be calculated from the temperature difference between a sample within a rock column and the surface, and the geothermal gradient at a certain time (Figs. M III-5, 6). In the Deep Freeze Range, the temperature difference between samples from basement top and surface at 180 Ma (75° – 80°C/25° – 30°C; Jenkyns et al., 2012) refers to basement burial of ~1 – 1.2 km probably related to Beacon and Ferrar rock overburden, while the temperature difference at 35 Ma (~40°C/-10° – -5°C; e.g. Poole et al., 2005) indicates higher burial to depths of 1.8 – 2 km that requires 0.6 – 1 km sediment accumulation between Jurassic and Eocene. This burial history is in accordance with the Mesozoic evolution of the Eisenhower Range where similarly thick Beacon/Ferrar rocks and

post-Ferrar deposits were predicted (Prenzel et al., in review). In the Prince Albert Mountains, Mesozoic temperatures beyond the upper limit of the AFT system (Fig. M III-5) do not constrain maximum burial during the Ferrar event but, for the Jurassic geothermal gradient of the northern Terra Nova Bay region, require a Beacon/Ferrar overburden of at least 2 km. Better constrained is the Eocene overburden, when a temperature difference between the summits of Mount Priestley and Mount George Murray and surface (~80°C/-10° – -5°C) implies a burial depth of ~3.5 km. This reconstruction exceeds the maximum Beacon and Ferrar rock thickness of ~2 km observed in the internal western Prince Albert Mountains, and suggests additional ~1.5 km Beacon/Ferrar overburden and/or post-Ferrar sediment deposition on basement.

5.5.3) Basement exhumation

Thermal history models of Deep Freeze Range and Prince Albert Mountains identify a ~5 myr episode of rapid Late Eocene/Early Oligocene exhumation that stagnates at ~30 Ma. Sample cooling of ~25°C at Deep Freeze Range and of ~35°C at Prince Albert Mountains (Fig. M III-5) indicate quite similar exhumation of 1 km and 1.4 km, respectively. This is in accordance to the calculated thickness of post-Ferrar sediments for the Deep Freeze Range (see 5.2) and suggests similar sediment accumulation between Jurassic and Eocene of ~1.4 km for the Prince Albert Mountains. Subsequent Early Oligocene temperature difference between basement top and surface at Deep Freeze Range of ~25 – 30°C and at Prince Albert Mountains of ~55° – 60°C refer to basement burial of ~1 – 1.2 km and ~2 – 2.2 km, respectively. Basement burial of the Deep Freeze Range conforms to the calculated regional cumulative amount of Beacon and Ferrar rocks, while coeval higher burial at Prince Albert Mountains approximately agrees with the preserved cumulative thickness of Beacon and Ferrar rocks in the internal western Prince Albert Mountains (see 5.2). Thus, Early Oligocene stagnation of cooling seems to date (re-) exposure of the weathering-resistant Ferrar rocks after fast, complete erosion of little consolidated sediments.

Ferrar and/or basement rocks exposed today at the top of the mountain ranges restrict exhumation since the Early Oligocene predominantly to erosion along the present day glaciers (e.g. Priestley Glacier and David Glacier; Fig. M III-1). This argues for a change of exhumation style from downwearing to incision (Prenzel et al.,

in review) probably linked with the initiation of the fluvial drainage system in northern Victoria Land along predestined structures of the NW-SE trending Cenozoic fault system during the Eocene (e.g., Baroni et al., 2005; Storti et al., 2001, 2008). In contrast to the supposed Early Eocene age for the initiation of this drainage system (Baroni et al., 2005), the here predicted persistence of sediment deposition until ~35 Ma points to initiation of the fluvial drainage system, at least for Terra Nova Bay region, not prior to the Late Eocene. This agrees with the minimum age for the initiation of a fluvial drainage system in this region derived from 38 – 29 Ma magmatic rocks which are dissected by the Priestley Glacier (Armienti and Baroni, 1999; Baroni et al., 2005). Incision along the predestined structures was enhanced by isostatic rebound due to complete sediment removal at ~30 Ma, and probably by a change from fluvial to glacial erosion that happened sometimes between the occurrence of a first big ice sheet on Antarctica at ~34 Ma and the development of a persistent ice sheet with the preservation of a frozen landscape along the TAM at ~15 Ma (e.g., Strand et al., 2003; Sudgen and Denton, 2004).

Thermal history models show regional differential sample cooling to the present-day mean surface temperature. Cooling stagnation between ~30 Ma and onset of final rapid cooling at ~15 Ma at Deep Freeze Range contrasts with continuous cooling to surface temperatures at ~18 Ma at Prince Albert Mountains (Fig. M III-5). Thereby, cooling of ~10°C between 30 and 15 Ma at Deep Freeze Range corresponds to exhumation of ~0.5 km (~30 m/Ma) while cooling of ~55°C at Prince Albert Mountains between 33 and 18 Ma suggests exhumation of ~2.2 km (~145 m/Ma) at same time. This points to faster exhumation of the Prince Albert Mountains within first 15 myr since sediment removal. The onset of final rapid cooling of Deep Freeze Range at ~15 Ma (Fig. M III-5) coincides temporally with the preservation of a frozen landscape along the TAM (e.g., Sudgen and Denton, 2004). Thus, initiation of freezing erosive-protecting conditions at higher elevations and wet-based erosive-strengthening conditions at low elevation glaciers may have intensified glacial incision since ~15 Ma (cf. Stern et al., 2005; Prenzel et al., in review). Cooling of basement top of ~25°C to surface temperature between 15 and 8 Ma (Fig. M III-5) requires basement incision of ~1 km with a rate of ~125 m/Ma.

The date of basement surface exposure at Deep Freeze Range coincides with that of ~5 Ma derived by cosmogenic nuclide data for the summit exposure of Mount Keinath at the southern Deep Freeze Range (Oberholzer et al., 2003) while earlier

basement top exposure in the Prince Albert Mountains is consistent with results of cosmogenic ^{21}Ne data from the Dry Valleys ~50 km south of Mawson Glacier (Fig. M III-1) that infer only minor modifications of the landscape surface over at least the last ~15 myr (Summerfield et al., 1999). Ongoing cooling of samples that have reached surface temperature is attributed to ongoing incision of the basement along the glaciers and a correspondent development of an orographic gradient. Potential persistent incision with same rate until today assumes total incision depth of ~1.9 km in the Deep Freeze Range and of ~4.8 km in the Prince Albert Mountains.

5.6) Basin evolution and long-term landscape development of the Terra Nova Bay region

Burial increase from northern to southern Terra Nova Bay region in the order of 1.5 km related to a higher thickness of Beacon/Ferrar rocks in the south correlates with the present-day elevation of the Kukri Peneplain that decreases in approximately the same order from Deep Freeze Range (3100 – 2700 m) to Prince Albert Mountains (~1250 m). Accordingly, the lower Beacon/Ferrar rock thickness in the north seems to refer to differences in the Jurassic topography within the Terra Nova Bay region probably related to basement declination prior to or associated with the Ferrar event. This may be conceivably explained by a (pre-) Ferrar position of the Eisenhower and Deep Freeze Ranges at the margin of a wide paleodepression within the area of the Prince Albert Mountains that hosted the main feeder of Ferrar magmatism. The Mesa Range north of the Terra Nova Bay showing basement top elevation (1600 – 1000 m; e.g., Elsner, 2010) and Ferrar rock thickness (≥1500 m; see 2) similar to these of the Prince Albert Mountains suggests another potential Jurassic surface depression in this region. Considerable lower elevation of basement top along the adjacent Rennick Glacier/Graben (Fig. M III-1) declining below sea-level in its northern part (Elsner, 2010) can be explained by a later opening, downfaulting and inversion of the graben structure predominantly triggered by the Cenozoic propagation of the right-lateral faulting within the continental crust of northern Victoria Land (Rossetti et al., 2003) long after Ferrar rock emplacement. Predicted variations of Ferrar rock thickness within the Terra Nova Bay region and Mesa Range involving a Jurassic topography based on the present-day Kukri Peneplain elevation along the mountain ranges induce a consistent, plain topography subsequent to the Ferrar event.

This gives a good explanation for the calculated regional uniform post-mid Jurassic sedimentary cover (Fig. M III-8).

Consistent sedimentary overburden on Deep Freeze and Eisenhower Ranges and Prince Albert Mountains subsequent to the Ferrar event indicates a continuous, uniform sedimentary basin within the Terra Nova Bay region. The calculated sedimentary thickness between 0.6 and 1.4 km conforms to a sediment volume of 8500 – 20000 km^3 (Fig. M III-8). Considering additional 1 – 2 km Beacon/Ferrar rock overburden on basement (see 5.3; Prenzel et al., in review), such sedimentary thickness is supported by post-Ferrar temperatures of 50° – 125°C derived from diagenetic features, authigenic mineral phases and partially albitizised plagioclase within Beacon sandstones from numerous locations in the northern Terra Nova Bay region and Mesa Range (Fig. M III-7). Contrary, other independent temperature indicators within Beacon sandstones and Ferrar flood basalts from different locations in the Terra Nova Bay region and Mesa Range suggest much higher, strongly varying temperatures of 150° – 400°C which were reached diachronously between mid-Jurassic and Late Cretaceous times (summarized in Fig. M III-7). This comprises (i) secondary mineral phases within Beacon sandstones from the southern Terra Nova Bay region (200° and 300°C; Ballance and Watters, 2002; Bernet and Gaupp, 2005), (ii) the presence of prehnite, pumpellyite and other secondary phases within Ferrar lava flows from the Rennick Graben at the northern Mesa Range (200° – 400°C; Hornig, 1993), (iii) epidote coatings on fault planes along the Priestley Glacier observed recently by the authors (200° – 350°C; unpublished data from GANOVEX X 2009/2010), (iv) remagnitisation within Ferrar rocks in the Mesa Range (~150° – 250°C; Delisle and Fromm, 1984, 1989), and the disturbance of Rb-Sr and/or K-Ar and Ar-Ar systems of (v) Ferrar volcanic rocks from the Mesa Range (150° – 350°C; Fleming et al., 1996; Faure and Mensing 1993), and (vi) apophyllite from the Prince Albert Mountains (~200° – 350°C Molzahn et al., 1999). These temperatures are exclusively restricted to regions north of Deep Freeze Range and south of David Glacier which are assumed to have hosted the main feeder of Ferrar magmatism, or areas at/near main tectonic structures underlying the Priestley Glacier, Rennick Graben and David Glacier (e.g., Storti et al., 2008). Instead of burial, temperatures ≥150°C thus seems to be affected by a Jurassic/Cretaceous heatflow within the Prince Albert Mountains and Mesa Range much higher than this one represented by the Jurassic geothermal gradient of ~45°C/km for the northern Terra Nova Bay

region, or Jurassic/Cretaceous short-term heating events probably attributed to hot fluid-rock interaction along faults as recognized locally for the Eisenhower Range and for various areas south of the David Glacier (Prenzel et al., in review; Molzahn et al., 1999). Similar heatflow variation is documented for example for Cretaceous – Eocene sedimentary basins at the south-eastern Australian coast (Mitchell et al., 1997).

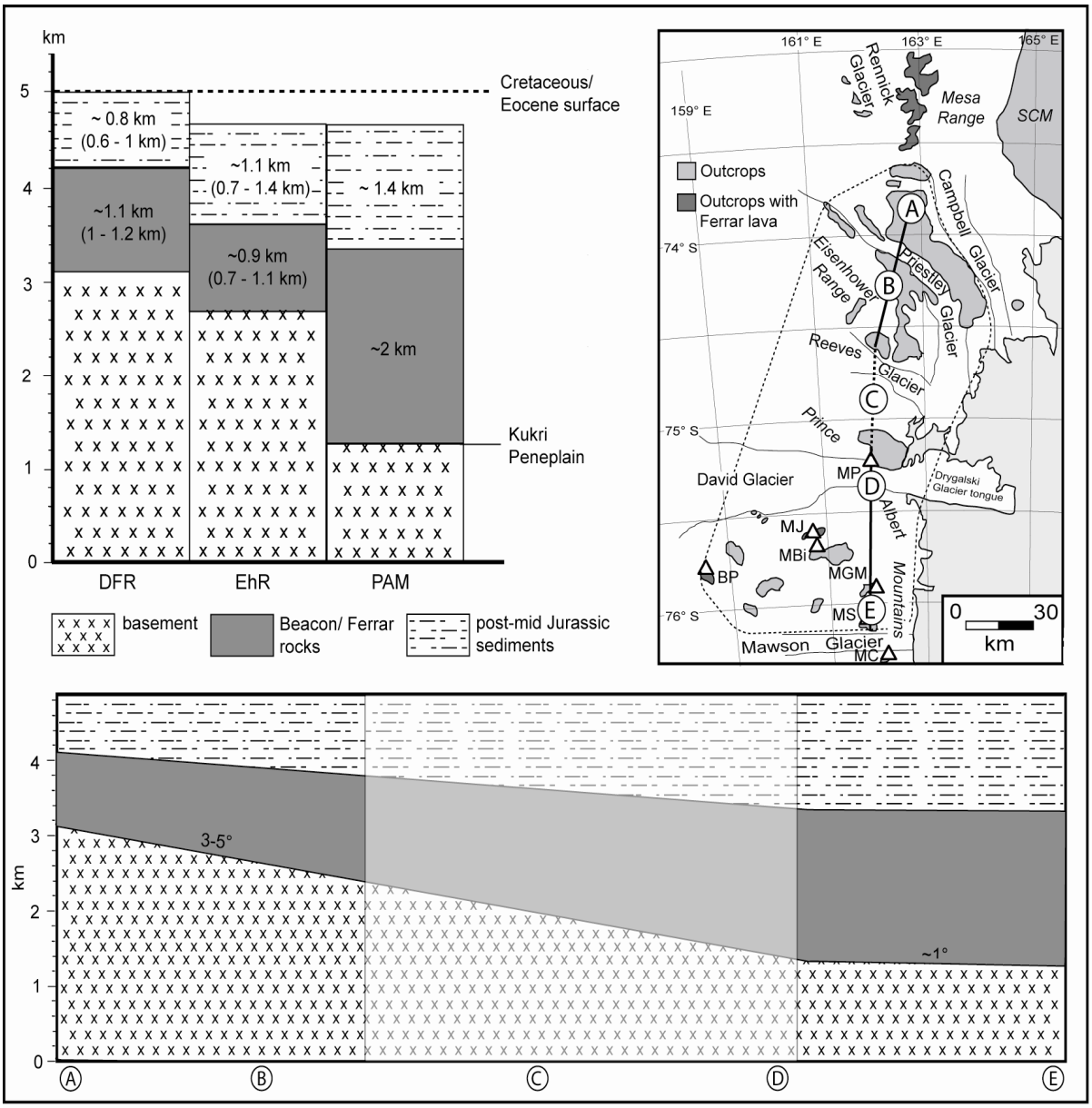

Figure M III-8: Calculated Cretaceous/Eocene rock column above Kukri Peneplain in the Deep Freeze Range (DFR), Eisenhower Range (EhR) and Prince Albert Mountains (PAM), and predicted variation of basement overburden from northern to southern Terra Nova Bay region (A to E; for more information see text). The dotted line marks the area used for volume calculation of post-mid Jurassic sedimentary overburden on the Jurassic surface.

The precise time of basin formation is uncertain, but post-Ferrar sediment deposition points to ongoing sediment accumulation subsequent to the existence of the Permian-Triassic *Transantarctic Basin* within the Terra Nova Bay region (e.g., Collinson et al., 1994). Thus, Ferrar rock emplacement seems not to mark the termination of regional subsidence, and instead probably occurred during an ongoing process of crustal thinning, subsidence and sediment accumulation. Potential mid-Jurassic basin formation may be linked with the initiation of extension within the West Antarctic Rift System at ~180 Ma during Early Gondwana break-up that also triggered the Ferrar magmatism. Correspondingly, post-Ferrar sediments may partially represent inputs from same sources as assumed for the Late Triassic – Early Jurassic sediments of the *Transantarctic Basin* which includes areas south of the Prince Albert Mountains (southern Victoria Land, Central TAM) and northeast of the Deep Freeze Range, as well as magmatic arcs along the active margin of Gondwana (e.g., Collinson et al., 1994; Elsner, 2010). However, areas in a position more distal to the West Antarctic Rift System such as the USARP Mountains northeast of the Mesa Range (Fig. M III-1) that experienced much less Cretaceous – Cenozoic extension than the Terra Nova Bay and adjacent regions are favoured as mid-Jurassic to Eocene sediment sources.

The here predicted longevity of the sedimentary basin until the Late Eocene, supported by the N-S trending Cretaceous sedimentary depocenters adjacent to the Terra Nova Bay coast (e.g., Victoria Land Basin; Fig. M III-1) and N-S fracturing along the Prince Albert Mountains (Salvini et al., 1997), indicates a relatively stable regional stress field of E-W extension during Mesozoic Ross Sea opening. This is in accordance with the reconstruction of Antarctica-Australia break-up since the Jurassic that shows extremely slow, approximately E-W directed extension in the Ross Sea until rapid Eocene movement of Australia towards north induced final separation from Antarctica and opening of the Tasman gateway (e.g., White et al., 2013; Stickley et al., 2004). This together with extension that remained continental until the development of first seafloor in the mid-Cretaceous (Boger, 2011) provides ideal conditions for Mesozoic basin evolution. Accordingly, Mesozoic – Eocene basin existence within the Terra Nova Bay region argues for an extension between Antarctica and Australia that began in the west, and propagated eastward as the Australian plate rotated clockwise relative to the Antarctic plate (cf. White et al., 2013).

Regional consistent rapid exhumation between ~35 and ~30 Ma indicates coeval simultaneous initiation of basin inversion that temporally overlaps with tectonic activity evidenced by ~34 Ma pseudotachylytes and ~35 Ma magmatic dykes at the southern tip of the Priestley Glacier/Fault (Müller et al., 1990; Di Vincenzo et al., 2004; Rossetti et al., 2006), as well as with the ages of the N-S elongated Cenozoic magmatic belt between 38 and 29 Ma along the Priestley Fault (Tonarini et al., 1997; Armienti and Baroni, 1999). Offshore, Late Eocene/Early Oligocene basin inversion agrees with the Eocene/Oligocene age proposed for the widespread seismic unconformity in the sedimentary rocks within the depocenters adjacent to the Terra Nova Bay coast (e.g. Victoria Land Basin; Fig. M III-1) that is interpreted to separate Mesozoic and Cenozoic deformation events (Busetti, 1994; Salvini et al., 1997), and with an Oligocene age for oldest synrift deposits recorded SW of the Victoria Land Basin (Cape Roberts Science Team, 1998, 1999). These indications strongly link basin inversion and (re-) exposure of the Jurassic surface with right lateral strike-slip and transtensional faulting during the Eocene (Salvini et al., 1997) and a correspondent major tectonic reorganization in the Ross Sea region from Cretaceous orthogonal rifting to Cenozoic oblique rifting (e.g., Davey and Brancolini, 1995; Storti et al., 2008). This seems to be related to a phase of increased Eocene extension during final separation of Antarctica and Australia (see above). Increased Eocene extension within the Ross Sea adjacent to the Terra Nova Bay coast is supported by the coeval reactivation of the Victoria Land Basin as represented by the Cenozoic formation of the Terror Rift that may have enhanced the lithospheric differentiation between northern Victoria Land and thinned crust offshore (Salvini et al., 1997). Extrapolation of the Adare Trough at Cape Adare (Fig. M III-1) southwards points to a significant Eocene – Oligocene extension in the Victoria Land Basin of up to 180 km (Cande et al., 2000; Davey et al., 2006). This implies Late Eocene sedimentary basin termination without any significant change in the general tectonic regime.

Basin inversion triggered by increased extension within the Ross Sea since the Late Eocene suggests the depositional environment of the Mesozoic – Eocene sediments within the present-day Ross Sea. Oligocene drill core sediments from the Eastern Ross Sea contain high illite concentrations indicative for sedimentary terrestrial source rocks (Ehrmann, 1998). These drill core sediments recording numerous ice shield advances and retreats with ice movement predominantly from the west imply potential removal of the post-mid Jurassic sedimentary sequence related to an ice

flow from the west with a subsequent influx of the eroded material into the Ross Sea. This is consistent with the occurrence of Cretaceous and Paleocene terrestrial fossils within Ross Sea deposits (e.g. Truswell and Drewry, 1984; Villa et al., 2011). Additionally, the Ross Sea as potential depositional environment is supported by the presumable close connection between Late Eocene sediment removal and contemporaneous initiation of the Terror Rift that associated troughs contain a sediment thickness of up to 12 km (Cooper et al., 1987).

Subsequent to basin inversion, regional lower exhumation within last 30 myr at Deep Freeze Range and northern Eisenhower Range (<2 km) than at southern Eisenhower Range (~3.3 km) and Prince Albert Mountains (~4.8 km; Prenzel et al., in review) is obviously related to a change of exhumation style from downwearing to backstepping incision from the coast towards the interior by a combination of fluvial and glacial incision, climate cooling, and isostatic surface rebound in response to sediment removal at ~30 Ma (Prenzel et al., in review). Assuming sediment density of ~1.7 – 2.5 g/cm^3 and using a simplified equation for isostatic compensation (Middleton and Willcock, 1994), removal of the complete sedimentary material results in surface rebound between 0.3 – 0.8 km at Deep Freeze Range and 0.7 – 1.1 km at Prince Albert Mountains. Generally deeper incision at the coast can be attributed to the vicinity of the adjacent West Antarctic Rift System and a correspondent stronger influence of the West Antarctic Rift shoulder uplift.

5.7) Conclusion

Thermal history models indicate burial of the Jurassic surface on Deep Freeze Range and Prince Albert Mountains subsequent to Ferrar magmatism at 182 Ma until initiation of rapid exhumation at the Late Eocene. Paleotemperatures from the vertical sample arrays indicate an increased Jurassic gradient of 45°C/km in the Deep Freeze Range and a moderate Cretaceous – Eocene geothermal of ~25°C/km within Deep Freeze Range and Prince Albert Mountains. Deeper burial of the Prince Albert Mountains (~3.4 km) than of the Deep Freeze Range (2 – 2.2 km) is attributed to a ~1 km higher thickness of Beacon and Ferrar rocks in the southern Terra Nova Bay region. The calculated post-mid Jurassic sediment thickness only varies slightly and is in the order of 1 km in both regions. Rapid Late Eocene/Early Oligocene exhumation of both regions infers fast erosion of the complete sedimentary sequence and (re-) exposure of underlying Ferrar rocks within ~5 myr. Subsequent higher final

exhumation of the Prince Albert Mountains refers to faster and deeper basement incision than in the Deep Freeze Range.

Burial and exhumation evolution of Deep Freeze Range and Prince Albert Mountains analogous to this of the Eisenhower Range evidences a consistent basin evolution within the entire Terra Nova Bay region. This comprises nearly equal amounts of Late Jurassic to Eocene sediment deposition and Late Eocene/Early Oligocene sediment removal. The calculated Beacon/Ferrar thickness in the Deep Freeze Range resembles this assumed for the Eisenhower Range, while the higher thickness of Beacon and Ferrar rocks within the Prince Albert Mountains coincides with the maximum thickness of these rocks preserved in its western part and in the Mesa Range. Higher thickness of Beacon and Ferrar rocks in the southern Terra Nova Bay region and in the Mesa Range is probably related to differences in the pre-Ferrar topography throughout northern Victoria Land. This is here explained by potential Jurassic surface depressions north and south of the Deep Freeze and Eisenhower Ranges which mainly hosted the feeder of Ferrar magmatism.

The uniform post-mid Jurassic sedimentary sequence within the entire Terra Nova Bay region infers a consistent and plain Mesozoic – Eocene topography subsequent to the Ferrar event attributed to a regional consistent sedimentary basin with uniform depth of ~1 km. Jurassic/Cretaceous temperatures of up to ~400°C derived locally by numerous independent temperature indications for various areas of the Terra Nova Bay region are confined to areas at/near main faults or areas of main Ferrar magmatism, and thus can be related to short-term heating events along faults or regional elevated heatflow. Mid-Jurassic basin formation with subsequent Mesozoic – Eocene sediment accumulation is explained by initiation of extension within the West Antarctic Rift System at ~180 Ma and a continuous stable stress field of low E-W extension during Ross Sea opening until the Late Eocene. Late Eocene/Early Oligocene basin inversion is linked with right lateral strike-slip and transtensional faulting attributed to major Eocene tectonic reorganization in the Ross Sea region from Cretaceous orthogonal to Cenozoic oblique rifting related due a phase of increased extension within the Ross Sea due to final Eocene separation of Antarctica from Australia. Differential regional Ferrar rock/basement incision subsequent to the sediment removal with higher incision at the coast than in the interior is related to a change of exhumation style from downwearing to backstepping incision probably due to a stronger influence of West Antarctic rift shoulder uplift at the coast.

Acknowledgement

This study was funded by DFG grants LI745/12-1 (F.L.) and LA 1080/7-1 (A.L.) of the Deutsche Forschungsgemeinschaft (DFG) within priority program SPP 1158 “Antarctic Research with comparative investigations in Arctic ice areas”. Frank Lisker and Jannis Prenzel thank the Bundesanstalt für Geowissenschaften und Rohstoffe, Hannover, for the invitation to participate in the Antarctic GANOVEX X expedition. We wish to thank the crews of MS Italica and Helicopters New Zealand for logistic support and the members of the GANOVEX team for cooperative fieldwork and stimulating discussions. F. Balsamo, G. Di Vincenzo, M. Elsner, J. Lindow, S. Rocchi, F. Rossetti, R. Schöner and F. Storti are acknowledged for helpful comments.

Appendix:

Modeling procedure and constraints

We applied a large number of random thermal history paths for each sample via HeFTy inverse modeling. The inverse models served as base to identify the best composite thermal history by HeFTy forward modeling. The intra-sample AHe single grain age dispersion especially of the samples from Mount Gibbs did not allow common modeling of the complete AHe data for each sample, and the best modeling results of overdispersed AHe age data were produced using the AHe single grain ages nearest to the samples AHe weighted age using the radiation damage model of Flowers et al. (2009). The predicted HeFTy forward model was validated by multiple QTQt modeling. Since QTQt does neither allow integrating the Sm concentration of an apatite nor modeling abraded grains we only modeled the U and Th component of non-abraded grains.

The initially set conditions for HeFTy modeling comprise seven time-temperature constraints: (1) initial high temperatures immediately after the intrusion of the Granite Harbour Intrusives [500 – 450 Ma; 150° – 300°C]; (2) a long time period with a large temperature range until the Ferrar event [500 – 180 Ma; 0° – 300°C]; (3) near surface temperatures concluded from superficially emplaced volcanic rocks of the Ferrar Event [185 – 175 Ma; 0°C – 170°C depending on the sample position in vertical relation to the paleosurface and the geothermal gradient; Jurassic geothermal gradient 15° – 70°C/km]; (4) a subsequent high temperature range inferred from sample ages younger than the genetic Ferrar rock age [180 – 85 Ma; 40° – 250°C]; (5) decreasing temperatures in the Cenozoic [85 – 25 Ma; 20° – 160°C] inferred from the boomerang pattern of the apatite FT ages against the MTL (Fig. M III-2c); (6) subsequent near surface temperatures [85 – 0 Ma; -38°– 20°C]; and (7) the present-day mean surface temperature depending on the sample elevation [0 Ma; -35° – -15°C].

Time-temperature conditions consistent with the constraints 1, 3 and 6 used above were set for QTQt modeling. There, the constraints were specified for the highest sample and imposed automatically on the other samples. Since QTQt does not allow negative values the present temperature was set to zero.

Supplementary data M III-1

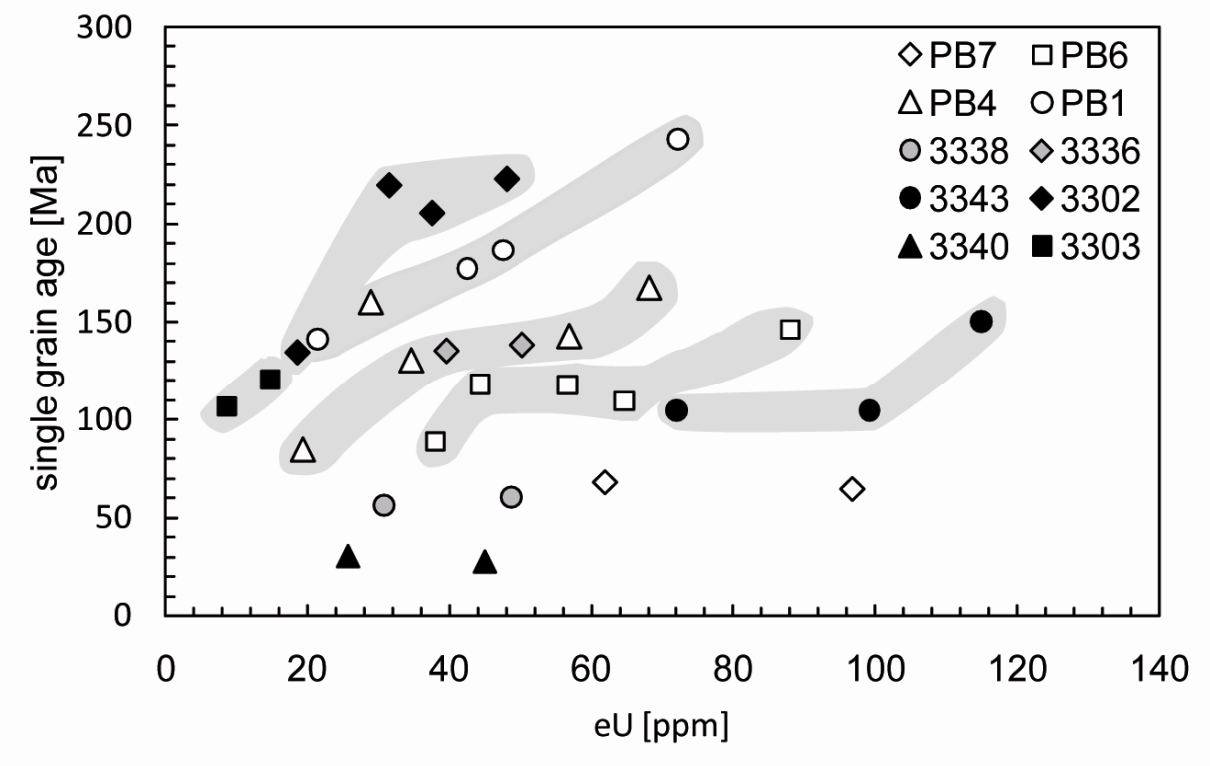

Supplementary data M III-1: (U-Th-Sm)/He (AHe) single grain ages vs. effective U concentration (eU) for the samples from the Archambault Ridge and Mount Gibbs. The relationship between single grain ages and eU encircled by dashed white lines is rather vague due to the sparse amount of analyzed apatite grains.

Supplementary data M III-2

Sample	Elevation [m]	ξ	Dated grains [N]	AFT age [Ma] (predicted age)	MTL [µm] (n)	MTL c-axis [µm] (predicted MTL)	SD [µm]	SD c-axis [µm] (predicted SD)	Dpar mean [µm]
AML9	750	353 ± 6	20	52±4	14.25±0.23 (100)	15.06 (14.72)	2.29	1.65 (1.87)	2.51
AML8	850	353 ± 6	20	63±3	13.92±2.29 (101)	14.78 (14.29)	2.29	1.60 (1.97)	2.42
AML7	1080	353 ± 6	20	71±5	12.16±0.33 (101)	13.94 (14.06)	3.30	1.84 (1.92)	2.28
AML15	1100	353 ± 6	17	67±7	13.09±0.29 (85)	14.39 (14.20)	2.69	1.57 (1.90)	2.01

Supplementary data M III-2: Table shows apatite fission track (AFT) data of four samples from Prince Albert Mountains (Mount George Murray and Mount Priestley) originally published by Storti et al. (2008). For the purpose of thermal history modeling, we here provide new Dpar measurements for all investigated grains to include an indicator for fission track annealing kinetic properties (e.g. Donelick, 1993; Carlson et al., 1999), quoting here the mean Dpar of each sample.

Supplementary data M III-3

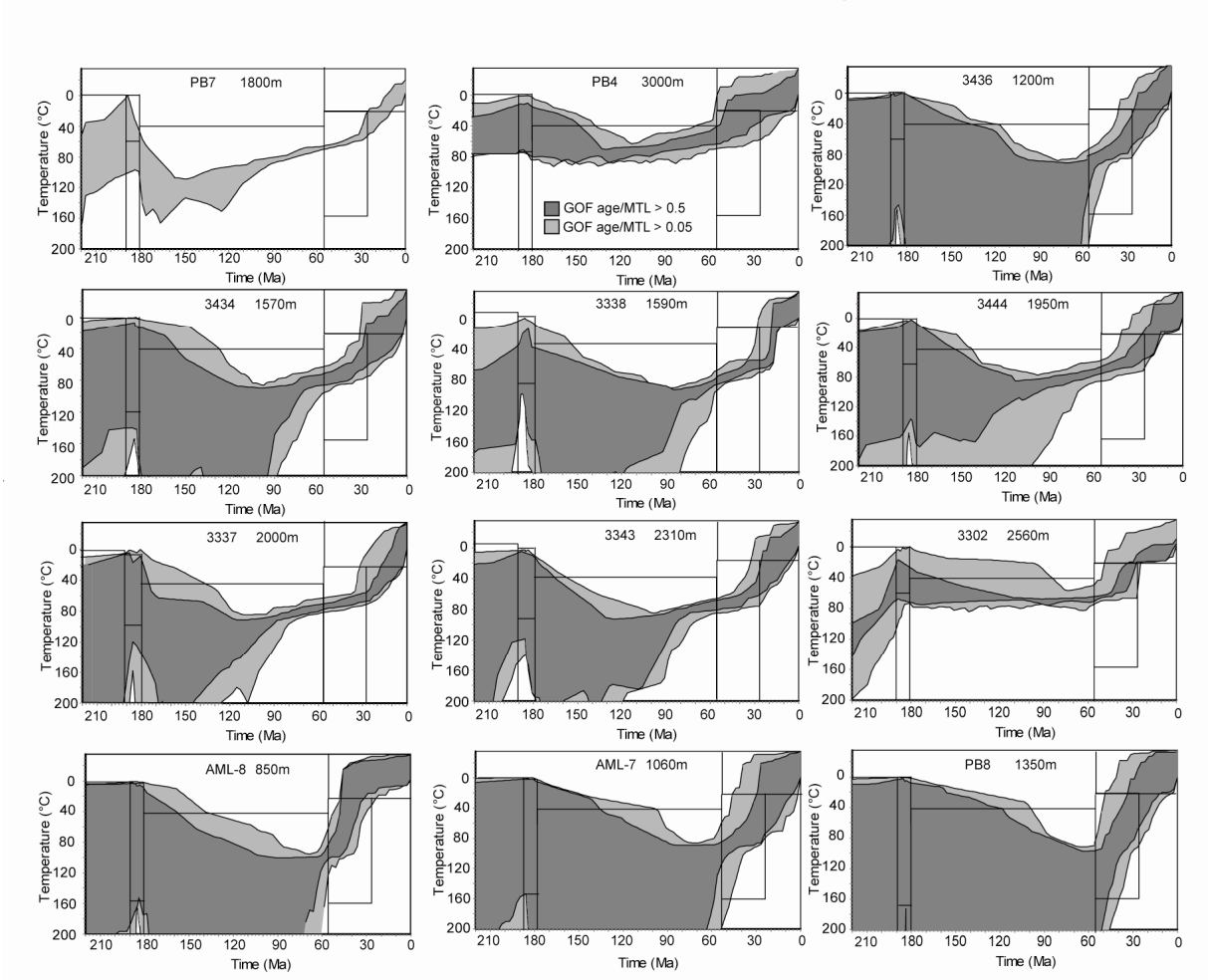

Supplementary data M III-3: Inverse modeling results of samples which are not shown in figure M III-4 (HeFTy, Ketcham 2005); Black boxes mark the time-temperature constraints set for HeFTy modeling (for detailed description see text). HeFTy was performed for all applicable samples using the Monte Carlo search method and a minimum of 100,000 randomly produced t-T-paths. The goodness of fit (GOF) of the apatite fission track (AFT) age data were determined for each sample using the annealing model of Ketcham et al. (2007) and c-axis projection, the GOF of the AFT length data is quoted using the Kuiper's Statistic method. A default initial track length of 15.99 µm and a length reduction of 0.892 µm were measured in Durango standard.

6) Conclusions

The innovative approach of this study providing a combined data set of independent and complementary thermochronological, maturity and sediment petrographic data from the Terra Nova Bay region allowed the reconstruction of a regional long-time burial, exhumation and long-time landscape evolution in a resolution that has been not matched by any case study in the TAM before. Besides new important knowledge about the regional post-mid Jurassic geological history, this approach demonstrates the strongly limited applicability of qualitative interpretation concepts of thermo-chronological data as tools to straightly date exhumation episodes and the importance of thermal history modeling for the interpretation of exhumation histories. These results are therefore fundamental for all thermochronological studies and are of interest for applications in geomorphology, geodynamics, tectonics, and basin evolution studies. The study also exemplifies the applicability of combined thermochronological data and complementary thermal information for the analysis of basin inversion associated with continental breakup, and demonstrates the influence of lithology, tectonics, and climate on exhumation in such a setting. This provides new insights on timing, magnitude and mechanism of exhumation and uplift of the Transantarctic Mountains.

The comparison of AFT data compiled for same samples via external detector technique and population technique supports previous cases made for integration of kinetic parameters and individual grain-age evaluation, even from granitic rocks of the same intrusion. Age comparison additionally illustrates that samples above a *break in slope* usually record larger deviations between population and external detector ages than samples below a break in slope. This is attributed to varying residence times of apatites with different chemical composition and track annealing kinetic properties within the PAZ.

Thermal history models of AFT and AHe data from different regions in the Terra Nova Bay region (Deep Freeze Range, Eisenhower Range, Prince Albert Mountains) incorporating the geological and thermal frame record a quite uniform thermal history. This comprises a complex history of Mesozoic (re-) heating/burial subsequent to the Ferrar event and cooling/exhumation since the Late Eocene/Early Oligocene that contrasts with the traditional qualitative interpretation of thermochronological data based on the *break in slope* concept inferring stepwise cooling/exhumation since the

Early Cretaceous with a substantially earlier onset of final exhumation at the Paleocene. Thermal history modeling experiments demonstrate that a *break in slope* does not necessarily date cooling/exhumation events and that its position and shape are the result of numerous factors such as the thermal history prior to the onset of final cooling, maximum paleotemperatures, cooling rate, and geothermal gradient.
It also evidences that a *break in slope* cannot resolve complex thermal histories and that a solely qualitative interpretation of an AFT pattern may result in an incorrect record of the thermal history. Hence, a *break in slope* only provides minimum time constraints for the onset of cooling, and cannot substitute thermal history modeling. The same caution generally applies to steep age gradients with altitude. This shows that earlier qualitative thermochronological studies of vertical profiles from the TAM and elsewhere need to be validated by thermal history modeling.

The regression of paleotemperatures versus sample altitudes refers to almost identical geothermal gradients throughout the entire Terra Nova Bay region. This comprises a Jurassic geothermal gradient between 45°±14 °C/km and 47°±30 °C/km for the Deep Freeze Range, the Priestley Glacier and the southern Eisenhower Range, as well as a Cretaceous – Eocene geothermal gradient between 24°±7 °C/km and 30°±6 °C/km for the Deep Freeze Range, the Eisenhower Range, the Priestley Glacier and the Prince Albert Mountains. The Cretaceous gradient is in tight accordance with coeval geothermal gradients of 25 °C/km calculated for the northern TAM and the USARP Mountains. The high Jurassic geothermal gradient is attributed to Late Jurassic – Early Cretaceous rifting processes and associated Ferrar magmatic intrusions and extrusions within the extensional setting of the TAM region while the subsequent change to a much lower, moderate Cretaceous – Eocene gradient is related to basal heatflow decline due to isobaric cooling.

Thermal history models indicate for the basement top in the entire region long-lasting Mesozoic temperatures of ≥80 °C which coincide with these of ~60° – 100 °C derived by organic maturation data from overlying Beacon sandstones from the Eisenhower Range and independent paleotemperature indications of ~50° – 125 °C derived from authigenic mineral phases and incomplete albitizised feldspar within Beacon sandstones from the northern Terra Nova Bay region. A mid-Cretaceous short-term heat pulse of ~100 °C recognized locally adjacent to the Priestley Fault is attributed to circulation of hydrothermal fluids along the fault during Late Mesozoic and

Cenozoic rifting. Strongly varying, diachronously reached Jurassic/Cretaceous temperatures between ~150° and ~400 °C derived locally by numerous independent temperature indications within Beacon sandstones and Ferrar rocks for various regions of the Terra Nova Bay region and Mesa Range are confined to areas at/near main faults or areas of main Ferrar rock emplacement. These elevated temperatures are related to short-term heating events along faults with associated hot fluid-rock interactions as recognized locally for the Eisenhower Range and for various areas south of the David Glacier, or to an elevated heatflow within the areas of main Ferrar rock emplacement.

Paleotemperatures which systemically increase from basement top to bottom together with geothermal gradients infer regional burial of the Jurassic surface to depth between ~2.2 km in the northern Terra Nova Bay region and ~3.4 km in the southern Terra Nova Bay region. This burial increases from Jurassic to Eocene and correspondingly cannot be explained by Beacon and Ferrar rock overburden only. Thus, additional required post-Ferrar sediment accumulation persisting until rapid Late Eocene exhumation provides evidence for a Mesozoic – Eocene sedimentary basin existence within the Terra Nova Bay region. Deeper burial of southern than of northern Terra Nova Bay region is attributed to a higher thickness of Beacon and Ferrar rocks of ~1 km in the south probably related to a pre-Ferrar position of the Eisenhower Range and Deep Freeze Range at the margin of a paleodepression within the Prince Albert Mountains that predominantly hosted the feeder of Ferrar magmatism. Such potential relationship between Jurassic topography and Ferrar rock emplacement is supported by basement top elevation and Ferrar rock thickness in the Mesa Range similar to these of the Prince Albert Mountains suggesting a further Jurassic paleodepression north of Deep Freeze and Eisenhower Ranges. Contrary to regional variations of Beacon and Ferrar rock thickness, the documented post-mid Jurassic sedimentary thickness only varies slightly throughout the region between ~0.6 – 1 km in the Deep Freeze Range, ~0.7 – 1.4 km in the Eisenhower Range, and ~1.4 km in the Prince Albert Mountains. This quite uniform Mesozoic – Eocene sedimentary sequence within the entire region refers to a consistent and plain topography subsequent to the Ferrar event.

Regional consistent sedimentary overburden on the Jurassic surface between 0.6 and 1.4 km conforms to a sediment volume of 8500 – 20000 km^3 within the entire Terra Nova Bay region. Post-mid Jurassic burial related to sediment deposition infers

ongoing sediment accumulation subsequent to the existence of the Permian-Triassic Transantarctic Basin, and that Ferrar rock emplacement probably occurred during an ongoing process of crustal thinning, subsidence and sediment accumulation, and does not represent the termination of regional basin existence. Mid-Jurassic basin formation and subsequent sediment accumulation until the Late Eocene is explained by initiation of extension within the West Antarctic Rift System at ~180 Ma with a continuous stable stress field of low E-W extension during Ross Sea opening until ~35 Ma. Besides potential provenances for the Mesozoic – Eocene sediments similar to these of the sediment infillings of the Transantarctic Basin (e.g. southern Victoria Land, Central TAM, Wilson Terrane, magmatic arcs along the active margin of Gondwana), favoured sediment sources are areas in a position more distal to the West Antarctic Rift System such as the USARP Mountains north of the Terra Nova Bay region that experienced much less Cretaceous – Cenozoic extension than the TAM.

Regional uniform rapid Late Eocene/Early Oligocene exhumation is attributed to fast erosion of the complete sedimentary sequence and (re-) exposure of underlying Ferrar rocks within ~5 myr. This basin inversion is linked with right lateral strike-slip and transtensional faulting attributed to major Eocene tectonic reorganization in the Ross Sea region from Cretaceous orthogonal to Cenozoic oblique rifting due to a phase of increased extension that induced the final separation of Antarctica and Australia. At supraregional scale, basin inversion coincides with climate change represented by the formation of the East Antarctic continental ice shield, and tectonic processes such as the rifting of the West Antarctic Rift System and the onset of sea floor spreading and opening of the Tasman gateway between Antarctica and Australia. Offshore sediment record from the Ross Sea containing Cretaceous and Paleocene terrestrial fossils and high illite concentrations indicative for sedimentary terrestrial source rocks suggests the depositional environment of the Mesozoic – Eocene sediments within the present-day Ross Sea.

Regional differential sample cooling to the present-day surface temperature subsequent to stagnation of rapid exhumation and (re-) exposure of Ferrar rocks at ~30 Ma documents differential basement incision due to glacial erosion along main tectonic structures and contemporaneous isostatic rebound. Exhumation stagnation in the interior of the northern Terra Nova Bay region between ~30 Ma and onset of final rapid exhumation at ~15 Ma contrasts to contemporaneous ongoing exhumation

with basement top exposure at ~18 Ma at the coastal regions in the southern Eisenhower Range and Prince Albert Mountains. Increased incision since ~15 Ma in the northern Terra Nova Bay region coeval with the development of a persistence ice sheet on East Antarctica infers intensified glacial incision within last ~15 Ma by the preservation of a frozen landscape along the TAM with freezing erosive-protecting conditions at higher altitudes and wet-based erosive-strengthening conditions at low elevation glaciers. Total incision within the Terra Nova Bay region since ~30 Ma increases from the northern tip of the Eisenhower Range escarpment (~1.8 km) and the Deep Freeze Range (~1.9 km) southwards along the length of the Priestley Glacier (~2.3 km) to the southern Eisenhower Range (~3.3 km) and the coastal region of the Prince Albert Mountains (~4.8 km) suggesting backstepping erosion due to different intensive glacial incision from the coast northwards. Higher basement incision at the coast than in the interior is attributed to a change of exhumation style from downwearing to backstepping incision subsequent to sediment removal probably related to the vicinity of the West Antarctic Rift System and corresponding necking, rift shoulder uplift and isostatic compensation. Basement surface exposure in the interior of the northern Terra Nova Bay region between ~3 Ma (Eisenhower Range) and ~8 Ma (Deep Freeze Range) is in accordance with regional summit exposure ages of ~5 Ma derived by cosmogenic nuclide data from the southern Deep Freeze Range, while earlier basement top exposure in the southern Eisenhower Range and in the Prince Albert Mountains at ~18 Ma is consistent with results of cosmogenic data from the Dry Valleys that infer only minor modifications of the landscape surface over at least the last ~15 myr. Further cooling of a sample at the surface refers to the development of an orographic gradient due to ongoing incision of the subjacent basement and the formation of topography.

Appendix A – Apatite Fission Track data

A1 - Apatite fission track data (table)

Sample	Lat. S Long.E	Elevation [m]	ξ	ρ_D [10^6cm^{-2}] (N_D)	ρ_S [10^6cm^{-2}] (N_S)	ρ_I [10^6cm^{-2}] (N_I)	P(χ^2) [%]	Dated grains [N]	AFT age [Ma] (predicted age)	MTL [µm] (n)	MTL c-axis [µm] (predicted MTL)	SD [µm]	SD c-axis [µm] (predicted SD)	Dpar mean [µm]	AHe central age [Ma]	unc. AHe single age [Ma] (predicted age)	GOF AFT age/MTL AHe age
Northern Eisenhower Range																	
3468	73.909	2132	320	17.9	9.2	15.7	99	25	165.0±12.0	11.00±0.24	12.67	2.46	1.51	1.89	86.55±4.24	91.3±9.0/81.3±8.0	0.90/0.05
	161.457		±10	(17974)	(389)	(666)			(163.0)	(106)	(12.76)		(1.66)			(94.3/94.8)	0.51/0.09
3469	73.931	2401	320	17.9	12.7	17.7	100	20	203.0±17.0	11.15±0.22	12.86	2.27	1.34	1.91	152.9±17.94	94.8±5.3	0.52/0.50
	161.569		±10	(17974)	(289)	(401)			(214.0)	(104)	(13.19)		(1.46)			(91.7)	0.56
3470	73.978	2620	320	18.0	12.9	14.1	93	20	259.0±18.0	11.22±0.23	12.75	2.39	1.48	1.92	172.98±16.28	109.2±6.8	0.60/0.24
	161.692		±10	(922)	(470)	(513)			(269.0)	(104)	(13.33)		(1.34)			(105.0)	0.54
Priestley Glacier																	
3450	74.198	1150	320	15.8	8.1	28.5	99	20	71.0±6.8	12.20±0.31	13.53	2.36	1.64	2.15	70.45±5.19	72.0±5.0	0.05/0.25
	162.749		±10	(15653)	(157)	(555)			(84.5)	(57)	(13.59)		(1.62)			(62.1)	0.05
3448	74.185	1300	320	23.4	19.8	83.2	95	24	88.6±5.0	12.29±0.20	13.51	2.04	1.46	2.04	-	-	0.94/0.77
	162.717		±10	(17974)	(547)	(2292)			(88.2)	(100)	(13.67)		(1.58)				-
3452	74.205	1430	320	15.7	26.3	71.3	100	30	92.4±6.4	12.49±0.24	13.64	2.02	1.48	2.15	50.32±3.39	36.4±2.3	0.83/0.52
	162.748		±10	(15653)	(358)	(970)			(93.7)	(70)	(13.66)		(1.55)			(36.7)	0.89
3453	74.21	1625	320	15.7	28.7	70.4	99	20	102.0±5.0	12.46±0.21	13.64	2.05	1.50	2.12	-	-	0.62/0.97
	162.748		±10	(15653)	(991)	(2429)			(104.0)	(100)	(13.79)		(1.52)				-
3460	74.217	1675	320	15.7	23.1	54.4	59	20	106.0±5.0	12.13±0.22	13.37	2.2	1.61	1.96	90.03±8.40	56.1±3.5	0.50/0.55
	162.533		±10	(15653)	(1004)	(2362)			(110.0)	(103)	(13.83)		(1.50)			(50.5)	0.11
3454	74.216	1780	320	15.7	18.7	45.7	74	20	102.3±5.0	12.35±0.22	13.71	2.3	1.61	1.99	-	-	0.99/0.95
	162.758		±10	(15653)	(901)	(2200)			(102.0)	(107)	(13.72)		(1.57)				-
3455	74.218	1900	320	15.7	16.3	37.1	85	30	109.3±5.0	11.72±0.22	13.25	2.36	1.40	1.99	66.82±9.84	43.2±2.7	0.51/0.18
	162.757		±10	(15653)	(1443)	(3291)			(112.0)	(111)	(13.63)		(1.51)			(38.9)	0.12
3456	74.224	2070	320	15.7	21.2	43.4	77	20	121.0±6.0	11.43±0.24	13.00	2.38	1.54	2.03	104±9.36	73.5±4.6	0.05/0.06
	162.76		±10	(15653)	(902)	(1848)			(133.0)	(100)	(13.56)		(1.59)			(64.3)	0.05
3459	74.231	2280	320	15.6	29.8	46.8	100	20	157.6±9.0	11.14±0.24	12.74	2.41	1.54	1.96	130.09±8.82	134.7±8.3	0.54/0.51
	162.768		±10	(15653)	(605)	(950)			(163.0)	(101)	(13.02)		(1.72)			(139.9)	0.54
3458	74.235	2400	320	15.6	42.5	55.6	100	20	188.6±9.0	11.19±0.23	12.80	2.30	1.44	2.07	120.22±12.76	75.2±4.7	0.84/0.51
	162.773		±10	(15653)	(1561)	(2042)			(187.0)	(100)	(13.18)		(1.59)			(74.9)	0.96
3457	74.241	2530	320	15.6	24.6	30.2	100	20	201.0±12.0	11.20±0.24	12.86	2.52	1.61	2.02	100.51±11.14	69.9±4.3/72.8±4.5	0.50/0.73
	162.784		±10	(15653)	(680)	(833)			(210.0)	(110)	(13.25)		(1.56)			(69.4/63.8)	0.92/0.05
Southern Eisenhower Range																	
3475	74.71	430	320	18.1	5.2	46.5	98	22	32.4±2.3	13.79±0.19	14.54	1.91	1.61	2.29	42.98±3.3	38.1±4.4	0.11/0.05
	162.62		±10	(17974)	(281)	(2507)			(36.1)	(100)	(14.52)		(1.47)			(30.0)	0.07
BC7	74.75	660	320	18.1	5.6	46.0	100	25	35.3±2.6	13.33±0.23	14.29	1.95	1.40	2.34	-	-	0.92/0.20
	162.63		±10	(17974)	(251)	(2057)			(35.0)	(70)	(14.16)		(1.72)				-
3466	74.44	780	320	17.9	4.8	36.9	99	20	37.5±3.5	13.45±0.17	14.31	1.71	1.38	2.11	40.87±4.81	27.0±1.7	0.70/0.20
	162.72		±10	(17974)	(142)	(1080)			(38.9)	(100)	(14.03)		(1.74)			(12.3)	0.00
3465	74.42	1030	320	18.0	7.9	58.0	100	24	39.1±2.5	13.36±0.20	14.25	1.99	1.55	2.03	37.48±3.32	24.5±4.1	0.58/0.57
	162.70		±10	(17974)	(367)	(2697)			(40.4)	(100)	(13.94)		(1.80)			(18.2)	0.13
3464	74.47	1535	320	18.1	5.0	18.9	100	25	75.5±7.1	11.58±0.26	13.08	2.62	1.84	1.99	42.94±5.05	25.1±3.1	0.51/0.07
	162.63		±10	(17974)	(157)	(598)			(80.2)	(100)	(13.41)		(1.71)			(21.4)	0.24
3462	74.29	1720	320	182	5.1	15.9	99	20	92.9±8.1	11.21±0.37	12.93	2.45	1.41	1.99	-	-	0.65/0.53
	162.36		±10	(17974)	(195)	(606)			(96.8)	(43)	(13.50)		(1.60)				-
3463	74.36	2014	320	18.0	10.7	22.2	99	23	137.0±9.0	11.69±0.24	13.05	2.43	1.85	2.34	-	-	0.98/0.50
	161.85		±10	(17974)	(384)	(799)			(137.0)	(100)	(13.47)		(1.71)				-
3472	74.63	2180	320	15.6	10.8	18.4	96	25	144.0±8.0	11.22±0.27	12.88	2.66	1.72	2.19	82.48±12.32	59.6±3.7	0.07/0.05
	162.58		±10	(15663)	(750)	(1284)			(155.0)	(100)	(13.04)		(1.76)			(52.2)	0.05

Table continued

Sample	Lat. S Long.E	Elevation [m]	ξ	ρ_D [10^6cm^{-2}] (N_D)	ρ_S [10^6cm^{-2}] (N_S)	ρ_i [10^6cm^{-2}] (N_i)	P(χ^2) [%]	Dated grains [N]	AFT age [Ma] (predicted age)	MTL [µm] (n)	MTL c-axis [µm] (predicted MTL)	SD [µm]	SD c-axis [µm] (predicted SD)	Dpar mean [µm]	AHe central age [Ma]	unc. AHe single age [Ma] (predicted age)	GOF AFT age/MTL AHe age
Mount Matz																	
BC4	74.67 162.20	700	320 ±10	23.6 (17974)	3.7 (167)	26.5 (1205)	100	24	52.2±4.6 (52.4)	12.73±0.35 (40)	13.94 (13.92)	2.18	1.49 (1.88)	2.14	69.59±7.11	47.3±4.7 (34.6)	0.95/0.16 0.03
BC5	74.70 162.26	940	320 ±10	23.6 (23364)	5.8 (499)	40 (3426)	100	30	54.8±3.1 (54.1)	13.26±0.22 (80)	14.19 (13.91)	1.97	1.51 (1.88)	2.34	47.37±3.44	33.7±2.1 (20.5)	0.82/0.50 0.00
BC3	74.77 162.37	1220	320 ±10	23.6 (17974)	8.5 (305)	46.4 (1660)	99	20	69.1±4.8 (70.0)	11.60±0.28 (100)	13.22 (13.46)	2.77	1.66 (1.74)	2.2	81.56±4.98	59.4±3.7 (36.7)	0.67/0.66 0.00
BC2	74.92 162.50	1450	320 ±10	23.6 (23364)	7.9 (333)	36.3 (1539)	98	20	81.3±5.5 (80.5)	11.54±0.29 (100)	13.15 (13.59)	2.93	1.77 (1.78)	2.36	67.8±5.36	35.9±2.0 (22.0)	0.88/0.53 0.00
BC1	74.77 162.39	1590	320 ±10	23.6 (23364)	8.2 (740)	31.1 (2824)	86	25	98.3±5 (96.7)	11.63±0.27 (84)	13.11 (13.56)	2.68	1.76 (1.73)	1.90	79.59±10.16	49.4±3.1 (25.3)	0.75/0.82 0.00
Mount Nansen																	
C17	74.72 162.74	220	366 ±12	7.07 (5541)	7.8 (577)	28.04 (2062)	83	20	36.6±2.7 (33.1)	14.01±0.13 (101)	14.76 (14.76)	1.29	1.00 (1.09)	1.81	-	-	0.16/0.62 -
C9	74.73 162.69	300	366 ±12	7.07 (5541)	2.3 (281)	9.5 (1133)	70	28	32±2.4 (-)	-	-	-	-	1.79	-	-	-
C6	74.78 162.50	1020	366 ±12	7.07 (5541)	4.6 (481)	12.6 (1277)	88	30	48.5±3.1 (-)	13.22±0.55 (18)	-	2.35	-	1.57	-	-	-
C5	74.68 162.50	1390	366 ±12	7.07 (5541)	4 (113)	6.53 (187)	53	12	77.5±9.8 (-)	-	-	-	-	1.61	-	-	-
C4	74.66 162.53	1780	366 ±12	7.07 (5541)	6 (586)	9.1 (903)	7	30	82.1±6.1 (-)	12.85±0.42 (26)	-	2.14	-	1.70	-	-	-
C3	74.65 162.55	1950	366 ±12	7.07 (5541)	9 (852)	11.4 (1095)	30	30	99.8±6 (99.1)	12.26±0.31 (43)	13.51 (13.51)	2.02	1.53 (1.67)	1.62	-	-	0.90/0.60 -
C1	74.47 162.62	2380	366 ±12	7.07 (5541)	19.4 (1083)	14.2 (790)	<5	25	175.0±14 (179.0)	11.5±0.26 (101)	13.06 (13.10)	2.63	1.77 (1.60)	1.73	-	-	0.68/0.99 -
Archambault Ridge																	
3338	73.75 163.15	1590	320 ±10	14.5 (7360)	13.4 (168)	51.7 (652)	100	20	59.6±5.5 (63.2)	12.38±0.21 (100)	13.63 (13.52)	2.06	1.50 (1.72)	1.83	58.2±6.9	39.3±4.0 (21.8)	0.50/0.51 0.00
3339	73.75 163.15	1740	320 ±10	14.5 (7360)	15.1 (160	54.7 (580)	100	20	63.7±6.0	12.43±0.51 (16)		2.04		1.84			
3337	73.69 163.16	2000	320 ±10	14.5 (7360)	31.6 (530)	96.1 (1615)	97	20	75.8±4.5 (76.7)	11.76±0.23 (105)	13.25 (13.49)	2.3	1.50 (1.64)	1.91			0..83/0.11
3343	73.73 163.1	2310	320 ±10	14.5 (7360)	42.0 (866)	86.4 (1712)	93	20	112.7±5.9 (115)	11.3±0.24 (100)	12.96 (13.31)	2.36	1.50 (1.53)	1.92	104.7±12.3	63.4±5.0 (60.9)	0.64/0.80 0.62
3302	73.69 162.74	2560	320 ±10	14.5 (7360)	38.3 (368)	54.9 (527)	98	20	160±12.0 (165)	11.04±0.22 (100)	12.71 (13.15)	2.17	1.40 (1.51)	1.89	133.4±15.9	134.8±10.0 (128.5)	0.66/0.50 0.53
3336	73.69 162.99	2600	320 ±10												137.1±16.1		
3340	73.65 162.65	2690	320 ±10	14.5 (7360)	15.7 (190	21.7 (262)	100	20	166.7±16.7 (169)	11.05±0.87 (15)	13.04 (12.37)	3.36	21.0 (1.67)	1.92	30.0±3.4	18.8±2.0 (18.7)	0.86/0.21 0.96
3303	73.68 162.6	2790	320 ±10	14.5 (7360)	16.9 (216)	19.9 (313)	100	20	194.4±17.3 (223)	11.35±0.88 (15)	12.84 (13.62)	2.19	1.66 (1.23)	1.91	112.8±13.5	82.7±5.2 (80.0)	0.05/0.42 0.60

Table continued

Sample	Lat. S Long.E	Elevation [m]	ξ	ρ_D [10^6cm^{-2}] (N_D)	ρ_S [10^6cm^{-2}] (N_S)	ρ_i [10^6cm^{-2}] (N_i)	P(χ^2) [%]	Dated grains [N]	AFT age [Ma] (predicted age)	MTL [µm] (n)	MTL c-axis [µm] (predicted MTL)	SD [µm]	SD c-axis [µm] (predicted SD)	Dpar mean [µm]	AHe central age [Ma]	unc. AHe single age [Ma] (predicted age)	GOF AFT age/MTL AHe age
Mount Gibbs																	
PB7		1800	320 ±10	17.1 (8556)	30.1 (472)	101.2 (1589)	64	20	80.8±5.0 (89.4)	12.03±0.18 (100)	13.38 (13.40)	1.78	1.32 (1.60)	1.95	66.2±7.8	38.9±2.4 (32.6)	0.08/0.09 0.07
PB6		2470	320 ±10	20.8 (10402)	31.5 (865)	77.5 (2131)	17	20	134.3±7.0 (137)	11.35±0.22 (120)	12.75 (12.96)	2.46	1.74 (1.83)	2.05	110.1±14.0	110.1±6.8 (106.6)	0.60/0.30 0.61
PB4		3000	320 ±10	20.8 (10402)	43.2 (1454)	69.7 (2348)	42	20	205.2±9.9 (205)	11.26±0.22 (120)	12.76 (13.11)	2.43	1.54 (1.58)	2.01	130.9±16.5	99.5±6.2/97.1±6.0 (102.6/87.0)	0.81/0.54 0.62/0.09
PB1		3120	320 ±10	20.8 (10402)	42.4 (1565)	55.1 (2032)	57	20	251.6±11.4 (246)	11.5±0.23 (116)	12.92 (12.92)	2.45	1.60 (1.50)	2.05	181.8±21.8	121.8±7.5/134.5±8.3 (115.9/137.9)	0.65/0.53 0.43/0.68
Tourmaline Plateau																	
3435	74.09 163.57	1060	320 ±10	13.5 (13562)	6.1 (98)	25.9 (420)	100	20	50.4±5.9 (46.5)	12.53±0.38 (42)	13.75 (13.68)	2.47	1.67 (1.83)	1.87			0.51/0.79
3436	74.09 163.57	1200	320 ±10	13.5 (13562)	9.1 (152)	38.2 (642)	100	20	51.1±4.9 (48.0)	12.81±0.33 (101)	14.11 (13.70)	2.21	1.46 (1.73)	1.93			0.52/0.54
3437	74.09 163.56	1380	320 ±10	13.6 (13562)	4.9 (148)	17.6 (531)	100	20	60.2±5.9 (57.2)	12.29±0.26 (104)	13.83 (13.72)	2.61	1.53 (1.74)	1.88			0.61/0.50
3434	74.1 163.33	1570	320 ±10	13.6 (13562)	4.5 (107)	14.5 (342)	100	20	67.6±7.8 (67.0)	12.03±0.24 (97)	13.45 (13.60)	2.38	1.55 (1.68)	1.92			0.94/0.54
3441	74.1 163.32	1640	320 ±10	13.6 (13562)	8.6 (193)	27.7 (620)	95	20	67.6±5.8	12.0±0.7 (12)		2.41		1.85			
3443	74.11 163.28	1830	320 ±10	13.6 (13562)	9.7 (149)	27.5 (424)	100	20	76±7.6 (80.2)	12.12±0.25 (99)	13.60 (13.47)	2.51	1.52 (1.64)	1.91			0.58/0.70
3444	74.11 163.27	1950	320 ±10	13.6 (13562)	6.8 (106)	18.8 (291)	100	20	78.8±9.3 (84.6)	12.01±0.21 (101)	13.44 (13.64)	2.14	1.46 (1.60)	1.89			0.54/0.55
3445	74.12 163.23	2040	320 ±10	13.7 (13562)	17.7 (256)	44.8 (650)	100	20	85.6±6.8	11.83±0.55 (12)		1.91		1.89			
3446	74.12 163.22	2215	320 ±10	13.7 (13562)	11.8 (99)	25.4 (213)	100	15	101.2±12.7	(3)				1.81			

A1: Apatite fission track (AFT) and (U-Th-Sm)/He (AHe) data of the northern Terra Nova Bay region. AFT ages were determined by counting spontaneous and induced fission tracks according to the Zeta calibration method (e.g., Hurford and Green, 1982, 1983) for dosimeter glass CN5, and calculated using Trackkey (Dunkl, 2006). Zeta values are 320±10 (Prenzel) and 366±12 (Balestrieri). Errors are quoted as ±1σ (Green, 1981). If possible, 100 fission track lengths for each sample were measured following the recommendations of Laslett et al. (1982). Dpar was measured as indicator for fission track annealing kinetic properties (e.g., Donelick, 1993; Carlson et al., 1999). Corresponding AHe central ages are shown if available. The goodness of fit (GOF) between measured and predicted AFT ages, fission track lengths, and AHe single grain ages is quoted for HeFTy c-axis projected forward models using the radiation damage model of Flowers et al. (2009).

A2 - Apatite fission track age-elevation plot

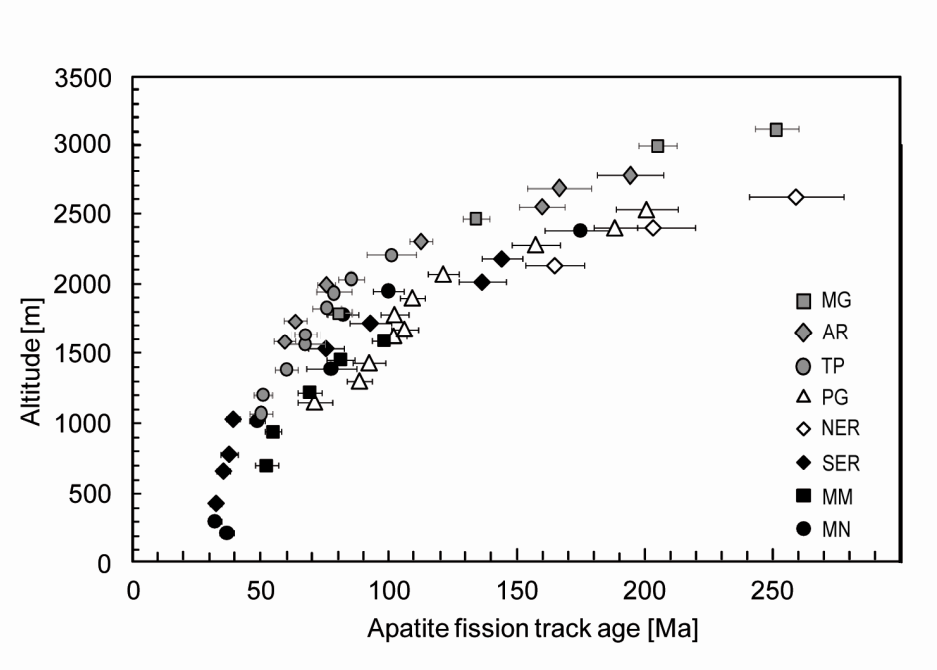

A2: Plot showing apatite fission track (AFT) ages vs. sample altitude. The complete AFT data from the Terra Nova Bay region (54 samples) comprising vertical profiles from the area southwest (MM: Mount Matz; MN: Mount Nansen; NER: northern Eisenhower Range; PG: Priestely Glacier; SER: southern Eisenhower Range; 34 samples) and northeast of the Priestley Glacier (AR: Archambault Ridge; MG: Mount Gibbs; TP: Tourmaline Plateau; 20 samples) show ages between 32±2 Ma and 259±18 Ma which closely correlate with sample altitude (220 – 3120 m).

A3 - Apatite fission track age-mean track lengths plot

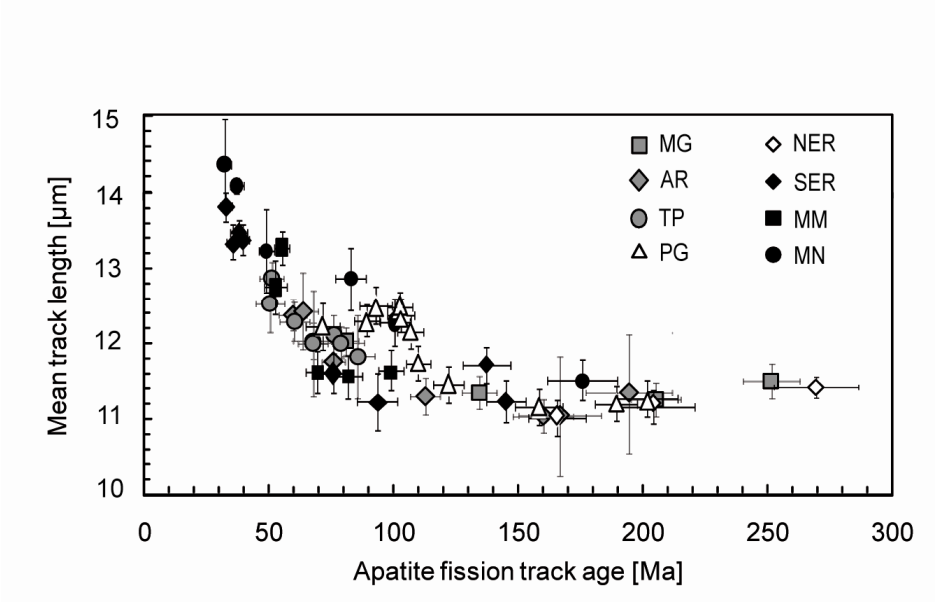

A3: The relation between apatite fission track (AFT) ages and mean track lengths (MTL) shows a concave “boomerang” pattern as described by Green (1986); ; AR: Archambault Ridge; MG: Mount Gibbs; MM: Mount Matz; MN: Mount Nansen; NER: northern Eisenhower Range; PG: Priestley Glacier; SER: southern Eisenhower Range; TP: Tourmaline Plateau.

A4 - Radial plots

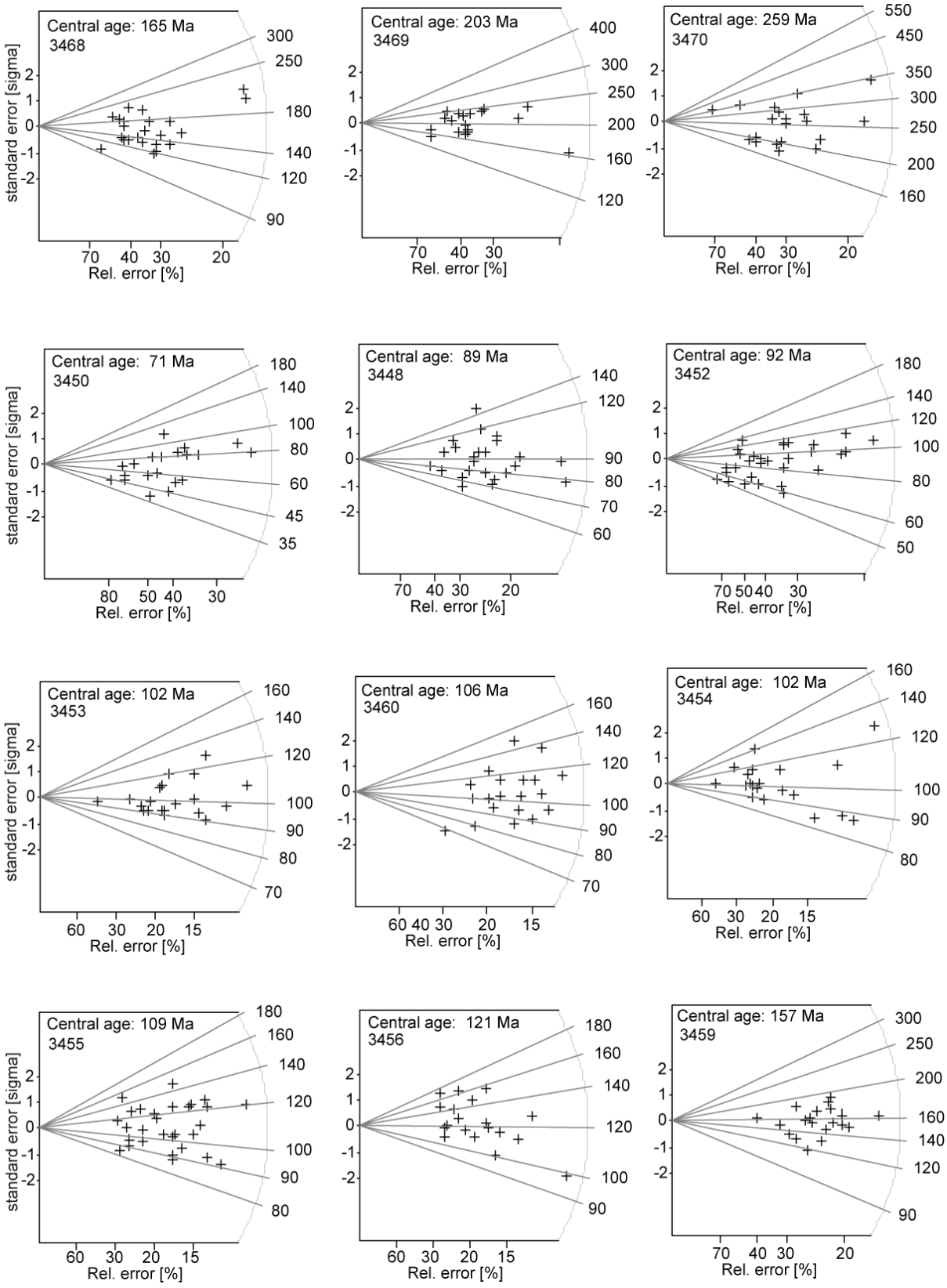

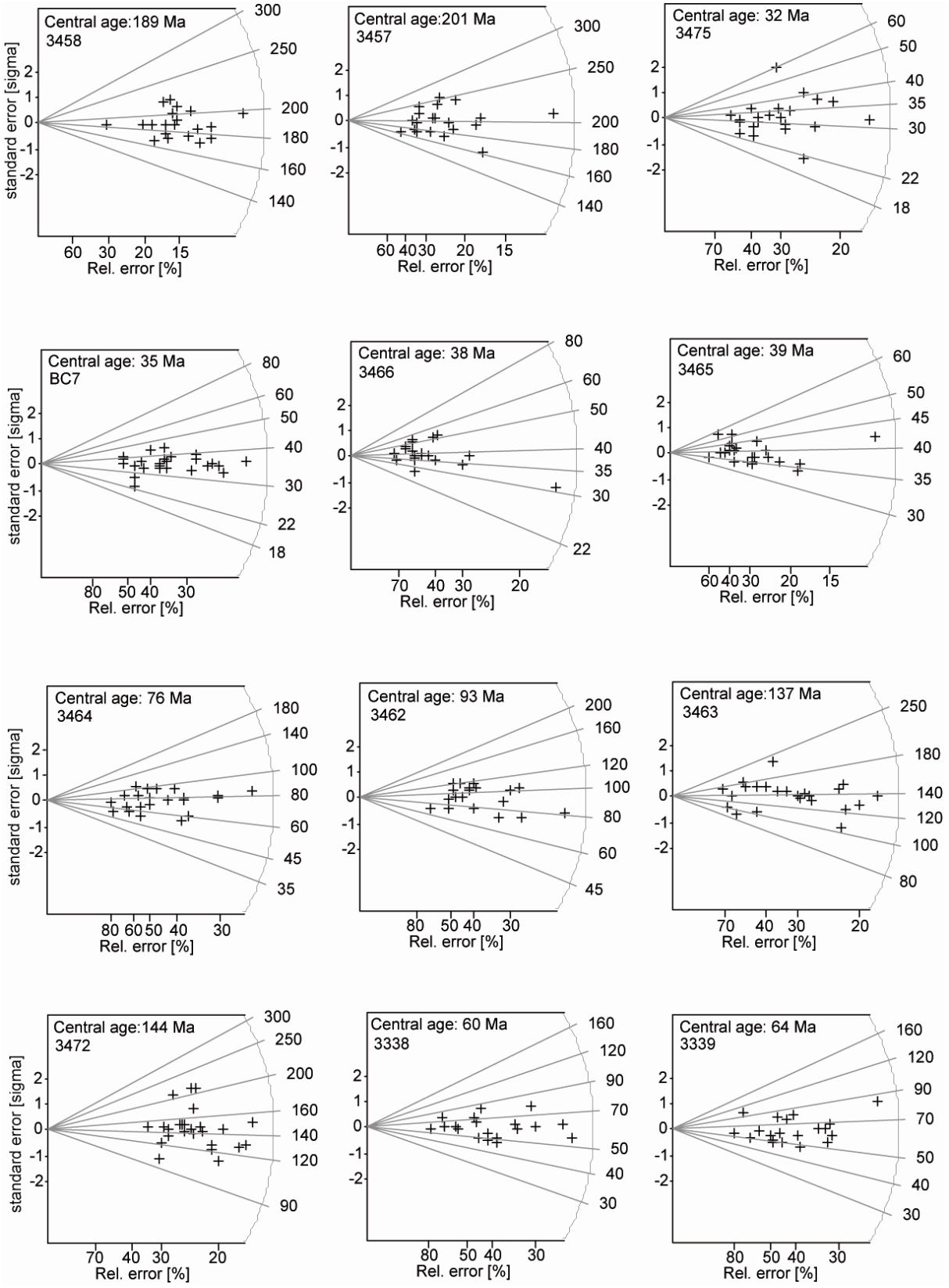
Central age:189 Ma
3458
Central age:201 Ma
3457
Central age: 32 Ma
3475
Central age: 35 Ma
BC7
Central age: 38 Ma
3466
Central age: 39 Ma
3465
Central age: 76 Ma
3464
Central age: 93 Ma
3462
Central age:137 Ma
3463
Central age:144 Ma
3472
Central age: 60 Ma
3338
Central age: 64 Ma
3339
standard error [sigma]
Rel. error [%]

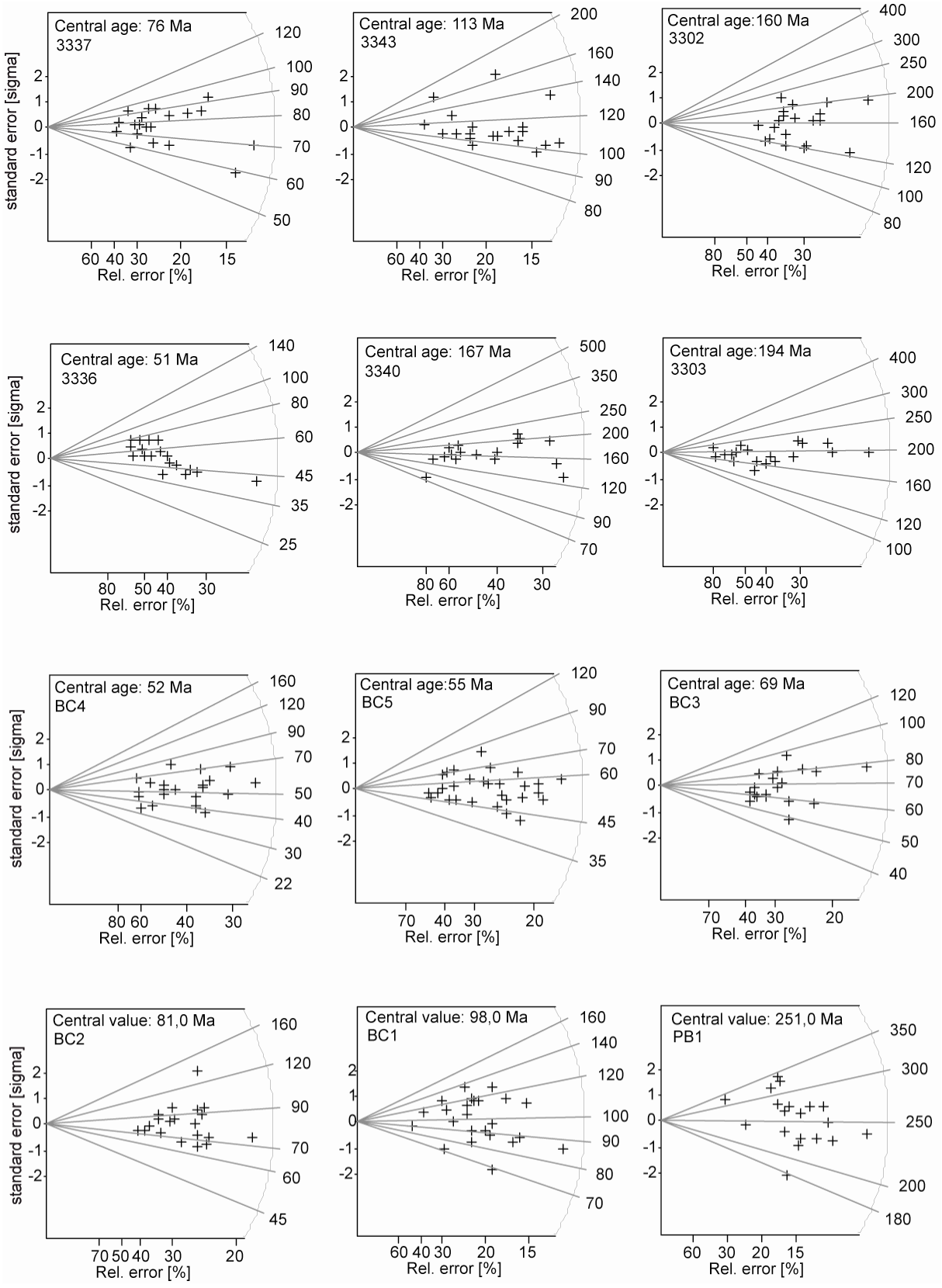
Central age: 76 Ma
3337
Central age: 113 Ma
3343
Central age:160 Ma
3302
Central age: 51 Ma
3336
Central age: 167 Ma
3340
Central age:194 Ma
3303
Central age: 52 Ma
BC4
Central age:55 Ma
BC5
Central age: 69 Ma
BC3
Central value: 81,0 Ma
BC2
Central value: 98,0 Ma
BC1
Central value: 251,0 Ma
PB1
standard error [sigma]
Rel. error [%]

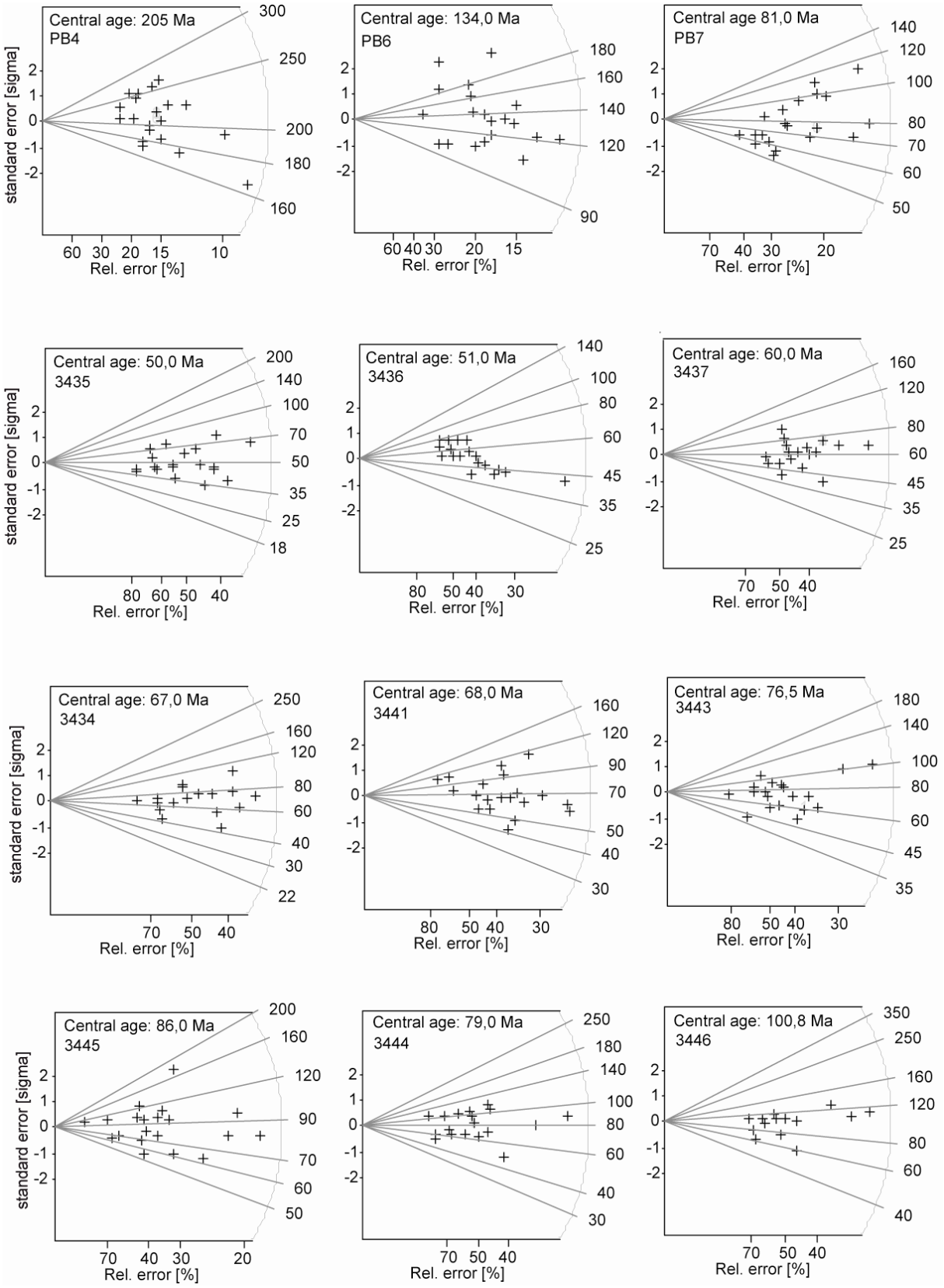

A4: Radial plots show single grain ages of the samples from the Archambault Ridge, Priestley Glacier, Mount Gibbs; northern and southern Eisenhower Range (including Mount Matz) and Tourmaline Plateau.

A5 – Samples fission track lengths distributions

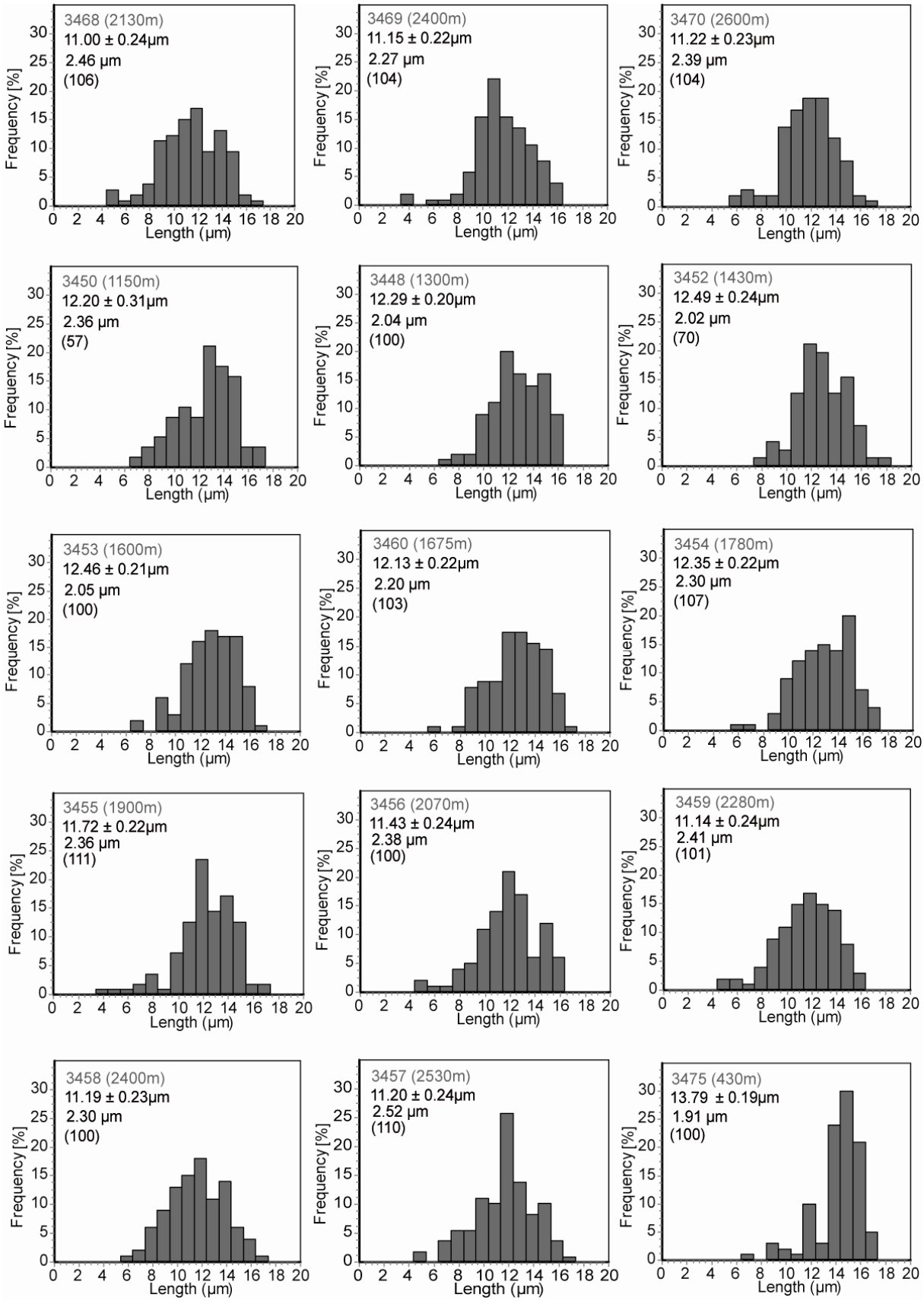

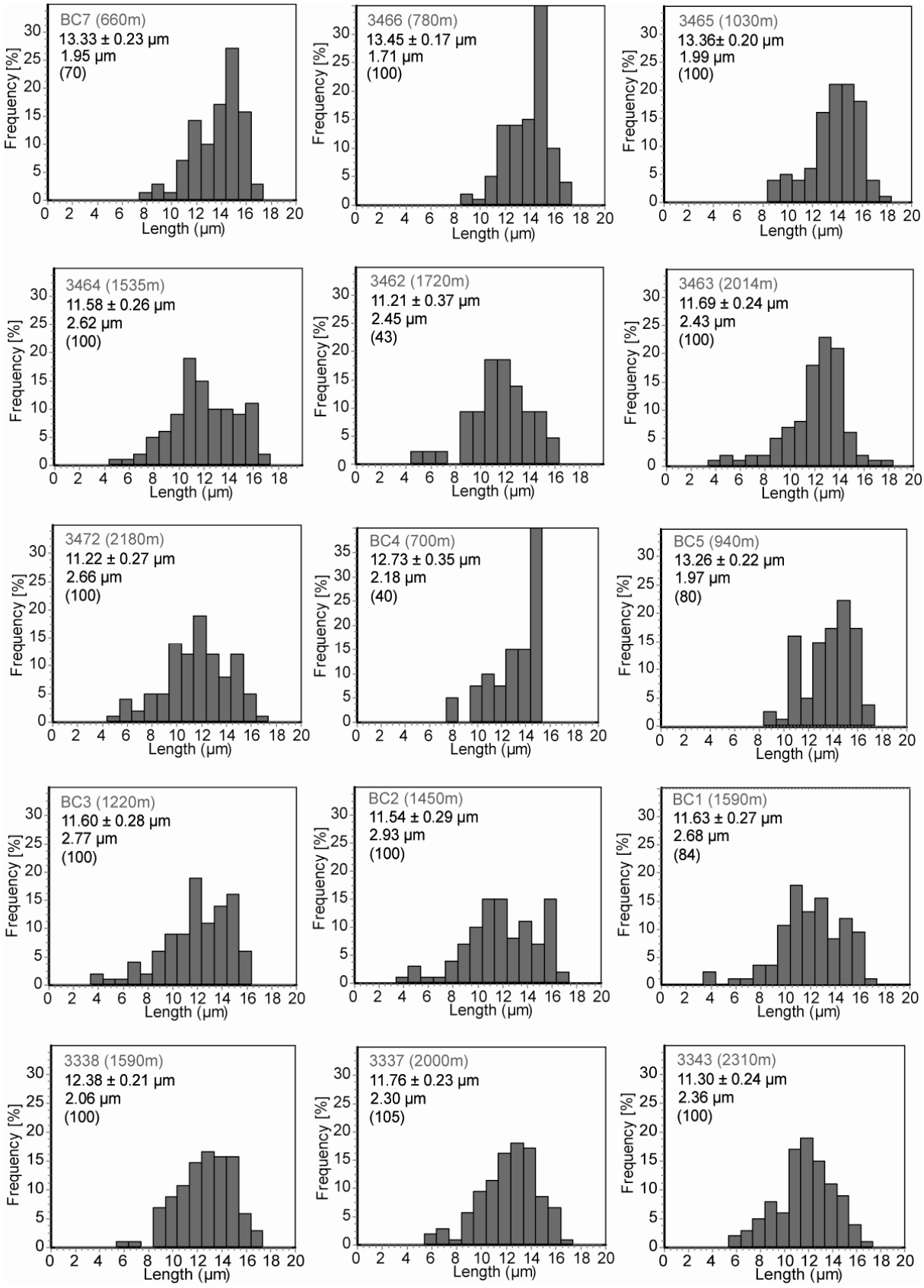
BC7 (660m)
13.33 ± 0.23 µm
1.95 µm
(70)
3466 (780m)
13.45 ± 0.17 µm
1.71 µm
(100)
3465 (1030m)
13.36± 0.20 µm
1.99 µm
(100)
3464 (1535m)
11.58 ± 0.26 µm
2.62 µm
(100)
3462 (1720m)
11.21 ± 0.37 µm
2.45 µm
(43)
3463 (2014m)
11.69 ± 0.24 µm
2.43 µm
(100)
3472 (2180m)
11.22 ± 0.27 µm
2.66 µm
(100)
BC4 (700m)
12.73 ± 0.35 µm
2.18 µm
(40)
BC5 (940m)
13.26 ± 0.22 µm
1.97 µm
(80)
BC3 (1220m)
11.60 ± 0.28 µm
2.77 µm
(100)
BC2 (1450m)
11.54 ± 0.29 µm
2.93 µm
(100)
BC1 (1590m)
11.63 ± 0.27 µm
2.68 µm
(84)
3338 (1590m)
12.38 ± 0.21 µm
2.06 µm
(100)
3337 (2000m)
11.76 ± 0.23 µm
2.30 µm
(105)
3343 (2310m)
11.30 ± 0.24 µm
2.36 µm
(100)
Frequency [%]
Length (µm)

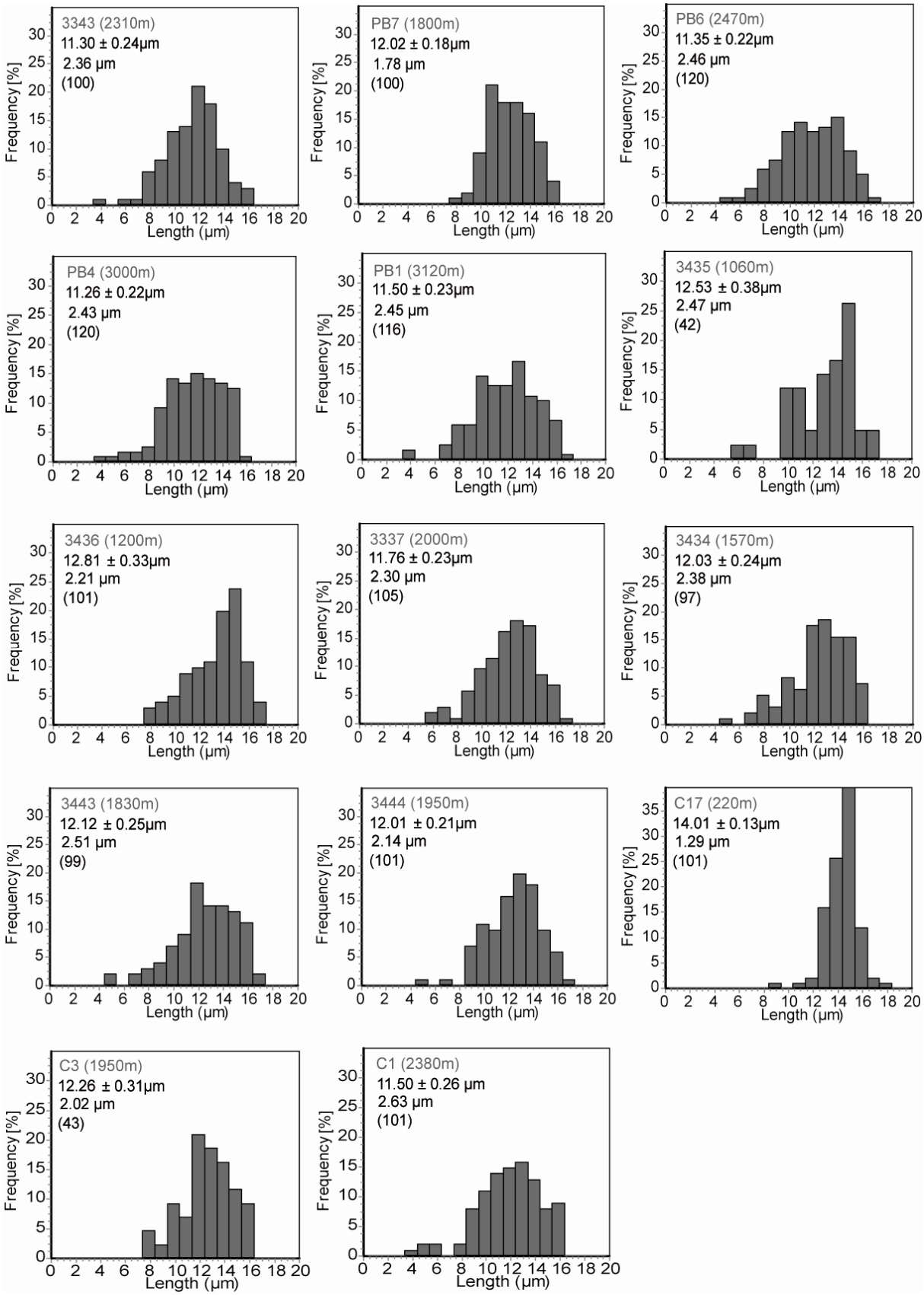

A5: Fission track length distribution pattern from all sample with a number of ≥40 confined track lengths. Samples MTL and associated standard deviations range from 11.00±0.24 – 14.01±0.13 µm and 3.36 µm – 1.29 µm.

Appendix B - U-Th-Sm/He-data

B1 - U-Th-Sm/He-data (table)

Sample	Elevation [m]	Length [µm]	Width [µm]	Sp.radius [µm]	Mass [µg]	4He [ncc]	eU [ppm]	Total Sm [ppm]	Total Th [ppm]	Total U [ppm]	Uncorr. age [Ma]	FT corr.	Corr. age [Ma]	2σ error [Ma[	AFT age [Ma]
Eisenhower Range															
3475-a	430	143	62	36	1.38	0.08	20.27	17.30	15.37	16.54	22.12	0.63	35.26	4.15	32.4±2.3
3475-b	430	150	81	45	2.46	0.18	22.65	18.56	10.19	20.11	26.57	0.70	37.82	4.45	32.4±2.3
3475-c	430	185	98	61	4.46	0.40	22.90	20.76	15.73	19.05	32.64	0.76	43.21	5.08	32.4±2.3
3475-d	430	124	86	51	1.46	0.17	35.47	25.66	15.25	31.67	27.71	0.70	39.86	4.69	32.4±2.3
3475-e (A)	430	79	65	41	0.97	0.11	17.59	19.93	38.75	8.40	51.26		51.26	3.18	32.4±2.3
3475-f (A) #	430	92	83	49	1.66	0.15	19.54	13.56	25.86	13.41	38.07		38.07	2.36	32.4±2.3
Mean													40.91	4.15	
Wt mean													41.06	3.49	
Central													42.98	3.30	
3466-a	780	108	70	42	1.31	0.13	30.83	62.45	37.00	21.62	26.99	0.64	42.39	4.99	37.5±3.5
3466-b	780	131	92	55	1.77	0.22	35.97	68.64	31.67	27.94	28.03	0.71	39.35	4.63	37.5±3.5
Mean													40.87	4.81	
Wt mean													40.76	4.80	
Central															
3465-a	1030	159	80	45	2.58	0.28	35.12	57.08	34.91	26.45	25.35	0.70	36.07	4.24	39.1±2.5
3465-b #	1030	159	98	60	2.50	0.46	53.79	93.46	68.86	36.88	28.28	0.73	38.54	4.53	39.1±2.5
3465-c #	1030	126	79	47	1.29	0.27	70.41	102.37	78.61	51.15	24.50	0.67	36.50	4.30	39.1±2.5
Mean													37.04	4.36	
Wt mean													36.98	4.35	
Central													37.48	3.32	
3464-a #	1530	137	64	37	1.10	0.08	24.15	94.06	21.72	18.17	25.08	0.58	42.94	5.05	75.5±7.1
3464-b *	1530	88	65	35	0.58	0.16	19.70	122.76	19.46	13.95	112.52	0.59	191.83	22.57	75.5±7.1
3468-a x	2130	145	84	50	1.71	0.32	17.89	86.79	22.45	11.81	85.79	0.69	124.22	14.62	164.9±11.6
3468-b x	2130	93	66	39	1.03	0.24	23.83	63.92	26.54	17.03	80.81	0.61	132.60	15.60	164.9±11.6
3468-c x	2130	172	79	45	2.24	0.42	19.96	73.76	15.36	15.65	77.50	0.67	115.95	13.64	164.9±11.6
3468-d (A) #	2130	78	65	41	0.63	0.06	9.15	51.70	14.54	5.26	81.25		81.25	5.04	164.9±11.6
3468-e (A) #	2130	75	64	40	0.57	0.13	21.20	65.89	26.19	14.46	91.34		91.34	5.66	164.9±11.6
Mean													83.34	5.17	
Wt mean													84.95	5.27	
Central													86.55	4.24	
3472-a #	2180	196	103	66	3.58	0.75	28.90	26.70	25.41	22.73	59.60	0.76	78.94	9.29	144.4±7.9
3472-b	2180	137	76	46	1.36	0.54	48.03	30.56	71.69	31.09	67.31	0.66	101.27	11.92	144.4±7.9
3472-c	2180	113	95	55	1.53	0.27	25.38	22.03	21.68	20.13	56.19	0.71	78.72	9.26	144.4±7.9
3472-d	2180	110	70	38	1.11	0.17	23.50	17.21	24.04	17.75	52.15	0.60	87.18	10.26	144.4±7.9
Mean													81.61	10.18	
Wt mean													81.25	9.98	
Central													82.48	12.32	
3469-a	2400	149	71	43	1.31	0.49	28.24	65.00	40.43	18.21	108.27	0.65	167.85	19.75	203.5±16.5
3469-b #	2400	120	82	48	1.28	0.57	38.45	79.16	57.27	24.38	94.80	0.68	140.39	16.52	203.5±16.5
3469-c	2400	262	109	71	7.76	1.09	11.04	34.36	17.55	6.63	103.99	0.79	132.12	15.55	203.5±16.5
3469-d	2400	172	119	73	3.93	1.03	19.36	54.48	30.24	11.80	107.81	0.78	138.97	16.35	203.5±16.5
3469-e	2400	124	60	39	0.78	0.30	28.97	65.89	55.72	15.38	108.87	0.58	188.99	22.24	203.5±16.5
Mean													153.66	17.04	
Wt mean													148.40	16.78	
Central													152.90	17.94	
3470-a *	2620	164	74	48	1.80	0.15	14.05	46.80	23.13	8.22	47.59	0.64	74.50	8.77	259.5±18.4
3470-b #	2620	140	64	43	1.43	0.39	20.19	63.83	42.01	9.80	109.18	0.63	174.29	20.51	259.5±18.4
3470-c	2620	169	82	53	2.83	1.00	20.95	57.94	33.99	12.48	137.27	0.71	193.71	22.79	259.5±18.4
3470-d	2620	174	79	52	1.93	0.27	12.26	57.58	27.18	5.38	94.86	0.68	140.09	16.48	259.5±18.4
Mean													169.36	19.93	
Wt mean													163.21	19.20	
Central													172.98	16.28	

Mount Matz

BC4-a	700	170	93	60	3.70	0.42	14.98	25.30	24.26	9.10	62.59	0.74	84.93	9.99	52.2±4.6
BC4-b *	700	136	101	61	2.20	0.58	21.30	56.11	23.39	15.31	101.73	0.73	138.45	16.29	52.2±4.6
BC4-c	700	209	78	52	2.29	0.55	35.34	38.13	64.01	20.10	55.44	0.68	81.15	9.55	52.2±4.6
BC4-d	700	119	110	63	2.05	0.15	12.87	20.01	18.71	8.33	47.31	0.74	63.58	7.48	52.2±4.6
BC4-g (A)	700	81	80	45	0.85	0.10	19.22	35.00	27.91	12.39	49.82		49.82	3.09	52.2±4.6
BC4-e (A)	700	95	93	52	1.33	0.38	31.91	45.08	56.11	18.45	73.01		73.01	4.53	52.2±4.6
BC4-f (A)	700	84	82	47	1.00	0.36	33.57	46.62	63.57	18.36	88.41		88.41	5.48	52.2±4.6
Mean													73.48	10.29	
Wt mean													64.69	3.73	
Central													69.59	7.11	
BC5-a	940	139	103	62	2.30	0.45	43.96	36.10	57.20	30.33	36.50	0.74	49.32	5.80	54.1±3.8
BC5-b	940	147	95	58	2.16	0.36	41.25	43.83	53.66	28.36	33.66	0.72	46.51	5.70	54.1±3.8
BC5-c	940	150	113	61	3.96	0.51	31.22	29.55	42.36	21.10	33.73	0.74	45.52	5.36	54.1±3.8
Mean													47.12	5.62	
Wt mean													47.03	5.61	
Central													47.37	3.44	
BC3-a	1220	141	94	58	3.11	0.46	21.82	6.03	23.71	16.26	56.05	0.73	76.96	9.06	69.1±4.8
BC3-b	1220	115	80	49	1.83	0.38	27.44	7.06	38.05	18.54	61.05	0.68	90.12	10.60	69.1±4.8
BC3-c	1220	124	95	57	1.72	0.13	11.20	36.89	18.00	6.65	54.98	0.72	76.86	9.04	69.1±4.8
BC3-d	1220	158	119	71	5.59	0.87	21.63	7.50	21.61	16.54	59.39	0.78	76.17	8.96	69.1±4.8
BC3-e (A)	1220	65	64	36	0.44	0.13	30.60	11.35	59.95	16.58	79.67		79.67	4.94	69.1±4.8
Mean													79.96	8.52	
Wt mean													79.46	7.25	
Central													81.56	4.98	
BC2-a	1450	217	70	47	2.69	0.40	23.76	15.89	23.24	18.21	51.57	0.69	75.23	8.85	81.3±5.5
BC2-b	1450	136	77	49	1.37	0.15	25.01	41.13	37.35	15.94	35.91	0.67	53.86	6.34	81.3±5.5
BC2-c *	1450	122	76	47	1.20	0.30	19.15	43.27	31.78	11.35	110.81	0.63	169.03	19.89	81.3±5.5
BC2-d	1450	137	68	44	1.10	0.21	33.46	20.01	30.20	26.25	46.37	0.63	73.30	8.62	81.3±5.5
Mean													67.46	7.94	
Wt mean													62.32	7.57	
Central													67.80	5.36	
BC1-a	1590	145	101	63	3.74	0.43	13.41	12.58	17.17	9.30	70.36	0.75	94.35	11.10	98.3±5.0
BC1-b	1590	121	87	48	1.91	0.16	19.85	18.21	25.71	13.70	34.73	0.67	51.98	6.12	98.3±5.0
BC1-c	1590	129	87	54	2.48	0.20	12.19	14.44	18.55	7.75	55.05	0.71	77.83	9.16	98.3±5.0
BC1-d	1590	159	80	46	2.14	0.26	20.52	20.70	26.17	14.24	49.30	0.67	74.02	8.71	98.3±5.0
BC1-e	1590	146	98	61	2.95	1.00	35.68	33.94	49.63	23.83	77.93	0.73	106.39	12.52	98.3±5.0
Mean													80.91	9.52	
Wt mean													71.42	8.40	
Central													79.59	10.16	

Priestley Glacier

3450-a	1150	167	129	77	7.00	0.48	11.58	1.20	3.51	10.75	48.91	0.80	61.35	7.22	71.0±6.8
3450-b	1150	143	112	67	4.49	0.35	10.53	2.16	2.75	9.87	56.63	0.77	74.03	8.71	71.0±6.8
3450-c (A) #	1150	80	77	44	0.77	0.35	50.87	6.32	21.96	45.71	72.16		72.16	4.47	71.0±6.8
3450-d*	1150	117	89	53	1.20	0.17	46.34	3.95	8.91	44.23	26.23	0.69	38.28	4.50	71.0±6.8
Mean													69.18	6.80	
Wt mean													69.94	5.79	
Central													70.45	5.19	
3452-a *	1430	112	62	39	1.10	0.42	28.21	13.55	32.44	20.55	112.27	0.61	184.40	21.70	92.4±6.4
3452-b #	1430	169	114	70	3.56	0.84	53.55	14.56	10.91	50.87	36.35	0.77	47.08	5.54	92.4±6.4
3452-c	1430	211	86	57	3.96	0.70	36.86	10.45	31.55	29.44	39.53	0.74	53.74	6.32	92.4±6.4
Mean													50.41	5.93	
Wt mean													49.97	5.88	
Central													50.32	3.39	
3460-a #	1675	99	83	51	1.01	0.41	59.85	32.59	38.26	50.65	56.10	0.67	83.47	9.82	106.2±5.2
3460-b *	1675	157	78	50	2.40	0.54	12.61	4.71	6.58	11.03	145.26	0.70	207.96	24.47	106.2±5.2
3460-c	1675	154	128	75	6.33	2.73	39.33	23.68	22.45	33.88	83.51	0.79	105.67	12.43	106.2±5.2
Mean													94.57	11.13	
Wt mean													92.00	10.82	
Central													90.03	8.40	

3455-a	1900	182	99	62	3.67	0.89	50.81	51.86	36.41	41.84	39.37	0.73	54.28	6.39	109.3±4.8
3455-b*	1900	162	77	87	2.70	1.20	35.19	25.09	25.15	29.10	117.03	0.72	168.76	19.86	109.3±4.8
3455-c	1900	191	108	68	5.61	0.79	19.35	21.72	18.04	14.95	61.42	0.77	80.40	9.46	109.3±4.8
3455-d #	1900	119	88	56	2.68	0.32	32.06	29.78	23.06	26.41	43.15	0.67	64.24	7.56	109.3±4.8
Mean													66.31	7.80	
Wt mean													67.86	7.98	
Central													66.82	9.84	
3456-a	2070	153	84	50	2.28	0.89	49.13	28.47	22.35	43.66	65.68	0.68	96.59	11.37	121.4±6.2
3456-b *	2070	248	92	61	5.27	0.92	54.34	30.15	22.29	48.86	26.38	0.76	34.89	4.11	121.4±6.2
3456-c #	2070	203	81	59	3.34	1.66	55.53	26.08	15.30	51.72	73.53	0.72	102.06	12.01	121.4±6.2
3456-d	2070	166	114	70	5.40	1.77	31.32	30.69	21.17	26.10	85.94	0.78	110.74	13.03	121.4±6.2
Mean													103.13	12.14	
Wt mean													102.49	12.06	
Central													104.00	9.36	
3459-a	2280	150	66	41	1.34	1.94	157.0	48.54	78.73	138.23	75.91	0.60	125.74	14.79	157.6±9.5
3459-b	2280	126	92	56	1.38	0.97	39.36	19.00	24.50	33.48	145.68	0.61	238.54	28.07	157.6±9.5
3459-c	2280	147	67	42	1.67	0.67	63.04	31.39	33.56	54.94	52.54	0.71	73.74	8.68	157.6±9.5
3459-d (A)	2280	62	59	30	0.34	0.14	26.68	25.51	30.26	19.40	125.68		125.68	7.79	157.6±9.5
3459-e (A) #	2280	63	59	30	0.34	0.27	49.28	31.60	37.20	40.34	134.72		134.72	8.35	157.6±9.5
Mean													139.68	10.31	
Wt mean													133.13	8.92	
Central													131.38	11.07	
3458-a	2400	142	131	76	3.77	2.64	67.60	18.89	15.80	63.75	85.11	0.79	108.36	12.75	188.6±8.5
3458-b #	2400	136	80	41	1.79	1.36	82.93	22.62	22.78	77.42	75.19	0.69	114.54	13.48	188.6±8.5
3458-c	2400	136	76	48	1.94	1.62	75.50	17.61	17.22	71.33	90.92	0.61	133.64	15.72	188.6±8.5
Mean													118.85	13.98	
Wt mean													117.04	13.77	
Central													120.22	12.76	
3457-a #	2530	153	68	44	1.25	0.35	33.11	25.13	28.08	26.34	69.86	0.64	109.96	12.94	201.1±12.0
3457-b	2530	141	76	48	2.07	0.22	18.10	16.19	18.98	13.53	49.13	0.68	71.88	8.46	201.1±12.0
3457-c	2530	115	104	60	1.78	0.88	46.18	28.20	42.04	36.14	87.31	0.73	119.12	14.02	201.1±12.0
3457-d #	2530	135	76	48	1.98	0.43	24.22	17.55	21.29	19.11	72.79	0.68	106.88	12.58	201.1±12.0
Mean													101.96	13.18	
Wt mean													93.85	13.12	
Central													100.51	11.14	
Mount Gibbs															
PB7-a #	1800	115	64	41	0.80	0.37	96.72	118.43	91.09	74.40	38.88	0.60	64.51	7.59	77.1±4.7
PB7-b	1800	120	64	41	1.25	0.40	61.98	62.08	14.90	57.91	42.71	0.63	67.99	8.00	77.1±4.7
Mean													66.25	7.80	77.1±4.7
Wt mean													66.16	7.78	77.1±4.7
PB6-a	2470	182	89	58	2.52	1.56	64.65	96.61	41.96	53.95	78.68	0.72	109.28	12.86	134.3±7.0
PB6-b	2470	182	67	81	5.10	6.41	87.99	140.02	48.57	75.32	117.02	0.80	146.09	17.19	134.3±7.0
PB6-c	2470	160	85	55	2.90	1.33	44.40	57.31	16.19	40.07	84.85	0.72	118.04	13.89	134.3±7.0
PB6-d	2470	151	81	55	1.94	0.57	38.14	71.76	17.36	33.39	62.85	0.71	88.74	10.44	134.3±7.0
PB6-e	2470	189	91	60	2.74	1.62	56.65	91.76	20.45	50.99	85.59	0.73	117.73	13.85	134.3±7.0
PB6-f (A) #	2470	71	66	38	0.48	0.37	58.37	69.92	23.98	52.11	110.08		110.08	6.83	134.3±7.0
Mean													114.99	12.51	
Wt mean													110.13	13.98	
Central													115.40	14.04	
PB4-a	3000	91	77	45	0.80	0.10	19.33	97.67	22.31	13.18	54.24	0.64	84.69	9.97	205.2±9.9
PB4-b #	3000	167	82	53	1.97	1.36	56.95	129.84	31.76	48.29	99.53	0.70	143.01	16.83	205.2±9.9
PB4-c	3000	150	65	43	1.14	0.40	28.92	57.98	23.83	22.81	99.85	0.62	160.38	18.87	205.2±9.9
PB4-d #	3000	228	103	63	4.97	2.03	34.64	69.38	28.37	27.36	97.09	0.74	130.58	15.36	205.2±9.9
PB4-e (A)	3000	80	75	42	0.69	0.971	68.27	125.38	42.76	57.09	167.75		167.75	10.40	205.2±9.9
Mean													137.28	15.37	
Wt mean													130.89	16.51	
Central													136.93	14.26	

PB1-a #	3120	214	96	63	4.97	3.47	42.52	70.42	12.04	39.02	134.50	0.76	177.24	20.85	251.6±11.4
PB1-b	3120	154	121	64	4.65	1.29	21.38	51.33	7.16	19.20	107.03	0.76	141.46	16.64	251.6±11.4
PB1-c	3120	200	86	53	3.07	4.62	72.29	77.04	14.42	68.17	170.01	0.70	243.18	28.61	251.6±11.4
PB1-d #	3120	176	70	46	1.56	1.10	47.57	70.58	16.20	43.10	121.83	0.65	186.72	21.97	251.6±11.4
PB1-e (A)	3120	79	75	43	0.71	1.18	95.22	99.97	80.54	75.54	142.54		142.54	8.84	251.6±11.4
PB1-f (A)	3120	88	86	49	1.06	2.22	61.69	80.38	12.20	58.06	273.49		273.48	16.96	251.6±11.4
PB1-g (A)	3120	71	65	38	0.47	1.18	54.04	62.70	19.54	48.88	236.47		236.47	14.66	251.6±11.4
Mean													200.16	18.36	
Wt mean													181.79	21.75	
Central													211.46	26.89	
Archambault Ridge															
3338-a #	1590	152	109	66	4.51	0.72	30.68	65.67	22.42	24.83	42.85	0.76	56.23	6.62	59.6±5.5
3338-b #	1590	91	77	45	1.35	0.31	48.70	26.92	8.77	46.39	39.29	0.65	60.42	7.11	59.6±5.5
Mean													58.32	6.86	
Wt mean													58.17	6.88	
3343-a #	2300	91	67	40	0.63	0.64	99.25	44.85	11.05	96.23	63.36	0.60	104.78	12.33	112.7±5.9
3343-b #	2300	119	83	50	1.31	0.82	72.09	44.80	8.26	69.73	71.67	0.68	104.69	12.32	112.7±5.9
3343-c*	2300	249	77	49	3.08	4.41	115.0	44.38	11.40	111.90	102.24	0.68	150.37	17.69	112.7±5.9
Mean													104.73	12.32	
Wt mean													104.73	12.32	
3302-a X	2560	109	73	41	1.21	0.70	37.59	38.72	5.70	35.88	126.57	0.62	205.79	24.21	160.0±12.0
3302-b X	2560	89	66	36	0.80	0.59	48.18	38.59	13.35	44.69	125.33	0.56	223.18	26.26	160.0±12.0
3302-c X	2560	99	76	41	1.17	0.61	31.53	33.67	9.53	28.98	135.33	0.62	219.91	25.87	160.0±12.0
3302-d (A)*	2560	50	47	31	0.18	0.07	56.75	49.80	140.54	23.65	53.31		53.31	3.31	160.0±12.0
3302-e (A) #	2560	72	65	38	0.46	0.14	18.57	31.90	11.40	15.61	134.77		134.77	8.36	160.0±12.0
Mean											130.50	15.8			
Wt mean											133.35	15.9			
3336-a	2600	108	75	45	0.97	0.54	50.30	44.90	11.21	47.25	90.17	0.65	138.58	16.31	
3336-b	2600	120	70	41	1.22	0.49	39.66	39.43	12.18	36.44	82.63	0.61	135.56	15.95	
Mean													137.07	16.13	
Wt mean													137.04	16.13	
3340-a #	2690	120	72	42	1.31	0.08	25.76	42.49	30.71	18.21	18.80	0.62	30.51	3.59	166.7±16.7
3340-b #	2690	95	70	42	0.73	0.07	45.08	44.08	45.68	34.04	17.15	0.62	27.71	3.26	166.7±16.7
Mean													29.11	3.43	
Wt mean													28.98	3.44	
3303-a	2800	112	80	44	1.47	0.11	8.67	29.53	17.85	4.24	67.43	0.63	106.76	12.56	194.4±17.3
3303-b #	2800	120	87	53	1.42	0.21	14.78	34.46	33.90	6.57	82.73	0.69	120.48	14.18	194.4±17.3
Mean													113.62	13.37	
Wt mean													112.79	13.47	

B1: (U-Th-Sm)/He AHe data: In total, 121 AHe single grain analyses (2 – 7 per sample) have been analyzed from 31 samples from the northern Terra Nova Bay region. Grains were selected to obtain ideal apatite crystals (euhedral form, no inclusions, grain diameter > 60 µm). Mechanical abrasion was applied to large apatite crystals with diameter >100 µm. ^{4}He intergrowth equation (e.g., described by Farley, 2002) was applied to determine the AHe age of each apatite grain based on raw data of ^{4}He, ^{238}U, ^{232}Th and ^{147}Sm nuclides, and the measured dimensions of the crystal for the alpha correction (Farley et al., 1996). The table shows dimension, shape (1=complete; 1.5 = one termination missing; 2 = both terminations missing; 3 = rounded), mass, raw data (^{4}He, effective U, ^{238}U, ^{232}Th, ^{147}Sm), FT correction factor, uncorrected and FT-corrected age of each analyzed apatite single grain. Single grains with "A" in brackets of the grain label mark mechanical abraded grains. The error of each single grain is quoted as 2σ. The mean, weighted mean (Wt) and central age of each sample were calculated after single grain outliers (*) have been excluded. Central ages were calculated with the HelioPlot program of Vermeesch (2010). To identify single grain age outliers from the observed data, we used the statistical criterion of Chauvenet (Long and Rippeteau, 1974). Grains of sample 3468 marked with "x" were supposedly affected by ^{4}He implantation, and hence the uncorrected ages were used for age calculation (see also appendix 2). Single grain ages marked with "#" were used for HeFTy modeling. The corresponding apatite fission track age of each sample is shown for comparison.

B2 – *Apatite U-Th-Sm/He age-elevation plot*

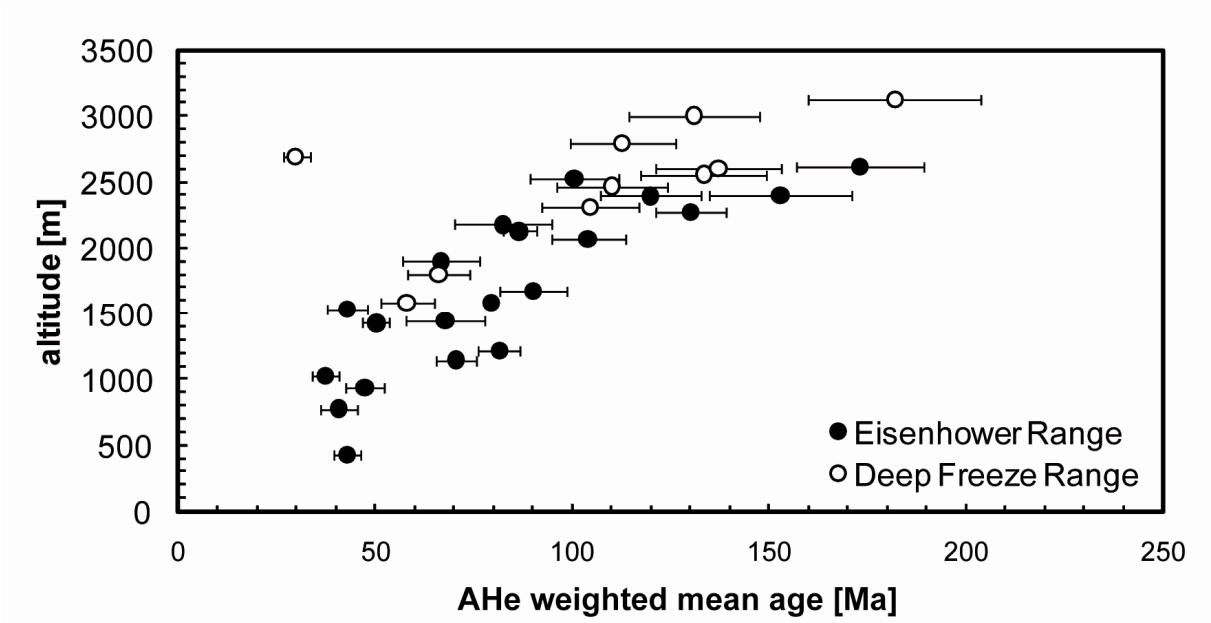

B2: Apatite (U-Th-Sm)/He (AHe) weighted mean ages from the northern Terra Nova Bay region (Eisenhower Range, Deep Freeze Range) versus sample altitudes. Ages between 28±3 and 182±22 Ma closely correlate with sample altitude between 430 and 3120 m.

B3 – Apatite fission track and U-Th-Sm/He age-elevation plot

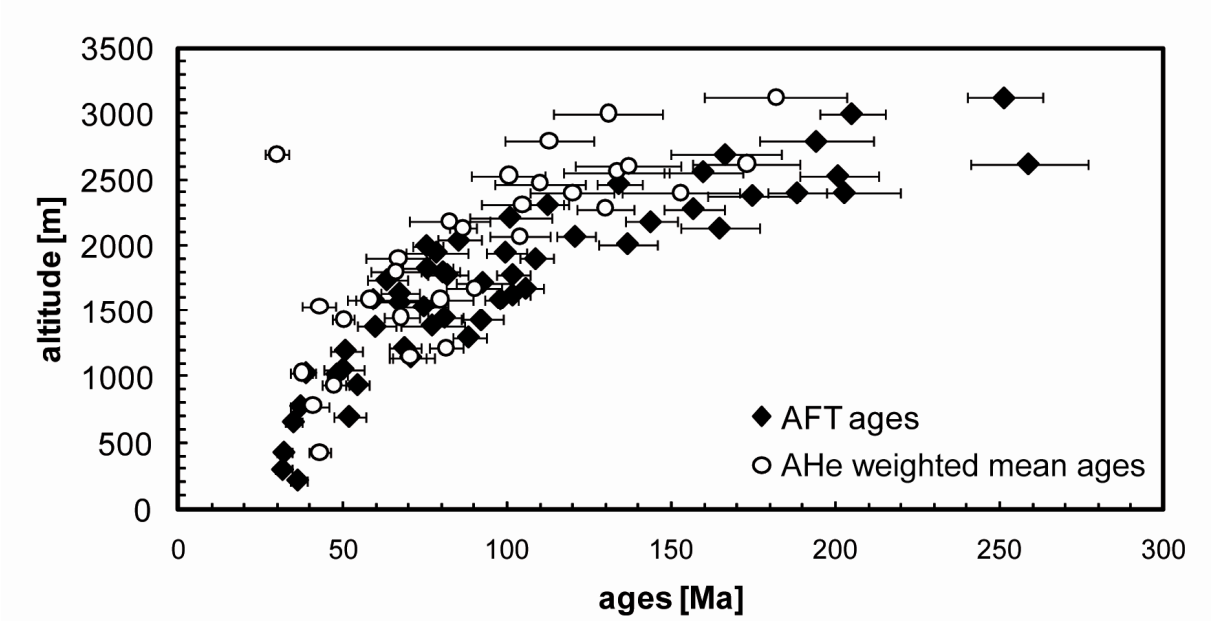

B3: Apatite fission track (AFT) ages and apatite (U-Th-Sm)/He (AHe) weighted mean ages of the complete data set versus sample altitudes. Ages closely correlate with altitudes. AHe ages are mostly younger than the corresponding AFT age.

Appendix C – Thermal history models

C1 – HeFTy inverse models

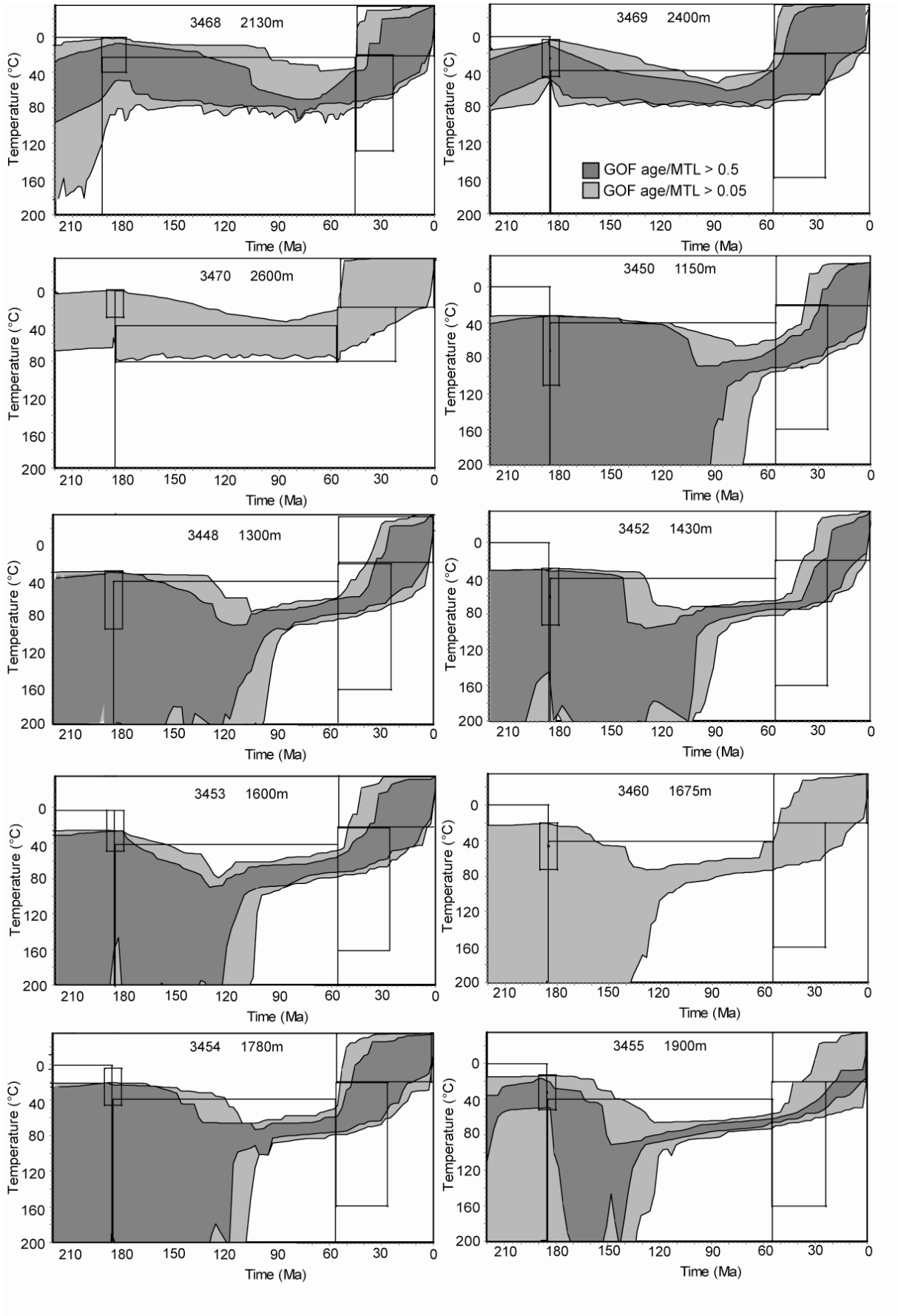

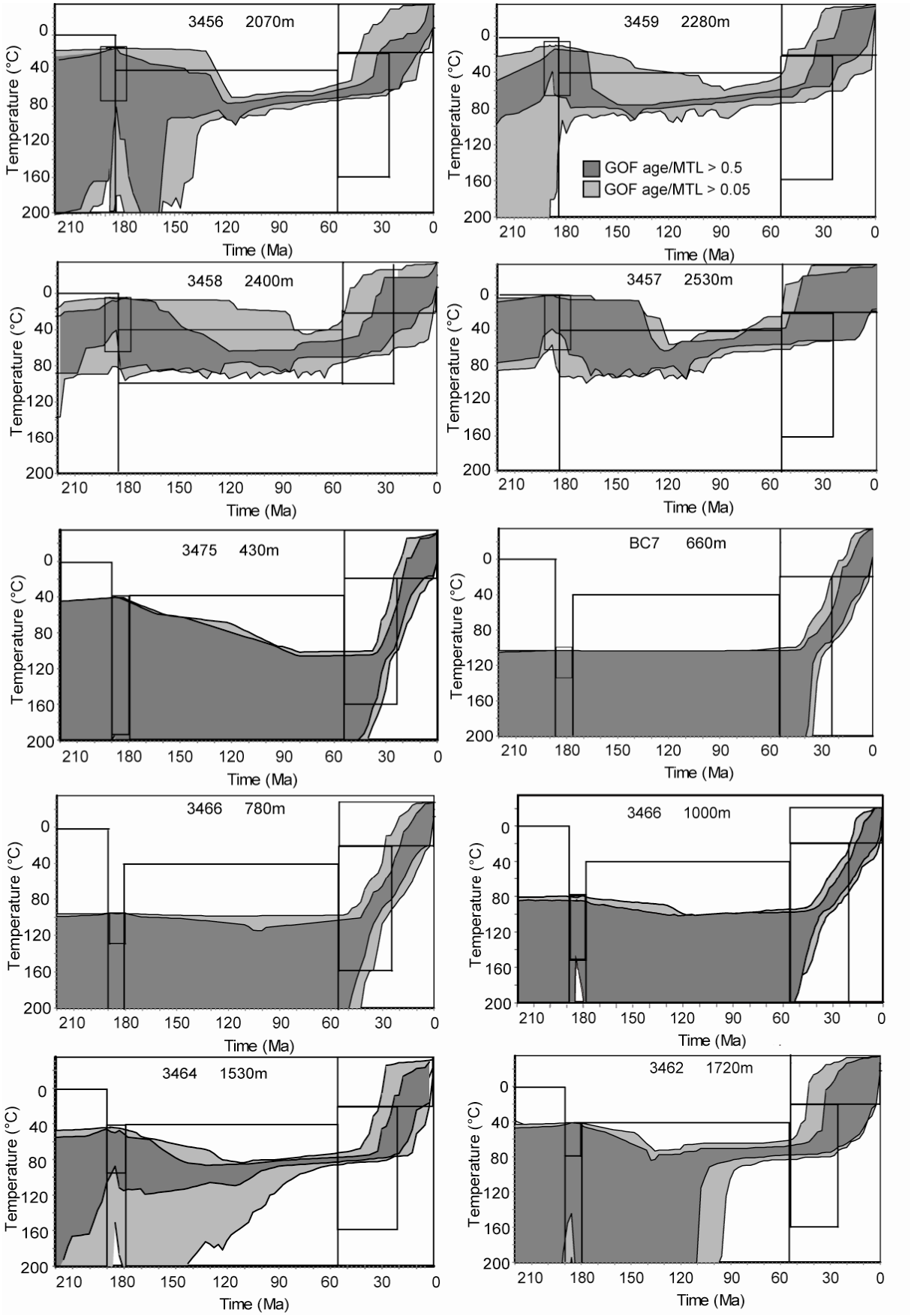
3456 2070m
3459 2280m
GOF age/MTL > 0.5
GOF age/MTL > 0.05
3458 2400m
3457 2530m
3475 430m
BC7 660m
3466 780m
3466 1000m
3464 1530m
3462 1720m
Temperature (°C)
Time (Ma)
0
40
80
120
160
200
210
180
150
120
90
60
30
0

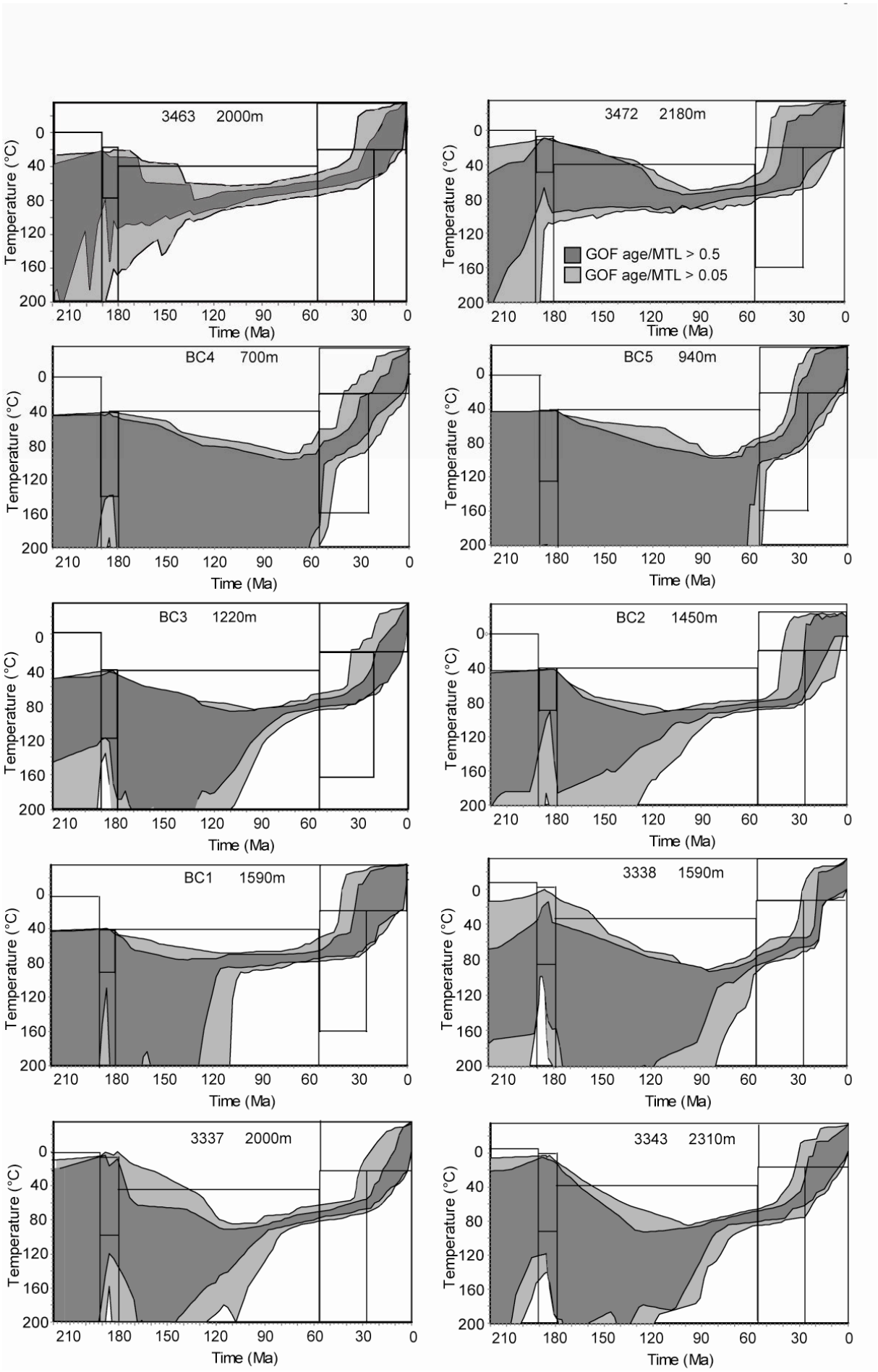
3463 2000m
3472 2180m
GOF age/MTL > 0.5
GOF age/MTL > 0.05
BC4 700m
BC5 940m
BC3 1220m
BC2 1450m
BC1 1590m
3338 1590m
3337 2000m
3343 2310m
Temperature (°C)
Time (Ma)
0
40
80
120
160
200
210
180
150
120
90
60
30
0

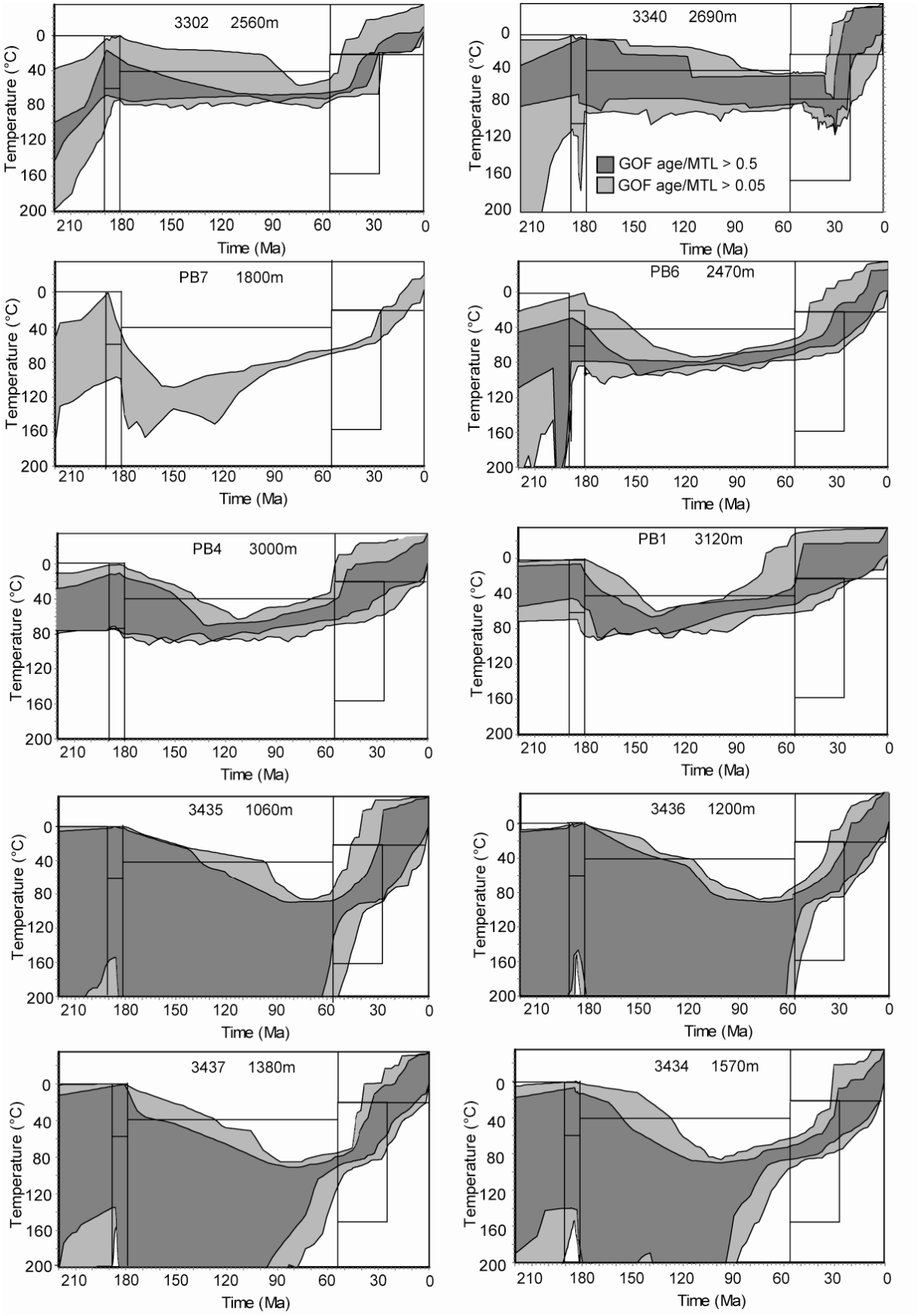
3302 2560m
3340 2690m
PB7 1800m
PB6 2470m
PB4 3000m
PB1 3120m
3435 1060m
3436 1200m
3437 1380m
3434 1570m
Temperature (°C)
Time (Ma)
GOF age/MTL > 0.5
GOF age/MTL > 0.05

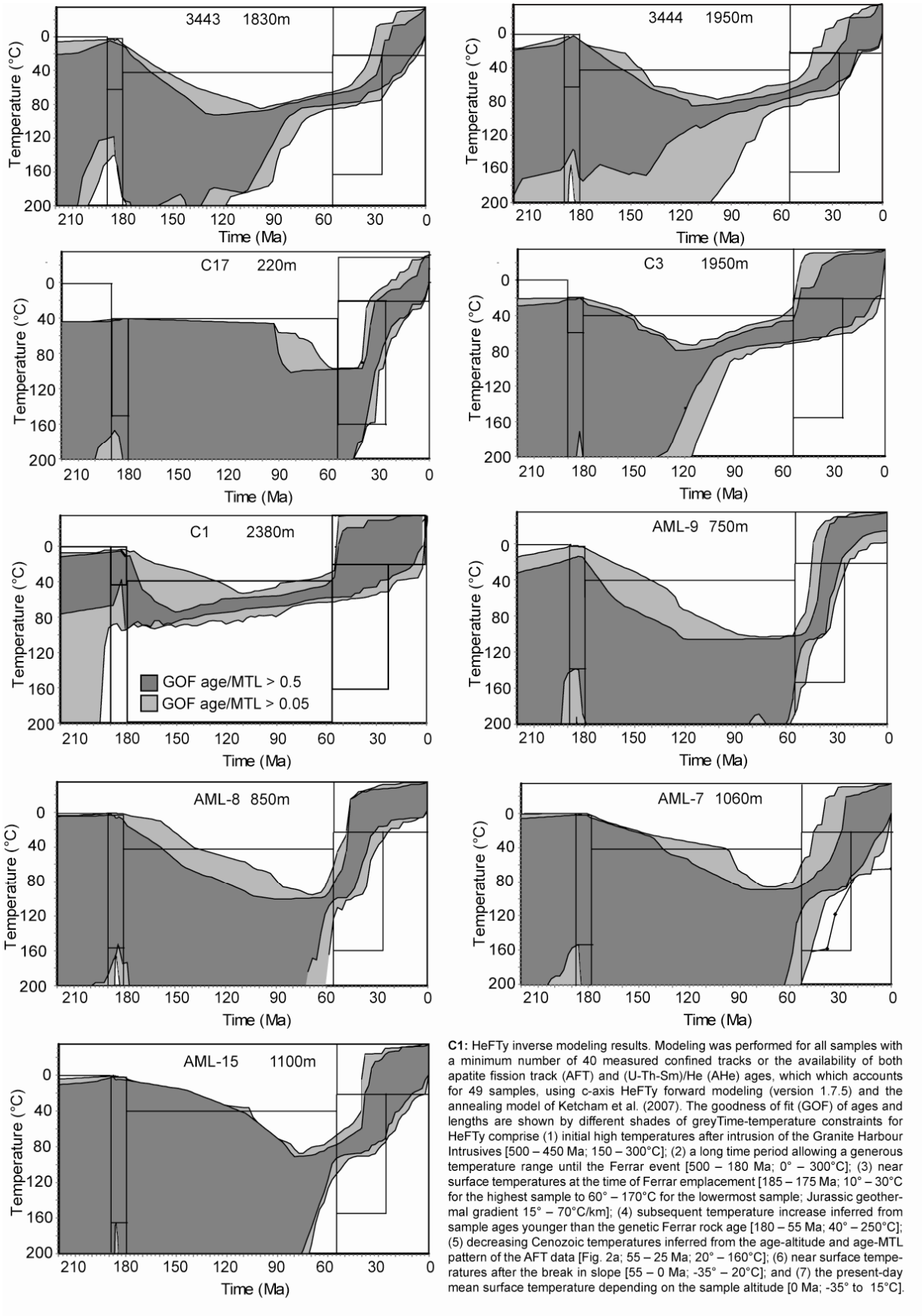

C1: HeFTy inverse modeling results. Modeling was performed for all samples with a minimum number of 40 measured confined tracks or the availability of both apatite fission track (AFT) and (U-Th-Sm)/He (AHe) ages, which which accounts for 49 samples, using c-axis HeFTy forward modeling (version 1.7.5) and the annealing model of Ketcham et al. (2007). The goodness of fit (GOF) of ages and lengths are shown by different shades of greyTime-temperature constraints for HeFTy comprise (1) initial high temperatures after intrusion of the Granite Harbour Intrusives [500 – 450 Ma; 150 – 300°C]; (2) a long time period allowing a generous temperature range until the Ferrar event [500 – 180 Ma; 0° – 300°C]; (3) near surface temperatures at the time of Ferrar emplacement [185 – 175 Ma; 10° – 30°C for the highest sample to 60° – 170°C for the lowermost sample; Jurassic geothermal gradient 15° – 70°C/km]; (4) subsequent temperature increase inferred from sample ages younger than the genetic Ferrar rock age [180 – 55 Ma; 40° – 250°C]; (5) decreasing Cenozoic temperatures inferred from the age-altitude and age-MTL pattern of the AFT data [Fig. 2a; 55 – 25 Ma; 20° – 160°C]; (6) near surface temperatures after the break in slope [55 – 0 Ma; -35° – 20°C]; and (7) the present-day mean surface temperature depending on the sample altitude [0 Ma; -35° to 15°C].

C2 – HeFTy forward models

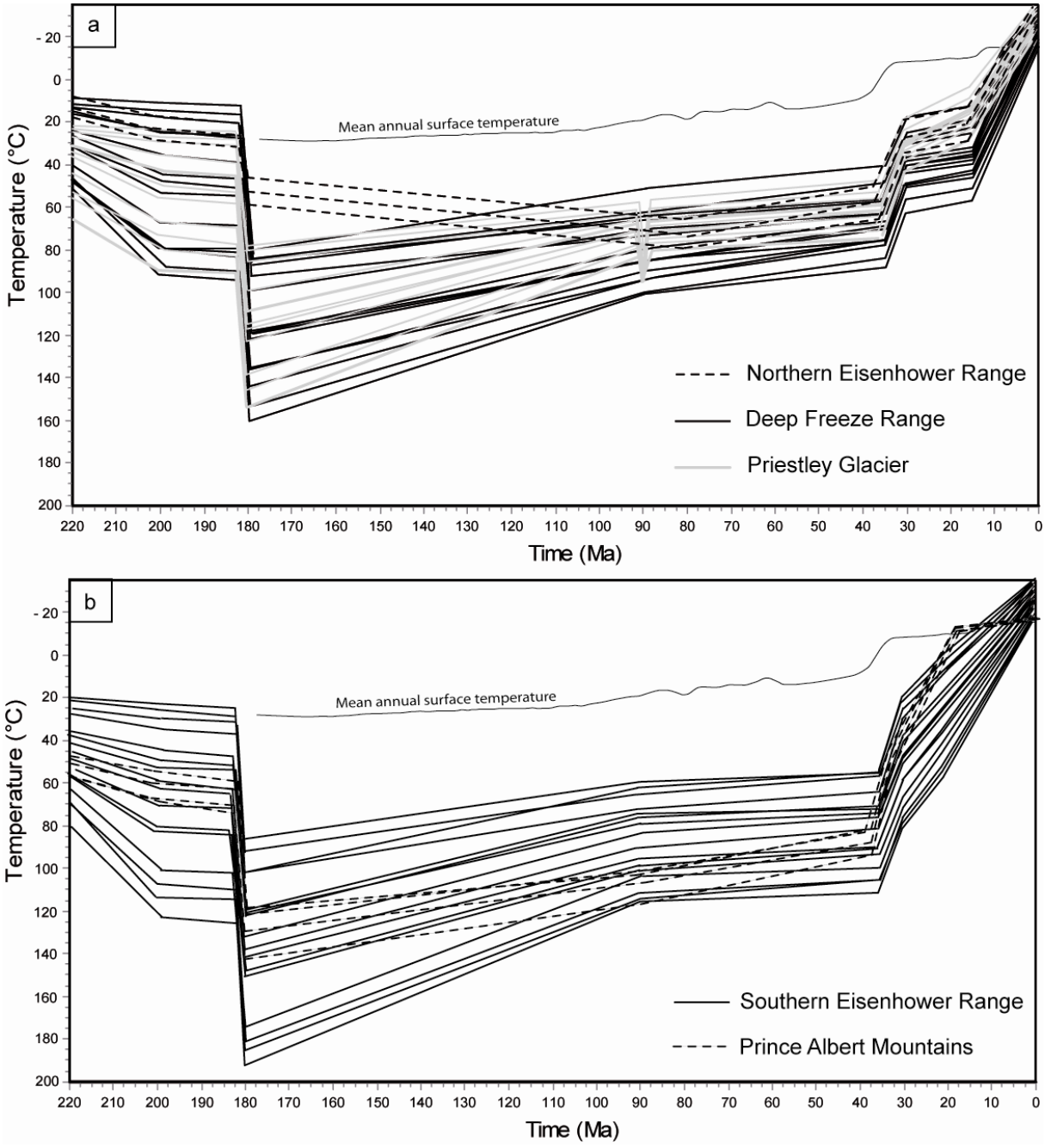

C2: HeFTy forward models of the vertical sample sets from the (a) interior of the Terra Nova Bay region and (b) coast. HeFTy forward modeling generated a common thermal history for the complete sample set of the Terra Nova Bay region. This comprises (I) low/ near surface temperatures during the Late Triassic and Early Jurassic; (II) increasing temperatures towards mid- to Late Jurassic; (III) decreasing temperatures in Late Jurassic and Early Cretaceous times; (IV) subsequent constant to slightly decreasing temperatures until the Eocene; and (V) fast final cooling to surface temperatures since Late Eocene with a decelerated cooling rate since the Early Oligocene. The implementation of a reheating pulse (~100°C) at ~90 Ma in the Priestley Glacier profile optimizes the fit between measured and predicted data. Thermal histories show minor regional differences in final cooling pattern to surface temperature. Cooling stagnation in the interior of the northern Terra Nova Bay region between ~30 Ma and onset of final rapid cooling at ~15 Ma contrasts to contemporaneous ongoing cooling to surface temperatures at ~18 Ma at the coastal regions in the southern Eisenhower Range and Prince Albert Mountains.

C3 – QTQt models

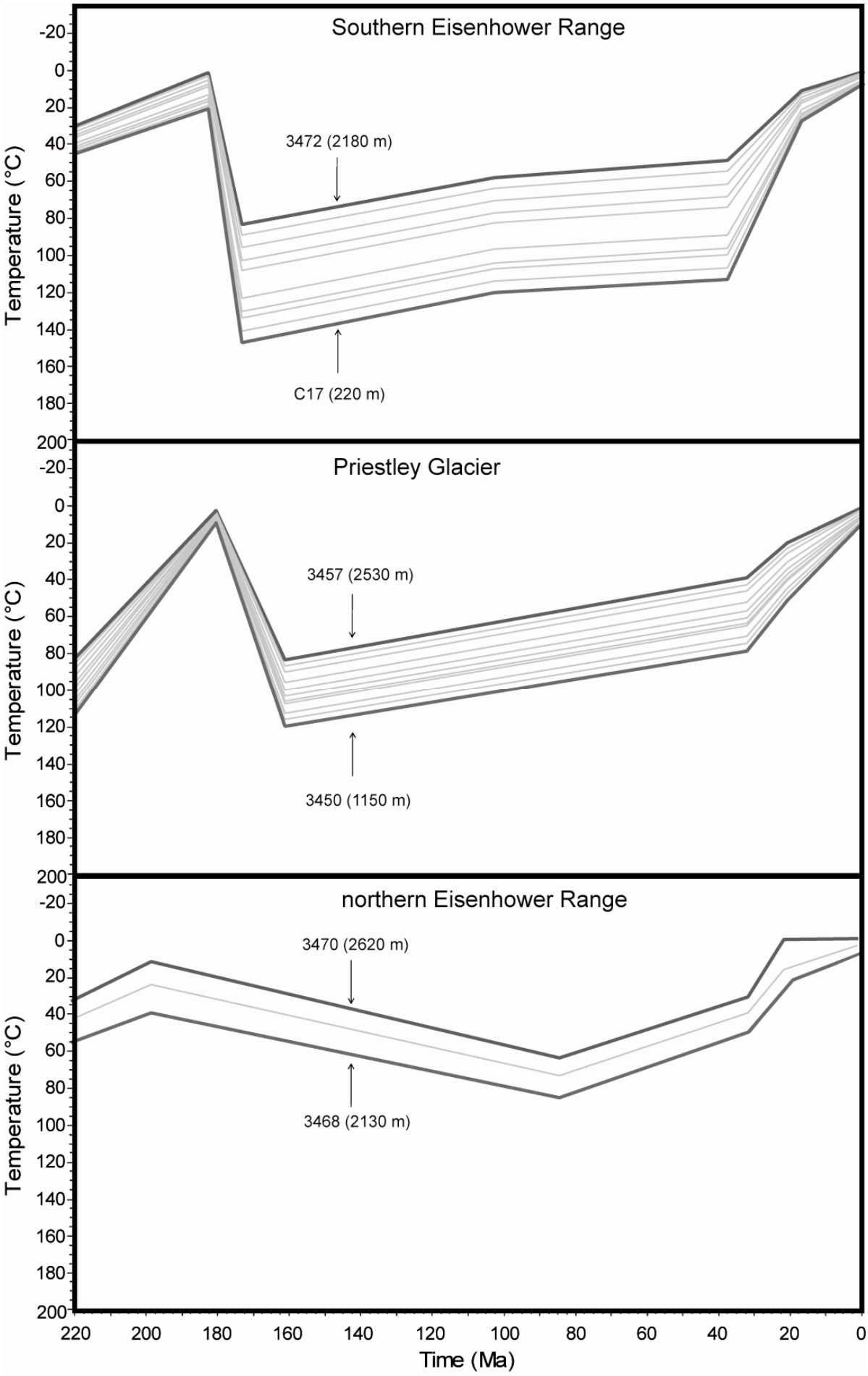

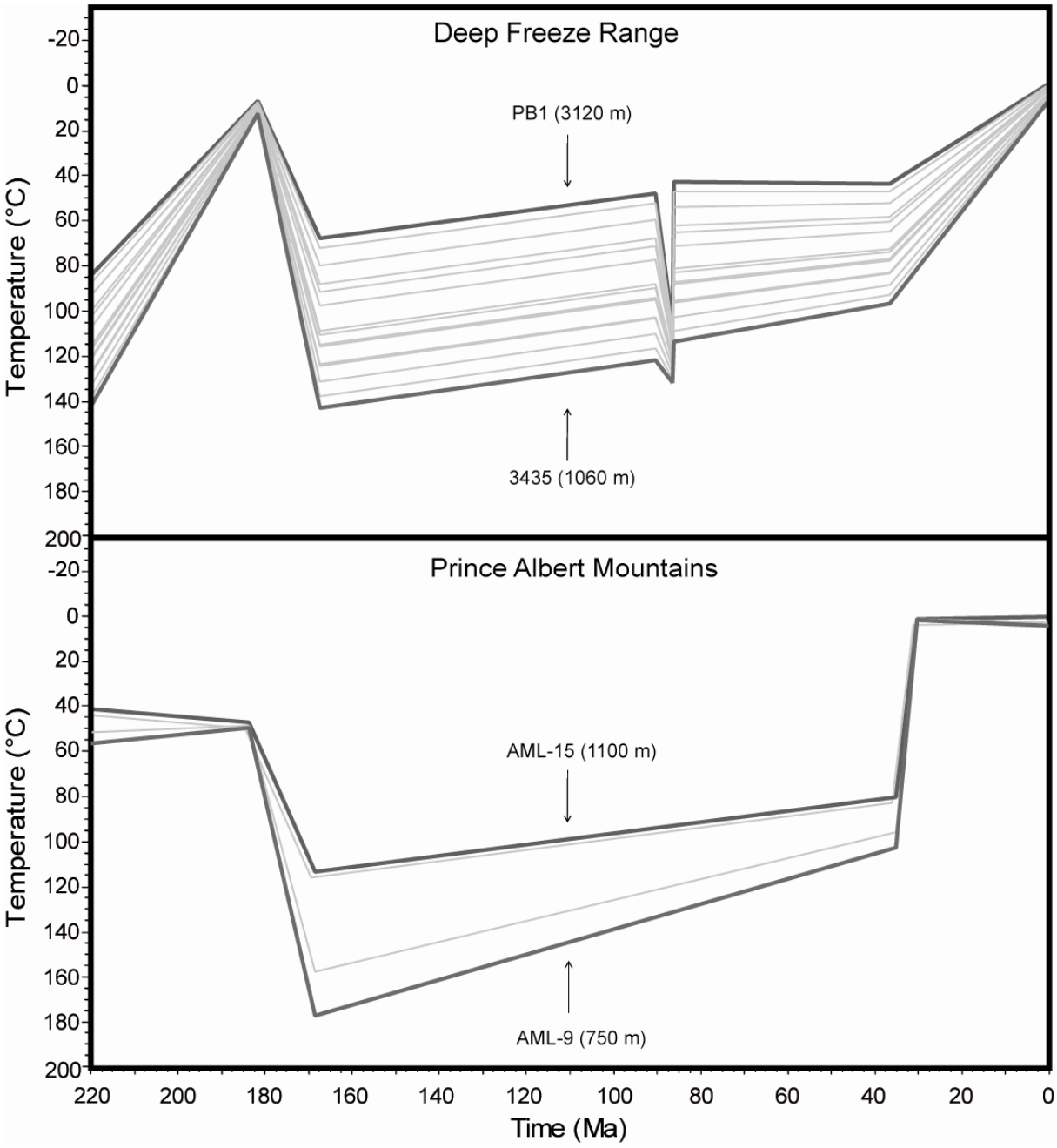

C3: QTQt models from southern Eisenhower Range, Priestley Glacier, northern Eisenhower Range, Deep Freeze Range and Prince Albert Mountains. QTQt modeling produced thermal histories similar to the HeFTy forward models. Differences between HeFTy and QTQt approach are mainly present for the Late Eocene cooling pattern to surface temperatures, and the paleotemperature estimates of the individual samples. These differences have been attributed to the missing Sm component of the apatites and the non-negative set present-day temperature for QTQt modeling.

Appendix D – Conference contributions

Talks:

Thermochronologische Beprobung während GANOVEX X und anschließende Untersuchungen

J. Prenzel[1], F. Lisker[1]
[1] University of Bremen, FB5 Geosciences, Klagenfurther Straße, 28359 Bremen, Germany

April 9, 2010. 32. Treffen der Deutschen Gesellschaft für Polarforschung; Schloss Porz-Wahn; Köln, Deutschland.

Neue thermochronologische Daten von der Eisenhower Range im Nord-Viktoria-Land

J. Prenzel[1], F. Lisker[1], M.L. Balestrieri[2], A. Läufer[3], C. Spiegel[1]
[1] University of Bremen, FB5 Geosciences, Klagenfurther Straße, 28359 Bremen, Germany
[2] CNR, Institute of Earth Sciences and Earth Resources, Via La Pira 4, 50121 Florence, Italy
[3] Bundesanstalt für Geowissenschaften und Rohstoffe, Stilleweg 2, 30655 Hannover, Germany

April 15, 2011. 34. Treffen der Deutschen Gesellschaft für Polarforschung; Universität Bremen; Bremen, Deutschland.

New evidence on the existence of a Late Jurassic-Paleocene Victoria Land Basin from thermochronological studies in the Eisenhower Range, Transantarctic Mountains

J. Prenzel[1], F. Lisker[1], M.L. Balestrieri[2], A. Läufer[3], C. Spiegel[1]
[1] University of Bremen, FB5 Geosciences, Klagenfurther Straße, 28359 Bremen, Germany
[2] CNR, Institute of Earth Sciences and Earth Resources, Via La Pira 4, 50121 Florence, Italy
[3] Bundesanstalt für Geowissenschaften und Rohstoffe, Stilleweg 2, 30655 Hannover, Germany

July 11, 2011. 11th International Symposium on Antarctic Earth Sciences; John McIntyre Conference Centre, Edinburgh, Scotland.

Burial and exhumation of the Eisenhower Range in northern Victoria Land, Transantarctic Mountains

J. Prenzel[1], F. Lisker[1], M.L. Balestrieri[2], A. Läufer[3], C. Spiegel[1]
[1] University of Bremen, FB5 Geosciences, Klagenfurther Straße, 28359 Bremen, Germany
[2] CNR, Institute of Earth Sciences and Earth Resources, Via La Pira 4, 50121 Florence, Italy
[3] Bundesanstalt für Geowissenschaften und Rohstoffe, Stilleweg 2, 30655 Hannover, Germany

May 5, 2012. 35. Treffen der Deutschen Gesellschaft für Polarforschung; Universität Jena; Jena, Deutschland.

The break in slope revisited: thermal history models from the Eisenhower Range, Transantarctic Mountains

J. Prenzel[1], F. Lisker[1], M.L. Balestrieri[2], A. Läufer[3], C. Spiegel[1]
[1] University of Bremen, FB5 Geosciences, Klagenfurther Straße, 28359 Bremen, Germany
[2] CNR, Institute of Earth Sciences and Earth Resources, Via La Pira 4, 50121 Florence, Italy
[3] Bundesanstalt für Geowissenschaften und Rohstoffe, Stilleweg 2, 30655 Hannover, Germany

August 25, 2012; 13th International Conference on Thermochronology; Guilin Lijiang Waterfall Hotel; Guilin, China.

Burial and exhumation of the Terra Nova Bay region, Transantarctic Mountains

J. Prenzel[1], F. Lisker[1], M.L. Balestrieri[2], A. Läufer[3], C. Spiegel[1]
[1] University of Bremen, FB5 Geosciences, Klagenfurther Straße, 28359 Bremen, Germany
[2] CNR, Institute of Earth Sciences and Earth Resources, Via La Pira 4, 50121 Florence, Italy
[3] Bundesanstalt für Geowissenschaften und Rohstoffe, Stilleweg 2, 30655 Hannover, Germany

March 18, 2013. 25th International Congress on Polar Research; Universität Hamburg, Hamburg, Germany.

Poster:

Thermochronological studies in the Terra Nova Bay Region, Transantarctic Mountains, Antarctica

J. Prenzel[1], F. Lisker[1], M.L. Balestrieri[2], A. Läufer[3], C. Spiegel[1]
[1] University of Bremen, FB5 Geosciences, Klagenfurther Straße, 28359 Bremen, Germany
[2] CNR, Institute of Earth Sciences and Earth Resources, Via La Pira 4, 50121 Florence, Italy
[3] Bundesanstalt für Geowissenschaften und Rohstoffe, Stilleweg 2, 30655 Hannover, Germany

August 17, 2010. 12th International Conference on Thermochronology; Sir Charles Wilson conference venue, Glasgow, Scotland.

Werkzeuge zur Untersuchung antarktischer Hebungsprozesse und deren Grenzen

J. Prenzel[1], F. Lisker[1]
[1] University of Bremen, FB5 Geosciences, Klagenfurther Straße, 28359 Bremen, Germany

September 6, 2010; 24. Internationale Polartagung der Deutschen Gesellschaft für Polarforschung; Universitätszentrum Obergurgl, Österreich.

Thermochronological studies in the Terra Nova Bay region, Transantarctic Mountains

J. Prenzel[1], F. Lisker[1], M.L. Balestrieri[2], A. Läufer[3], C. Spiegel[1]
[1] University of Bremen, FB5 Geosciences, Klagenfurther Straße, 28359 Bremen, Germany
[2] CNR, Institute of Earth Sciences and Earth Resources, Via La Pira 4, 50121 Florence, Italy
[3] Bundesanstalt für Geowissenschaften und Rohstoffe, Stilleweg 2, 30655 Hannover, Germany

October 6, 2011. DFG Koordinationsworkshop 2011, Ebernburg, Bad Münster am Stein, Germany.

Thermochronological studies in the Terra Nova Bay region, Transantarctic Mountains

J. Prenzel[1], F. Lisker[1], M.L. Balestrieri[2], A. Läufer[3], C. Spiegel[1]
[1] University of Bremen, FB5 Geosciences, Klagenfurther Straße, 28359 Bremen, Germany
[2] CNR, Institute of Earth Sciences and Earth Resources, Via La Pira 4, 50121 Florence, Italy
[3] Bundesanstalt für Geowissenschaften und Rohstoffe, Stilleweg 2, 30655 Hannover, Germany

March 18, 2013. 25th International Congress on Polar Research; Universität Hamburg, Hamburg, Germany.

The influence of climate and tectonics on uplift and denudation of the Terra Nova Bay region, Transantarctic Mountains

J. Prenzel[1], F. Lisker[1], M.L. Balestrieri[2], A. Läufer[3], C. Spiegel[1]
[1] University of Bremen, FB5 Geosciences, Klagenfurther Straße, 28359 Bremen, Germany
[2] CNR, Institute of Earth Sciences and Earth Resources, Via La Pira 4, 50121 Florence, Italy
[3] Bundesanstalt für Geowissenschaften und Rohstoffe, Stilleweg 2, 30655 Hannover, Germany

September 27, 2013. DFG Koordinationsworkshop 2013, Ruhruniversität Bochum, Bochum, Germany.

References

Armienti, P., Baroni, C., 1999. Cenozoic climatic change in Antarctica recorded by volcanic activity and landscape evolution, Geology, 27, 617– 620.

Balestrieri, M.L., Bigazzi, G., Ghezzo, C., Lombardo, B., 1994. Fission track dating of apatites from the Granite Harbour Intrusive Suite and uplift-denudation history of the Transantarctic Mountains in the area between the Mariner and David Glaciers (northern Victoria Land, Antarctica). Terra Antartica, 1(1), 82-87.

Balestrieri, M.L., Bigazzi, G., Ghezzo, C., 1997. Uplift-denudation of the Transantarctic Mountains between the David and the Mariner glaciers, northern Victoria Land (Antarctica); constraints by apatite fission-track analysis. In: C.A. Ricci (Editor), The Antarctic region; geological evolution and processes; proceedings of the VII international symposium on Antarctic Earth sciences. Terra Antartica, 547-554.

Ballance, P.F., and Watters, W.A., 2002. Hydrothermal alteration, contact metamorphism, and authigenesis in Ferrar Supergroup and Beacon Supergroup rocks, Carapace Nunatak, Allan Hills, and Coombs Hills, Victoria Land, Antarctica. New Zea. J. Geol. Geoph., 45, 71-84.

Barbarand, J., Carter, A., Wood, I.G., Hurford, A.J., 2003a. Compositional and structural control of apatite fission-track annealing. Chem. Geol. 198, 107-137.

Barbarand, J., Hurford, A.J., Carter, A.., 2003b. Variation in apatite fission-track length measurement: implications for thermal history modelling. Chem Geol,, 198 (1-2), 77-106.

Barker, C.E., and Pawlewicz, M.J., 1994. Calculation of vitrinite reflectance from thermal histories and peak temperatures, a comparison of methods. In: P.K. Mukhopadhyay and W.G. Dow (Editors), Vitrinite reflectance as a maturity parameter, applications and limitations: Am. Chem. Soc., Symposium Series 570, 216-229, Washington, D.C.

Barrett, P.J., 1991. The Devonian to Jurassic Beacon Supergroup of the Transantarctic Mountains and correlatives in other parts of Antarctica. In: Tingey RJ, ed. The geology of Antarctica. Oxford, Clarendon Press, 120-152.

Barrett, P., 1999. Antarctic Climate History over the Last 100 Million Years. Terra Antartica Reports, 3, 53-72.

Baroni, C.N., Ciccacci, V., Righini, S., Giovanni, S., Cristina, M., 2005, Fluvial origin of the valley system in northern Victoria Land (Antarctica) from quantitative geomorphic analysis. Geol. Soc. Amer. Bul., 117, 212-228.

Beard, D.C., and Weyl, P.K., 1973. Influence of texture on porosity and permeability of unconsolidated sand. AAPG Bulletin, 57, 349-369.

Berner, U., Scheeder, G., Kus, J., Voigt, S., Schneider, J.W.,2009. Organic geochemical characterization of terrestrial source rocks of the Triassic Madygen Formation (southern Tien Shan, Kyrgyzstan). Oil Gas-Eur Mag,, 35, 135-139.

Bernet, M., and Gaupp, R., 2005. Diagenetic history of Triassic sandstone from the Beacon Supergroup in central Victoria Land, Antarctica, New Zea. J. Geol. Geoph., 48, 447-458.

Bird, D. K., and Spieler, A. R., 2004, Epidote in Geothermal Systems. Rev. Mineral. Geochem, ed. A. Liebscher and G. Franz, 56, 235-300.

Boger, S.D., 2011. Antarctica – Before and after Gondwana. Gondwana Research, 19-2, 335-371.

Bomfleur, B., Schneider, J., Schöner, R., Viereck-Goette, L., and Kerp, H., 2011. Fossil sites in the continental Victoria and Ferrar groups (Triassic–Jurassic) of north Victoria Land, Antarctica. Polarforschung, 80, 88-99.

Borg, S.G., Stump, E., Chappell, B.W., McCulloch, M.T., Wyborn, D., Armstrong, R.L., and Holloway, J.R., 1987. Granitoids of northern Victoria Land, Antarctica: Implications of chemical and isotopic variations to regional crustal structure and tectonics: Am. J. Sci., 287, 127–169.

Brancolini, G., Cooper, A.K.,. Coren, F., 1995. Seismic facies and glacial history in the western Ross Sea (Antarctica), in Geology and Seismic Stratigraphy of the Antarctic Margin. Antarct. Res. Ser, 68, edited by A. K. Cooper et al., 209 – 234, AGU, Washington, D. C.

Bray, R.J., Green, P.F., Duddy, I.R., 1992. Thermal history reconstruction using apatite fission track analysis and vitrinite reflectance; a case study from the UK East Midlands and southern North Sea. In: Exploration Britain; Geological Insights for the Next Decade, Geological Society Special Publications, 67 (Ed. by R.F.P. Hardman), 2-25.

Burnham, A.K. and Sweeney, J.J., 1989. A chemical kinetic model of vitrinite reflectance maturation. Geochim. Cosmochim. Ac., 53, 2649-2657.

Busetti, M., 1994. A new age constraint for the age of unconformity U6 in the Ross Sea, Terra Antartica,1, 523 – 526.

Cande, S. C., Stock, J.M., Müller, R.D., Ishihara, T., 2000. Cenozoic motion between East and West Antarctica. Nature, 404, 145 – 150.

Cape Roberts Science Team, 1998. Initial report on CRP-1 Cape Roberts Project, Antarctica, Terra Antartica. 5, 1 – 187.

Cape Roberts Science Team, 1999. Studies from the Cape Roberts Project, Ross Sea, Antarctica: Initial report on CRP-2/2A. Terra Antartica, 6, 1 – 173.

Carlson, W.D., Donelick, R.A. and Ketcham, R.A., 1999. Variability of apatite fission-track annealing kinetics: I. Experimental results. Amer. Mineral., 84, 1213-1223.

Casnedi, R., Di Giulio, A., Rossi, A., 1994. The Sandstones of the Beacon Supergroup near Terra Nova Bay (Northern Victoria Land, Antarctica): Preliminary Results of Facies and Petrological Analyses. Terra Antartica, 1, 92-94.

Collinson, J.W., Isbell, J.L., Elliot, D.H., Miller, M.F., Miller, J.M.G., Veevers, J.J. 1994. Permian-Triassic Transantarctic Basin. Geol. Soc. Am. Memoir, 184, 173-222.

Cooper, A. K., Davey, F.J., Behrendt, J.C., 1987. Seismic stratigraphy and structure of the Victoria Land Basin, western Ross Sea, Antarctica, in The Antarctic Continental Margin: Geology and Geophysics of the Western Ross Sea, Earth Sci. Ser., 5B, edited by A. K. Cooper and F. J. Davey, 27 – 76, Circum-Pacific Counc. of Energy and Miner. Resour., Houston, Tex.

Davey, F. J., Brancolini, G., 1995. The Late Mesozoic and Cenozoic structural setting of the Ross Sea region, in Geology and Seismic Stratigraphy of the Antarctic Margin, Antarct. Res. Ser., 68, edited by A. K. Cooper et al., 167 – 182, AGU, Washington, D. C.

Davey, F. J., Cande, S.C., Stock, J.M., 2006. Extension in the western Ross Sea region-links between Adare Basin and Victoria Land Basin, Geophys. Res. Lett., 33.

Delisle, G. and Fromm, K., 1984. Paleomagnetic investigation of Ferrar Supergroup rocks, North Victoria Land, Antarctica. Geol. Jahrb., B 60, 41–55.

Delisle, G. and Fromm, K., 1989. Further evidence for a Cretaceous thermal event in North Victoria Land. Geol. Jahrb., E 38, 143–151.

Di Vincenzo, G., Rocchi, S., Rossetti, F., Storti, F., 2004. 40Ar–39Ar dating of pseudotachylytes: the effect of clast-hosted extraneous argon in Cenozoic fault-generated friction melts from the West Antarctic Rift System. EPSL, 223 (3-4), 339-364.

Donelick, R.A., 1993. Apatite etching characteristics versus chemical composition. Nucl. Tracks Radiat. Meas., 21, 604.

Dumitru, T.A., 1993. A new computer-automated microscope stage system for fission-track analysis. Nucl. Tracks Radiat. Meas., 21, 575-580.

Dunkl, I., 2002. TRACKKEY: a Windows program for calculation and graphical presentation of fission track data. Computers and Geosciences, 28, 3-12.

Ehrenberg, S.N., 1989. Assessing the relative importance of compaction processes and cementation to reduction of porosity in sandstones. Discussion, compaction and porosity evolution of Pliocene sandstones, Ventura basin, California: Discussion. AAPG Bulletin, 73, 1274-1276.

Ehrmann, W.U. and Mackensen, A., 1992. Sedimentological evidence for the formation of an East Antarctic ice sheet in Eocene/Oligocene time. Palaeogeogr. Palaeoclimatol. Palaeoecol., 93, 85–112.

Ehrmann, W., 1998. Implications of late Eocene to early Miocene clay mineral assemblages in McMurdo sound (Ross sea, Antarctica) on paleoclimate and ice dynamics. Paleogeogr. Paleoclimatol. Paleoecol., 139, 213-231.

Elliot, D.H. and Foland, K.A., 1986. Potassium-Argon age determinations of the Kirkpatrick Basalt, Mesa Range. In Stump e. (ed.) Geological investigations in Northern Victoria Land, Antarctic research series, 46, American Geophysical Union, Washington D.C., 279-288.

Elliot, D.H., 1992. Jurassic magmatism and tectonism associated with Gondwanaland break-up: an Antarctic perspective, in Storey, B.C., Alabaster, T., and Pankhurst, R.J., eds., Magmatism and the Causes of Continental Break-up: Geol. Soc. Spec. Publ. London, 165-184.

Elliot, D.H., 2000. Stratigraphy of Jurassic pyroclastic rocks in the Transantarctic Mountains. J. Afr. Earth. Sci., 31(1), 77-89.

Elliot, D.H. and Fleming, T.H., 2008. Physical volcanology and geological relationships of the Jurassic Ferrar Large Igneous Province, Antarctica. J. Volcanol. Geoth. Res., 172, 20.

Elsner, M., 2010. Triassic to Early Jurassic sandstones in North Victoria Land – Composition, provenance, and diagenesis: PhD thesis, Friedrich-Schiller-Universität Jena, 184 p.

Encarnación, J., Fleming, T.H., Elliot, D.H., Eales, J.V., 1996. Synchronous emplacement of Ferrar and Karoo dolerites and the early breakup of Gondwana. Geology, 24, 535–538.

Farley, K.A.,Wolf, R.A., Silver, L.T., 1996. The effects of long alpha-stopping distances on (U–Th)/He ages. Geochim. Cosmochim. Ac., 60 (21), 4223– 4229.

Farley, K.A., 2002. (U-Th)/He Dating: Techniques, Calibrations, and Applications. Reviews in Mineral and Geochem, 47, 819-844.

Faure, G., Mensing, T.M., 1993. K–Ar dates and paleomagnetic evidence for Cretaceous alteration of Mesozoic basaltic lava flows, Mesa Range, Northern Victoria Land, Antarctica. Chem. Geol. Isotope Geoscience Section. 109, 305–315.

Ferrar, H.T., 1907. Report on the field geology of the region explored during the “Discover” Antarctic Expedition, 1901-04: London, Nati. Antarctic Exped, Nat. History, 1, Geology, 1-100.

Fitzgerald, P.G., Sandiford M, Barrett PJ, Gleadow AJW, 1986. Asymmetric extension associated with uplift and subsidence of the Transantarctic Mountains and Ross Embayment. EPSL, 81, 67-78.

Fitzgerald, P.G., and Gleadow, A.J.W., 1988. Fission-track geochronology, tectonics and structure of the Transantarctic Mountains in Northern Victoria Land, Antarctica. Chem. Geol., 73,169–98.

Fitzgerald, P.G., 1994. Thermochronologic constraints on post-Palaeozoic tectonic evolution of the central Transantarctic Mountains, Antarctica. Tectonics, 13.

Fitzgerald PG, Sorkhabi RB, Redfield TF, Stump E. 1995. Uplift and denudation of the central Alaska Range; a case study in the use of apatite fission track thermochronology to determine absolute uplift parameters. J. Geophys. Res. 100:20175–91.

Fitzgerald, P.G., 2002. Tectonics and landscape evolution of the Antarctic Plate since the breakup of Gondwana, with an emphasis on the West Antarctic Rift System and the Transantarctic Mountains. Bull. Roy. Soc. New. Zeal., 35, 453-469.

Fitzgerald, P.G., Baldwin, S.L., Webb, L.E., O'Sullivan, P.B., 2006. Interpretation of (U–Th)/He single grain ages from slowly cooled crustal terranes: A case study from the Transantarctic Mountains of southern Victoria Land. EPSL, 225 (1-2), 91-120.

Fleming, T.H., Foland, K.A., Elliot, D.H., 1993. Direct dating ofmid-Cretaceous alteration of the Kirkpatrick Basalt in North Victoria Land: argon-40rargon-39 and rubidium/ strontium ages for apophyllite. Ant. J. US, 28, 38–40.

Fleming, T.H., Elliot, D.H., Foland, K.A., 1996. Alteration events recorded in Jurassic Tholeiites Kirkpatrick Basalt from the Transantarctic Mountains: evidence ofCretaceous tectonic activity. *In:* Geodynamic Evolution of the Transantarctic Mountains and the West Antarctic Rift System. Proceedings of a Workshop. Byrd Polar Research Center, The Ohio State University, Columbus, OH, pp. 1–57, BPRC Report No. 9.

Flower, B.P. and Kennett, J.P., 1994. The middle Miocene climatic transition: East Antarctic ice sheet development: Deep ocean circulation and global carbon cycling. Palaeogeogr. Palaeoclimatol. Palaeoecol., 108, 537–555.

Flowers, R. M., Ketcham, R.A., Shuster, D.L., Farley, K.A., 2009. Apatite (U–Th)/He thermochronometry using a radiation damage accumulation and annealing model. Geochim. Cosmochim. Ac., 73 (8), 2347–2365.

Flowers, R. M., 2009. Exploiting radiation damage control on apatite (U–Th)/He dates in cratonic regions. EPSL, 277, 148–155.

Gallagher, K., Brown, R., Johnson C., 1998. Fission track analysis and its applications to geological problems. Annu. Rev. Earth Planet., 26, 519–72.

Gallagher, K., Stephenson, J., Brown, R., Holmes, C. and Fitzgerald, P., 2005. Low temperature thermochronology and modelling strategies for multiple samples 1: vertical profiles. EPSL, 237, 193-208.

Gallagher, K., 2012. Transdimensional inverse thermal history modelling for quantitative thermochronology, J. Geophys. Res. (Solid Earth).

GANOVEX Team, 1987. Explanatory Notes of the Geological Maps 1:500 000 of North Victoria Land, Antarctica. Geol. Jb., B66.

Gleadow, A.J.W., 1981. Fission-track dating methods: What are the real alternatives? In: Nucl.Tracks, 5 (1-2), 3-14.

Gleadow, A.J.W. and Duddy, I.R., 1981. A Natural Long-Term Track Annealing Experiment for Apatite. Nuclear Tracks, 5, 169-174.

Gleadow, A.J.W., Kelvey, B.C., Ferguson, K.U., 1984. Uplift History of the Transantarctic Mountains in the Dry Valleys area, Antarctica, from AFT ages. New. Zeal. J. Geol. Geophys., 457-464.

Gleadow, A.J.W., 1984. AFT dating methods II: A manual of principles and techniques. In: Workshop on AFT Analysis; Principles and Applications. James Cook University, Townsville.

Gleadow, A.J.W., and Fitzgerald, P.F., 1987. Uplift history and structure of the Transantarctic Mountains: New evidence from fission track dating of basement apatites in the Dry Valleys area, southern Victoria Land. ESPL, 82, 1-14.

Goodge, J.W., 2007. Metamorphism in the Ross orogen and its bearing on Gondwana margin tectonics Geol. Soc. Amer. Spec. Pap., 419, 185-203.

Goodge, J.W., Fanning, C.M., Norman, M.D. and Bennett, V.C., 2012. Temporal, Isotopic and Spatial Relations of Early Paleozoic Gondwana-Margin Arc Magmatism, Central Transantarctic Mountains, Antarctica. J. Petrol., 53(10), 2027-2065.

Green, P.F., 1981. A new look at statistics in fission-track dating. Nucl.Tracks, 5, 77-86.

Green, P.F., 1985. A comparison of zeta calibration baselines in zircon, sphene and apatite. Chem. Geol. (Isot. Geosci. Sect.) 58, 1–22.

Green, P.F., 1986. On the thermo-tectonic evolution of Northern England: Evidence from AFT analysis. Geol. Mag., 123, 493-506.

Green, P.F., Duddy, I.R., Gleadow, A.J.W., Tingate, P.R. and Laslett, G.M., 1986. Thermal annealing of AFT in apatite 1. A qualitative description: Chem. Geol., 59, 237-253.

Heimann, A., Fleming, T.H., Elliot, D.H., Foland, K.A., 1994. A short interval of Jurassic continental flood basalt volcanism in Antarctica as demonstrated by 40Ar/39Ar geochronology. EPSL, 121, 19–41.

Hornig, I., 1993. High-Ti and Low-Ti Tholeiites in the Jurassic Ferrar Group, Antarctica. Geol. Jahrb., E 47, 335–369.

House, M., Farley, K., Stockli, D., 2000. Helium chronometry of apatite and titanite using Nd-YAG laser heating. EPSL, 183, 365–368.

Hurford, A.J. and Green, P.F., 1982. A users' guide to AFT dating calibration. EPSL 59, 343-354.

Hurford, A.J. and Green, P.F. 1983. The zeta age calibration of AFT dating. Chem. Geol. (Isotope Geoscience Section), 1, 285-317.

Jacobs, J. and Lisker, F., 1999. Post-Permian tectono-thermal evolution of western Dronning Maud Land, E-Antarctica: an apatite fission-track approach. Antarctic Science, 11, 451-460.

Jenkyns, H. C., Schouten-Huibers, L., Schouten, S., Sinninghe Damsté, J. S., 2012. Warm Middle Jurassic–Early Cretaceous high-latitude sea-surface temperatures from the Southern Ocean. Clim. Past, 8, 215-226.

Kerr, A., and Huybrechts, P., 1999. The response of the East Antarctic ice sheet to the evolving tectonic configuration of the Transantarctic Mountains. Global Planet Change, 23, 213-229.

Ketcham, R.A., Donelick, R.A., Carlson, W.D., 1999. Variability of apatite fission-track annealing kinetics III: Extrapolation to geological time scales. Amer. Mineral., 84, 1235-1255.

Ketcham, R.A., 2005. Forward and inverse modeling of low-temperature thermochronometry data. Rev. Mineral. Geochem. 58, 275-314.

Ketcham, R.A., Carter, A.C., Donelick, R.A., Barbarand, J., Hurford, A.J., 2007. Improved measurement of fission-track annealing in apatite using c-axis projection. Am. Mineral., 92, 789–798.

Laslett, G.M., Kendall, W.S., Gleadow, A.J.W., Duddy, I.R., 1982. Bias in measurement of fission-track length distributions, Nucl.Tracks, 6, 79-85.

Laslett, G.M., Galbraith, R., Green, P.F., 1994. The analysis of projected fission track lengths, Nucl. Tracks, 23, 103–23.

LeMasurier, W. E. and Thomson, J. W., 1990. Volcanoes of the Antarctic plate and Southern Oceans. Antarctic Research Series, 48. Washington D.C., American Geophysical Union.

Lisker, F., 2002. Review of AFT studies in northern Victoria Land – Passive margin evolution versus uplift of the Transantarctic Mountains. Tectonophysics, 349(1-4), 57-73.

Lisker, F., Läufer, A., Rossetti, F., Olesch, M., Schäfer, T., 2006. The Transantarctic Beacon Basin: New insights from AFT data and structural data from the USARP Mountains and adjacent areas (northern Victoria Land, Antarctica). Basin Res., 18 (4), 315-340.

Lisker F and Läufer A, 2007. A Cretaceous Victoria Basin between Australia and Antarctica inferred from volcanoclastic deposits, thermal indications and thermochronological data. USGS OF-2007-1047, Extented Abstract 211.

Lisker, F. and Läufer, A.L., 2011. Thermochronological research in northern Victoria Land (Antarctica): a key to the final pre-disintegration palaeogeography of Panthalassian Gondwana. Polarforschung, 80 (2), 100-110.

Lisker, F. and Läufer, A.L., 2013. The Mesozoic Victoria Basin: Vanished link between Antarctica and Australia. Geology, doi: 10.1130/G33409.1.

Long, A., Rippeteau, B., 1974. Testing contemporaneity and averaging radiocarbon dates. Am. Antiquity, 39 (2), 205– 215.

Meesters, A. and Dunai, T., 2002. Solving the production–diffusion equation for finite diffusion domains of various shapes part 2, application to cases with alpha ejection and non-homogeneous distribution of the source. Chem. Geol., 186, 3–4, 345–363.

Merino, E., Girard, J.-P., May, M.T., Ranganathan, V., 1997. Diagenetic mineralogy, geochemistry, and dynamics of Mesozoic arcoses, Hartford rift basin, Connecticut, U.S.A.: J. Sed. Res., 67, 212-224.

Middleton, G.V. and Wilcock, P.R., 1994. Mechanics in the Earth and Environmental Sciences, Cambridge University Press, Cambridge, 459 pp.

Mitchell, M.M., 1997. Elevated mid-Cretaceous palaeotemperatures in the western Otway Basin: consequences for hydrocarbon generation models. Aust. Pet. Explor. Assoc. J., 37, 505–523.

Molzahn, M., Wörner, G., Henjes-Kunst, F., Rocholl, A., 1999. Constraints on the Cretaceous thermal event in the Transantarctic Mountains from alteration processes in Ferrar flood basalts: Global Planet. Change, 23, 45-60.

Moore, M. E., Gleadow ,A. J.W., Lovering, J. F., 1986. Thermal evolution of rifted continental margins: new evidence from fission. EPSL, 78, 255-270.

Morad, S., Bergan, M., Knarud, R., Nystuen, J.P., 1990. Albitization of Detrital Plagioclase in Triassic Reservoir Sandstones from the Snorre Field, Norwegian North Sea: J. Sed. Petrol. 60, 411-425.

Müller, P., Schmidt-Thome, M., Kreuzer, H., Tessensohn, F., Vetter, U., 1990. Cenozoic peralkaline magmatism at the western margin of the Ross Sea, Antarctica, Mem. Soc. Geol. Ital., 43, 315–336.

Musumeci, G., Pertusati, P.C., Ribecai, C., Meccheri, M., 2006. Early Jurassic fossiliferous black shales in the Exposure Hill Formation, Ferrar Group of northern Victoria Land, Antarctica. Terra Antartica Rep., 12, 91.

Naeser N.D., Naeser C.W., McCulloh T.H., 1989. The application of fission-track dating to the depositional and thermal history of rocks in sedimentary basins. In: Naeser, N. D. and McCulloh, T. H. (Eds), Thermal History of Sedimentary Basins. Springer-Verlag, 157-180.

Noh, J.H. and Boles, J.R., 1993. Origin of zeolite cements in the Miocene sandstones, North Tejon oil fields, California: J. Sed. Petrol., 63, 248-260.

Oberholzer, P., Baroni, C., Schaefer, J.M., Orombelli, G., Ivy- Ochs, S., Kubik, P.W., Baur, H., Wieler, R., 2003. Limited Pliocene/ Pleistocene glaciation in Deep Freeze Range, northern Victoria Land, Antarctica, derived from in-situ cosmogenic nuclides. Antarct. Sci., 15, 493.

O'Sullivan, P.B. and Parrish, R.R., 1995. The importance of apatite composition and single-grain ages when interpreting AFT data from plutonic rocks: a case study from the Coast Ranges, British Columbia. EPSL, 132, 213-224.

Pfuhl, H.A. and McCave, I.N., 2005. Evidence for late Oligocene establishment of the Antarctic Circumpolar Current..EPSL, 235, 715-728.

Poole, I., Cantrillc, D., Utescher, T., 2005. A multi-proxy approach to determine Antarctic terrestrial palaeoclimate during the Late Cretaceous and Early Tertiary. Palaeogeogr. Palaeoclimatol. Palaeoecol., 222, 95–121.

Prenzel, P., Lisker, F., Balestrieri, M.L., Läufer, A., Spiegel, C., 2013. The Eisenhower Range, Transantarctic Mountains: A natural laboratory to evaluate qualitative interpretation concepts of thermochronological data. Chem. Geol., 352, 176-187.

Prenzel, P., Lisker, F., Schöner, R., Elsner, M., Balestrieri, M.L., Läufer, A., Spiegel, C., in review. Burial and exhumation of the Eisenhower Range, Transantarctic Mountains – Results from apatite fission track and (U-Th-Sm)/He-data, …, in review.

Priestley, R. E. and David, T. W. E, 1912. Geological notes of the British Antarctic Expedition,1907-09, Proceeding of the 11th International Geological Congress, Stockholrn, 2, 2767-811.

Ritter, U., 1984. The Influence of time and temperature on vitrinite reflectance. Organic Geochemistry, 6, 473-480.

Rossetti, F., Lisker, F., Storti, F., Läufer, A., 2003. Tectonic and denudational history of the Rennick Graben (northern Victoria Land): Implications for the evolution of rifting between East and West Antarctica. Tectonics, 22(2), 1016.

Rossetti, F., Storti, F., Busetti, M., Lisker, F., Di Vincenzo, G., Läufer, A.L., Rocchi, F., Salvini, F., 2006. Eocene initiation of Ross Sea dextral faulting and implications for East Antarctic neotectonics. J. Geol. Soc., London, 163, 119-126.

Salvini, F., G. Brancolini, M. Busetti, F. Storti, F. Mazzarini,, F. Coren (1997), Cenozoic geodynamics of the Ross Sea Region, Antarctica: Crustal extension, intraplate strike-slip faulting and tectonic inheritance. J. Geophys. Res., 102, 24, 669 – 696.

Salvini, F. and Storti, F., 1999. Cenozoic tectonic lineaments of the Terra Nova Bay region, Ross Embayment. Antarctica, Global Planet. Sci., 23, 129 – 144.

Schöner, R., Viereck-Goette, L., Schneider, J., Bomfleur, B., 2007. Triassic-Jurassic sediments and multiple volcanic events in North Victoria Land, Antarctica: A revised stratigraphic model. In Cooper, A.K., Raymond, C.R., and others, eds., Antarctica: A Keystone in a Changing World – Online Proceedings of the 10th ISAES: Washington, DC, The National Academies Press.

Schöner, R., Bomfleur, B., Schneider, J., Viereck-Götte, L., 2011. A systematic description of the Triassic to Lower Jurassic Section Peak Formation in North Victoria Land (Antarctica). Polarforschung, 80 (2), 71-87.

Shuster, D. L., Flowers, R. M., Farley, K. A, 2006. The influence of natural radiation damage on He diffusion kinetics in apatite. EPSL, 249, 148–161.

Skinner, D.N.B. and Ricker, J., 1968. The geology of the region between the Mawson and Priestley Glaciers, North Victoria Land, Antarctica. New Zea. J. Geol. Geoph., 11-4, 1041-1075.

Spiegel, C., Kohn, B., Belton, D., Berner, z., Gleadow, A., 2009. Apatite (U–Th–Sm)/He thermochronology of rapidly cooled samples: The effect of He implantation. EPSL, 285, 105-114.

Stern, T.A., Baxter, A.K., Barrett, P.J., 2005. Isostatic rebound due to glacial erosion within the Transantarctic Mountains. Geology, 33-3, 221-224.

Stickley, C.E. , Brinkhuis, H., Schellenberg, S.A., Sluijs, A., Röhl, U., Fuller, M., Grauert, M., Huber, M., Warnaar, J. and Williams, G.L., 2004. Timing and nature of the deepening of the Tasmanian Gateway. Paleoceanography, 19, PA4027.

Storti, F., Rossetti, F., Salvini, F., 2001. Structural architecture and displacement accommodation mechanisms at the termination of the Priestley Fault, northern Victoria Land, Antarctica. Tectonophysics, 341, 141 – 161.

Storti, F., Rossetti, F., Läufer, A.L., Salvini, F., 2006. Consistent kinematic architecture in the damage zones of intraplate strike-slip fault systems in North Victoria Land, Antarctica, and implications for fault zone evolution. J. Struc. Geol., 28, 50-63.

Storti, F., Salvini, F., Rossetti, F., Phipps Morgan, J., 2007. Intraplate termination of transform faulting within the Antarctic continent. EPSL, 260, 115–126

Storti, F., Balestrieri, M.L., Balsamo, F., Rossetti, F., 2008. Structural and thermochronological constraints to the evolution of the West Antarctic Rift System in central Victoria Land. Tectonics, 27, TC4012.

Strand, K., Passchier, S., and Näsi, J., 2003. Implications of quartz grain microtextures for onset Eocene/Oligocene glaciation in Prydz Bay, ODP site 1166, Antarctica. Palaeogeogr. Palaeoclimatol. Palaeoecol., 198, 101–111.

Stump, E., 1995. The Ross Orogen of the Transantarctic Mountains. Cambridge University Press, Cambridge, 284 p.

Sugden, D.E. and Denton, G.H., 2004, Cenozoic landscape evolution of the Convoy Range to McKay Glacier area, Transantarctic Mountains: Onshore to offshore synthesis. Geol. Soc. Am. Bull., 116, 840–857.

Summerfield, M.A., Stuart, F.M., Cockburn, H.A.P., Sugden D.E., Denton, G.H.. Dunai, T., Marchant, D.R., 1999. Long-term rates of denudation in the Dry Valleys, Transantarctic, Mountains, southern Victoria Land, Antarctica based on in-situ-produced cosmogenic ^{21}Ne. Geomorphology, 27, 113–129.

Sweeny, J.J. and Burnham, A.K., 1990. Evaluation of a simple model of vitrinite reflectance based on chemical kinetics. AAPG Bulletin, 74, 1559–1570.

Taylor, B., 1969. Methodus Incrementorum Directa et Inversa [Direct and Reverse Methods of Incrementation]. London, 1715, 21–23 (Proposition VII, Theorem 3, Corollary 2). Translated into English in D. J. Struik, A Source Book in Mathematics 1200–1800. Cambridge, Massachusetts: Harvard University Press, 1969), 329–332.

Thorn, V.C. and DeConto, R., 2006. Antarctic climate at the Eocene/Oligocene boundary — climate model sensitivity to high latitude vegetation type and comparisons with the palaeobotanical record. Palaeogeogr. Palaeoclimatol. Palaeoecol., 231, 134–157.

Tissot, B.P. and Welte, D.H.,1984. Petroleum Formation and Occurence, Springer, Berlin, 699.

Tonarini, S., Rocchi, S., Armienti, P., Innocenti, F., 1997. Constraints on timing of Ross Sea rifting inferred from Cainozoic intrusions from northern Victoria Land, Antarctica. in The Antarctic Region: Geological Evolution and Processes, edited by C. A. Ricci, 511 – 521, Terra Antartica Publ., Siena.

Truswell, E.M. and Drewry, D.J., 1984. Distribution and provenance of recycled palynomorphs in surficial sediments of the Ross Sea, Antarctica: Mar. Geol., 59/1-4, 187–214.

U.S. Department of the Interior, 1968a. Topographic Reconnaissance Map Mount Melbourne, Antarctica. 1:250,000 U.S. Geological Survey, Washington DC.

U.S. Department of the Interior, 1968b. Topographic Reconnaissance Map Mount Murchison, Antarctica. 1:250,000 U.S. Geological Survey, Washington DC.

U.S. Department of the Interior, 1968c. Topographic Reconnaissance Map Reeves Neve, Antarctica. 1:250,000 U.S. Geological Survey, Washington DC.

U.S. Department of the Interior, 1968d. Topographic Reconnaissance Map Sequence Hills, Antarctica. 1:250,000 U.S. Geological Survey, Washington DC.

Van der Wateren, F.M., Dunai, T.J., Van Balen, R.T., Klas, W., Verbers, A.L.L.M., Passchier, S., Herpers, U., 1999. Contrasting Neogene denudation of different structural regions in the Transantarctic Mountains rift flank constrained by cosmogenic isotope measurements. Global Planet. Change, 23, 145-172.

Veevers, J.J., 2006. Updated Gondwana (Permian-Cretaceous) earth history of Australia. Gondwana Res., 9, 231-260.

Vermeesch, P., 2010. HelioPlot, and the treatment of overdispersed (U-Th-Sm)/He data. Chem. Geol., 271 (3-4), 108-111.

Viereck-Götte, L., Schöner, R., Bomfleur, B. , Schneider, J., 2007. Multiple shallow level sill intrusions coupled with hydromagmatic explosive eruptions marked the initial phase of Ferrar large igneous province magmatism in nVL, Antarctica. In Cooper, A.K., Raymond, C.R., and others, eds., Antarctica: A Keystone in a Changing World – Online Proceedings of the 10th ISAES: Washington, DC, The National Academies Press.

Villa G., Persico D., Wise S., Gadaleta A., 2011. Calcareous nannofossil evidence for Marine Isotope Stage 31 (1 Ma) in Core AND-1B,ANDRILL McMurdo Ice Shelf Project (Antarctica). Global Planet. Change, 96/97, 75-86.

Wagner, G.A., 1972. The geological interpretation of fission track ages. Trans. Am. Nucl. Soc., 15, 117.

Wagner, G.A., Gleadow, A.J.W., Fitzgerald, P.G., 1989. The significance of the partial annealing zone in AFT analysis: Projected track length measurements and uplift chronology of the Transantarctic Mountains. Chem. Geol., 79, 295-305.

White, L.T., Gibson, G.M., Lister, G.S., 2013. A reassessment of paleogeographic reconstructions of eastern Gondwana: Bringing geology back into the equation. Gondwana Research, 24, 984–998.

Wolf, R.A., Farley, K.A., Kass, D.M., 1998. A sensitivity analysis of the apatite (U-Th)/He thermochronometer, Chem. Geol., 148, 105-114.

Worden, R.H. and Burley, S.D., 2003. Sandstone diagenesis: the evolution of sand to stone, in Worden, R.H. and Burley, S.D., eds., Sandstone Diagenesis: Recent and Ancient: Oxford, Reprint Series 4 of the Int. Ass. Sediment., 3-44.

Wörner, G., 1990. Kirkpatrick Lavas, Exposure Hill Formation and Ferrar Sills in the Prince Albert Mountains, Victoria Land, Antarctica. Polarforschung, 60, 2, 87-90.